

A Thesis Submitted for the Degree of PhD at the University of Warwick

Permanent WRAP URL:

<http://wrap.warwick.ac.uk/144585>

Copyright and reuse:

This thesis is made available online and is protected by original copyright.

Please scroll down to view the document itself.

Please refer to the repository record for this item for information to help you to cite it.

Our policy information is available from the repository home page.

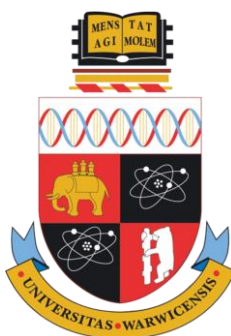
For more information, please contact the WRAP Team at: wrap@warwick.ac.uk

Thermally-induced chemical transformations and self-assembly of short peptides on metal surfaces

by

Jonathan D Blohm

A thesis submitted in partial fulfilment of the requirements for
the degree of Doctor of Philosophy in Chemistry



University of Warwick, Department of Chemistry

March 2020

Contents

List of Figures and Tables.....	V
Acknowledgments.....	XV
Declaration.....	XVI
Abstract.....	XVII
List of Abbreviations	XVIII
Chapter 1: Introduction	1
1.1 Practical applications of short peptides.....	1
1.2 The self-assembly of small molecules on metal surfaces	6
1.3 Characterising self-assembly on a surface.....	10
1.4 Thermally-induced chemical transformation of short peptides.....	12
1.5 Self-assembly of short peptides on surfaces	14
1.6 Project goals and thesis structure.....	14
1.7 References	18
Chapter 2: Experimental	28
Experimental and theoretical methods.....	28
2.1 UHV STM	28
2.1.1 Theoretical background: Scanning Tunnelling Microscopy	28
2.1.2 UHV	31
2.1.3 STM instrument	32
2.1.4 UHV system design	36
2.1.5 Samples and preparation.....	37
2.1.6 Organic Molecular Beam Epitaxy.....	40
2.1.7 STM data gathering.....	42
2.2 Additional experimental techniques and theoretical methods.....	43
2.2.1 Mass spectrometry	43
2.2.2 Sublimability tests.....	44
2.2.3 X-ray Photoelectron Spectroscopy	46
2.2.4 Molecular models and simulations.....	47
2.3 References	51
Chapter 3: Design and construction of a new UHV-STM system.....	54
3.1 Design philosophy.....	54
3.2 STM head	55
3.3 Vacuum chamber design.....	57

3.4 Support frame and baking tent design	63
3.4 Final system build	67
Chapter 4: The sublimation of short peptides	70
4.1 Background	70
4.2 Sublimation of the alanine series of peptides	72
4.2.1 L-Alanine	73
4.2.2 Di-(L)-Alanine	73
4.2.3 Tri-(L)-Alanine.....	74
4.2.4 Tetra-(L)-Alanine	75
4.2.5 Penta-(L)-Alanine	76
4.3 Sublimation of the phenylalanine series of peptides	77
4.3.1 L-Phenylalanine.....	77
4.3.2 Di-(L)-Phenylalanine.....	78
4.3.3 Tri-(L)-Phenylalanine.....	78
4.3.4 Tetra-(L)-Phenylalanine.....	79
4.4 Conclusions	80
4.5 Addendum: additional peptides	82
4.6 References	83
Chapter 5: Chemical transformations of the Phe-Phe dipeptide	85
5.1 Background	85
5.2 Scanning tunnelling microscopy	87
5.2.1 L-Phe-L-Phe	87
5.2.2 Cyclo-(L-Phe-L-Phe) – cFF.....	90
5.2.3 Dehydrogenated Cyclo-(L-Phe-L-Phe).....	98
5.3 X-Ray Photoelectron Spectroscopy.....	105
5.3.1 Dehydrogenated Cyclo-(L-Phe-L-Phe).....	105
5.3.2 Cyclo-(L-Phe-L-Phe)	107
5.3.3 L-Phe-L-Phe	109
5.4 Concluding remarks	112
5.5 References	114
Chapter 6: Self-assembly of aromatic dipeptides on metal surfaces	116
6.1 Self-assembly of D-Phe-L-Phe and L-Phe-D-Phe on metal surfaces.....	116
6.1.1 Background	116
6.1.2 Sublimation of DFLF and LFDF.....	116
6.1.3 Self-assembly of cFF(L/D) on Cu(110)	118
6.1.4 Self-assembly of cFF(L/D) on Au(111).....	123

6.1.5 Concluding remarks	126
6.1.6 References	128
6.2 Self-assembly of L-Tyr-L-Tyr on metal surfaces	129
6.2.1 Background	129
6.2.2 Sublimation of L-Tyr-L-Tyr.....	130
6.2.3 Self-assembly of Cyclo-(L-Tyr-L-Tyr) on Gold (111): Scanning Tunnelling Microscopy.....	131
6.2.4 Self-assembly of Cyclo-(L-Tyr-L-Tyr) on Gold (111): Density Functional Theory and Molecular Dynamics.....	137
6.2.5 Self-assembly of Cyclo-(L-Tyr-L-Tyr) on Gold (111): X-Ray Photoelectron Spectroscopy.....	144
6.2.6 Effect of annealing on the self-assembly of Cyclo-(L-Tyr-L-Tyr) on Gold (111): Scanning Tunnelling Microscopy.....	146
6.2.7 Effect of annealing on the self-assembly of Cyclo-(L-Tyr-L-Tyr) on Gold (111): Density Functional Theory and Molecular Dynamics	150
6.2.8 Effect of annealing on the self-assembly of Cyclo-(L-Tyr-L-Tyr) on Gold (111): X- Ray Photoelectron Spectroscopy	155
6.2.9 Partial annealing of Cyclo-(L-Tyr-L-Tyr) on Gold (111).....	157
6.2.10 Self-assembly of Cyclo-(L-Tyr-L-Tyr) on Cu (110)	158
6.2.11 Self-assembly of Cyclo-(L-Tyr-L-Tyr) on Cu (110): Scanning Tunnelling Microscopy.....	159
6.2.12 Self-assembly of Cyclo-(L-Tyr-L-Tyr) on Cu (110): Density Functional Theory..	163
6.2.13 Effect of annealing on the self-assembly of Cyclo-(L-Tyr-L-Tyr) on Cu(110): Scanning Tunnelling Microscopy.....	164
6.2.14 Effect of annealing on the self-assembly of Cyclo-(L-Tyr-L-Tyr) on Cu(110): Density Functional Theory	171
6.2.15 Concluding remarks	172
6.2.16 References	174
6.3 Self-assembly of L-Trp-L-Trp on metal surfaces.....	178
6.3.1 Background	178
6.3.2 Sublimation of L-Trp-L-Trp	178
6.3.3 Self-assembly of Cyclo-(L-Trp-L-Trp) on Cu(110)	179
6.3.4 Self-assembly of Cyclo-(L-Trp-L-Trp) on Au(111)	187
6.3.5 Conclusion.....	188
6.3.6 References	190
Chapter 7: Conclusions	191
7.1 Conclusion and outlook	191
7.2 References	197

List of Figures and Tables

Figure 1.1: a) Top-down Scanning Electron Microscopy image of vapour-deposited dipeptide nanotubes. b) Side view of vertically aligned nanotubes; thickness 40 μ m. Both adapted from reference [25].	2
Figure 1.2: The general structure of a 2,5-diketopiperazine, or DKP. The R groups represent the unaltered side chains of the original peptide residues.	3
Figure 1.3: Gold nanoparticles (GNPs) functionalised with peptides used to detect Hg ²⁺ ions in solution. A colour change from red to purple is observed, which can be reversed with EDTA sequestration. Reproduced from reference [82].	5
Figure 1.4: The hierarchy of protein self-assembly structures, using a model peptide. Image by Thomas Shafee, distributed under a CC-BY 4.0 license.	9
Figure 1.5: Schematic representation of an STM experiment, in constant current mode. A voltage, V , is applied between tip and sample, and a current, I , measured and stabilised via a feedback loop. Piezoelectric actuators control movement of the tip on the x , y and z axes. Further details can be found in chapter 2, Experimental. Image adapted from reference [110].	10
Figure 1.6: STM images of: a) A deposition of L-Phe-L-Phe molecules on Cu(110), annealed to 400K. b) The same deposition annealed to 450K. The evident change in self-assembly pattern was attributed to conformational change. Adapted from reference [118].	13
Figure 2.1. Schematic of energy level alignment and quantum tunnelling at a metal-surface interface, with separation d along an arbitrary distance axis z , against an energy axis E . Subscript t denotes the tip and s the surface. a) The Fermi energies are shown equal (i.e. the same material), meaning no net current will flow. b) The effect of applying a potential bias V is seen, in this case favouring net electron flow from tip to surface. The now favourable energy difference is indicated by the dashed lines.	29
Figure 2.2. a) Image of the STM head from the SPECS Aarhus advertising material, b) Sample plate (orange) inserted into the STM (green), inverted so that the mounted sample faces the tip approaching from below.	32
Figure 2.3. Illustration of the operation of a piezo inchworm motor. Black colouration indicates the active piezos in each step, with the arrows showing the direction of movement. After step 6, the cycle repeats as necessary. Image in the public domain.	34
Figure 2.4. Room temperature STM image of a typical Au(111) herringbone reconstruction pattern, captured using the SPECS Aarhus system described in this thesis. The bright lines mark the boundary between fcc and hcp regions.	39
Figure 2.5. a) Render of a standard sample holder plate, without mounted sample. b) Photograph of a sample holder inserted into the manipulator arm, protruding as highlighted in blue. The wobblestick is visible below.	39
Figure 2.6. The system used for testing the sublimation of peptide samples, with key sections highlighted. Green: Central chamber for target slides; Blue: QCM apparatus above the main chamber, in-line with the deposition beam ; Orange: Crucible furnace mounted below the main chamber; Red: transfer arm with pressure gauge below.	46

Figure 2.7. Energy-minimised model of cyclo-(L-Tyr-L-Tyr) using the MMFF94 force field. Similar structures can be found across the literature, for example see refs. 34, 42, and 46.	50
Figure 3.1. The Aarhus STM 150. This a standardised model provided by SPECS, and as such some components will appear different to the real product. In particular, the radiation shields fitted to our system are absent in the diagram, and the optional AFM assembly shown was not purchased.	57
Figure 3.2. a) The analysis chamber, with pumps and other external components hidden for clarity. b) View through the main analysis chamber viewport.	59
Figure 3.3. Overhead view of the full system, with the analysis chamber highlighted green and the preparation chamber highlighted red. The central axis along which the manipulator arm travels is indicated in blue. All system functions can be accessed with only small deviations from this axis.	59
Figure 3.4. a) The preparation chamber, with pumps and other external components hidden for clarity. b) Rear view, with OMBD apparatus mounted.	61
Figure 3.5. The compact vertical loadlock chamber.	62
Figure 3.6. The manipulator head, viewed from the side accessed by the wobblesticks. Blank sample plates can be seen highlighted in green.	63
Figure 3.7. The support frame structure and complete set of chambers. The preparation chamber ion pump is shown to illustrate the role of the supporting plate.	63
Figure 3.8. a) Frame-mounted support for the manipulator arm, highlighted in green. b) Steel plate and springs mounted under the ion pump to partition its heavy load, highlighted green.	64
Figure 3.9. Side views of the full system, divided into major sections by colour. The analysis chamber is highlighted green, the preparation chamber red, the loadlock orange and the manipulator blue. Top: viewed from the 'front' side where the wobblesticks are accessed. Bottom: viewed from the 'back' side where the STM is mounted.	65
Figure 3.10. Side and overhead views of the system with the baking tent model in blue... ..	67
Figure 3.11. Photographs of the constructed system. Above: viewed from the 'front' side where the wobblesticks are accessed. Left: viewed from the 'back' side where the STM is mounted.	68
Figure 3.12. Photograph of the baking tent, viewed from the back (STM) side of the system.	69
Figure 4.1. a) General structure of a peptide with n repeat units. b) Structure of L-Alanine c) Structure of L-Phenylalanine.	72
Figure 4.2. Mass spectra of [top] non-sublimed L-Alanine and [bottom] L-Alanine sublimed at 423K. Molecular ion occurs at $\sim m/z$ 90.	73
Figure 4.3. Mass spectra of [top] non-sublimed Di-L-Alanine and [bottom] Di-L-Alanine sublimed at 423K. Molecular ion occurs at $\sim m/z$ 161.	73
Figure 4.4. Mass spectra of [top] non-sublimed Tri-L-Alanine and [bottom] Tri-L-Alanine sublimed at 463K. Molecular ion occurs at $\sim m/z$ 232.	74

Figure 4.5. Mass spectra of [top] non-sublimed Tetra-L-Alanine and [bottom] Tetra-L-Alanine sublimed at 523K. Molecular ion occurs at $\sim m/z$ 303.	74
Figure 4.6. Mass spectra of [top] non-sublimed Penta-L-Alanine and [bottom] Penta-L-Alanine sublimed at 533K. Molecular ion occurs at $\sim m/z$ 374.	76
Figure 4.7. Mass spectrum of Penta-L-Alanine from a crucible heated to 533K.	76
Figure 4.8. Mass spectra of [top] non-sublimed L-Phenylalanine and [bottom] L-Phenylalanine sublimed at 378K. Molecular ion occurs at $\sim m/z$ 166.	77
Figure 4.9. Mass spectra of [top] non-sublimed Di-L-Phenylalanine and [bottom] Di-L-Phenylalanine sublimed at 413K. Molecular ion occurs at $\sim m/z$ 313.	77
Figure 4.10. Mass spectra of [top] non-sublimed Tri-L-Phenylalanine and [bottom] Tri-L-Phenylalanine sublimed at 473K. Molecular ion occurs at $\sim m/z$ 460.	78
Figure 4.11. Mass spectra of [top] non-sublimed Tetra-L-Phenylalanine and [bottom] Tetra-L-Phenylalanine sublimed at 473K. i) Spectra featuring the group of peaks around the molecular ion, occurring at $\sim m/z$ 607. ii) Spectra focusing on the main fragment peaks....	79
Figure 5.1. Molecular structures of i) L-Phe-L-Phe, ii) Cyclo-(L-Phe-L-Phe) or cFF, iii) singly dehydrogenated Cyclo-(L-Phe-L-Phe) or sdcFF, and iv) doubly dehydrogenated Cyclo-(L-Phe-L-Phe) or ddcFF.	86
Figure 5.2. a) Typical STM image of a deposition of L-Phe-L-Phe on room temperature Cu(110), illustrating the chains and smaller clusters commonly observed. b) At low temperature (77K), the small clusters dominate, and chains are absent.	87
Figure 5.3. Analysis of the orientation of the molecular chains with respect to the $[1\bar{1}0]$ axis, and the orientation and periodicity of molecular features. A scaled model of L-Phe-L-Phe is superimposed for illustrative purposes.	87
Figure 5.4. Appearance of a deposition of L-Phe-L-Phe after annealing to 400K. The new chain orientation with respect to the $[1\bar{1}0]$ axis is indicated. Note that some chains, as illustrated in b), feature defects with molecules offset from their nearest neighbours.	88
Figure 5.5. Comparison of the measured size (FWHM) of molecular features in the pre-anneal STM images with predicted lengths of L-Phe-L-Phe and Cyclo-(L-Phe-L-Phe) from gas-phased minimised Avogadro models. Scaled models of each molecule are also overlain onto the STM image for illustration.	89
Figure 5.6. Models of both L-Phe-L-Phe (a) and Cyclo-(L-Phe-L-Phe) (b) overlaid onto the original self-assembly pattern. Potential hydrogen bonding is indicated with black dashed lines. Inset images are approximately 2.2nm x 2.2nm.	90
Figure 5.7. Typical STM image of a deposition of cFF on room temperature Cu(110).	91
Figure 5.8. A comparison of the chains observed for depositions of a) L-Phe-L-Phe and b) cFF. The chain orientations are also labelled with respect to the $[1\bar{1}0]$ axis of the surface.	91
Figure 5.9. Comparison of the key dimensions of molecular features in STM images from depositions of a) L-Phe-L-Phe and b) cFF. Scaled models of cFF are overlain for illustration.	92

Figure 5.10. STM images from a deposition of cFF annealed to 400K. The new chain orientation is indicated, and similar defects to the annealed deposition of L-Phe-L-Phe can be observed.	92
Figure 5.11. a) STM image from a low temperature (77K) experiment with cFF on Cu(110), illustrating the clusters observed. b) Low temperature image from a deposition of L-Phe-L-Phe, reproduced from Figure 5.2 for comparison.	93
Figure 5.12. Models of cFF overlaid onto the self-assembly pattern of cFF on Cu(110). Potential hydrogen bonding is indicated with black dashed lines. Inset image is approximately 2.0nm x 2.2nm.	95
Figure 5.13. Even as coverage is increased, cFF on Cu(110) resists island formation in favour of chains.	96
Figure 5.14. The molecular structures of cFF and ddcFF, with the location of the potential dehydrogenation reaction highlighted.	97
Figure 5.15. Gas-phase models of a) cFF, and b), ddcFF, demonstrating the difference in conformation between the two, especially from a side-view.	97
Figure 5.16. A comparison of STM data from a deposition of cFF, a) before annealing, and b) after annealing. The difference in contrast across a molecule is noticeable, and is highlighted with line profiles (dashed lines). Z(pm) values broadly correlate with molecular height. ...	98
Figure 5.17. Typical STM image from a deposition of ddcFF on Cu(110) at room temperature.	99
Figure 5.18. a) Models of two non-equivalent mirror image conformations of ddcFF, and how these might form mirror-image assemblies. b) Overlay of assembly models onto an STM image, demonstrating the equal prevalence of both conformations and therefore modes of assembly.	101
Figure 5.19. Irregular and asymmetrical clusters from a deposition of sdcFF on a low temperature (140K) Cu(110) surface.	103
Figure 5.20. High coverage of molecules adsorbed on Cu(110) and annealed to 450K, from a proposed deposition of L-Phe-L-Phe. As reproduced from Lingenfelder ⁵ . a) 15x10.4nm STM image, b) LEED pattern, c) 5x4nm high resolution STM image.	103
Figure 5.21. Brickwork pattern of ddcFF molecules on Cu(110), only observed at high coverage. Overlaid models indicate how the molecules might be arranged in order to produce such an assembly.	104
Figure 5.22. C 1s, N 1s and O 1s XPS spectra of a deposition of ddcFF on Cu(110). The raw data and background traces are in blue, while peak fittings are coloured red, orange and green, in order of ascending binding energy. The residual trace of combined peak fitting is in black, where applicable.	106
Figure 5.23. C 1s, N 1s and O 1s XPS spectra of a deposition of cFF on Cu(110). Raw data in blue, with peak fittings in red, orange and green, in order of ascending binding energy. The residual trace of combined peak fitting is in black, where applicable.	107
Figure 5.24. C 1s, N 1s and O 1s XPS spectra of cFF on Cu(110) after annealing to 400K. Raw data in blue, with peak fittings in red, orange and green, in order of ascending binding energy. The residual trace of combined peak fitting is in black, where applicable.	109

Figure 5.25. C 1s, N 1s and O 1s XPS spectra of cFF, deposited from a crucible of FF, on Cu(110). Raw data in blue, with peak fittings in red, orange and green, in order of ascending binding energy. The residual trace of combined peak fitting is in black, where applicable.	110
Figure 5.26. C 1s, N 1s and O 1s XPS spectra of cFF, deposited from a crucible of FF, on Cu(110) at high coverage. Raw data in blue, with peak fittings in red, orange and green, in order of ascending binding energy. The residual trace of combined peak fitting is in black, where applicable.	112
Figure 6.1. Mass spectra of a) DFLF and b) LFDF. In each set, the top spectra correspond to the non-sublimed molecules while the bottom spectra are from the sublimed material. The molecular ion in both cases occurs at $\sim m/z$ 313. The lack of peaks below m/z 300 illustrates that fragmentation does not occur. The peak at m/z 301.1 is a common plasticiser.	117
Figure 6.2. Molecular models of a) DFLF, b) LFDF, and c) cFF(L/D). Though the linear molecules are enantiomers, the cyclised product cFF(L/D) is the same in each case, since the N and C termini have formed an amide bond indistinguishable from the existing "peptide bond". cFF(L/D) therefore always has one L and one D stereocentre.	118
Figure 6.3. High coverage deposition of cFF(L/D) on Cu(110) annealed to 400K. A number of small islands containing ordered molecules are observed, with disordered material in the gaps between islands.	119
Figure 6.4. The two types of molecular island of cFF(L/D) on Cu(110), more clearly distinguished at a smaller image scale. Left: Island types indicated in green and blue. Right: the two islands types are shown to be mirror images of one another about the $[1\bar{1}0]$ plane (image size 5nm x 5nm).	120
Figure 6.5. Analysis of the distribution of cFF(L/D) island types on Cu(110). Across the surface an approximate 50:50 ratio is found.	121
Figure 6.6. Molecular models of cFF (left) and cFF(L/D) (right), viewed along the plane of the central ring. The differences at the chiral centres causes a different conformation to arise as the lowest energy structure.	121
Figure 6.7. Comparison of the molecular orientations of ddcFF (left) and ddcFF(L/D) (right) on Cu(110). The difference between the orientations is only a few degrees in each case. ddcFF image scales: 18.5nm x 18.5nm, inset 9.2nm x 9.2nm. ddcFF(L/D) image scale: image size 5nm x 5nm.	122
Figure 6.8. Proposed self-assembly pattern of ddcFF(L/D) molecules on Cu(110), enforced by the high coverage.	122
Figure 6.9. Large islands of self-assembled cFF(L/D) molecules on Au(111) oriented in various directions.	124
Figure 6.10. a) Proposed self-assembly model for cFF(L/D) on Au(111), b) A suggestion for how cFF molecules could theoretically hydrogen bond on Au(111), though such an assembly is a poor match for the resolved features in the STM image.	125
Figure 6.2.1. Molecular structures of i) L-Tyr-L-Tyr, and ii) Cyclo-(L-Tyr-L-Tyr).	129
Figure 6.2.2. Mass spectra of [top] non-sublimed L-Tyr-L-Tyr and [bottom] L-Tyr-L-Tyr sublimed at 515K. Molecular ion occurs at $\sim m/z$ 345.	130

Figure 6.2.3. Typical STM images from a deposition of cYY on Au(111). Molecules are only imaged within ordered islands such as these, in a range of orientations across the surface.	131
Figure 6.2.4. Sequential STM images of cYY on Au(111), with a time difference of approximately 180s. The outline of the original island in green illustrates the change that occurs between the two images.	132
Figure 6.2.5. Sampling the orientation of recorded islands, and plotting against the three surface orientations of the Au(111) surface underneath. The long axis of the gold herringbone, [112], is also indicated.	133
Figure 6.2.5. Sampling the orientation of recorded islands, and plotting against the three surface orientations of the Au(111) surface underneath. The long axis of the gold herringbone, [112], is also indicated.	134
Figure 6.2.7. Models of cYY overlaid on to the self-assembly pattern on Au(111), with key dimensions labelled. The gap between adjacent offset chains of molecules is apparent..	135
Figure 6.2.8. Enlarged view of the assembly of cYY on Au(111). Potential hydrogen bonding is indicated with black dashed lines. Inset image is approximately 2 nm x 2 nm.	135
Figure 6.2.9. Top-down view of mirror-image models of cYY, alongside potential landing conformations on the surface (adapted from DFT, see Figure 6.2.10). The non-equivalent nature of these “flipped” conformers with respect to the surface is apparent.	137
Figure 6.2.10. A comparison of the two landing conformations of cYY on Au(111). The adsorption of the “up” and “down” conformations are modelled, giving rise to the on-surface conformers “A” and “B”. The results of energy minimisation calculations by both DFT and the GoIP-CHARMM Force Field (FF) are also shown.	138
Figure 6.2.11. DFT Models of dimers of cYY in both surface conformations, to evaluate the energy gain from hydrogen bond formation. While DFT and FF energy calculations differ from one another, the overall result clearly indicates both species should form stable on-surface hydrogen bonds, cYY-B slightly more favourably.	139
Figure 6.2.12. Comparison of experimental cYY periodicity data with values obtained from a radial distribution function performed on MD simulations.	140
Figure 6.2.13. Images obtained from MD simulations of charged and neutral deprotonated cYY molecules in chains on Au(111). The results cannot reproduce the STM data, but do demonstrate the repulsion between, but not within, charged molecular chains.	141
Figure 6.2.14. Comparison of experimental cYY periodicity data with a radial distribution function of MD simulations of molecules in different charge states.	142
Figure 6.2.15. DFT models of a single cYY molecule on Au(111), with two gold adatoms. a) An unmodified, protonated cYY molecule. b) A doubly deprotonated molecule, with H atoms bonded independently to the adatoms. The energy minima of these systems were used to calculate the displayed energy cost of the on-surface deprotonation.	143
Figure 6.2.16. C 1s, N 1s and O 1s XPS spectra of a deposition of cYY on Au(111). The raw data and background traces are in blue, while peak fittings are red, orange and green, in order of ascending binding energy. The residual trace of combined peak fitting is in black, where applicable. The peak at 528eV is from trace antimony present on the surface. The N 1s spectrum has a rising background due to a large Au peak.	145

Figure 6.2.17. Typical STM images from a deposition of cYY on Au(111) annealed to 475K. Molecules are imaged exclusively in islands of this type, in a single orientation across the surface.	147
Figure 6.2.18. The dehydrogenation of cYY into ddcYY. Hydrogen atoms are lost across the alkyl carbons, creating an alkene group between each phenol group and the central diketopiperazine ring.	147
Figure 6.2.19. Sequential images of an island edge of annealed cYY on Au(111), illustrating the reversibility of the molecular interactions occurring at room temperature. Approximately 90s have passed between adjacent images.	149
Figure 6.2.20. Illustration of the “S” and “Z” type of molecular features observed in the assembly of annealed cYY on Au(111). These features are recognisable across the surface.	149
Figure 6.2.21. Overlaid models of ddcYY on the annealed assembly, demonstrating how the two types of ddcYY adsorption might give rise to the pattern observed, via a hydrogen-bonded network.	150
Figure 6.2.22. DFT models of the 2 viable stereoisomers of ddcYY on Au(111), in side and top-down views. DFT and GoIP-CHARMM Force Field (FF) calculations of the energy difference between the two adsorbed isomers are also presented, indicating the greater stability of the “X” species.	151
Figure 6.2.23. Gas phase models of the two adsorption modes of ddcYY, adjacent to archetypal S and Z molecular features from STM data on Au(111). The shape of each model broadly correlates to the shape of the STM features.	152
Figure 6.2.24. The progression of an MD simulation of 16 ddcYY molecules, 8 each of the S and Z-type species. The pre-ordered cluster remains stable at 450 K. Cell size $76 \times 79 \text{ \AA}^2$	153
Figure 6.2.25. Comparison of experimental ddcYY periodicity data with a radial distribution function from MD simulations.	153
Figure 6.2.26. A modified model of the assembly of ddcYY on Au(111), using molecular conformations arising from the computational data. The potential for hydrogen bonding between phenol groups and proximal amide groups is indicated with black dashed lines. Inset image is approximately 2.2 nm x 2.2 nm.	154
Figure 6.2.27. C 1s, N 1s and O 1s XPS spectra of a deposition of annealed cYY on Au(111). The raw data and background traces are in blue, while peak fittings are red, orange and green, in order of ascending binding energy. The residual trace of combined peak fitting is in black, where applicable. The peak at 528eV is from trace antimony present on the surface. The N 1s spectrum has a rising background due to a large Au peak.	155
Figure 6.2.28. STM data from the partial annealing of cYY on Au(111), displaying an island of mixed molecular features. a) Examples of how cYY and ddcYY could fit the assembly: a cYY pair highlighted green, a ddcYY pair highlighted blue, and a mixed pair in red. b) An illustration of hydrogen bonding possibilities, with a particular focus on the end-to-end phenolic bonding. Inset image is approximately 2.2nm x 2.2nm.	157
Figure 6.2.29. Typical STM data from a deposition of cYY on Cu(110). Though the molecules are highly mobile, the vast majority of stable images display chains of molecules in the same orientation, as demonstrated here.	159

Figure 6.2.30. a) Overlay of a single cYY conformer to illustrate how the chains might be assembled on Cu(110). Periodicity standard deviation: 0.19Å b) Suggested surface-mapped overlay of cYY molecules based on established surface orientations for the Cu(110) crystal in use. The rows of atoms presenting “top” sites are coloured green, with alternate rows coloured brown. 160

Figure 6.2.31. Typical STM image of cYY on Cu(110) at high coverage (approximately 0.85 monolayers). Large numbers of small and moderately sized chains can be seen, while no condensation into large islands is observed. 161

Figure 6.2.32. A side-by-side comparison of STM images of a) cYY on Cu(110), and b) cFF on Cu(110). While cFF forms longer chains on average, both molecules assemble resist island formation and display a range of chain lengths. The density of packing of the chains is also similar, suggesting this is largely governed by the molecule’s core, not the side groups.. 162

Figure 6.2.33. DFT models of cYY on Cu(110), using “up” and “down” landing conformers as starting points. A small energy difference of 0.03eV separates the two, suggesting both might occur on the surface, in contrast to the behaviour observed on Au(111). 163

Figure 6.2.34. Typical STM images post-annealing a deposition of cYY on Cu(110) to 425K. Standard deviation for: lengthways periodicity 0.58Å, ‘diagonal’ periodicity 0.72Å. 164

Figure 6.2.35. a) Models of ddcYY overlaid on to the post-anneal data on Cu(110). Two adatoms of Cu, to scale, are illustrated in yellow to demonstrate the potential for adatom coordination to explain the lengthways molecular spacing. b) Suggested surface-mapped overlay of ddcYY molecules, with a simplified image also transposed over the data. The rows of atoms presenting “top” sites are coloured green, with alternate rows coloured brown. 165

Figure 6.2.36. Illustration of the restrictions placed on the assembly of ddcYY by the registry with the Cu(110) surface. a) Models at a separation observed experimentally. b) Assembly close enough for hydrogen bonding, but causing nitrogen atoms to lose access to surface top sites. c) Maintaining nitrogen atoms on ridge sites causes steric clashes due to molecular proximity. 166

Figure 6.2.37. Very low coverage STM data of annealed cYY on Cu(110). Lateral packing is not observed, and only isolated molecules or short chains are recorded across the surface. The adatom-based assembly also appears to prevalent at this coverage. 167

Figure 6.2.38. High coverage STM data of annealed cYY on Cu(110). A greater proportion of islands are observed at this coverage, but a general agglomeration still does not occur. 168

Figure 6.2.39. Evidence of the growth of a second layer of molecules of ddcYY on Cu(110). There are few occurrences of this phenomenon, but any ordered chains are in the same orientation, suggesting a favoured mode of bonding to the adlayer below. 168

Figure 6.2.40. a) Surface-mapped overlay of ddcYY molecules arising from different landing conformers of cYY, and how they might relate to the molecular features from STM. The rows of atoms presenting “top” sites are coloured green, with alternate rows coloured brown. b) Overlay of the Cu(110) surface structure and both ddcYY surface conformers, demonstrating the fit to the experimental data. 169

Figure 6.2.41. Step faceting of the Cu(110) surface where molecules of ddcYY appear to have adsorbed in rows. Such facets were relatively rare, but were stable across sequential scans. 170

Figure 6.2.42. Overlaid ddcYY molecules to illustrate how a chain might form by the faceted Cu(110) step. Amide groups of adjacent molecules are theoretically close enough for hydrogen bonding.	171
Figure 6.2.43. a) Model of the adsorption of ddcYY to Cu(110) as proposed from the STM data. b) Most-stable surface conformation of ddcYY on Cu(110), as determined by DFT. The similarity to the STM model is apparent. c) Side view of ddcYY adsorption on Cu(110) from DFT.	172
Figure 6.3.1. Mass spectra of [top] non-sublimed L-Trp-L-Trp and [bottom] L-Trp-L-Trp sublimed at 555K. Molecular ion occurs at $\sim m/z$ 391.	178
Figure 6.3.2. Typical STM images from a deposition of cWW on Cu(110). Only narrow, isolated islands are recorded, frequently with visible copper- oxygen (2x1) reconstruction stripes visible in the centre.	180
Figure 6.3.3. a) A closer view of Cu-O (2x1) striping on Cu(110) and the narrow molecular islands surrounding this phenomenon. b) An overlay of the (2x1) reconstruction on to the striping in the STM image. The dark circles between rows of reconstructed copper are the adsorbed oxygen atoms.	180
Figure 6.3.4. a) A complete molecular island without any visible Cu-O (2x1) reconstruction. b) Different features imaged within the island - a twin-lobed molecular feature in green and apparent single-lobed feature in blue.	181
Figure 6.3.5. A scaled model of cWW overlain across two apparent single-lobed features, demonstrating the scale of the features with respect to an intact molecule. This Figure is hypothetical and does not represent a proposed conformation that could give rise to the observed data.	182
Figure 6.3.6. a) Top-down and side views of an energy-minimised ddcWW molecule (Avogadro). b) Overlain assembly of ddcWW on to rows of molecular features from STM. The shape and scale of these molecules is a good match for the data.	183
Figure 6.3.7. a) Overlain ddcWW molecules aligned with the Cu-O (2x1) reconstruction for a regular, repeating surface registry. This demonstrates how the observed features in the STM conform to this surface arrangement. b) A denser packing of ddcWW molecules that permits stronger intermolecular reactions, but disrupts the anchoring to the Cu-O (2x1) reconstruction.	184
Figure 6.3.8. Typical STM image from a deposition of cWW on Cu(110), subsequently cooled to 115K. The assembly appears largely unchanged by the reduced thermal motion of molecules.	185
Figure 6.3.9. Low temperature (115K) STM images of the cWW deposition on Cu(110). a) Molecules demonstrated to still predominantly form rows around Cu-O (2x1) reconstruction patterns, though a larger island can be observed. b) Smaller scale scan of the larger island, illustrating the different type of molecular ordering within.	186
Figure 6.3.10. STM images from a deposition of cWW on Au(111). Such chains were the largest form of assembly observed across the surface, and exclusively found at steps. ..	187
Figure 6.3.11. Overlain assembly of cWW molecular models on Au(111). The potential for hydrogen bonding between adjacent molecules is indicated in black. The conformation of the molecular models is illustrative and does not propose a firm theory for the adsorption. Inset image approximately 2.6nm x 2.6nm.	187

Figure 6.3.12. Sequential STM images of a deposition of cWW on Au(111), with approximately 90s passing between each image. The chain of molecules can be observed to shrink before completely disbanding, leaving the step free of adsorbed molecules. 189

Table 2.1. A reference list of all peptides used in STM experiments in this thesis, their sources, and their sublimation temperatures. 42

Table 4.1. Additional peptides whose sublimation was studied by the methods described in this chapter, with brief notes on the outcome of the experiment. 82

Table 5.1. Key parameters from depositions of both L-Phe-L-Phe and cFF, for direct comparison. 94

Table 5.2. Comparison of STM parameters from an annealed deposition of cFF, and a deposition of ddcFF. 99

Acknowledgments

A thesis bears one name but is always the product of the efforts of many people. I have to thank all the colleagues who supported the work herein, both directly and indirectly, especially those in the Costantini group at Warwick – with special note to Luis, Dan, James, Phil, and Harry, as well as the older cohort of Tom, Ada, Ben and Nataliya. Thanks also go to the neighbouring Stavros group for moral support. The largest thanks must go to Prof. Giovanni Costantini who guided me through the whole process as my supervisor, since my master's degree and even before. Further afield, I am very grateful to Wolfgang Stiepany for imparting his knowledge on vacuum chamber design and many related issues, and Prof. Stephan Rauschenbach for his insight into building an adaptable new system.

I'd also like to offer thanks to the excellent technical staff at Warwick, with special mention going to Rod Wesson at the electronics workshop for his outstanding work and his endlessly cheery demeanour, as well as the mass spectrometry team of Phil Aston and Dr Lijiang Song.

Finally, I should thank my family, friends and loved ones who supported me through this long process and helped me see it to completion.

Declaration

This thesis is submitted to the University of Warwick in support of my application for the degree of Doctor of Philosophy in Chemistry. It has been composed by myself and has not been submitted in any previous application for any degree. Laboratory work and data analysis were performed under the supervision of Prof. Giovanni Costantini between October 2012 and April 2017. All work presented here, including data generated and data analysis, was carried out by the author except in the cases outlined below:

In Chapter 3, the presented vacuum chamber designs, while proprietary, were reviewed and supported by Wolfgang Stiepany of the Max Planck Institute for Solid State Research (Stuttgart), as well as the Costantini group at Warwick. The specific technical aspects of the manipulator head were specified by Wolfgang Stiepany in collaboration with the supplier, VAb Vakuum-Anlagenbau GmbH. The design of the baking tent, while also proprietary, was supported by the supplier Hemi Heating AB.

As listed in chapters 2 and 4, certain peptides were synthesised at Warwick by Dr Lona Alkhalaf of the Challis group.

The Scanning Tunnelling Microscopy data presented in chapter 5 were obtained by Ben Moreton and Dr Nataliya Kalashnyk, formerly of the Costantini group. Data analysis is by the author.

X-ray Photoelectron Spectroscopy experiments, the results of which are presented in chapters 5 and 6.2, were performed in collaboration with James Lawrence of the Costantini group, and Dr Marc Walker of the Warwick X-ray facility. Data analysis is by the author.

Density Functional Theory and Molecular Dynamics calculations presented in chapter 6.2 were carried out by Dr Zak Hughes and Prof. Tiffany Walsh of Deakin University, Australia.

Abstract

Peptides have been identified as having high potential for creating molecular building blocks for nanoscience, due to their intrinsic biocompatibility, wide availability, and chiral properties. In particular, these molecules are well suited to the fabrication of functional thin films via supramolecular self-assembly, because of their wide-ranging functionalities around a common core, in addition to chemical motifs that facilitate self-assembly, as observed abundantly in nature. However, relatively few studies of such molecules on surfaces can be found, leaving a gap in the exploration of the potential of the class. Therefore, the primary goal of this thesis is to investigate the self-assembly of short peptides, specifically on metal surfaces. However, in order to ensure high quality thin films are manufactured, peptides should ideally be deposited on a surface in vacuum via molecular beam epitaxy, a technique that can result in their decomposition. An understanding of the capabilities and limits of this technique, in particular with respect to peptides, is currently limited, and so part of this thesis focuses on tackling this shortfall in a methodical manner. Depending on the primary structure of the peptide studied, mass spectrometry data indicated a sublimation limit can be found at just a few residues ($\sim 4/5$). Additionally, these investigations demonstrated the possibility for cyclisation by thermal action for aromatic dipeptides, forming diketopiperazines. Scanning tunnelling microscopy and X-ray photoelectron spectroscopy data for ultrathin films of aromatic dipeptides and diketopiperazines follow, and reveal interesting self-assembly behaviour that also sheds light on previous peptide studies in the literature. Furthermore, it proved possible to chemically modify the diketopiperazines by on-surface annealing, resulting in stark changes to their assembly, and offering a simple pathway to challenging synthetic products. Key results from the study of L-Tyr-L-Tyr are supported by computational data for a more complete picture of the nature of the observed assemblies.

List of Abbreviations

1D, 2D, 3D	1-dimensional, 2-dimensional, 3-dimensional
AcN	Acetonitrile
AFM	Atomic Force Microscopy
AuNPs	Gold Nanoparticles
CAD	Computer-Aided Design
cFF	Cyclo-(L-Phe-L-Phe)
cFF(L/D)	Cyclo-(Phe-Phe) where either Phe is L, with the other D
CHARMM/GoIPCHARMM	A specific set of force fields for molecular dynamics
cWW	Cyclo-(L-Trp-L-Trp)
cYY	Cyclo-(L-Tyr-L-Tyr)
DFT	Density Functional Theory
DFLF	D-Phe-L-Phe
DKP	Diketopiperazine
DOS	Density of States
ESI	Electrospray Ionisation
fcc	Face-centred cubic
FF	Force Field (<i>or in-context, Phe-Phe</i>)
fwhm	Full-width-half-maximum
hcp	Hexagonal close-packed
HREELS	High-Resolution Electron Energy Loss Spectroscopy
HV	High Vacuum
LDOS	Local Density of States
LEED	Low Energy Electron Diffraction
LFDF	L-Phe-D-Phe
MD	Molecular Dynamics
MeOH	Methanol
MMFF94	A force field used by Avogadro software
MS	Mass Spectrometry
NEG	non-evaporable getter pump
NEXAFS	Near Edge X-ray Absorption Fine Structure
(O)MBE	(Organic) Molecular Beam Epitaxy
PVD	Physical Vapour Deposition
QCM	Quartz Crystal Microbalance UHV UltraHigh Vacuum
RAIRS	Reflection Absorption Infrared Spectroscopy
revPBE-vdW-DF	A specific DFT functional
RGA	Residual gas analysis/analyser
SPM	Scanning Probe Microscopy
STEP	Standard for the Exchange of Product model data, a file type
STM	Scanning Tunnelling Microscope/Microscopy
vdW	Van der Waals interactions
XPS	X-ray Photoelectron Spectroscopy

Further amino acid abbreviations are by standard convention, as well as described in-text.

Chapter 1: Introduction

1.1 Practical applications of short peptides

Peptides, or chains of amino acids joined by amide bonds, form the building blocks of large proteins well-known to biology from a range of structural and functional purposes in nature. Proteins consist of one or more polypeptide chains, typically comprising hundreds or even thousands of amino acid subunits, folded into a unique and complex three-dimensional structure. A short peptide, or oligopeptide, refers to an intermediate chain length between a single amino acid and a polypeptide, typically describing two to twenty amino acid residues. While the importance of polypeptides has long been known, short peptides have themselves generated substantial research interest in recent years, as molecules with specific applications in their own right.¹⁻⁴

Significant research attention has been given to the use of peptides to form hydrogels, materials that can adsorb large quantities of water without degrading, due to the hydrophilic nature of their internal structure. Hydrogels have a range of potential applications;^{5,6} these include tissue engineering, drug delivery, wound dressing, and agriculture; all based on their capability to store and slowly release water, including dissolved compounds or even cells. Historically, hydrogels have been created using polymers rather than small molecules, since each of the long chains can act as an individual fibre of the gel structure, with cross-linking or other interchain forces completing the porous network.⁷ This includes the use of biopolymers such as polypeptides,⁸⁻¹⁰ which are inherently biocompatible and can be drawn from a naturally occurring pool of molecules. Over time, oligopeptides of 20 and 16 amino acid residues that could assemble into a large matrix in solution were found to be equally capable of making effective hydrogels.¹¹⁻¹³ This led to progressively shorter sequences being investigated, such as a 12-residue peptide from Kisiday et al¹⁴ which, in a 4-week in-vitro test, provided a stable hydrogel scaffold for a cartilage-like extracellular matrix. Even more strikingly, certain dipeptides and tripeptides have displayed the ability to form hydrogels under mild conditions in solution.¹⁵⁻¹⁷ Such short sequences so far have required the presence of aromatic side chains on the amino acid residues, with Fmoc-Phe-Phe-OH the prototypical case.¹⁵ The use of small molecules offers a number of advantages over polymeric materials, in particular in terms of the rational design of the target molecule and its intermolecular interactions, thereby offering some control over the type of nanostructures

formed – though the conditions of the assembly process are also important.¹⁸ Furthermore, a hydrogel network based on a small molecule is more easily scalable and potentially much lower in cost.

The phenylalanine dipeptide (L-Phe-L-Phe or FF), has also demonstrated the capability to assemble into nanotubes and fibres, structures with a number of functional uses. This phenomenon was first discovered by the group of Ehud Gazit, where discrete silver nanowires were grown within the peptide nanotubes to highlight their practical application.¹⁹ The L-Phe-L-Phe dipeptide was selected based on the prevalence of this motif and similar aromatic sequences in amyloid fibrils,²⁰⁻²² the well-known but poorly understood protein plaques involved in various diseases including Alzheimer's and type II diabetes^{23,24}. Significant effort has been invested in controlling the growth of these peptide nanotubes, based on varying the synthesis technique,^{25,26} C-terminus substitution,²⁷ and thermally-induced phase transformation,^{28,29} in doing so the properties of the nanotubes can be fine-tuned, opening up more possibilities for their utilisation. Examples of the varied application of these nanotubes include their use in electrochemical biosensors,^{30,31} as a piezoelectric material,³² as a way to store quantum dots and protect them from degradation,^{33,34} and as a source of mechanical strength in an epoxy matrix.³⁵ The diverse utility of this simple dipeptide strongly highlights the broad potential of short peptides as functional molecules.

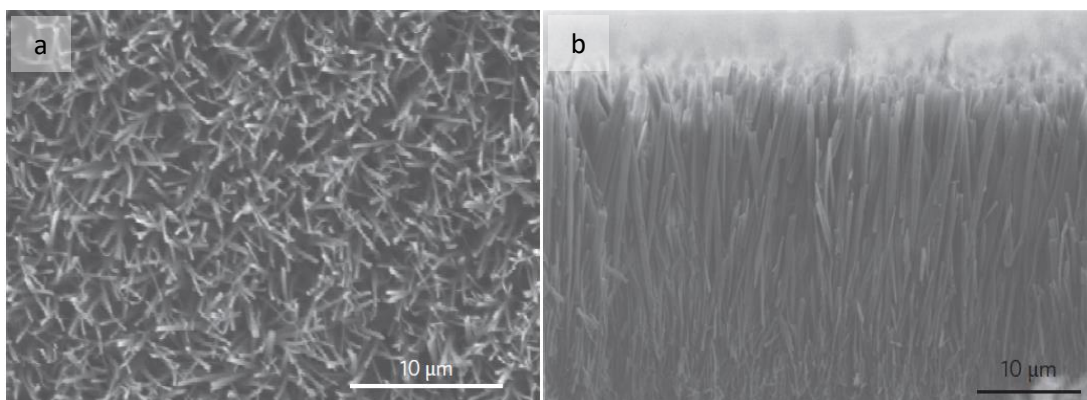


Figure 1.1: a) Top-down Scanning Electron Microscopy image of vapour-deposited dipeptide nanotubes. b) Side view of vertically aligned nanotubes; thickness 40μm. Both adapted from reference [25].

Another major area of research involving short peptides pertains to cyclic peptides, i.e. those where the C and N termini have reacted to form an amide bond, creating a ring structure from the peptide backbone. This class of molecules has been the subject of considerable research activity, from investigations into functional nanotubes³⁶ to therapeutic applications, including antifungal and anticancer activity.³⁷⁻³⁹ A particular focus is given here to 2,5-

diketopiperazines (DKPs, see Figure 1.2), a specific sub-class of cyclic peptide that is comprised of dipeptides cyclised into six-membered rings. The DKP motif is abundant in nature, either in isolation or as part of a larger structure, making it a feature of great interest for a wide range of biomimicry and medicinal purposes. In particular, the potential of DKPs as antimicrobial agents has generated substantial research activity^{38,40-45}, ever since the tuberculostatic action of the cycloserine dimer was discovered.⁴⁶ DKPs are especially advantageous for drug discovery since they offer a small, constrained backbone upon which multiple functionalities can be imposed by means of peptide side chains with varying stereochemistry. The core structure is relatively stable in comparison to linear peptides, while retaining biocompatibility. These properties of DKPs are also invaluable when turned to other applications, with DKPs showing potential for roles in catalysis,^{45,47,48} nanostructure formation,^{49,50} neurotransmission/neuroprotection,^{45,51} and a variety of other biological functions including tumour growth inhibition.^{45,52,53}

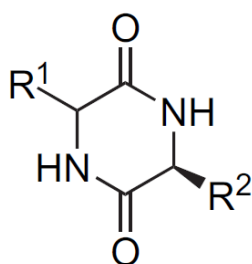


Figure 1.2: The general structure of a 2,5-diketopiperazine, or DKP. The R groups represent the unaltered side chains of the original peptide residues.

A number of further applications of peptides are underpinned by their interactions with surfaces, and these are of particular relevance to this thesis. Multiple avenues of research make use of such interactions, whether as a direct method of surface functionalisation, or as a means to disrupt the formation of undesirable surface adducts. The archetypal examples of these cases can be found in the fields of biofunctionalisation⁵⁴ (for the former) and anti-biofouling⁵⁵ (for the latter). Biofunctionalisation is concerned with modifying non-biological materials in such a way that they become biologically compatible, whilst adding functionality or maintaining existing functionality. In recent years, peptides have arisen as strong candidates for such an application, due to their advantageous properties already discussed here – including inherent biocompatibility, ready availability and/or simple synthesis, and the capability for diverse chemical modification of the side chains.⁵⁶⁻⁶¹ These characteristics enable the production of peptides that bind to a range of substrates, without hindering their application in a biological context. Biofouling instead refers to the unwanted build-up of biological material on a surface, such as layers of algae on ships and underwater cables, or films of microorganisms on ventilation systems. The reduction or prevention of the growth

of these coatings is a substantial undertaking, due to various economic and health concerns, and is termed anti-biofouling or antifouling. While this field may appear to be the antithesis of biofunctionalisation, peptides also find frequent application here,^{62,63} due to the same set of advantageous properties that they possess. As discussed, peptides can be designed in such a way that they bind to a range of surfaces; by doing so in an antifouling context, a film can be created that resists the adhesion of further molecules to the surface to be protected, for example by incorporating hydrophobic residues. Particular success has also been found in the application of antimicrobial and antifungal peptides onto biomedical devices,^{40,43,63} in order to ensure their sterility.

Other fields that make use of peptide-surface interactions include bioinspired mineralisation, cellular adhesion, and nanoparticle functionalisation. Bioinspired mineralisation refers to efforts to mimic the biomineralisation that is found abundantly in nature, i.e. the synthesis of inorganic minerals by living tissue. This is typically done by isolating or recreating sections of proteins responsible for this behaviour.⁶⁴ In this way, the highly specific interactions between the peptides and the relevant inorganic surfaces can be reproduced. As a result, numerous oligopeptides have been successfully employed for bioinspired mineralisation, including for silica precipitation, titanium dioxide synthesis and cadmium ion sequestration.⁶⁵

Cellular adhesion research involves the investigation and modification of the mechanisms by which cells can adhere to one another, or to other materials. Peptides and proteins are already heavily involved in these processes in nature by means of antigens and cell surface receptors, which are frequently composed of peptide chains. The application or even design of specific peptide chains that enable desirable cell-cell or cell-surface interactions is therefore an active area of research.⁶⁶⁻⁶⁸ The tripeptide sequence RGD (arginine-glycine-aspartic acid) is of particular note in such studies, given its frequent occurrence in the recognition sequence of peptides that bind to the integrin family of transmembrane receptors.^{68,69} As a result, the RGD sequence has received considerable attention in the synthesis of cell-adhering materials,⁷⁰ as well as inspiring a broader outlook in the design of peptide-based biomaterials.⁷¹ Peptide chains as large as perlecan domain IV (17 subunits in length) have been isolated and employed in cell adhesion research, enabling the creation of a polymer-based scaffold for studying prostate cancer cell pharmacokinetics.⁵⁶

Nanoparticles, defined as particles having all three dimensions on the 10^{-9} m to 10^{-7} m length scale, present an intermediate between the bulk properties of solids and atomistic/molecular level behaviour. The vast surface area available, with a variety of

chemical functionalisation possible, has enabled inorganic nanoparticles to see application in a range of fields,^{72,73} including electronics⁷⁴ and drug delivery.⁷⁵ Peptides are amongst the molecular species often used in functionalising such nanoparticles. A particular focus is given here to peptide-functionalised gold nanoparticles (AuNPs), due to the considerable interest that this category of nanoparticle has received⁷⁶ and the potential parallels between peptide-based AuNPs and the self-assembled thin films on gold surfaces explored in this thesis. Colloidal suspensions based on gold have been used for centuries as a means of colouring glass and ceramics, but only since the work of Michael Faraday in the 1850s⁷⁷ has an analysis of the origin of this colour been developed. These colloids are composed of AuNPs, which absorb and scatter visible light by means of surface plasmon resonance; the size, shape and aggregation of the nanoparticles directly influence the resultant colour⁷⁸. The optical properties of diverse AuNPs are the subject of ongoing research⁷⁹⁻⁸¹, but it is specifically the application of peptide-functionalised AuNPs that pertains most directly to the focus of this thesis. Here the optical properties of AuNPs can be adapted for analytical and diagnostic purposes, using colorimetric changes to detect the presence of heavy metals, enzymes, and even viruses in solution (see Figure 1.3).⁸² Furthermore, the use of peptides opens up a number of medical and biological applications, including drug delivery, gene therapy, anti-cancer treatments and photoresponsive therapeutics.^{82,83} Together with the flexibility of the Au-peptide interface, it is the diverse functionality available to peptides that is directly responsible for the myriad uses of peptide-functionalised AuNPs. Given the further development of the synthesis of these nanoparticles running in parallel to the aforementioned research,^{84,85} it is highly likely that many more applications will yet be discovered.

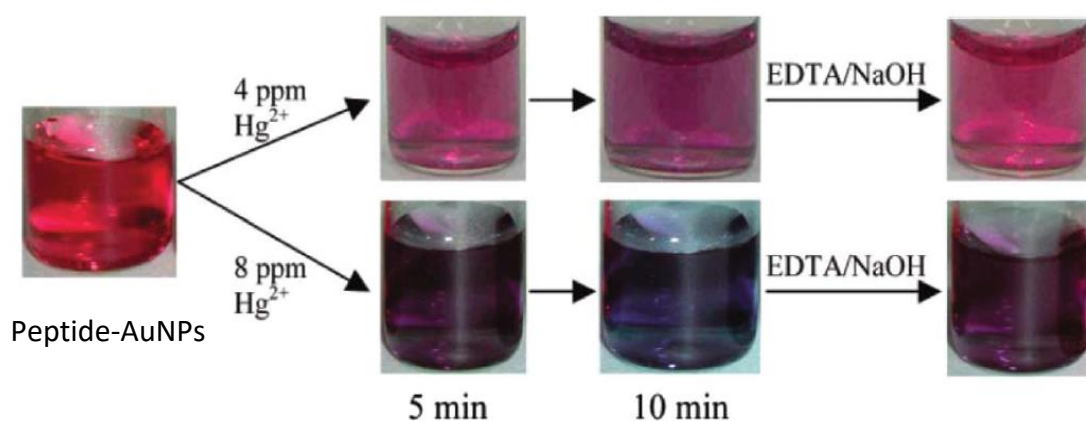


Figure 1.3: Gold nanoparticles (AuNPs) functionalised with peptides used to detect Hg²⁺ ions in solution. A colour change from red to purple is observed, which can be reversed with EDTA sequestration. Reproduced from reference [82].

With short peptides demonstrating great potential in such a wide range of research fields, their status as molecules of interest is clear. A recurring theme across many of the discussed applications of short peptides is their assembly into larger structures, by means of intermolecular forces rather than chemical reaction. This process is highly dependent on the size and chemical nature of the peptides involved, and is also heavily influenced by interactions with any surface to which the peptides may be adsorbed. Furthermore, the interactions of peptides with surfaces is in many cases instrumental to their intended application. These principles that underpin the practical uses of oligopeptides tie in strongly to a major focal point of this thesis: the self-assembly of small molecules on metal surfaces.

1.2 The self-assembly of small molecules on metal surfaces

Functionalising a surface with small molecules in order to produce a stable macroscopic material with practical applications is a long-term research goal of the surface science community. This process in essence defines the ‘bottom-up’ approach to surface engineering, as opposed to the ‘top-down’ strategy. Top-down strategies impose order on a surface externally, from ‘above’, and have proved highly successful for many years; with techniques such as lithography, stamping and moulding⁸⁶ providing excellent results in the production of ever-smaller computer components, as a stand-out example. However, such techniques struggle to operate at sub-nanometre length scales, a regime which must be explored if the miniaturisation of technology is to continue further. The use of small molecules that self-assemble into ordered arrays offers a way to build surface functionality from highly tuneable molecular units, i.e. creating a surface structure from the bottom-up.^{87,88}

Self-assembly is a term that defines the method by which certain molecules can pack together or ‘assemble’ into an ordered system. The ‘self’ prefix means that no external influence is applied to bring about the assembly – the molecules simply organise themselves into a thermodynamically favoured arrangement under equilibrium conditions. This means that typical driving factors such as elevated temperature or catalysis are absent, and so the assembly process is controlled almost entirely by the intrinsic intra- and intermolecular bonding of the molecules involved. This bonding is in itself a direct consequence of the chemical structure of the molecules, meaning that the control of self-assembly derives from the choice or design of specific molecular targets.

In the context of surface science, self-assembly in a single layer (also called a monolayer) occurs in 2-dimensions (2D), with the molecules of interest adsorbed to a surface or interface. The surface acts as a support for the assembly, with a varying degree of interaction depending on the choice of both surface and molecule. Constraining an assembly in this way reduces its complexity, making it simpler to understand and to manipulate through molecular design. Due to major advances in synthetic chemistry, it is possible to modify a variety of organic molecules with different functional groups, opening up the possibility for an extensive library of finely tuned self-assembly building blocks. This field of 2D self-assembly is therefore an area of considerable growth and new research activity.⁸⁸⁻⁹¹

Applying these synthetic strategies with an understanding of the aforementioned intermolecular bonding motifs enables the creation of simple model systems, which can be used in proof-of-concept experiments to demonstrate the broader potential of a class of molecules for self-assembly. Much of the research in the 2D self-assembly field pertains to such systems, and a number of different potential controls over the self-assembly process have been studied and published.^{88,89,91-96} Research of this fundamental nature is often complemented by theoretical simulations, which inherently require small/simple model systems in order to be computationally feasible. To maximise the value of such collaboration, the experimental data must offer molecular-scale information, acquired in pristine conditions (without impurities) that permit a straightforward analysis. Therefore, most experimental data acquired thus far has required the use of ultrahigh vacuum (UHV) conditions, both to facilitate the relevant analytical techniques and to offer the maximum cleanliness and stability to any self-assembled film, both of which are independently advantageous for experimentalists. Additionally, the surfaces employed are typically low Miller index cuts from crystalline samples, which serve to simplify the molecule-surface interfaces. In many cases, metal surfaces are used, since they bear greater technological relevance whilst being well-suited as part of a model system. While these measures make for a more straightforward analysis of the data, they also impose limitations on the extent of the conclusions that can be drawn. Though the smaller molecules typically employed can act as excellent model systems as discussed, they represent a limited pool since larger and more complex species cannot typically be processed intact in vacuum. Furthermore, macroscopic 'real-world' applications will usually expose a self-assembled film to atmospheric conditions, under which a given assembly may no longer be stable. There may also be harsher conditions involved such as solvent exposure, high temperatures, or physical abrasion, all of which would have a significant impact on the molecule-surface interface. Additionally, maintaining

a single specific surface of a metal becomes prohibitively expensive at larger dimensions, and as such the scalability of a self-assembled material depends on its behaviour across complex native metal surfaces, including across defects and discontinuities.

Therefore, despite the numerous advances made in controlling self-assembly on a surface, thin films grown in vacuum have still yet to make the transition to real-world application. Though there are several barriers to overcome, progress could be made by adapting the products of self-assembly in solution or even in Biology to a surface environment. These have been demonstrated as inherently stable under ambient (or close to ambient) conditions, and capable of large-scale order. In some cases, macroscale assemblies can be found, for example the action of self-assembling polymers,⁹⁷ polypeptides,⁹⁸ and carbohydrates.⁹⁹ Working with such materials is, in effect, working backwards from real-world macroscopic self-assembly to the nanoscale, and as such is a promising route to building a robust bottom-up strategy. Control over the assembly, even at the macroscopic scale, ultimately lies in the chemistry at the molecular and intermolecular level, meaning that there is great scope for bridging the nanoscale-macroscale gap. This would represent an important first step in the scale-up of self-assembled films and their transfer to ambient conditions and applications.

From the scalable classes of molecules mentioned, of particular interest are peptides, which represent a vast pool of naturally-occurring compounds ranging from short oligopeptides to large proteins. Peptides have long been known to demonstrate hierarchical assembly, known as 'primary', 'secondary', 'tertiary' and 'quaternary' structures in Biology (see Figure 1.4).¹⁰⁰ The largest of these, the quaternary structure, refers to the assembly of multiple polypeptide subunits into a combined functional protein, as for example in haemoglobin.¹⁰¹ Even at this scale, the assembly is still explicitly determined by the primary structure, i.e. the sequence of amino acid subunits, because the primary structure determines the secondary structure (the folding of chain sections), the secondary determines the tertiary (the overall polypeptide shape), and the tertiary the quaternary. In this way, long-range large-scale order is imposed by the chemical nature and assembly of small molecules. Additionally, as discussed in section 1.1, short peptides can also assemble into functional structures themselves. Peptides have therefore generated substantial interest in surface science, but not only due to their inherent ability to self-assemble. Peptides also have a number of other beneficial properties, including their chiral nature (a feature of significant value, for example in creating surface-active chiral agents such as molecular sensors,¹⁰²⁻¹⁰⁴ or in enantioselective heterogeneous catalysis^{105,106}), simple synthesis and ready availability, intrinsic biocompatibility, and naturally-occurring

functional group variation via the side chains. Together these features mean that peptides are easy to acquire and use, are highly customisable, and therefore offer a tuneable self-assembly process.¹⁰⁷⁻¹⁰⁹

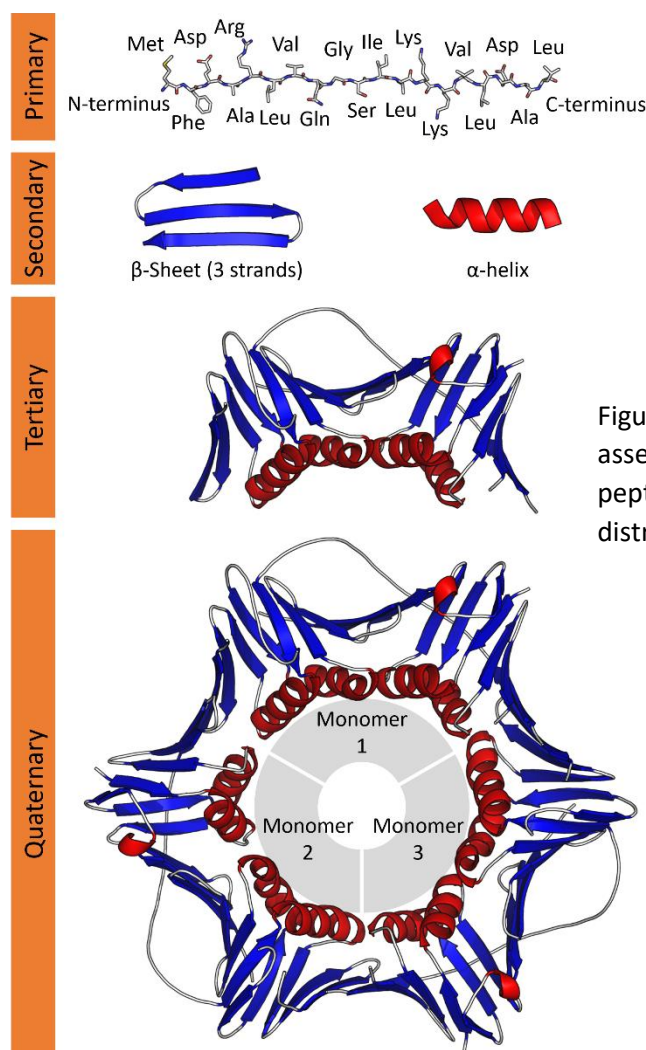


Figure 1.4: The hierarchy of protein self-assembly structures, using a model peptide. Image by Thomas Shafee, distributed under a CC-BY 4.0 license.

Due to the discussed appeal of these molecules, this thesis focuses on the study of short peptides and amino acids as model systems for self-assembly on surfaces. If the high potential of this class of molecules can be harnessed, the implications for the future of self-assembly as a relevant and directly applicable technique would be significant. In order to do so, the fundamentals of the behaviour of peptides on surfaces and their practicality as self-assembly candidates must be understood. Therefore, starting with the smallest, most basic peptides is essential, to simplify the analysis and to serve as a guide for larger molecules. In addition, the use of simple model systems allows close collaboration with computational chemistry, enabling a more detailed understanding of the assembly process while validating the simulations themselves, significantly broadening the scope of the work herein. This is exemplified in chapter 6.2.

1.3 Characterising self-assembly on a surface

Studying the self-assembly of peptides on a surface in UHV at the molecular scale requires specialist analytical techniques that can help elucidate the molecular structure of adsorbed species and the nature of the assembly present. Ideally such techniques operate with sub-nanometre resolution, so as to provide information at the atomic and molecular scale. Scanning Probe Microscopy (SPM) can offer sub-nanometre resolution routinely, through techniques such as Atomic Force Microscopy (AFM) and Scanning Tunnelling Microscopy (STM). STM in particular has a history of offering molecular and submolecular resolution ever since its inception in 1981,¹¹⁰ lending itself well to the study of self-assembly, and as such will serve as the primary experimental tool used in this thesis.

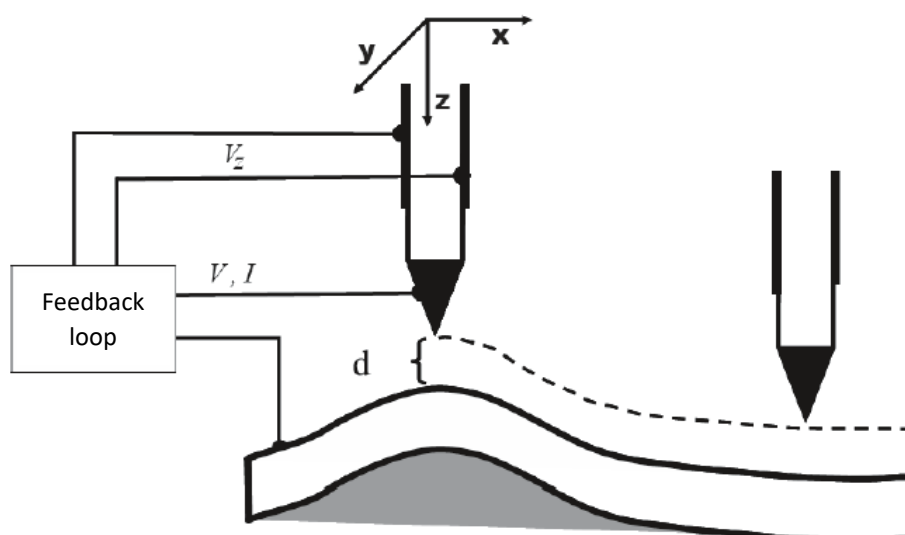


Figure 1.5: Schematic representation of an STM experiment, in constant current mode. A voltage, V , is applied between tip and sample, and a current, I , measured and stabilised via a feedback loop. Piezoelectric actuators control movement of the tip on the x , y and z axes. Further details can be found in chapter 2, Experimental. Image adapted from reference [110].

Additional analytical techniques that are surface-sensitive but provide data averaged over a larger length scale are highly useful as complementary strategies to STM. STM offers no direct chemical sensitivity and is impractical for long-range analysis, issues that are easily addressed by other techniques. Methods such as X-ray Photoelectron Spectroscopy (XPS), Low Energy Electron Diffraction (LEED), Reflection Absorption Infrared Spectroscopy (RAIRS) and High-Resolution Electron Energy Loss Spectroscopy (HREELS) can provide information on the chemical state of molecules across the whole surface, and thus help to build a broader picture of the overall assembly process rather than just the nanoscale ordering. In this thesis,

XPS is used in cases where the chemical state of a molecule was unclear from STM data alone, and provides data that enables an on-surface reaction to be tracked. In addition, computer modelling and simulations are employed to assist in the analysis of STM data.

Many of the experimental techniques used in analysing self-assembly on a surface operate either preferentially or exclusively under vacuum conditions, more specifically UHV. UHV conditions, defined as $<10^{-9}$ mbar, also offer the maximum control over the cleanliness of a sample to be studied, and therefore over the final nature of an adsorbed layer. A more detailed description of UHV as well as all experimental and theoretical methods can be found in chapter 2 (“Experimental”).

Generating an adsorbed layer of molecules on a surface in vacuum also makes use of specialist techniques. Solution-based methods employed in ambient conditions are simple to use and control, but the quality of the deposited film can be degraded by impurities present and by contamination from the environment. Transferring samples prepared in this way to vacuum can be suboptimal as a result, and is a time-consuming process. In vacuum, tailored techniques such as Pulsed Jet Deposition,¹¹¹ Pulsed Laser Deposition¹¹² and Molecular Beam Epitaxy (MBE)¹¹³ enable molecular deposition without breaking the vacuum, enabling greater regulation of the nature of the deposited film generated. In particular, MBE (also called OMBE when working with organic molecules) is capable of an extremely high level of control over the rate of molecular deposition and total exposure time, and as such is a widely-used method for creating thin films on surfaces.¹¹⁴ OMBE operates by sublimation of the molecules of interest at a specified temperature, thus generating a molecular beam to which the surface can be exposed for a measured length of time. Controlling the rate, time and temperature of the deposition directly affects the quality of the surface molecular layer, making it much more likely that the desired coverage and surface chemistry are attained. Furthermore, OMBE creates molecular films with abrupt interfaces, which are essential for many applications, as well as permitting sequential deposition of different molecules without the concerns of solvent compatibility. The process is also highly reproducible. For these reasons, molecular depositions are performed by OMBE throughout this project.

1.4 Thermally-induced chemical transformation of short peptides

In parallel with the self-assembly of short peptides on surfaces, this thesis explores some of the thermally-induced chemical transformations that these molecules can exhibit. Since OMBE uses thermal sublimation to produce a molecular beam, a molecule to be deposited must be stable enough to remain intact at the temperatures required to effect sublimation. If OMBE remains as a dominant deposition technique in vacuum, then the capability of peptides to sublime intact is essential in assessing their suitability as self-assembly candidates. Furthermore, as a direct consequence of investigations into sublimation in this thesis, some peptides were found to undergo a chemical reaction when a self-assembled monolayer on a surface is heated.

The question of whether or not a molecule can be sublimed intact is ultimately resolved by a balance between intra- and intermolecular forces. In order for sublimation to occur, all the intermolecular bonds must be broken, while fragmentation results after only a single intramolecular bond breaks. Therefore, as the number of intermolecular bonds increases, or if stronger intermolecular bond types are added, fragmentation becomes more likely as one attempts to sublime the molecules.¹¹⁵ This is noticeably manifested when comparing larger molecules to smaller ones, which for peptides means those with longer backbone chains and larger side groups, and therefore higher molecular weight. While most amino acids have been reported to survive the sublimation process – through the interpretation of data from analytical techniques including XPS, Near Edge X-ray Absorption Fine Structure (NEXAFS) and Reflection Absorption Infrared Spectroscopy (RAIRS)¹¹⁶⁻¹³⁹ – only a relatively small number of short peptides appear to have been successfully sublimed and studied. These include numerous dipeptides^{118,126,140-147} and tripeptides,^{140,141,146,148-152} but the list becomes much smaller when moving to tetrapeptides,¹⁵³ or indeed longer peptides. The lack of data for peptides beyond four amino acid residues already suggests an issue with subliming such molecules, but a systematic study of the effect of peptide length on sublimation is nonetheless absent. The relationship between chain length of peptides and their sublimation behaviour is thus the focus of chapter 4 (“The sublimation of short peptides”), which also doubles as a test of the limits of the sublimation technique itself. A further point of study arises when it becomes clear that certain peptides have a tendency to cyclise when sublimed, meaning that it must also be determined whether they can be deposited on a surface in vacuum in their native form or only the cyclic form.

The cyclisation of a specific peptide, Phe-Phe, is of particular interest since this molecule has already received substantial interest in the literature, including a study of its self-assembly on Cu(110) (see Figure 1.6).^{118,142} In this study, the deposited molecules (described as linear L-Phe-L-Phe) were found to change their self-assembly pattern upon on-surface annealing, a transformation attributed to conformational change. However, in light of new sublimation data contained in this thesis, it is apparent that the cyclisation of L-Phe-L-Phe likely plays a role, and as such further investigation of this molecule and its on-surface reactions becomes a point of interest. The cyclisation of a dipeptide such as L-Phe-L-Phe produces a DKP, a molecule of great interest in research as described in section 1.1, which adds additional significance to the outcome of the experiments discussed here. Following on from this, similar dipeptides to L-Phe-L-Phe can be identified to explore the generality of the phenomenon, based on common structural elements such as an aromatic group in the side chains.

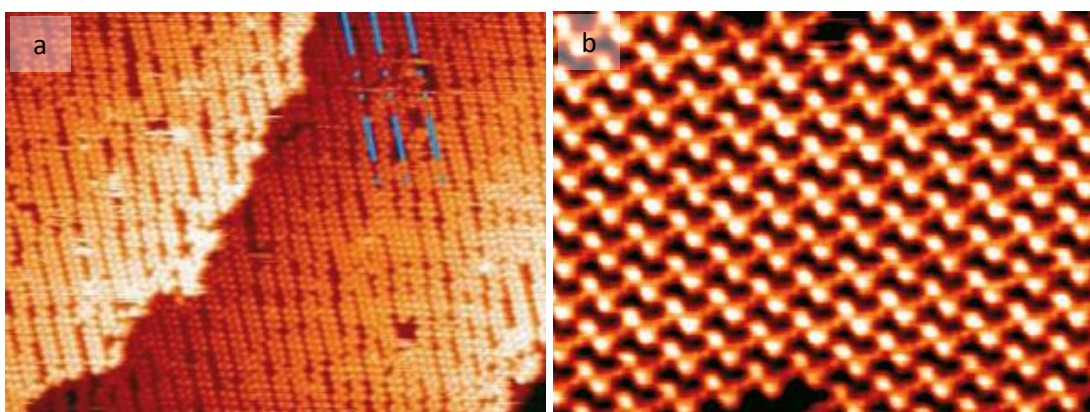


Figure 1.6: STM images of: a) A deposition of L-Phe-L-Phe molecules on Cu(110), annealed to 400K. b) The same deposition annealed to 450K. The evident change in self-assembly pattern was attributed to conformational change. Adapted from reference [118].

These reactions are highly relevant to the creation of functional, ordered molecular films on surfaces, as the change of structural chemistry has a substantial impact on intermolecular bonding and molecule-surface registry, both of which strongly influence the self-assembly process. Furthermore, any on-surface reaction initiated simply by heating offers the possibility to transform a molecule-surface system from one state to another, changing its functionality in-situ. While only demonstrated here for a system composed of short peptides, the prospective broader utility of the process in general is high.¹⁵⁴ Additionally, performing a reaction of this nature on a surface can be viewed as an alternative synthetic pathway to traditional organic chemistry, potentially simplifying and avoiding a complex multi-step procedure.^{45,155}

1.5 Self-assembly of short peptides on surfaces

Despite the significant interest that peptides offer as a class of molecules for functionalising surfaces, relatively little experimental data can be found concerning their on-surface self-assembly behaviour, particularly in terms of UHV studies at the molecular level. One reason for this is the equally limited data on the sublimability of peptides, and the potential for fragmentation as described above. A small number of studies of self-assembled amino acid^{116-125,127-134,136-139} and peptide thin films on metal surfaces can be found however, which together can provide insight into how the peptides selected for study in this thesis might behave. The short peptide sequences studied to date are Gly-Pro-Glu,^{141,148,151} Glu-Cys-Gly,^{140,149,150} Gly-Pro,^{140,141} Ala-Ala,¹⁴⁵ Ala-Ala-Ala,¹⁵² Leu-Leu-Leu,¹⁵² Gly-His,¹⁴⁶ Gly-His-Gly,¹⁴⁶ Gly-Gly-His,¹⁴⁶ Gly-Gly,¹⁴⁷ Lys-Phe-Phe-Glu and Lys-Val-Val-Glu,¹⁵³ and as previously mentioned, Phe-Phe.^{118,142-144} A range of experimental techniques are employed to probe the resultant thin films, including NEXAFS, LEED, RAIRS, XPS, and STM, with the latter being of the most interest due to the focus of this thesis. Focusing specifically on STM data, the list of peptides studied is reduced to Gly-Pro-Glu on Au(110) and (111), Phe-Phe on Cu(110), Ala-Ala on Cu(110), and Lys-Phe-Phe-Glu and Lys-Val-Val-Glu on Au(111). In most cases the peptides were capable of self-assembling into highly ordered networks, though any assembly of Gly-Pro-Glu is masked by its tendency to alter the reconstruction of the gold surface on which it is deposited.^{148,151} Both Ala-Ala¹⁴⁵ and Phe-Phe^{118,142,143} assemble preferentially into chains, with molecules aligning in a regular fashion but largely in 2-dimensions. Lys-Phe-Phe-Glu and Lys-Val-Val-Glu both assemble into islands dominated by a row-by-row pattern of molecules,¹⁵³ though conformational differences are discernible between the two. These results, while few in number, indicate the potential not only for ordered, self-assembled peptide thin films, but the variation possible in the size and structure of the domains created, simply through small variations in amino acid residue and peptide length. Such differences occurring within a very limited set of peptides also serves to illustrate the lack of existing knowledge in this area, and highlights the need for a body of fundamental high-resolution data.

1.6 Project goals and thesis structure

As discussed, this project is focused on the study of amino acids and short peptides, in order to assess their potential as building blocks for functional self-assembled thin films. To

evaluate the possibilities of working with such a broad set of molecules as peptides, a logical series of test cases should be used, to serve as a baseline for the peptides class in general. The alanine series was identified as a strong model candidate, since alanine is the simplest chiral peptide with only a methyl group in its side chain. Therefore, the first stage of experiments consists of sublimation tests on alanine and its oligopeptide derivatives, of increasing chain length. This is followed by a series based on a somewhat more complex amino acid residue, phenylalanine, and the effect on sublimation described. Phenylalanine residues will have different intermolecular interactions to alanine, but remain unable to form stronger bonds such as hydrogen bonds or Coulombic interactions. The structure of molecules before and after sublimation is determined by electrospray ionisation (ESI) mass spectrometry.

Due to the cyclisation of L-Phe-L-Phe encountered in the sublimation experiments, and the history of research into this molecule, self-assembly experiments involving L-Phe-L-Phe became a priority. L-Phe-L-Phe was deposited on a Cu(110) surface and studied by STM, followed by cyclic derivatives used to determine the nature of the thermally induced on-surface reaction. In addition, the cyclisation and self-assembly of diastereomers of L-Phe-L-Phe are examined, to explore the effect chirality has on the reactions of this molecule. Leading on from this, other naturally occurring, proteinogenic aromatic dipeptides are studied on Cu(110) and Au(111) surfaces to identify any trend in behaviour of dipeptides with aromatic side chains. The specific dipeptides studied in this way are L-Tyr-L-Tyr and L-Trp-L-Trp. Homopeptides are used in order to simplify the interpretation of the data. L-His-L-His could also be considered for such experiments since it contains the aromatic imidazole groups in its side chains, but this group is also relatively basic (pK_aH 6.04¹⁵⁶) and thus can be protonated even in mild pH conditions, giving rise to different reactivity. Furthermore, L-Phe-L-Phe, L-Tyr-L-Tyr and L-Trp-L-Trp are all hydrophobic peptides,^{157,158} whereas the imidazole groups lend more hydrophilicity to L-His-L-His. Therefore, L-His-L-His is currently omitted in order to establish a clearer trend of the behaviour of aromatic dipeptides without additional factors to consider.

In support of the STM data, XPS experiments are performed that assist with the identification of surface species in experiments on L-Phe-L-Phe and L-Tyr-L-Tyr. Also, the conclusions of the L-Tyr-L-Tyr experiments are supported by theoretical atomistic simulations.

The longer-term scope of this project is to work with a broader range of peptides, both in terms of functional groups and chain length, to investigate further possibilities in self-

assembly and on-surface reactions. However, as already discussed, OMBE as a deposition technique becomes limited when molecules of interest fragment under the conditions used for sublimation. This restriction is one of the driving factors behind a search for alternative strategies for depositing molecules in vacuum. Of particular interest is the adaptation of ESI to molecular deposition, as the technique is well-known in mass spectrometry as a 'soft' ionisation method, i.e. one that is unlikely to fragment the sample.^{159,160} The use of ESI in preparing functionalised surfaces in vacuum is a growing field,¹⁶¹⁻¹⁶⁷ with molecules as large as proteins^{161,163,168} and DNA¹⁶⁵ already having been successfully deposited and analysed by STM. In order to fully explore the use of peptides for self-assembly, a wide range of candidates must be readily available for deposition, and so techniques such as ESI that can circumvent the limitations of OMBE could be invaluable to the future of this project. For this reason, it was resolved that a new UHV system that could accommodate alternative vacuum deposition techniques be constructed, with a particular focus on incorporating ESI deposition. An OMBE source would still be essential due to the study of sublimation and thermal cyclisation of short peptides as has been described. In advance of the presentation of data in this thesis, the specifications of this new system are presented.

Therefore, this thesis is divided up into 7 chapters, the first of which is this introduction. In chapter 2, the specific experimental and theoretical techniques used throughout this work are discussed in-depth. Subsequently, chapter 3 presents the details of the planning and construction of the new UHV system, including the rationale behind each of the major design choices.

Chapters 4 through 6 are concerned with experimental results and their analysis. Chapter 4 covers the sublimation of short peptides, using mass spectrometry to identify the products of this process, and provides a basis for the further investigations of the thermal transformations of this class of molecule. Particular interest is given to the thermal cyclisation of Phe-Phe.

Chapter 5 is focussed on the dipeptide L-Phe-L-Phe and derivatives thereof, presenting a thorough analysis of the deposition of these species on a Cu(110) surface, as well as thermal transformations on-surface after annealing. The effects of modifying the chiral centres in this molecule are also investigated, including on a Au(111) surface, in order to provide a complete picture of the ways in which the effective stereochemistry of the surface can be controlled.

Chapter 6 expands the scope of some of the conclusions of chapters 4 and 5 by means of experiments with other dipeptides containing aromatic side groups. Specifically, depositions of the dipeptides L-Tyr-L-Tyr and L-Trp-L-Trp are studied on a Cu(110) surface, and in the case of L-Tyr-L-Tyr, also on Au(111). The data for L-Tyr-L-Tyr is also supported by computer simulations, enabling a greater understanding of both the initial self-assembly and the transformations brought about by surface annealing.

Finally, chapter 7 summarises the conclusions of the experiments described in this thesis, as well as presenting the broader outlook that these conclusions give rise to. In addition, potential future experiments are discussed that would continue the work herein and serve to further enhance the impact of this work.

1.7 References

1. E. Gazit, "Self-Assembly of short peptides for nanotechnological applications", in *NanoBioTechnology: BioInspired Devices and Materials of the Future*, ed. O. Shoseyov and I. Levy, Humana Press, Totowa, New Jersey, 2008, ch. 5, p385-396.
2. K. Fosgerau and T. Hoffmann, "Peptide therapeutics: current status and future directions", *Drug Discov. Today*, 2015, **20** (1), 122-128.
3. J. H. Collier and T. Segura, "Evolving the use of peptides as components of biomaterials", *Biomaterials*, 2011, **32** (18), 4198-4204.
4. K. L. Duncan and R. V. Ulijn, "Short peptides in minimalistic biocatalyst design", *Biocatalysis*, 2015, **1** (1), 67-81.
5. E. Caló and V.V. Khutoryanskiy, "Biomedical applications of hydrogels: a review of patents and commercial products", *Eur. Polym. J.*, 2015, **65**, 252-267.
6. M. R. Guilherme, F. A. Aouada, A. R. Fajardo, A. F. Martins, A. T. Paulino, M. F. T. Davi, A. F. Rubira and E. C. Muniz, "Superabsorbent hydrogels based on polysaccharides for application in agriculture as soil conditioner and nutrient carrier: a review", *Eur. Polym. J.*, 2015, **72**, 365-385.
7. B. D. Ratner and A. S. Hoffman, "Synthetic hydrogels for biomedical applications", in *Hydrogels for medical and related applications*, ed. J.D. Andrade, ACS, Washington DC, 1976, ch. 1, p1-36.
8. P. Giusti, L. Lazzeri, N. Barbani, P. Narducci, A. Bonaretti, M. Palla and L. Lelli, *J. Mater. Sci.: Mater. Med.*, 1993, **4**, 538-542
9. S. Srivastava, S. D. Gorham and J. M. Courtney, *Biomaterials*, 1990, **11**, 162-168.
10. W. Petka, J. L. Harden, K. McGrath, D. Wirtz and D. Tirrell, *Science*, 1998, **281**, 389-392.
11. J. P. Schneider, D. J. Pochan, B. Ozbas, K. Rajagopal, L Pakstis and J. Kretsinger, *J. Am. Chem. Soc.*, 2002, **50** (124), 15030-15037.
12. S. Zhang, T. C. Holmes, C. M. DiPersio, R. O. Hynes, X. Su and A. Rich, *Biomaterials*, 1995, **16** (18), 1385-1393.
13. T. C. Holmes, S. de Lacalle, X. Su, G. Liu, A. Rich and S. Zhang, *Proc. Natl. Acad. Sci.*, 2000, **97** (12), 6728-6733.
14. J. Kisiday, M. Jin, B. Kurz, H. Hung, C. Semino, S. Zhang, and A. J. Grodzinsky, *Proc. Natl. Acad. Sci.*, 2002, **99** (15), 9996-10001.

15. A. Mahler, M. Reches, M. Rechter, S. Cohen and E. Gazit, *Adv. Mater.*, 2006, **18** (11), 1365-1370.
16. P. W. J. M. Frederix, G. G. Scott, Y. M. Abul-Haija, D. Kalafatovic, C. G. Pappas, N. Javid, N.T. Hunt, R.V. Ulijin and T. Tuttle, *Nat. Chem.*, 2014, **7**, 30-37.
17. C. Colquhoun, E. Draper, R. Schweins, M. Marcello, L. Serpell, D. Vadukul and D. Adams, *Soft Matter*, 2017, **13**, 1914-1919.
18. J. Raeburn, A. Zamith Cardoso, and D. J. Adams, "The importance of the self-assembly process to control mechanical properties of low molecular weight hydrogels", *Chem. Soc. Rev.*, 2013, **42**, 5143-5156.
19. M. Reches and E. Gazit, *Science*, 2003, **300**, 625-627.
20. E. Gazit, *FASEB J.*, 2002, **16**, 77-83.
21. C. H. Görbitz, *Chem. Commun.*, 2006, **22**, 2332-2334.
22. R. Cukalevski, B. Boland, B. Frohm, E. Thulin, D. Walsh and S. Linse, *ACS Chem. Neurosci.*, 2012, **3** (12), 1008-1016.
23. J. Hardy, and D. Allsop, *Trends Pharmacol. Sci.*, 1991, **12**, 383-388.
24. D. J. Selkoe, *Neuron*, 1991, **6**, 487-498.
25. L. Adler-Abramovich, D. Aronov, P. Beker, M. Yevnin, S. Stempler, L. Buzhansky, G. Rosenman and E. Gazit, *Nat. Nanotechnol.*, 2009, **4** (12), 849-854.
26. M. Wang, L. Du, X. Wu, S. Xiong, P. K. Chu, *ACS Nano*, 2011, **5** (6), 4448-4454.
27. M. Zhou, A. M. Smith, A. K. Das, N. W. Hodson, R. F. Collins, R. V. Ulijin and J. E. Gough, *Biomaterials*, 2009, **30** (13), 2523-2530.
28. A. Heredia, I. Bdikin, S. Kopyl, E. Mishina, S. Semin, A. Sigov, K. German, V. Bystrov, J. Gracio and A.L. Kholkin, *J. Phys. D*, 2010, **43** (46), 462001-462006.
29. N. Amdursky, P. Beker, I. Koren, B. Bank-Srour, E. Mishina, S. Semin, T. Rasing, Y. Rosenberg, Z. Barkay, E. Gazit and G. Rosenman, *Biomacromolecules*, 2011, **12** (4), 1349-1354.
30. Y. Wu, F. Wang, K. Lu, M. Lv and Y. Zhao, *Sens. Actuators B. Chem.*, 2017, **244**, 1022-1030.
31. M. Moazeni, F. Karimzadeh, A. Kermanpur and A. Allafchian, *AIP Conf. Proc.*, 2018, **1920**, 020032(1)-020032(6).
32. K. Ryan, J. Beirne, G. Redmond, J. I. Kilpatrick, J. Guyonnet, N. V. Buchete, A. L. Kholkin and B. J. Rodriguez, *ACS Appl. Mater. Interfaces*, 2015, **7** (23), 12702-12707.
33. N. Amdursky, M. Molotskii, E. Gazit and G. Rosenman, *J. Am. Chem. Soc.*, 2010, **132** (44), 15632-15636.

34. X. Yan, Y. Cui, Q. He, K. Wang and J. Li, *Chem. Mater.*, 2008, **20** (4), 1522-1526.
35. N. Even, L. Adler-Abramovich, L. Buzhansky, H. Dodiuk and E. Gazit, *Small*, 2011, **7** (8), 1007-1011.
36. R. Chapman, M. Danial, M. L. Koh, K. A. Jolliffe and S. Périer, "Design and properties of functional nanotubes from the self-assembly of cyclic peptide templates", *Chem. Soc. Rev.*, 2012, **41** (18), 6023-6041.
37. R. E. Moore, "Cyclic peptides and depsipeptides from cyanobacteria: a review", *J. Ind. Microbiol.*, 1996, **16** (2), 132-143.
38. L. Feliu, G. Oliveras, A. D. Cirac, E. Besalú, C. Rosés, R. Colomer, E. Bardají, M. Planas and T. Puig, *Peptides*, 2010, **31** (11), 2017-2026.
39. A. Tapeinou, M. T. Matsoukas, C. Simal and T. Tselios, *Biopolymers*, 2015, **104** (5), 453-461.
40. F. Costa, I. F. Carvalho, R. C. Montelaro, P. Gomes and M. C. L. Martins, *Acta Biomater.*, 2011, **7** (4), 1431-1440.
41. L. H. Peng, Y. F. Huang, C. Z. Zhang, J. Niu, Y. Chen, Y. Chu, Z. H. Jiang, J. Q. Gao and Z. W. Mao, *Biomaterials*, 2016, **103**, 137-149.
42. M. AlMatar, E. A. Makky, G. Yakıcı, I. Var, B. Kayar and F Köksal, "Antimicrobial peptides as an alternative to anti-tuberculosis drugs", *Pharmacol. Res.*, 2017, **128**, 288-305.
43. M. K. Kwak, R. Liu and S. O. Kang, *Food Control*, 2017, **85**, 223-234.
44. L. Lombardi, A. Falanga, V. Del Genio and S. Galdiero, "A new hope: self-assembling peptides with antimicrobial activity" *Pharmaceutics*, 2019, **11** (4), 166-182.
45. A. D. Borthwick, "2,5-Diketopiperazines: synthesis, reactions, medicinal chemistry, and bioactive natural products", *Chem. Rev.*, 2012, **112** (7), 3641-3716.
46. J. Michalsky, J. Ctvrtnik, Z. Horakova and V. Bydzovsky, *Experientia*, 1962, **18**, 217-8.
47. J. Oku and S. Inoue, *J. Chem. Soc. Chem. Commun.*, 1981, **5**, 229-230.
48. M. Durini, F. A. Sahr, M. Kuhn, M. Civera, C. Gennari, and U. Piarulli, *Eur. J. Org. Chem.*, 2011, **20**, 5599-5607.
49. S. Kogikoski, S. Khanra, W. A. Alves and S. Guha, *J. Chem. Phys.*, 2017, **147** (8), 084703-084712.
50. D. Datta, O. Tiwari and K. N. Ganesh, *Nanoscale*, 2018, **10** (7), 3212-3224.
51. J. Guan, R. Zhang, L. Dale-Gandar, S. Hodgkinson and M. H. Vickers, *Behav. Brain Res.*, 2010, **210** (2), 221-228.

52. A. Mollica, R. Costante, S. Fiorito, S. Genovese, A. Stefanucci, V. Mathieu, R. Kiss and F. Epifano, *Fitoterapia*, 2014, **98**, 91-97.
53. Z. Z. Wu, G. F. Ding, F. F. Huang, Z. S. Yang, F. M. Yu, Y. P. Tang, Y. L. Jia, Y. Y. Zheng and R. Chen, *Mar. Drugs*, 2018, **16** (4), 125-139.
54. G. S. Nyanhongo, W. Steiner, G. Gübitz, B. Yeniad, H. Naik and A. Heise, *Biofunctionalization of polymers and their applications*, Springer-Verlag, Berlin, 2011.
55. D. M. Yebra, S. Kiil and K. Dam-Johansen, *Prog. Org. Coat.*, 2004, **50** (2), 75-104.
56. O. Hartman, C. Zhang, E. L. Adams, M. C. Farach-Carson, N. J. Petrelli, B. D. Chase and J. F. Rabolt, *Biomaterials*, 2010, **31** (21), 5700-5718.
57. D. Khatayevich, M. Gungormus, H. Yazici, C. So, S. Cetinel, H. Ma, A. Jen, C. Tamerler and M. Sarikaya, *Acta Biomater.*, 2010, **6** (12), 4634-4641.
58. E. Estephan, M. B. Saab, V. Agarwal, F. J. G. Cuisinier, C. Larroque and C. Gergely, *Adv. Funct. Mater.*, 2011, **21** (11), 2003-2011.
59. T. Hanawa, *J. Periodontal Implant Sci.*, 2011, **41** (6), 263-272.
60. J. Conde, J. T. Dias, V. Grazú, M. Moros, P. V. Baptista and J. M. de la Fuente, *Front. Chem.*, 2014, **2**, 48-74.
61. E. Jorgenson and A. Ianoul, *J. Phys. Chem. B*, 2017, **121** (5), 967-974.
62. P. Jorge, A. Lourenço and M. O. Pereira, "New trends in peptide-based anti-biofilm strategies: a review of recent achievements and bioinformatic approaches", *Biofouling*, 2012, **28** (10), 1033-1061.
63. G. P. Sakala and M. Reches, "Peptide-based approaches to fight biofouling", *Adv. Mater. Interfaces*, 2018, **5** (18), 1800073-1800098.
64. J. I. B. Janairo, *Peptide-mediated biomineralization*, Springer Nature, Singapore, 2016.
65. W. J. Crookes-Goodson, J. M. Slocik and R. R. Naik, *Chem. Soc. Rev.*, 2008, **37** (11), 2403-2412.
66. R. G. LeBaron and K. A. Athanasiou, "Extracellular matrix cell adhesion peptides: functional applications in orthopaedic materials", *Tissue Eng.*, 2000, **6** (2), 85-103.
67. M. B. Rahmany and M. van Dyke, "Biomimetic approaches to modulate cellular adhesion in biomaterials: a review", *Acta Biomater.*, 2013, **9** (3), 5431-5437.
68. N. Huettner, T. R. Dargaville and A. Forget, "Discovering cell-adhesion peptides in tissue engineering: beyond RGD" *Trends Biotechnol.*, 2018, **36** (4), 372-383.

69. S. E. D'Souza, M. H. Ginsberg and E. F. Plow, "Arginyl-glycyl-aspartic acid (RGD): a cell adhesion motif", *Trends Biochem. Sci.*, 1991, **16**, 246-250.
70. U. Hersel, C. Dahmen and H. Kessler, "RGD modified polymers: biomaterials for stimulated cell adhesion and beyond", *Biomaterials*, 2003, **24** (24), 4385-4415.
71. J. H. Collier and T. Segura, *Biomaterials*, 2011, **32** (18), 4198-4204.
72. I. Khan, K. Saeed and I. Khan, "Nanoparticles: properties, applications and toxicities", *Arab. J. Chem.*, 2017, DOI: 10.1016/j.arabjc.2017.05.011
73. A. M. Ealias and M. P. Saravanakumar, "A review on the classification, characterisation, synthesis of nanoparticles and their application", *IOP Conf. Ser. Mater. Sci. Eng.*, 2017, **263**, 032019-032032.
74. I. Matsui, "Nanoparticles for electronic device applications: a brief review", *J. Chem. Eng. Jpn.*, 2005, **38**, 535-546.
75. Y. F. Wang, L. Liu, X. Xue and X. J. Liang, "Nanoparticle-based drug delivery systems: what can they really do in vivo?", *F1000Res.*, 2017, **6**, 681-688.
76. M. C. Daniel and D. Astruc, "Gold nanoparticles: assembly, supramolecular chemistry, quantum-size-related properties, and applications toward biology, catalysis and nanotechnology", *Chem. Rev.*, 2004, **104**, 293-346.
77. M. Faraday, *Phil. Trans. R. Soc. Lond.*, 1857, **147**, 145-181.
78. S. Link and M. A. El-Sayed, *J. Phys. Chem. B*, 1999, **103** (40), 8410-8426.
79. R. Elghanian, J. J. Storhoff, R. C. Mucic, R. L. Letsinger and C. A. Mirkin, *Science*, 1997, **277**, 1078-1081.
80. X. Huang, P. K. Jain, I. H. El-Sayed and M. A. El-Sayed, *Nanomedicine*, 2007, **2**, 681-693.
81. J. M. Slocik, A. O. Govorov and R. R. Naik, *Nano Letters*, 2011, **11**, 701-705.
82. J. Zong, S. L. Cobb and N. R. Cameron, *Biomater. Sci.*, 2017, **5**, 872-886.
83. D. A. Giljohann, D. S. Seferos, W. L. Daniel, M. D. Massich, P. C. Patel and C. A. Mirkin, *Angew. Chem. Int. Ed.*, 2010, **49**, 3280-3294.
84. R. Lévy, N. T. K. Thanh, R. C. Doty, I. Hussain, R. J. Nichols, D. J. Schiffrin, M. Brust and D. G. Fernig, *J. Am. Chem. Soc.*, 2004, **126**, 10076-10084.
85. J. M. Slocik, M. O. Stone and R. R. Naik, *Small*, 2005, **1**, 1048-1052.
86. B. D. Gates, Q. Xu, M. Stewart, D. Ryan, C. G. Wilson and G. M. Whitesides, "New Approaches to Nanofabrication: Molding, printing, and other Techniques" *Chem. Rev.*, 2005, **105** (4), 1171-1196.

87. J. M. Lehn, "Supramolecular Chemistry—Scope and Perspectives Molecules, Supermolecules, and Molecular Devices (Nobel Lecture)", *Angew. Chem. Int. Ed.*, 1988, **27** (1), 89-112.
88. J. V. Barth, G. Costantini and K. Kern, "Engineering atomic and molecular nanostructures at surfaces", *Nature*, 2005, **437**, 671–679.
89. K. S. Mali and S. de Feyter, "Principles of molecular assemblies leading to molecular nanostructures", *Philos. Trans. R. Soc. London, Ser. A*, 2013, **371** (2000), DOI: 10.1098/rsta.2012.0304.
90. A. Kumar, K. Banerjee and P. Liljeroth, "Molecular assembly on two-dimensional materials", *Nanotechnology*, 2017, **28**, 082001-082046.
91. L. Sosa-Vargas, E. Kim and A. J. Attias, "Beyond 'decorative' 2D supramolecular self-assembly: strategies towards functional surfaces for nanotechnology", *Mater. Horiz.*, 2017, **4**, 570-583.
92. J. V. Barth, J. Weckesser, G. Trimarchi, M. Vladimirova, A. De Vita, C. Cai, H. Brune, P. Günter and K. Kern, *J. Am. Chem. Soc.*, 2002, **124** (74), 7991-8000.
93. M. Stöhr, M. Wahl, C. H. Galka, T. Riehm, T. A. Jung and L. H. Gade, *Angew. Chem. Int. Ed.*, 2005, **44** (45), 7394-7398.
94. S. L. Tait, Y. Wang, G. Costantini, N. Lin, A. Baraldi, F. Esch, L. Petaccia, S. Lizzit and K. Kern, *J. Am. Chem. Soc.*, 2008, **130** (6), 2108-2113.
95. A. Della Pia, M. Riello, A. Floris, D. Stassen, T. S. Jones, D. Bonifazi, A. De Vita and G. Costantini, *ACS Nano*, 2014, **8** (12), 12356-12364.
96. D. M. Packwood, P. Han and T. Hitosugi, *Nat. Commun.*, 2017, **8**, 14463.
97. N. Pippa, S. Pispas and C. Demetzos, "Polymer self-assembled nanostructures as innovative drug nanocarrier platforms", *Curr. Pharm. Des.*, 2016, **22** (19), 2788-2795.
98. L. Liu, K. Busutil, S. Zhang, Y. Yang, C. Wang, F. Besenbacher and M. Dong, "The role of self-assembling polypeptides in building nanomaterials", *Phys. Chem. Chem. Phys.*, 2011, **13** (39), 17435-17444.
99. A. Roy, S. L. Shrivastava and S. M. Mandal, "Self-assembled carbohydrate nanostructures: synthesis strategies to functional application in food", in *Novel Approaches of Nanotechnology in Food*, ed. A. M. Grumezescu, Academic Press, Cambridge, Massachusetts, 2016, ch. 5, p133-164.
100. C. Branden and J. Tooze, *Introduction to protein structure*, 2nd edn, Garland Science, New York, 1998.

101. J. A. Lukin, G. Kontaxis, V. Simplaceanu, Y. Yuan, A. Bax and C. Ho, *Proc. Natl. Acad. Sci.*, 2003, **100** (2), 517-520.
102. E. Pazos, O. Vázquez, J. L. Mascareñas and M. E. Vázquez, "Peptide-based fluorescent biosensors", *Chem. Soc. Rev.*, 2009, **38** (12), 3348-3359.
103. S. Pavan and F. Berti, "Short peptide as biosensor transducers", *Anal. Bioanal. Chem.*, 2012, **402** (10), 3055-3070.
104. Q. Liu, J. Wang and B. J. Boyd, "Peptide-based biosensors", *Talanta*, 2015, **136**, 114-127.
105. M. Studer, H. U. Blaser and C. Exner, *Adv. Synth. Catal.*, 2003, **345** (12), 45-65.
106. K. Wilson, A. F. Lee and C. J. Baddeley, "Enantioselective heterogeneous catalysis", in *Heterogeneous catalysts for clean technology*, ed. K. Wilson and A. F. Lee, Wiley-VCH, Weinheim, Germany, 2013, ch. 5, p103-124.
107. S. Han, S. Cao, Y. Wang, J. Wang, D. Xia, H. Xu, X. Zhao and J. R. Lu, *Chem. Eur. J.*, 2011, **17** (46), 13095-13102.
108. Y. Zhao, J. Wang, L. Deng, P. Zhou, S. Wang, Y. Wang, H. Xu and J. R. Lu, *Langmuir*, 2013, **29** (44), 13457-13464.
109. C. Bortolini, L. Liu, T. Gronewold, C. Wang, F. Besenbacher and M. Dong, *Soft Matter*, 2014, **10** (31), 5656-5661.
110. i) G. Binnig, H. Rohrer, C. Gerber and E. Weibel, *Appl. Phys. Lett.*, 1982, **40** (2), 178-180. ii) G. Binnig and H. Rohrer, in *Nobel Lectures in Physics 1981-1990*, ed. G. Eksping, World Scientific, Singapore, 1993, pp. 389-409.
111. T. Yamada, H. Suzuki, H. Miki, G. Maofa and S. Mashiko, *J. Phys. Chem. B*, 2005, **109** (8), 3183-3188.
112. S. G. Hansen. and T. E. Robitaille, *Appl. Phys. Lett.*, 1988, **52** (1), 82-83.
113. A. Y. Cho and J. R. Arthur, *Prog. Solid State Chem.*, 1975, **10**, 157-192.
114. M. A. Herman and H. Sitter, *Molecular beam epitaxy: fundamentals and current status*, 2nd edn, Springer-Verlag, Berlin, 1996.
115. L. Grill, *J. Phys. Condens. Matter*, 2010, **22** (8), 084023-084036.
116. V. Humblot, C. Méthivier, R. Raval and C. M. Pradier, *Surf. Sci.*, 2007, **601**, 4189-4194.
117. R. T. Seljamäe-Green, G. J. Simpson, F. Grillo, J. Greenwood, S. M. Francis, N. Schaub, P. Lacovig and C. J. Baddeley, *Langmuir*, 2014, **30**, 3495-3501.
118. M. Lingenfelder, PhD thesis, 2007, EPF Lausanne, Switzerland.
119. A. Naitabdi and V. Humblot, *Appl. Phys. Lett.*, 2010, **97**, 223112.

120. V. Humblot, F. Tielens, N. B. Luque, H. Hampartsoumian, C. Méthivier and C. M. Pradier, *Langmuir*, 2014, **30**, 203-212.
121. G. J. Fleming, K. Adib, J. A. Rodriguez, M. A. Barteau, J. M. White and H. Idriss, *Surf. Sci.*, 2008, **602**, 2029-2038.
122. S. M. Barlow, S. Louafi, D. Le Roux, J. Williams, C. Muryn, S. Haq and R. Raval, *Surf. Sci.*, 2005, **590**, 243-263.
123. S. M. Barlow, K. J. Kitching, S. Haq and N. V. Richardson, *Surf. Sci.*, 1998, **401**, 322-335.
124. T. Eralp, A. Shavorskiy, Z. V. Zheleva, G. Held, N. Kalashnyk, Y. Ning and T. R. Linderoth, *Langmuir*, 2010, **26**, 18841-18851.
125. A. Kühnle, T. R. Linderoth, M. Schunack and F. Besenbacher, *Langmuir*, 2006, **22**, 2156-2160.
126. D. Gross and G. Grodsky, *J. Am. Chem. Soc.*, 1955, **77(6)**, 1678-1680.
127. J. W. Kim, Y. M. Lee, S. M. Lee, M. J. Son, H. Kang and Y. Park, *Langmuir*, 2010, **26**, 5632-5636.
128. V. Feyer, O. Plekan, T. Skála, V. Cháb, V. Matolín and K. C. Prince, *J. Phys. Chem. B*, 2008, **112**, 13655-13660.
129. E. Mateo Marti, S. M. Barlow, S. Haq and R. Raval, *Surf. Sci.*, 2002, **501**, 191-202.
130. E. Mateo Marti, C. Méthivier and C. M. Pradier, *Langmuir*, 2004, **20**, 10223-10230.
131. J. Williams, S. Haq and R. Raval, *Surf. Sci.*, 1996, **268**, 303-309.
132. T. E. Jones, M. E. Urquhart and C. J. Baddeley, *Surf. Sci.*, 2005, **587**, 69-77.
133. A. G. Thomas, W. R. Flavell, C. P. Chatwin, A. R. Kumarasinghe, S. M. Rayner, P. F. Kirkham, D. Tsoutsou, T. K. Johal and S. Patel, *Surf. Sci.*, 2007, **601**, 3828-3832.
134. M. Smerieri, L. Vattuone, T. Kravchuk, D. Costa and L. Savio, *Langmuir*, 2011, **27**, 2393-2404.
135. A. V. Tarasevych, A. E. Sorochinsky, V.P. Kukhar and J. C. Guillemin, *Orig. Life Evol. Biosph.*, 2013, **43**, 129-135.
136. M. Mahapatra, L. Burkholder, S. P. Devarajan, A. Boscoboinik, M. Garvey, Y. Bai and W. T. Tysoe, *J. Phys. Chem. C*, 2015, **119**, 3556-3563.
137. F. Kling, M. Kittelmann and A. Kühnle, in *Imaging and Manipulation of Adsorbates Using Dynamic Force Microscopy*, ed. P. Moriarty and S. Gauthier, Springer, Cham, Switzerland, 2015, ch. 8, 119-129.
138. A. Kühnle, L. M. Molina, T. R. Linderoth, B. Hammer and F. Besenbacher, *Phys. Rev. Lett.*, 2004, **93**, 086101.

139. M. Mahapatra, J. Praeger and W. T. Tysoe, *J. Phys. Chem. C*, 2017, **121** (24), 13239-13248.
140. A. Vallée, V. Humblot, C. Méthivier and C. M. Pradier, *J. Phys. Chem. C*, 2009, **113**, 9336-9344.
141. C. Méthivier, V. Lebec, J. Landoulsi and C. M. Pradier, *J. Phys. Chem. C*, 2011, **115**, 4041-4046.
142. M. Lingenfelder, G. Tomba, G. Costantini, L. C. Ciacchi, A. De Vita and K. Kern, *Angew. Chem. Int. Ed.*, 2007, **46**, 4492-4495.
143. G. Tomba, M. Lingenfelder, G. Costantini, K. Kern, F. Klappenberger, J. V. Barth, L. C. Ciacchi and A. De Vita, *J. Phys. Chem. A*, 2007, **111**, 12740-12748.
144. Y. Wang, M. Lingenfelder, T. Classen, G. Costantini and K. Kern, *J. Am. Chem. Soc.*, 2007, **129**, 15742-15743.
145. I. Stensgaard, *Surf. Sci. Lett.*, 2003, **545**, L747-L752.
146. V. Feyer, O. Plekan, N. Tsud, V. Cháb, V. Matolín and K. C. Prince, *Langmuir*, 2010, **26**, 8606-8613.
147. V. Feyer, O. Plekan, N. Tsud, V. Lyamayev, V. Cháb, V. Matolín, K. C. Prince and V. Carravetta, *J. Phys. Chem. C*, 2010, **114**, 10922-10931.
148. V. Humblot, A. Tejada, J. Landoulsi, A. Vallée, A. Naitabdi, A. Taleb and C. M. Pradier, *Surf. Sci.*, 2014, **628**, 21-29.
149. A. Vallée, V. Humblot, C. Méthivier and C. M. Pradier, *Surf. Interface Anal.*, 2008, **40**, 395-399.
150. A. Vallée, V. Humblot, C. Méthivier and C. M. Pradier, *Surf. Sci.*, 2008, **602**, 2256-2263.
151. V. Humblot, A. Vallée, A. Naitabdi, F. Tielens and C. M. Pradier, *J. Am. Chem. Soc.*, 2012, **134**, 6579-6583.
152. S. M. Barlow, S. Haq and R. Raval, *Langmuir*, 2001, **17**, 3292-3300.
153. N. Kalashnyk, J.T. Nielsen, E.H. Nielsen, T. Skrydstrup, D. E. Otzen, E. Laegsgaard, C. Wang, F. Besenbacher, N. C. Nielsen and T. R. Linderroth, *ACS Nano*, 2012, **6**, 6882-6889.
154. R. Lindner and A. Kühnle, *ChemPhysChem*, 2015, **16** (8), 1582-1592.
155. S. Ando, A. L. Grote and K. Koide, *J. Org. Chem.*, 2011, **76**, 1155-1158.
156. R. H. Garrett and C. M. Grisham, *Biochemistry*, 4th edn, Cengage Learning, Boston, USA, 2008.
157. Y. Nozaki and C. Tanford, *J. Biol. Chem.*, 1971, **246** (7), 2211-2217.

158. J. L. Fauchère and V. Pliška, *Eur. J. Med. Chem.*, 1983, **18** (4), 369-375.
159. M. Yamashita and J. B. Fenn, *J. Phys. Chem.*, 1984, **88**, 4451–4459.
160. J. B. Fenn, M. Mann, C. K. Meng, S.F. Wong and C.M. Whitehouse, *Science*, 1989, **246**, 64-71.
161. V. N. Morozov and T. Y. Morozova, *Anal. Chem.*, 1999, **71** (7), 1415-1420.
162. J. Alvarez, R. G. Cooks, S. E. Barlow, D. J. Gaspar, J. H. Futrell and J. Laskin, *Anal. Chem.*, 2005, **77**, 3452–3460.
163. S. Rauschenbach, F. L. Stadler, E. Lunedei, N. Malinowski, S. Koltsov, G. Costantini and K. Kern, *Small*, 2006, **2**, 540–547.
164. J. N. O’Shea, J. B. Taylor, J. C. Swarbrick, G. Magnano, L. C. Mayor and K. Schulte, *Nanotechnology*, 2007, **18**, 035707.
165. C. Hamann, R. Woltmann, I. P. Hong, N. Hauptmann, S. Karan and R. Berndt, *Rev. Sci. Instrum.*, 2011, **82**, 033903.
166. G. Rinke, S. Rauschenbach, S. Schrettl, T. N. Hoheisel, J. Blohm, R. Gutzler, F. Rosei, H. Frauenrath and K. Kern, *Int. J. Mass Spectrom.*, 2015, **377**, 228–234.
167. S. J. Jethwa, M. Madsen, J. B. Knudsen, L. Lammich, K. V. Gothelf and T. R. Linderoth, *Chem. Comm.*, 2017, **53**, 1168–1171.
168. Z. Deng, N. Thontasen, N. Malinowski, G. Rinke, L. Harnau, S. Rauschenbach and K. Kern, *Nano Lett.*, 2012, **12**, 2452–2458.

Chapter 2: Experimental

Experimental and theoretical methods

In this section, the experimental details of the work in this thesis are described, as well as the theoretical methods employed. The UHV STM, as the primary tool used for gathering data, is discussed first, together with aspects of the system design and operation. Complementary techniques employed to support and enhance the STM experiments are described subsequently, namely mass spectrometry and X-ray photoelectron spectroscopy (XPS). The procedure for testing the sublimability of peptides is also discussed. Finally, the theoretical models used to assist the interpretation of specific STM datasets are detailed.

2.1 UHV STM

2.1.1 Theoretical background: Scanning Tunnelling Microscopy

Pioneered in 1981 by Binnig, Rohrer and co-workers,¹ STM permitted quantitative atomic resolution of surfaces for the first time, and thus revolutionised the field of surface science. This field has rapidly developed in recent years, due to the increasing ability of modern systems to routinely image molecular and even sub-molecular features at the surface-adlayer interface. As such, STM is an ideal technique for studying the supramolecular self-assembly patterns explored in this thesis.

The essence of STM lies in the phenomenon of quantum tunnelling, whereby conducting materials brought within a few Å of one another can produce a flow of current (with an applied potential bias) even though physical contact is not achieved (Figure 2.1). This occurs due to a small but finite overlap of the wavefunctions¹ of the two materials. The magnitude of this current depends exponentially on the separation of the materials, meaning that even movements on a subatomic length scale cause a substantial and measurable change in current. By creating a sharp tip from one of the materials, an extremely high spatial resolution of the remaining surface can also be attained, since the very end of the tip will give rise to the vast majority of the current. In the ideal case, the tip used will be terminated by a single atom, which allows for atomic resolution of the features on the surface.

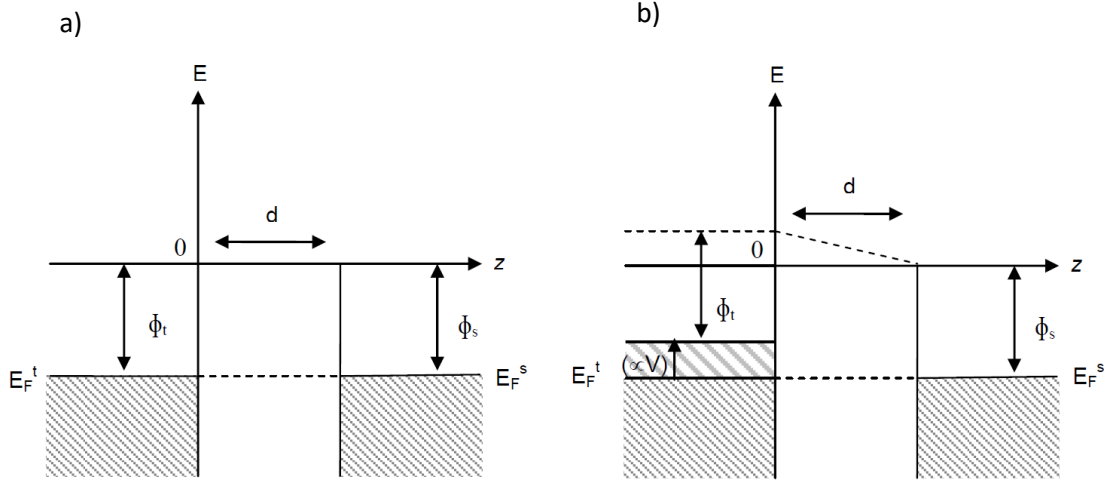


Figure 2.1. Schematic of energy level alignment and quantum tunnelling at a metal-surface interface, with separation d along an arbitrary distance axis z , against an energy axis E . Subscript t denotes the tip and s the surface. a) The Fermi energies are shown equal (i.e. the same material), meaning no net current will flow. b) The effect of applying a potential bias V is seen, in this case favouring net electron flow from tip to surface. The now favourable energy difference is indicated by the dashed lines.

However, the current measured by an STM tip is not only dependent on tip-surface separation and the surface topography, but also on the electronic density of states (DOS). A mathematical description of the tunnelling current can be derived from quantum theory, but is difficult to solve analytically without simplifications. Through several key assumptions, all of which can be safely made under typical STM experimental conditions, a simplified description of the tunnelling current is obtained. These assumptions include a perfectly sharp tip (atomically sharp), relatively small bias voltages, and a minimal contribution of thermal effects. The resultant equation can be expressed as:²

$$I = \frac{4\pi}{\hbar} \int_0^{eV} \rho_T(E_F^T - eV + \epsilon) \rho_S(E_F^S + \epsilon) e^{-2kd} d\epsilon$$

where I represents the tunnelling current, \hbar the Planck constant over 2π , ρ the DOS (T for tip, S for surface) at energy ϵ , E_F the Fermi energy, V the applied bias, d the tip-surface separation distance, and k a constant that includes the mass of an electron and the work function (ϕ).²

The equation above demonstrates that the tunnelling current is dependent exponentially on the tip-surface distance, which is, as discussed, the source of the extreme sensitivity of STM to surface topography. Once a tip is brought into tunnelling contact with a surface and a bias applied, it can be raster scanned over the surface in order to build up an image which represents the feedback from the tip-surface interaction at each point. Piezoelectric

materials, which change length in response to applied voltages, are used to control the position of the tip with sub-nanometre precision. The current readout from the tip is typically in the pA to nA range, which is small enough to be susceptible to electronic noise. A pre-amplifier is used to convert the signal to a voltage, and scale it up by a large factor (often $\sim 10^9$) to minimise this noise, before it is then sent to the STM controller hardware. Automated processes within computer software control the STM tip position in one of two scanning modes: constant current, or constant height mode. In the former, a target current is set and maintained by a feedback loop including the piezoelectrics and computer software. By monitoring the current feedback from the tip, the bias applied to the piezoelectrics can be constantly adjusted in order to maintain a constant magnitude of that current. The STM image in this case is constructed from the voltage adjustments made to the piezoelectrics in order to maintain the constant current. In constant height mode, the tip is simply held at the same height and the changes in current are recorded, reducing the overall complexity. Constant height mode performs exceptionally in cases of a highly flat scan area, but in many cases a surface has too many contours, meaning that a substantial risk of the tip 'crashing' into the surface exists. Constant current mode is therefore frequently preferred, as it greatly reduces the risk of tip crashes compared to constant height mode. In this thesis, constant current mode is used exclusively.

It is important to note that while an STM image can indeed represent surface topography, it also reveals electronic information about the surface, since the tunnelling current also depends on the local density of states (LDOS) of the surface. The LDOS represents the number of electronic states per interval of energy, with the relevant energy being the Fermi energy. A higher LDOS therefore corresponds to a higher probability of tunnelling, which leads to a higher current compared to a point of the same height with a lower LDOS. The final image is a convolution of the topography and LDOS of the surface. A clear example of the effect of the LDOS can be seen in the adsorption of oxygen atoms, which are electronegative, on metal surfaces. Despite the obvious height of the adsorbed object, the tendency is for a depression to appear in the STM image, due to the charge transfer from the substrate and a screening of the metal conduction electrons.

2.1.2 UHV

All of the STM experiments outlined in this thesis were performed in UHV conditions ($<10^{-9}$ mbar). Working in UHV is a significant advantage for STM, primarily due to the superior sample cleanliness that can be achieved and maintained for long periods, which in turn allows for precisely controlled surface molecular layers to be created. A simple calculation can be derived from kinetic gas theory to estimate the number of gas molecules colliding with a surface, at a given pressure and temperature.³ For instance, the arrival rate of N_2 at a surface, at room temperature and atmospheric pressure, can be estimated at 2.95×10^{23} molecules $cm^{-2} s^{-1}$. In a 'worst case' situation where all molecules stick to the surface, this would create a monolayer within approximately 4ns. Reducing the pressure to 10^{-10} mbar causes the time for monolayer formation to increase to over 10 hours. While real adsorption rates would be lower, and a number of other gases must be considered, it is clear that only UHV conditions can offer the chance to keep a surface pristine for STM studies (and indeed for other surface science techniques).

In order to achieve and maintain UHV conditions, a system of dedicated pumps and vacuum chambers must be setup. Such chambers are typically made of stainless steel, and subdivided into sections based on the required functionality. System components are mounted through a series of flanges, with electrical and mechanical feedthroughs as necessary so that the vacuum can be continuously maintained throughout normal operation. UHV pressures are obtained using different tiers of vacuum pump, starting with low vacuum roughing pumps. These pumps back turbomolecular pumps, which may already bring a system to UHV. In many cases, turbomolecular pumps are used to achieve the initial vacuum but are then superseded by pumps which operate only at or near UHV conditions (e.g. ion pumps and non-evaporable getter pumps). In the new instrument described in this thesis, scroll pumps were selected for the roughing pumps, and a combination of ion pumps and getter pumps for maintaining UHV. Pressures are monitored with a set of gauges, in this case Bayard-Alpert or 'hot cathode' gauges for HV-UHV ranges, and thermal conductivity (Pirani) gauges at higher pressures. The composition of gases within a vacuum chamber can also be analysed for reference, using a small quadrupole mass spectrometry device known as a residual gas analyser (RGA). Further details and discussion of the new UHV system build can be found in chapter 3 ("Design and construction of a new UHV-STM system").

Ultimately, to obtain UHV pressures inside the chambers, a vacuum system must also be 'baked' after every exposure to air. Air contains many contaminants, in particular water vapour, which stick to the walls of vacuum chambers in significant quantities. At a certain vacuum level (approximately 10^{-8} to 10^{-9} mbar) the outgassing rate of water from the chamber walls matches the rate at which the pumps remove gas, meaning the final UHV pressures cannot be obtained on a realistic timeframe. To overcome this problem, the system must be heated for a period of time in order to accelerate the removal of water. This process, known as baking, uses thermal shielding and large heaters to ensure the entire set of chambers is held at the same elevated temperature. Typical conditions are a 2-day bake at 120°C. Following a bake, the system is cooled, during which any filaments can be degassed, such as those in the RGA apparatus, to ensure later usage does not contaminate the chamber. Normal operation of the instrument can then resume once the instrument has fully cooled.

2.1.3 STM instrument

The STM instrument used for the majority of experiments described in this thesis is the Aarhus STM 150 (release 2), manufactured by SPECS GmbH (see Figure 2.2). The STM is mounted in a custom-designed set of UHV chambers, purchased separately and described in chapter 3. The procedure for designing the UHV chambers is described below, in 2.1.4 (UHV system design).

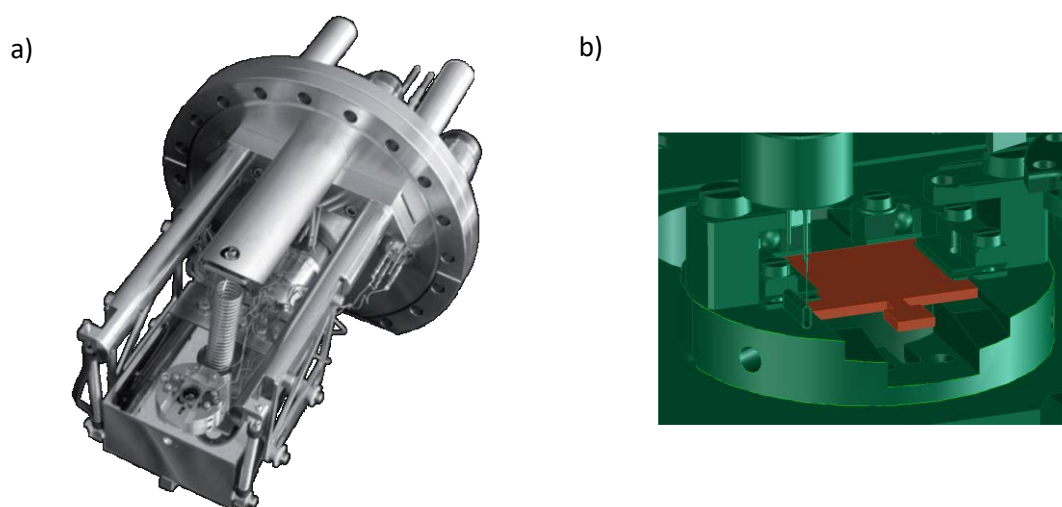


Figure 2.2. a) Image of the STM head from the SPECS Aarhus advertising material, b) Sample plate (orange) inserted into the STM (green), inverted so that the mounted sample faces the tip approaching from below.

The Aarhus 150 is a variable temperature STM, designed to operate in a temperature range of 90-400K. The scanner is embedded inside a heavy copper block suspended by springs, in an inverted configuration so that the tip approaches samples from below. The small mechanical loop of the scanner, combined with the heavy block and spring dampening, serves to minimise any mechanical noise that might affect the STM scans. Samples are inserted into the sample holder stage facing downwards, so that the tip can approach as indicated by Figure 2.2b. For sample transfer, a locking piston is employed that fixes the STM block in place, so that it is no longer hanging free from the support springs. For scanning, the piston must be retracted again so as not to electrically ground the system, and to minimise the effect of any external vibrations. Engaging the piston also permits rapid cooling of the STM, as it provides a strong thermal contact to the cryogenic cooling mechanism. This mechanism consists of two tubes for transporting cryogens that pass into and out of the piston arm, and can be accessed externally. One entrance is used to flow cryogen inside, while the other can be pumped on or simply left open for the exit flow. Once the desired temperature is reached in the STM, the flow can be reduced to a minimum and the piston retracted. The heat capacity of the large copper block, together with soft copper braids that maintain a limited contact with the heat sink of the cryogen flow, allows for the STM temperature to remain stable enough for several hours of scanning. The temperature of the copper block can be constantly monitored via a K-type thermocouple. Under these conditions, the tip is held at room temperature through dedicated counter-heating, so that the piezoconstants of the scanner can be kept the same.

In order to scan a sample, the tip must be brought safely into tunnelling contact (at a typical distance of about 1 nm) with the surface. This movement is performed through the use of several piezos in the form of an inchworm motor, with a further set of piezos being dedicated to moving the tip on a finer scale to perform scans. The inchworm motor functions by gripping and releasing the central rod on which the scanner is fixed in a cycle of steps, that once completed has caused the rod to move up (or down) by one increment (see Figure 2.3). In this way, the scanner moves closer to the surface in a way that is highly controllable through tuning of the piezo voltages and the time per movement cycle. The piezos for fine movement operate in a simpler fashion, with the scanner tube divided into four independent piezo sections that each correspond to a particular direction of movement in the X-Y plane. A final Z-piezo controls the Z movements required during scanning, on a smaller scale than those of the inchworm approach.

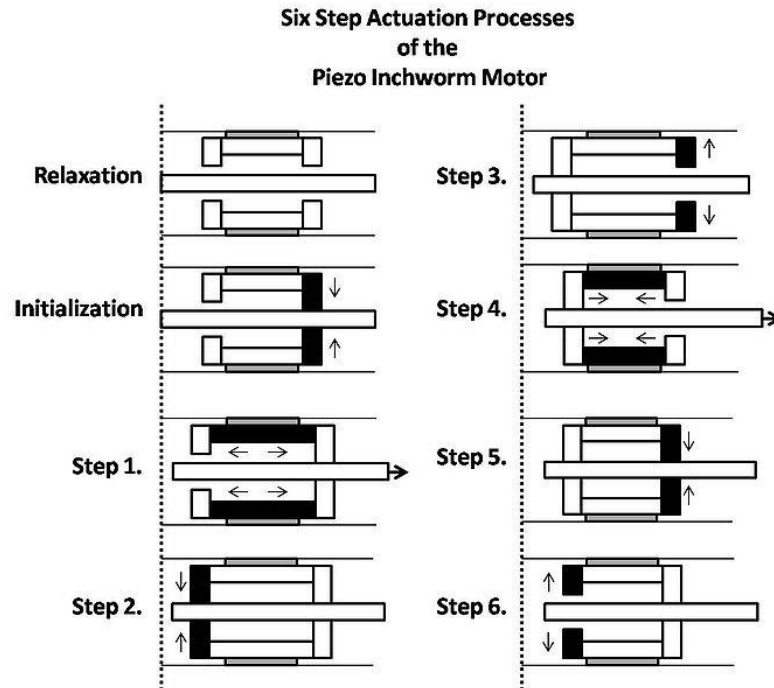


Figure 2.3. Illustration of the operation of a piezo inchworm motor. Black colouration indicates the active piezos in each step, with the arrows showing the direction of movement. After step 6, the cycle repeats as necessary. Image in the public domain.

The approach process is controlled in two stages through the STM software, the first manual and the second automated. The manual movement is required to reduce the time to approach, since the maximum travel of the scanner is several millimetres. The manual approach consists of driving the tip towards the surface at a relatively high speed until the tip-surface gap is greatly reduced. A viewport on the STM chamber can be used to guide the manual approach, as it provides visibility of the target surface in the sample holder. Using the tip's reflection once it becomes visible on the surface, the tip-surface distance can be reduced to 0.1mm or even less. Subsequently, the manual process should be stopped and the automated begun. The automatic approach involves a series of individual steps of the inchworm motor, with a full extension of the Z-piezo after each step to test if tunnelling contact is within its reach. If no tunnelling current is measured, the inchworm takes another step and the process continues as such. The user can set the parameters of the automatic approach, in order to find the balance between time taken and minimised risk of tip crashing. Once in tunnelling contact, the X-Y (lateral) scanning range of the STM is $1.5\mu\text{m} \times 1.5\mu\text{m}$, while the sensitive Z range is $(\pm) 175 \text{ nm}$. The lateral thermal drift under normal operating conditions is $<0.15 \text{ nm/min}$, and the vertical drift is $<0.05 \text{ nm/min}$, given a system at room temperature. Thermal drift refers to the tendency for the tip and sample to gradually move relative to one another, as a result of any temperature difference between them – a smaller

difference meaning a lower drift rate. In order to scan areas more than $\pm 0.75\mu\text{m}$ away from the initial approach centre point, the tip must be retracted and the sample holder moved manually with the wobblestick, before re-approaching.

The STM tips used in the Aarhus STM are pre-made by electrochemical etching of 0.3mm diameter tungsten wire, and the oxide layer is subsequently removed in vacuo using an ion sputter gun mounted to the STM chamber for this purpose. During sputtering, a target is bombarded with argon ions (Ar^+), generated in the ion gun and accelerated by a high voltage, resulting in layers of surface material being removed over time. In order to sputter the STM tip, a special sample holder with a central hole is placed in the sample stage. The tip is moved upwards so that it passes through this hole, exposing it to the ion beam while leaving the piezos and the rest of the scanner shielded by the sample holder plate. The whole stage is then grounded by engaging the locking piston, so that there is no build-up of positive charge on the tip or sample holder plate, allowing a sputter current to be recorded. Typical conditions for sputtering a new tip were an argon pressure of 1×10^{-5} mbar and a high voltage of 2kV, creating 5 μA of sputter current on the tip. A 15-minute sputter time was standard, but repeat cycles could be employed if the tip still did not produce suitable scans. The sputter gun was also used on occasion to assist in reforming in-use tips with persistent scanning issues, in order to reduce the need to replace a tip completely, which requires a vent of the system.

An electronic control system is used to both monitor and directly govern most of the STM's functions. The system used here is the Nanonis base package 4.5, also acquired from SPECS. All aspects of approaching the tip, moving the tip for scans, changing the scan conditions (bias voltage, current setpoint, time), measuring feedback including noise, and recording data are managed by the Nanonis system. Computer software provided with the Nanonis hardware enables the user to access the various functions and parameters. Both the control system and the instrument can be adapted for AFM functionality, operating in addition to or even simultaneously with STM scans. Furthermore, while our instrument can work at 90-400K, a model designed for temperatures up to 1300K is available. Neither of these options were selected and so are not described in detail here.

The experiments detailed in chapter 5 ("Chemical transformations of the Phe-Phe dipeptide") were not carried out with the Aarhus STM but with an existing low temperature STM from CreaTec Fischer GmbH. In comparison to the Aarhus STM, the CreaTec STM is always kept at liquid nitrogen temperatures (approx. 77K) using a bath cryostat, operates

with a Besocke-beetle type scanner, and is housed in a vacuum system purpose-built by the manufacturer.⁴ Much of the practical difference between the STMs is procedural and as such the data is very comparable, provided the lower temperature is considered in terms of the reduced thermal motion of molecules on the surface.

2.1.4 UHV system design

The new UHV system, together with its supporting frame and bakeout tent, was designed entirely within the SolidWorks 2012 CAD software (Dassault Systèmes). The software allows the user to transform 2D and/or 3D sketches into rendered 3D objects, which can be individually manipulated to edit their shape, size, material properties and aesthetics, and can also be combined into 'assemblies'. Constraints can be made on the relationships between different objects, so that features of the system can be re-designed and have the rest automatically update in response. New additions can also be readily incorporated in this way. This permits rapid and facile changes to a draft design, particularly useful when both costs and the instrument footprint must be brought to a reasonable minimum, meaning an optimal configuration can take several attempts.

The specific design for the UHV-STM setup described here was produced in an overarching assembly comprised of many sub-assemblies with varying complexity. In this way, the system as a whole could be viewed and edited, but also divided up into sections of differing sizes as required. The largest and most important sub-assemblies were designated "analysis chamber", "preparation chamber", "loadlock chamber" and "manipulator". The analysis chamber was based on the design of the SPECS turnkey system, since its primary functions were the same and only a few alterations were needed. The preparation chamber and loadlock chamber were custom-designed from scratch. The manipulator head was designed in collaboration with VAb Vakuum-Anlagenbau and Wolfgang Stiepany of the Max Planck Institute for Solid-State Research (Stuttgart), while the remainder of the manipulator build is standard VAb design and similar to that of the Createc LT instrument in our own laboratory. Furthermore, sample storage 'garages' were also designed with the help of Wolfgang Stiepany. It was possible to send drafts between collaborators by employing the technical drawing functionality, as well as saving files in the STEP format, which can be opened as 3D renders in most CAD software.

Another less discernible but equally important aspect of the UHV system is the supporting frame, which was also drafted in SolidWorks. The frame was modelled using drawings of Bosch profile frame pieces and connection components, downloaded from the manufacturer website to ensure the precise specifications were used. Once the desired thicknesses and lengths of frame profile were selected, they were sent to a local distributor (Mid West Automation) to be cut from stock.

To ensure the best pressures in the vacuum chambers, the system must be baked (see 2.1.2 [UHV]). The selected approach to the bake was the use of a 'tent' constructed of separate flexible parts that can be assembled together when required, and fan heaters inserted through the tent walls. The bakeout tent was planned out in a way that fit efficiently around the vacuum system, including frame, without creating technical and costly complications for manufacture. For this latter reason, work was conducted in close contact with Hemi Heating, exchanging files in a similar fashion to the main UHV system. Hemi were able to feedback with any issues foreseen in the design, such as manufacturing or material limitations. Exact reproductions of the tent within SolidWorks were unnecessary, and simple 'dummy' pieces could be used. Upon completion of these drawings at Warwick, Hemi were able to add in the precise technical details, before manufacturing the tent after a final approval.

Further details on the specifics of the UHV system design can be found in the next chapter, "Design and construction of a new UHV-STM system".

2.1.5 Samples and preparation

Two metal substrates were used for the studies described in this thesis, namely Cu(110) and Au(111). As discussed in chapter 1 ("Introduction"), low Miller index surfaces such as these are ideal for fundamental studies of self-assembly. The Cu(110) sample is a single crystal, while the Au(111) is a Physical Vapour Deposition(PVD)-grown film on mica. Such a film is composed of a number of 'grains' that grow in various orientations, creating boundaries where the grains meet. In practice, few grain boundaries are imaged in the STM since they occur every 5-10 μm by manufacturer specification, which is approximately 4-6 times greater than the maximum scan range of the instrument. Therefore, the Au(111) on mica sample is largely treated as behaving like a single crystal for the experiments herein.

The substrates selected represent different average molecule-surface interaction strengths as well as different surface atomistic structures. These factors strongly affect the self-assembly of deposited molecules, and so by working with two substrates distinct from one another in these respects, the relative strength and effect of (otherwise constant) intermolecular forces on an assembly can be probed in detail. More specifically, the typical organic molecule-surface interactions for a Cu(110) surface are stronger than those on Au(111),⁵ excluding compounds containing thiol groups.⁶⁻⁸ On a Cu(110) substrate therefore, the self-assembly of deposited peptides might be guided more by the surface than on a Au(111) substrate. Additionally, the (110) plane of a copper crystal is unreconstructed, meaning the surface atoms arrangement is that of an as-cut face-centred cubic (fcc) crystal. The resultant series of rows of copper atoms provides a contoured energy surface for the binding of molecules, and creates a plane of symmetry along the $[1\bar{1}0]$ axis, which bears particular relevance for stereochemical considerations. Furthermore, this structure results in a preferential direction for the diffusion of many species across the (110) surface, since a lower energy barrier typically exists for movement within a particular row of atoms, rather than across the rows. A (111) surface of gold, however, does display a reconstruction – into the so-called herringbone pattern.⁹ This reconstruction occurs due to the tendency for surface gold atom rows to contract unilaterally, which is locally energetically favourable for each atom, leaving 23 surface atoms over 22 hollow sites.⁹ In order to optimise the interactions with the layer below, the surface reforms, giving rise to the distinctive corrugation as demonstrated in Figure 2.4. The parallel corrugation lines separate fcc and hexagonal close-packed (hcp) regions of the surface in which surface atoms can sit on or close to hollow sites, while within the corrugation lines themselves atoms must sit on quasi-bridge sites. The fcc regions are larger since they are energetically favourable over the hcp due to their resemblance to the bulk phase.^{9,10} The hcp therefore lies between a pair of parallel lines, separated by 44Å, and the fcc is between neighbouring pairs, separated by 63Å. The unilateral nature of the original contraction still leaves a long-range strain in the other directions of the surface, which is compensated for by the zig-zag of the corrugation lines. This periodic direction change brings a contraction component into all three of the surface directions, thus relieving the long-range strain without preventing the local energetic benefit.¹⁰ In Figure 2.4, bright spots can be observed at the ‘elbow’ sites of the reconstruction pattern, which is a relatively common observation in STM scans of Au(111) surfaces. This occurs due to the particularly high reactivity of these elbow sites, meaning that even on a cleaned surface, impurities are found preferentially adsorbed here.

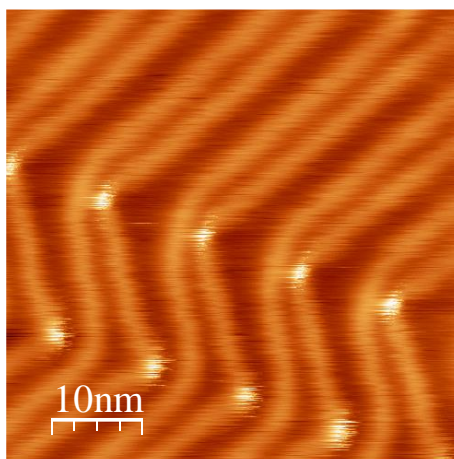


Figure 2.4. Room temperature STM image of a typical Au(111) herringbone reconstruction pattern, captured using the SPECS Aarhus system described in this thesis. The bright lines mark the boundary between fcc and hcp regions.

The Cu(110) and Au(111) samples used in this thesis were mounted on identical sample plates that are compatible with the Aarhus STM. The STM supports multiple sample holder types provided that they can be inserted for scanning upside down, and that they fit into the spring clamps of the sample stage. The simplest type of holder was employed for our samples, consisting of a single 18mm x 15.5mm plate (1mm thick) to which the sample is affixed by spot-welded tantalum foil. A small ‘handle’ protruding from one edge of the plate permits the sample holder to be locked into the head of the wobblesticks, and subsequently moved around in 3-dimensions and rotated as required (see Figure 2.5).

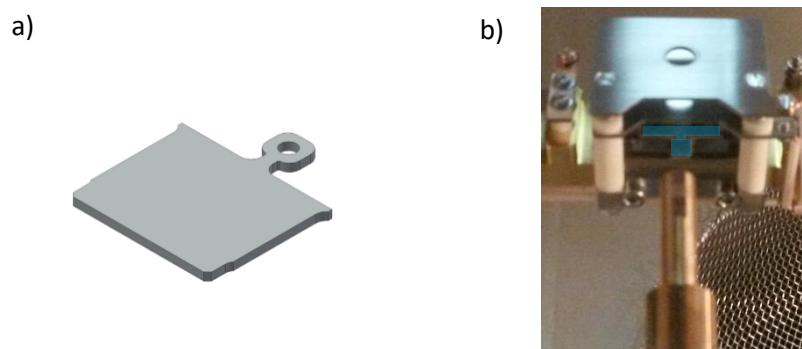


Figure 2.5. a) Render of a standard sample holder plate, without mounted sample. b) Photograph of a sample holder inserted into the manipulator arm, protruding as highlighted in blue. The wobblestick is visible below.

Once mounted and inserted into the vacuum chamber, a sample must be cleaned before use to allow for high quality STM scans to be obtained. Furthermore, the surface would ideally be atomically flat, so that molecules may assemble in 2-dimensions unfettered by high surface corrugation or defects. The process for obtaining a clean, flat surface in UHV consists of cycles of sputtering and annealing (heating). The sputtering process bombards the surface with Ar^+ ions, resulting in layers of atoms being ejected from the surface. This therefore removes adsorbed material but also damages the surface, and so an annealing cycle follows each sputter to allow the substrate atoms sufficient thermal energy to rearrange and form a stable and flat surface. The sputtering conditions used for the Cu(110) surface were an argon pressure of 1×10^{-5} mbar and a high voltage of 1kV, generating approximately $4 \mu\text{A}$ of current through the sample. Sputtering was typically carried out for 20 minutes. For the Au(111) surface, a slightly lower current of $3 \mu\text{A}$ was the target, in order to prolong the lifetime of the thin gold layer on mica. Annealing could be performed with one of two heaters fitted to the manipulator arm, an e-beam heater or a pyrolytic boron nitride (PBN) heater. The vast majority of experiments used the e-beam heater, located at the OMBE deposition stage (see chapter 3 for discussion of OMBE and ESI deposition stages). An e-beam heater operates by the generation of free electrons from a hot filament, which are then accelerated towards the target by means of a high voltage. The collision of the electron beam with the target induces a rapid local heating effect. The annealing conditions for both surfaces were 3.5A through the filament and a high voltage of 2kV, generating 10mA of current through the sample so that its temperature rises to 773K. Annealing typically lasted for 15 minutes, but could be continued if the surface was found to be corrugated in the STM. Additionally, while two cycles of sputtering and annealing was standard, repeat cycles could be used as necessary if the surface cleanliness was deemed insufficient.

2.1.6 Organic Molecular Beam Epitaxy

The molecular depositions onto metallic substrates described in this thesis were performed using Organic Molecular Beam Epitaxy (OMBE). This technique, applied in UHV conditions, offers a very high level of reproducibility and control over the cleanliness of the surface, molecular coverage, and the chemical state of deposited species. Molecules are placed into alumina crucibles that are heated by tungsten filaments in order to effect sublimation in vacuum, producing a molecular beam in front of which a target sample can be placed. Four

crucibles could be loaded with material into the OMBE 'source' mounted on the UHV chambers. The source used was purchased from Dodecon Nanotechnology GmbH, and features a cylindrical design with the four crucible cells positioned symmetrically. These cells are angled so that together they produce a focal point at which all four molecular beams would theoretically overlap, making sample positioning and co-depositions simpler. Each crucible cell has independent heating, as well as temperature measurement by means of a K-type thermocouple. The crosstalk between cells is <10K at a 300K temperature difference, which ensures that only the selected molecule will be deposited in any given experiment. The typical crucible used is a hollow 9mm length by 5mm diameter cylinder of alumina, open at one end. A shutter is mounted close to the crucible exit holes, with openings that can be rotated into position at the start and end of depositions to permit precise timing and therefore a predictable surface molecular coverage. This shutter also includes a pair of diametrically positioned openings for simultaneous co-depositions as required.

In order to avoid fragmenting the molecules to be deposited, a sublimation temperature must be determined in advance, since for excessively high temperatures the intramolecular bonds will start to break (this is discussed further in chapter 1 ["Introduction"] and chapter 4 [{"The sublimation of short peptides"}]). Having tested each molecule in a separate HV system as described in chapter 4, an approximate sublimation temperature was already determined. The specific design of each sublimation apparatus and the conditions therein mean that exact sublimation temperatures can only be ascertained in situ. The approximate values from the HV experiments were used as a guideline, and a slow ramping of temperature until molecules could be seen in STM scans was employed to obtain the 'real' sublimation temperature. Table 2.1 below shows the temperatures ultimately used for each molecule, and from where the molecules were acquired. All molecules were used as received, without further purification. Once in the OMBE source under vacuum, molecules were however outgassed, to remove residual solvents and water by heating the crucible to close to the sublimation temperature for approximately 30 minutes. If a significant pressure rise was detected from the gas produced during this process, the time was extended until the pressure recovered, ensuring a clean deposition of molecules when desired.

Molecule name	Sublimation T	Origin
L-Phe-L-Phe	443K	Sigma-Aldrich
Cyclo-(L-Phe-L-Phe)	443K	L. Alkhalaf, Challis group
Singly Dehydrogenated Cyclo-(L-Phe-L-Phe)	443K	L. Alkhalaf, Challis group
Doubly Dehydrogenated Cyclo-(L-Phe-L-Phe)	443K	L. Alkhalaf, Challis group
D-Phe-L-Phe	413K	Bachem
L-Phe-D-Phe	413K	Bachem
L-Tyr-L-Tyr	513K	Bachem
L-Trp-L-Trp	553K	Bachem

Table 2.1. A reference list of all peptides used in STM experiments in this thesis, their sources, and their sublimation temperatures.

2.1.7 STM data gathering

Preparation for an experiment with the Aarhus STM, starting with sample cleaning and ending with the first scans of a new molecular deposition, typically has a duration of 3 hours. The process is comprised of two cycles of sputtering and annealing, followed by a deposition from the OMBE source, and transfer to the STM. All depositions were onto room temperature samples and the majority of STM data was gathered at room temperature, and as such the transfer process was fast and straightforward. For experiments at low temperature, samples were transferred before engaging the locking piston and starting the cooling process, to ensure thermal equilibrium. The STM scans of particular depositions were taken over varying time periods, ranging from 1 hour to several days based on the quality of the deposition. Individual scans were also captured on different timescales, depending on the scan size and the desired resolution and image quality. An average scan took approximately 1 minute, but could be as short as 16s or as long as 15 minutes. All scans were taken in constant current imaging mode, typically with 10pA to 100pA of tunnel current as the target. The bias voltages used ranged from -2.5V to +2.5V, depending only on the most stable scanning conditions, since the resolution of the molecular features in this thesis proved to be largely unaffected by the bias sign or magnitude. In order to sample a significant area of the surface, scans were conducted across the whole 1.5 μ m x 1.5 μ m range in a number of distinct positions on the sample, accessed by macroscopic movements as described above in 2.1.3 (STM instrument). Analysis of the STM images gathered was performed using the free WSxM software.¹¹ The only major modification of the raw data was the application of plane flattening, to account for the tilt of the sample surface with respect

to the plane of the STM tip's movements. All distances and angles reported are as measured from this processed data, with quoted errors of one standard deviation where applicable.

2.2 Additional experimental techniques and theoretical methods

2.2.1 Mass spectrometry

Mass spectrometry is a widely-used technique for identifying unknown molecules, studying how molecules have been modified after a reaction, and for establishing the presence of known molecules and/or fragments in a solution or on a surface. The latter was particularly relevant for the sublimation tests of this thesis, where the primary goal was to recognise whether a particular amino acid or peptide remained intact after being sublimed. In addition, the mass difference between linear and cyclised peptides is an invaluable aid in identifying this transformation. Furthermore, due to the relative ease of use of mass spectrometry, and the low requirements for sample concentration, mass spectrometry was selected as the routine analysis technique for the sublimation experiments over other methods, such as Nuclear Magnetic Resonance (NMR) spectroscopy.

The instrument used for the majority of these experiments was an ESI time of flight (TOF) mass spectrometer, namely the Bruker MicroTOF of the Chemistry mass spectrometry facility at Warwick. This instrument features a resolution of >10,000 (full-width half-maximum/fwhm) and a mass accuracy of 5ppm in a mass range of 50-3,000 m/z. Solutions of sublimed and non-sublimed material were made up separately for comparison, with concentrations in the range of 1-10 μ M. The amino acids and many peptides were soluble in water, with L-Phe-L-Phe and derivatives instead dissolving in MeOH, and Tri-L-Phenylalanine through to Penta-L-Phenylalanine requiring acidification (1% formic acid) in AcN-H₂O to solubilise. The use of electrospray, a soft ionisation technique, avoids fragmentation within the mass spectrometer, and therefore the data obtained is solely due to the effects of the sublimation process on the molecules. By comparing the sublimed samples with the pristine, un-sublimed material, any differences can be identified, in particular focussing on the molecular ion peak and the presence of lower mass peaks corresponding to fragments.

A higher resolution instrument was used on occasions where a more detailed examination of specific fragment peaks was required. Greater resolution, coupled with an improved mass

accuracy, means that for a given peak, the m/z value can be more precisely determined. This substantially narrows the pool of valid molecular formulae that could yield an ion at a particular m/z value. Using the smaller pool of ions, it becomes possible to identify realistic fragments of the parent molecule, and thus better understand its sublimation behaviour. The instrument used for these experiments was the Bruker MAXIS II, a liquid chromatography-quadrupole TOF (LC-QTOF) which features a resolution of 80,000 (fwhm) and a mass accuracy of $<1\text{ppm}$ in a mass range of at least 50-20,000 m/z .

2.2.2 Sublimability tests

In order to have a molecular sublimation test that acts as a useful reference, one must employ a technique and environment similar to that of the intended UHV sample preparation, preferably without sacrificing speed and reliability. An existing HV system in the lab, constructed for a similar purpose, was ideal for carrying out such tests. The system comprises a small 5-way cross stainless-steel vacuum chamber, fitted with a linear drive transfer arm for positioning a deposition target, a custom-built crucible furnace for subliming powders, and a Quartz Crystal Microbalance (QCM) to measure deposition rates. The setup is completed by a fast-entry door, a wide-range vacuum gauge, and a turbomolecular pump backed by a rotary pump. Further discussion of this sublimation technique, known as OMBE was presented in 2.1.6 (Organic Molecular Beam Epitaxy).

Though the pressures attainable by this system are not as low as UHV, the difference in sublimation temperature between UHV and HV is much smaller than that between HV and ambient, and so the loss in accuracy is minimal. Additionally, the time gain from pumping to HV rather than UHV is substantial due to the absence of any baking. Therefore, the use of such a chamber allows for relatively rapid and reliable data gathering on the sublimation conditions of various molecules, and it is for these reasons that the HV system was employed during the experiments of this thesis.

The typical procedure for a sublimation test begins with loading a crucible with the relevant material, which for this project was always a powder. The crucible is mounted in its furnace in the vacuum chamber, and a glass slide inserted into the slot on the transfer arm, which is opposite the crucible aperture at an approximate distance of 450mm. The chamber is then sealed and pumped until it reaches a pressure in the 10^{-7} to 10^{-6} mbar region, i.e. HV.

Molecules were degassed in a similar fashion to that discussed in 2.1.6 (OMBE), but since many sublimation temperatures were not already known, the degassing temperature used was $\sim 373\text{K}$. The arm with the glass slide is retracted during this time. During a sublimation experiment, the crucible temperature is slowly ramped up, checking the QCM rate at each interval until an appreciable deposition rate is detected. Occasionally a sublimation temperature is already reported in the literature, in which case it can be used as a guide. Once a stable molecular beam is achieved in this way, the transfer arm is moved so that the glass slide intercepts the beam, thus beginning the deposition. Typically, a sample is left depositing for approximately 15 hours (overnight) before the crucible temperature is dropped to 0. This is to ensure a sufficient amount of material is present on the slide for detection by mass spectrometry. In order to obtain a mass spectrum, the chamber is vented to atmosphere and the slide removed and washed with an appropriate solvent. The solvent wash is used directly as a mass spectrometry sample, provided the solvent is appropriate, otherwise a dilution in MeOH/AcN is required. For comparison, a mass spectrum is also taken of a solution of unsublimed powder beforehand, as well as sample of clean solvent. Glass slides are washed with acetone, followed by the solvent to be used in the mass spectrometer, to minimise contaminants present before a deposition.

To assess whether it is possible to sublime a molecule intact, the “minimum” sublimation temperature is the key goal. This concept, however, is somewhat arbitrary due to its dependence on the precise conditions within an experimental setup and, in particular, on the choice of sublimation rate. In the experiments here, it was decided that the minimum sublimation temperature would generally be defined as the lowest value for which a signal in the mass spectrometer could be seen from the slide wash, determined in an iterative fashion as necessary. After observing a molecule’s fragmentation, an experiment was repeated in order to check if a lower sublimation temperature could be found. In some of these repeat experiments, deposited material can be detected in the mass spectrum despite the absence of a noticeable rate on the QCM. Such cases are found when gradually decreasing the temperature from a point where the QCM indicated a rate, but the mass spectrum indicated fragmentation. In doing so one tests the limit of sublimation, such that the rate is too low to appear above the noise in the QCM signal.

Uncertainties in temperature readings for the sublimation tests are expected to be $\pm 10^\circ\text{C}$, due to inherent issues of reproducibility with thermal conductivity by mechanical contact.

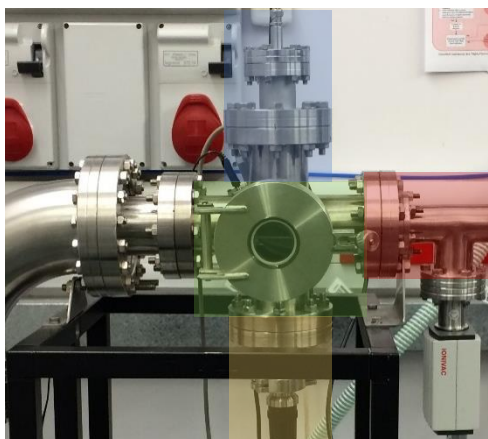


Figure 2.6. The system used for testing the sublimation of peptide samples, with key sections highlighted. Green: Central chamber for target slides; Blue: QCM apparatus above the main chamber, in-line with the deposition beam ; Orange: Crucible furnace mounted below the main chamber; Red: transfer arm with pressure gauge below.

2.2.3 X-ray Photoelectron Spectroscopy

XPS is a surface-sensitive analytical technique that provides information about the chemical composition of a target sample. At the heart of the technique is the photoelectric effect, whereby atoms subject to an electromagnetic beam can emit electrons. In this case, a monochromatic beam of X-rays is used, whose photons are absorbed by core-level electrons causing them to be ejected from the sample. Since emitted electrons must pass through any remaining sample material to escape (facing collisions, recombination, trapping etc.), the vast majority of detected photoelectrons are from the top few nm of the sample. This is the cause of the inherent surface sensitivity of XPS. The resultant kinetic energy of the emitted electrons can be measured and used to determine the binding energy of the electrons within the sample, though only for photoelectrons that have not undergone any interactions that induce energy loss. The following formula is used:¹²

$$E_B = hv - \Phi - KE$$

where E_B is the electron binding energy, hv is the energy of incident photons, Φ is the work function and KE is the photoelectron kinetic energy. Since the photon energy and the work function can be predetermined, the binding energy is thus easily calculated from measured kinetic energies. Binding energies of electrons are highly specific, not only to each element but also to the chemical bonds formed by that element within different environments (chemical shift). Additionally, the intensity of XPS peaks is proportional to the number of

atoms of each type present in a sample, as well as the photoionisation cross-section for the particular element. Therefore, an XPS spectrum can act as a molecular 'fingerprint', as the number, type and size of the peaks present provides detailed information on the chemical composition of the sample being studied. Precise quantitative evaluations of the ratio of each species on the surface can be challenging, however, due to difficulties in interpreting the exact size of a given peak and fitting its component curves. In addition, in some cases the depth attenuation of an XPS signal must be factored in, such as for layered systems, or those with molecules that are not parallel to the surface.

When XPS is applied to a thin molecular film on a metal surface, information can be obtained about the chemical state of the atoms within those molecules, allowing the structure to be much more precisely determined than with STM alone. The two techniques offer complementary information about a surface deposition, and so applying both together is highly advantageous. This proved particularly helpful for the studies of cyclo-L-Phe-L-Phe (cFF) and cyclo-L-Tyr-L-Tyr (cYY), and determining the extent of their dehydrogenation, if any. The XPS measurements were all performed on the Omicron UHV XPS system of Warwick's Interdepartmental Photoemission facility, located in the Physics department, on Cu(110) and Au(111) surfaces prepared in situ. This instrument uses a monochromated Al K α X-ray source, with beam energy 1486.6 eV. Following a full-width survey sweep to identify the peaks present in the sample, repeated scans were taken over energy ranges relevant to C1s, O1s, N1s and Cu2p_{3/2}/Au4f_{7/2} peaks as required. Typically, 20 scans were taken and averaged per data point. Fitting and analysis of XPS data was performed using the CasaXPS software.¹³ A Shirley-type background subtraction was applied across all the peaks, with fittings achieved through the use of a combination of Gaussian and Lorentzian functions, typically the GL(30) mix. Binding energies were calibrated with respect to the largest peak from the respective metal surface used, i.e. the Cu2p_{3/2} or Au4f_{7/2}. These peaks were comparable with literary references¹⁴ and demonstrated no marked changes in position before calibration, enabling their use as reliable reference points. Estimates of stoichiometry were obtained from the ratios of the areas of peaks to the photoionisation cross-section for the respective element.

2.2.4 Molecular models and simulations

Predicting the behaviour of molecular systems through theoretical modelling can help support the analysis of experimental data, as well as shed light on the reasons for any

observed behaviour, based on energy-minimised thermodynamic calculations. In principle, the time-independent Schrödinger equation can be used to describe the exact state of any system (not evolving over time), in terms of a wavefunction and its eigenvalues.^{15,16} However, exact solutions for the Schrödinger equation cannot be calculated for all but the simplest of cases, for example a single hydrogen atom. Approximations must be made in order to simplify the equation so that it can be solved for real molecular systems, largely by reducing the number of interdependent variables. Typically, these approximations are balanced between reducing the complexity of the calculation, and obtaining an accurate and reliable result. There are a number of approaches to this challenge, one of which is examined here: Density Functional Theory (DFT). Alternatively, some techniques use classical mechanics applied to 'particles' of interest, as another means of simplifying calculations on large systems, such as Molecular Dynamics (MD). Both techniques were used to assist the study of the adsorption of Cyclo-(L-Tyr-L-Tyr) (cYY) and its dehydrogenated form, on Au(111) and Cu(110) surfaces.

DFT is based on the principle that the electron density of a many-atom system (in its ground state) can be used to predict its electronic properties,¹⁷⁻¹⁹ a theory which relies on the Born-Oppenheimer approximation. Under the Born-Oppenheimer approximation, due to the orders of magnitude of difference in the relative mass (and therefore speed of motion) of atomic nuclei and electrons, the nuclei are considered to be stationary on the timescale of the electron movement. This effectively decouples electron-electron and electron-nuclei interactions, since the nuclei now present a stationary Coulomb potential field. The Hohenberg-Kohn theorems show that under these conditions, the potential field and the ground state electron density are explicitly linked by a unique functional, and therefore the total energy of the system can also be calculated.¹⁷ This represents a substantial simplification compared to the Schrödinger equation, as the individual movements of each electron no longer need be considered, with the overall electron density being the only variable. DFT can be used to calculate several key ground-state properties of a molecule-substrate interface, in particular proving effective at determining optimal adsorption conformations and their energies, and how these are affected by intermolecular interactions and the presence of adatoms.

The specific DFT calculations performed for this project were carried out by using the Quantum Espresso computer package.²⁰ Plane wave calculations using the revPBE-vdW-DF functional make up the majority of the DFT data, though a small number of calculations were

also performed using the optB88-vdW-DF functional to ensure another method produced the same trends. The revPBE-vdW-DF functional was selected because it has previously been used successfully to reproduce the experimental non-covalent adsorption energy of adsorbed molecules on the Au(111) surface.²¹⁻²⁸ The underlying metal surface is represented by a 'slab', which is four atomic layers thick in the case of Au(111) and seven atomic layers thick in the case of Cu(110). The supercell composed of the surface slab and molecule(s) was scaled so as to minimise adsorbate-adsorbate interactions that were not part of the intended calculation, for example across periodic boundaries when simulating small clusters or isolated molecules. For a single molecule on Au(111), a $p(8 \times 4)$ supercell was used, changed to $p(8 \times 5)$ and $p(10 \times 4)$ for pairs of molecules and adatom calculations respectively. For the single molecules on Cu(110), a $p(4 \times 8)$ supercell was used.

MD can be seen as a complementary technique to DFT, since it is focused on the study of atoms and molecules in motion. Larger scale DFT calculations for multiple molecules become prohibitively expensive in terms of computation time, particularly when evaluating a range of different possible molecular positions. MD however operates by solving Newton's equations of motion for the molecules of interest, using force fields (FF, from molecular mechanics) or interatomic potentials to define the interactions between them.²⁹ MD is used to simulate the movement of a group of molecules over a set period of time which, if long enough, permits the lowest energy configuration to be found. Such an approach is ideal for predicting the result of a self-assembly process, where a long-range thermodynamic optimisation is expected, provided thermal equilibrium is reached. The classical mechanics used in MD are of course an intrinsic simplification, such that the technique is not applicable for determining electronic properties, and can be ill-suited to determining accurate energy minima, in particular in cases where electron-electron interactions are more explicit, such as chemical bond formation. For cases such as these, DFT might be a more appropriate technique. However, the energy values produced by MD are self-consistent and can be defined relative to one another, meaning that comparing different self-assembly motifs is typically a reliable source of data.

The MD simulations for this project were carried out using the Gromacs 5.0.1 software package. Adsorbate molecules were modelled via the CHARMM22 FF, and their interactions with the Au(111) interface were described using the GoIP-CHARMM FF. The GoIP-CHARMM FF is a polarisable FF specifically designed to simulate peptides/proteins at gold interfaces.³⁰ The Au slab representing the (111) surface is assumed to be not reconstructed and is five

atomic layers thick. Molecules were simulated in groups of 8 and 12 in a $p(20 \times 24)$ supercell, groups of 16 in a $p(30 \times 27)$ supercell, and groups of 30 in a $p(42 \times 48)$ supercell. Simulations typically had a duration of 5 to 15 ns, at various temperatures between 300 and 500 K. A caveat exists for the stated MD temperature, as the GoIP-CHARMM FF is parameterised at 0 K and validated at 300 K. At higher temperatures, it is possible the FF is not reproducing the correct ensemble of conformations for that given temperature, and so the 'real' temperature may deviate from what is expected. Nevertheless, a higher set temperature will always give a higher real temperature regardless of its exact value, and so a broad comparison of the effects of raising temperature can still be made.

A number of simpler molecular models are used in this thesis to aid in the descriptions of the self-assembly patterns observed. These models, unless otherwise stated, are the product of the Avogadro software, and are energy-minimised conformations for isolated gas-phase molecules. The Avogadro default MMFF94 force field was used for these optimisations, since it is designed to work with common organic structures,³¹⁻³³ a category which covers small peptides. In some cases, the conformational search was guided by literary references, where simulations of similar molecules had already been performed. This strategy was particularly useful for cyclo-L-Phe-L-Phe (cFF) and cyclo-L-Tyr-L-Tyr (cYY), as a number of studies of diketopiperazines in general could be found.³⁴⁻⁴⁶ A recurring conformation was found across these references, that features both side groups projecting out from the same face of the DKP, with all three rings in approximately parallel orientations (Figure 2.7). Thus, these studies provided a starting point for the Avogadro minimisation, thus providing a more realistic conformer from this process. The nature of the Avogadro optimisations means they serve as a first approximation of how the molecules might be expected to land on the surfaces studied, but are not necessarily an accurate description of the final conformation once adsorbed. Therefore, the Avogadro conformers are only used as a guide, in the absence of more accurate dedicated DFT and MD simulations.

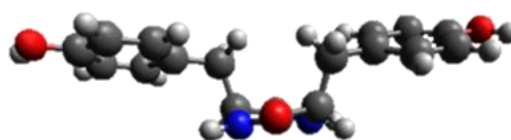


Figure 2.7. Energy-minimised model of cyclo-(L-Tyr-L-Tyr) using the MMFF94 force field. Similar structures can be found across the literature, for example see refs. 34, 42, and 46.

2.3 References

1. G. Binnig, H. Rohrer, C. Gerber and E. Weibel, *Appl. Phys. Lett.*, 1982, **40** (2), 178-180.
2. A. Della Pia and G. Costantini, "Scanning tunneling microscopy", in *Surface science techniques*, ed. G. Bracco and B. Holst, Springer-Verlag, Berlin, 2013, ch. 19, p565-597.
3. D. P. Woodruff and T. A. Delchar, *Modern techniques of surface science*, Cambridge University Press, Cambridge, 1986.
4. A. Della Pia, PhD thesis, University of Warwick, UK, 2013.
5. M. W. Roberts, "Surface reactivity of metal surfaces studied by scanning tunneling microscopy", in *Encyclopedia of materials: science and technology*, ed. K. H. J. Buschow, R. W. Cahn, M. C. Flemings, B. Ilshner, E. J. Kramer, S. Mahajan and P. Veyssi re, Elsevier, New York, 2001, p9050-9052.
6. G. E. Poirier, *Chem. Rev.*, 1997, **97** (4), 1117-1128.
7. H. Gr nbeck, A. Curioni and W. Andreoni, *J. Am. Chem. Soc.*, 2000, **122** (16), 3839-3842.
8. E. Pensa, E. Cort s, G. Corthey, P. Carro, C. Vericat, M. H. Fonticelli, G. Ben tez, A. A. Rubert and R. C. Salvarezza, *Acc. Chem. Res.*, 2012, **45** (8), 1183-1192.
9. J. V. Barth, H. Brune and G. Ertl, *Phys. Rev. B*, 1990, **42** (15), 9307-9318.
10. N. Takeuchi, C. T. Chan and K. M. Ho, *Phys. Rev. B*, 1991, **43**, 13899-13906.
11. I. Horcas, R. Fern ndez, J. M. G mez-Rodr guez, J. Colchero, J. G mez-Herrero and A. M. Baro, *Rev. Sci. Instrum.*, 2007, **78**, 013705-013712.
12. S. H fner, *Photoelectron spectroscopy: principles and applications*, 3rd edn, Springer-Verlag, Berlin, 2003.
13. N. Fairley, <http://www.casaxps.com>,   Casa software Ltd., 2005.
14. A. V. Naumkin, A. Kraut-Vass, S. W. Gaarenstroom and C. J. Powell, NIST Standard Reference Database 20 (Version 4.1), <https://srdata.nist.gov/xps/>, 2012 (accessed 2018).
15. L. K. Haines and D. H. Roberts, *Am. J. Phys.*, 1969, **37**, 1145-1154.
16. F. A. Berezin and M. Shubin, *Mathematics and applications: the Schr dinger equation*, Springer Netherlands, Dordrecht, 1991.
17. P. Hohenberg and W. Kohn, *Phys. Rev.*, 1964, **136** (3B), B864-B871.
18. W. Kohn, L. J. Sham, *Phys. Rev.*, 1965, **140** (4A), A1133-A1138.
19. T. Ziegler, *Chem. Rev.*, 1991, **91** (5), 651-667.

20. P. Giannozzi, S. Baroni, N. Bonini, M. Calandra, R. Car, C. Cavazzoni, D. Ceresoli, G. L. Chiarotti, M. Cococcioni and I. Dabo, *J. Phys. Condens. Matt.*, 2009, **21** (39), 395502-395520.
21. Z. E. Hughes, L. B. Wright and T. R. Walsh, *Langmuir*, 2013, **29**, 13217-13229.
22. J. Björk and S. Stafström, *ChemPhysChem*, 2014, **15**, 2851-2858.
23. J. Carrasco, W. Liu, A. Michaelides and A. Tkatchenko, *J. Chem. Phys.*, 2014, **140**, 084704.
24. D. J. Carter and A. L. Rohl, *J. Comput. Chem.*, 2014, **35**, 2263-2271.
25. M. Rosa, S. Corni and R. Di Felice, *Phys. Rev. B*, 2014, **90**, 125448.
26. W. Liu, F. Maa, M. Willenbockel, C. Bronner, M. Schulze, S. Soubatch, F. S. Tautz, P. Tegeder and A. Tkatchenko, *Phys. Rev. Lett.*, 2015, **115**, 036104.
27. Z. E. Hughes and T. R. Walsh, *Phys. Chem. Chem. Phys.*, 2016, **18**, 17525-17533.
28. Z. E. Hughes, A. Baev, P. N. Prasad and T. R. Walsh, *Phys. Rev. B*, 2017, **95**, 205425.
29. B. J. Alder and T. E. Wainwright, *J. Chem. Phys.*, 1959, **31** (2), 459.
30. L. B. Wright, M. P. Rodger, S. Corni and T. R. Walsh, *J. Chem. Theory Comput.*, 2013, **9**, 1616-1630.
31. T. A. Halgren, *J. Comput. Chem.*, 1996, **17** (5-6), 490-519.
32. T. A. Halgren, *J. Comput. Chem.*, 1996, **17** (5-6), 520-552.
33. T. A. Halgren, *J. Comput. Chem.*, 1996, **17** (5-6), 553-586.
34. C. F. Lin and L. E. Webb, *J. Am. Chem. Soc.*, 1973, **95**, 6803-6811.
35. E. Benedetti, R. E. Marsh and M. Goodman, *J. Am. Chem. Soc.*, 1976, **98**, 6676-6684.
36. M. Genest and M. Ptak, *Chem. Biol. Drug Des.*, 1978, **11** (3), 194-208.
37. M. Gdaniec and B. Liberek, *Acta Cryst.*, 1986, **42**, 1343-1345.
38. M. B. Avinash, D. Raut, M. K. Mishra, U. Ramamurty and T. Govindaraju, *Sci Rep.*, 2015, **5**, 16070.
39. A. Jeziorna, K. Stopczyk, E. Skorupska, K. Luberd-Durnas, M. Oszejca, W. Lasocha, M. Górecki, J. Frelek and M. J. Potrzebowski, *Cryst. Growth. Des.*, 2015, **15**, 5138-5148.
40. K. D. Kopple and D. H. Marr, *J. Am. Chem. Soc.*, 1967, **89**, 6191-6193.
41. K. D. Kopple and M. Ohnishi, *J. Am. Chem. Soc.*, 1969, **91**, 962-970.
42. J. Fleischhauer, J. Grötzinger, B. Kramer, P. Krüger, A. Wollmer, R. W. Woody and E. Zobel, *Biophys. Chem.*, 1994, **49**, 141-152.

43. A. Lewandowska, I. Carmichael, G. Hörner, G. L. Hug and B. Marciniak, *Chem. Phys. Lett.*, 2011, **512**, 123–128.
44. F. L. Bettens, R. P. A. Bettens, R. D. Brown and P. D. Godfrey, *J. Am. Chem. Soc.*, 2000, **122** (24), 5856-5860.
45. A. G. Abo-Riziq, B. Crews, J. E. Bushnell, M. P. Callahan and M. S. De Vries, *Mol. Phys.*, 2005, **103**, 1491–1495.
46. A. P. W. Arachchilage, F. Wang, V. Feyer, O. Plekan and K. C. Prince, *J. Chem. Phys.*, 2012, **136**, 124301.

Chapter 3: Design and construction of a new UHV-STM system

3.1 Design philosophy

As discussed in chapter 1 (“Introduction”), it was decided that a new UHV-STM system would be constructed to meet the needs of the proposed investigations into the vacuum deposition of large molecules, in particular oligopeptides. While OMBE studies could be carried out in an existing turnkey system, the particular desire to incorporate an electrospray deposition source necessitated building a new system, designed in such a way to accommodate the required components in an efficient manner. It was also resolved that the best way to create an effective setup that would both be cost-efficient and have a minimised footprint was to custom-design the system in-house. The STM head to be mounted into the new system would, however, be purchased, as a bespoke design here would be an unnecessary complication. Custom-designing the rest of the system allowed for specific tailoring towards having multiple integrated molecular deposition techniques, including electrospray deposition which typically requires differential pumping and ion optics, resulting in a relatively large build. Furthermore, producing new drafts or even minor revisions to the design was a faster process without the need to communicate with a third party. Any restrictions of the design based on the layout of the lab were also more easily worked around through direct access to the space.

The design philosophy of the new system can be summarised in three key aspects, which were then used to guide the overall structure of the vacuum system as well as individual choices about specific components. The first and most important criterion, as already mentioned, was that the system be designed with the electrospray setup in mind. More specifically, this meant not only ensuring sufficient space to build or attach the electrospray system, but constructing the main chambers in a way that is conducive to electrospray deposition without major modification. OMBE experiments were also essential, and so accommodating both facilities required some thought, especially in terms of the manipulator arm and the target sample plates. Additionally, the effects of the electrospray on the vacuum pressure had to be borne in mind.

Secondly, and directly related to the goal of comparing electrospray deposition with OMBE (and other deposition techniques), the system had to be designed for relatively rapid usage

and high sample turnover. To study the effectiveness of a deposition method, one ought to perform a large number of experiments to test a variety of conditions as well as ensuring reproducibility of data. To this end, it is advantageous to have a short time between molecular deposition and completion of an STM experiment, in order to enable a higher turnover rate. The main way of meeting this criterion was through the choice of the type of STM head itself, which is discussed below, but certain elements of the vacuum system also factored in this ethos.

Finally, the efficiency of the system was an important consideration, both in terms of its size and ease of use, and its cost. One simple way of ensuring the inclusion of all necessary components would be to have a very large preparation chamber, but this of course is costly and would slow down operations within the chamber, due to the travel distance between components. In vacuum, mechanical processes are already inherently much slower than in air, due to the limitations of air-vacuum coupled arms, manipulators, and actuators, and so further delay is highly undesirable. This also ties in to the second criterion of producing a fast, high turnover system. Larger chambers can also cause problems in terms of the footprint of the system, making it difficult to work around, connect to power and gas lines, and bake. Therefore efficient, operator-friendly use of space was essential in the design.

The system design and acquisition of components was split into two broad stages, as a result of the decision to custom-build the vacuum setup. The first step was a >6 month tendering process for the STM head, required due to the high cost of the item. In parallel to and following on from this, the vacuum chambers were designed and their manufacture arranged, along with the purchase of other essential components such as pumps, gauges, wobblesticks, the OMBE apparatus and the manipulator.

3.2 STM head

The STM head itself was chosen with the above design philosophy in mind. The ideal case was an STM that was compact and facilitated a higher sample turnover rate without compromising on scanning capabilities. Experimental flexibility in terms of sample type and experiment temperature was also considered advantageous, to permit greater variety in testing the OMBD and electrospray deposition processes. Low temperature capabilities are particularly useful, in order to minimise the thermal motion of deposited molecules, many of which have high mobility at room temperature, thus enabling better resolved STM images.

For these reasons, it was apparent that a variable temperature (VT) STM head was required, i.e. one which is designed to operate at either room temperature or with cryogenics (and sometimes at elevated temperatures). As well as the evident temperature flexibility of a VT-STM, there is an additional advantage of speed of use compared to a dedicated low temperature instrument. Low temperature STMs use a cryostat to maintain liquid nitrogen or liquid helium temperatures (77K or \approx 4K respectively), meaning that samples must always be cooled before scanning to avoid major drift issues from the thermal gradient. The time lost here can be significant, especially relative to scanning time if one only wishes to perform quick survey scans while testing a deposition technique. A VT instrument operating at room temperature avoids such considerations altogether, but maintains the ability to scan at low temperature if desired by means of a smaller in-built cryostat. The differences to be found in minimum temperature and maximum resolution were considered acceptable compromises for the benefit gained.

Of the responses to the tender, the STM head selected was the SPECS Aarhus 150. Technical details of the instrument are provided in chapter 2 (“Experimental”). Particular advantages of this model compared to its competitors were better low temperature stability, better vibrational stability, and a compact design. Resistance to external vibrations was especially important due to the intention to incorporate an electrospray deposition source into the system, meaning multiple pumping stages generating significant vibrational noise. This vibrational stability is provided by the small mechanical loop of the scanner, and the heavy metal block suspended by springs in which it resides. This block also acts as a sizable heat sink that helps with temperature stability, which combined with thermal radiation shields provides a stable operating temperature of \approx 115K with a liquid nitrogen flow. Additional features of the system to highlight include fast cooling (room temperature to 115K in approx. 1 hour), the capability for in-situ molecular deposition, and a simple sample stage design that enables quick transfer of samples into and out of the STM. Diagrams of the STM head can be found in Figure 3.1.

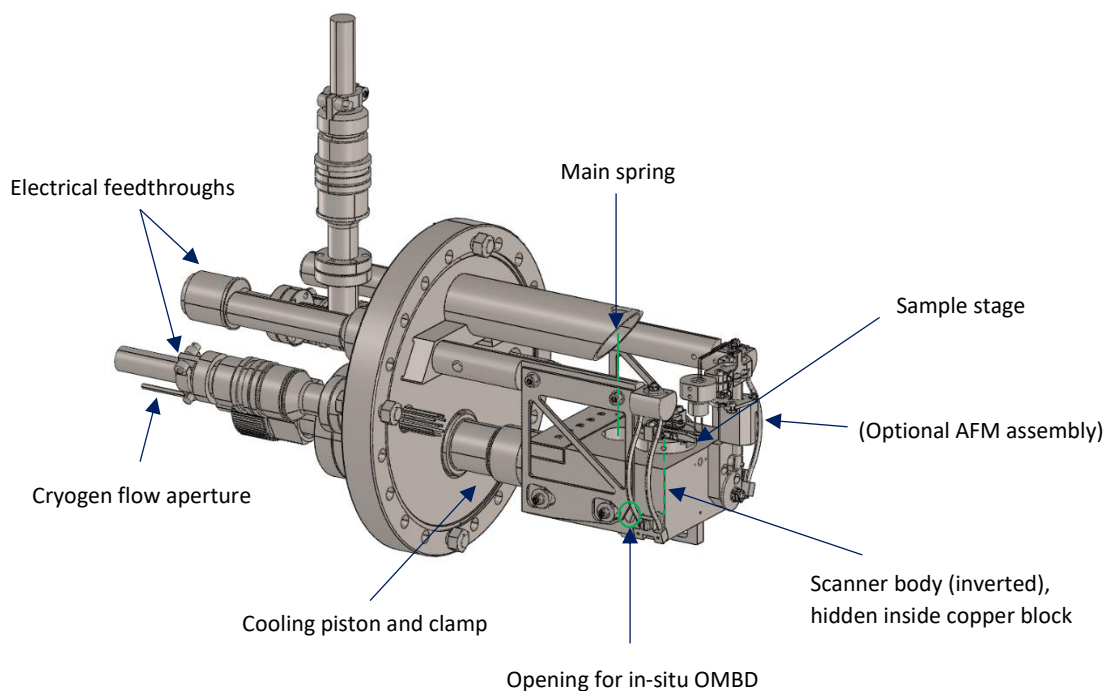


Figure 3.1. The Aarhus STM 150. This is a standardised model provided by SPECS, and as such some components will appear different to the real product. In particular, the radiation shields fitted to our system are absent in the diagram, and the optional AFM assembly shown was not purchased.

3.3 Vacuum chamber design

The design of the vacuum system in which the VT-STM would be housed was broken down into four major parts: the *analysis chamber* (STM chamber), *preparation chamber*, *loadlock chamber* and *manipulator arm*. This reflects an early design choice that the vacuum chambers would be separate entities (rather than, for example, being welded together with fixed gate valves incorporated, as seen in some commercial setups). Though the integrated approach can help reduce the system footprint and sample transfer times, the benefits of decoupling the chambers were considered more important. Primarily, the ability to isolate and detach chambers from one another is very useful if a fault develops, making repairs simpler and occasionally even permitting continuation of experiments, albeit in a limited capacity, in the remaining chambers. Furthermore, theoretically one could re-design a partitioned system to meet new requirements at a later date, which is not possible for an entirely integrated design. Major changes to a functioning UHV system may be unlikely, but having the possibility is useful when planning a significant expansion such as the electrospray deposition source. As discussed in chapter 2 (“Experimental”), all components were designed using the SolidWorks software package. Each section was created individually before

merging into a single large file, to check and finalise distances between components and their connections.

The logical starting point for the four key parts was the analysis chamber, since it houses the STM head, and other system functions revolve around the endpoint of an STM experiment. Annotated diagrams of the analysis chamber are presented in Figure 3.2a. The basis for the structure of this chamber was the SPECS 260mm diameter spherical chamber for an Aarhus STM, since this already contained optimised angles for in-situ OMBE deposition, tip sputtering, and observation of the tip position and sample transfers. Space for sample storage is also provided via the CF63 port adjacent to the viewport, through the use of a 'garage' mounted on a linear shift stage. The garage itself, also custom-designed, was built with simple space-efficient storage in mind, and simply comprises four sample holders of similar dimensions to the STM sample stage. Modifications to the base chamber were made according to custom requirements we had for our system. Due to the desire to have chambers that could operate independently of one another, the CF150 port that protrudes vertically down was extended, to allow for a turbomolecular pump to be incorporated in addition to the standard ion pump. This permits tip sputtering without the use of the preparation chamber as well as self-sufficiency in terms of pumping down and baking. The other adjustments made were relatively minor, being related to some of the smaller ports on the chamber, moved or replaced to accommodate the pumping change and offer more flexibility in the mounting of components. Overall the chamber design is compact and efficient, and allows for rapid sample transfers into and out of the STM via a wobblestick and the help of the viewport indicated in Figure 3.2b. Smooth operation of the STM itself is assured by staying close to the manufacturer's blueprint.

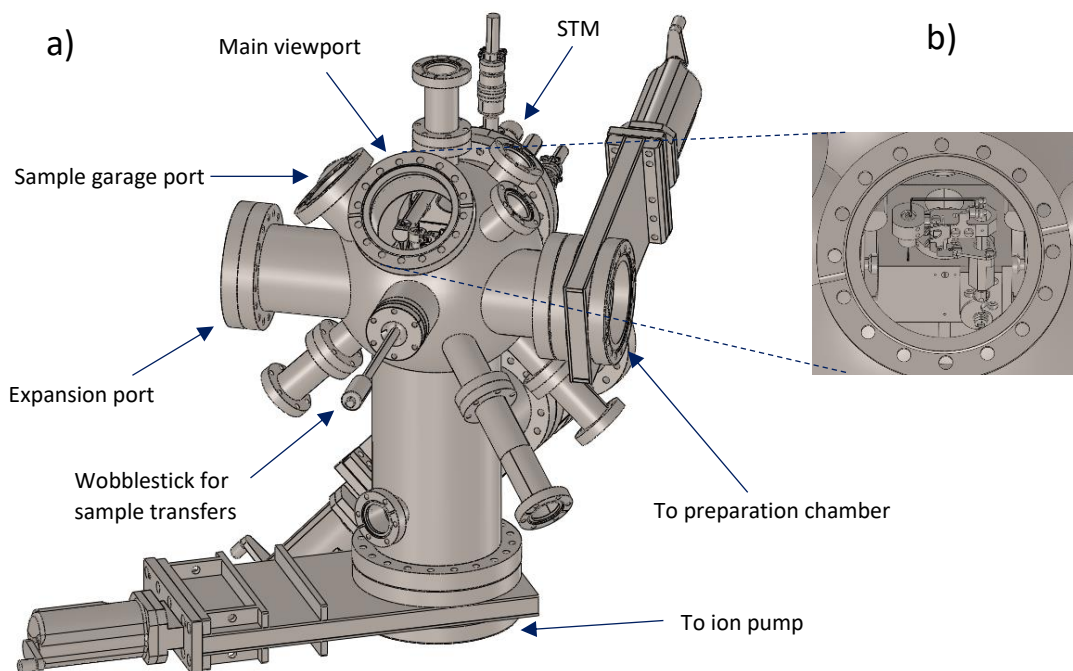


Figure 3.2. a) The analysis chamber, with pumps and other external components hidden for clarity. b) View through the main analysis chamber viewport.

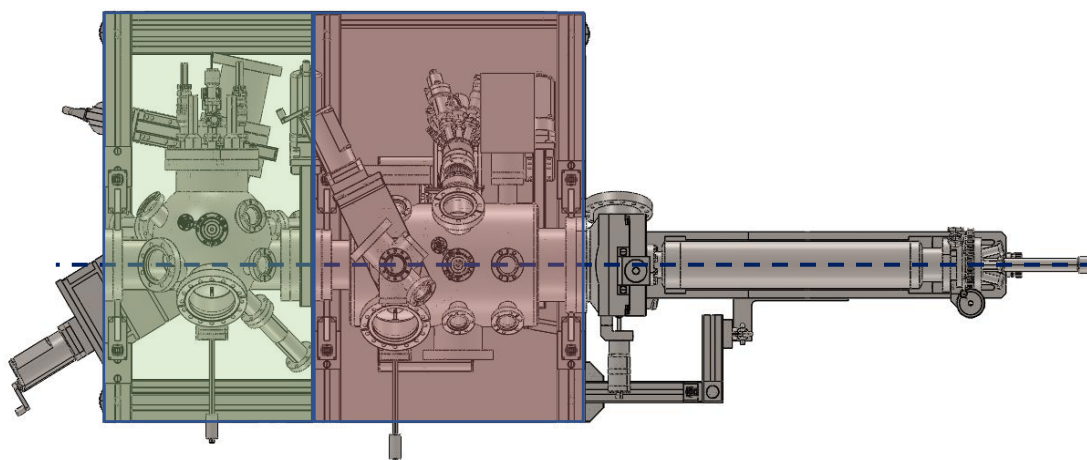


Figure 3.3. Overhead view of the full system, with the analysis chamber highlighted green and the preparation chamber highlighted red. The central axis along which the manipulator arm travels is indicated in blue. All system functions can be accessed with only small deviations from this axis.

The second key section to be designed, and the largest, was the preparation chamber. This has to house a large number of components for cleaning samples, depositing molecules, and analysing the ambient conditions via pressure and RGA, as well as transfer ports to the STM chamber and loadlock. Additionally, the XYZ manipulator must be mounted at the end of the preparation chamber so it can service the whole length of the vacuum system. Therefore,

this chamber had to be considerably larger than the analysis chamber, whilst still having a space-efficient design. Another important factor in the planning of the preparation chamber is the fast usage/high throughput criterion of the overall ethos, meaning that ideally all functions (especially different types of molecular deposition) can be performed on a single axis. This means a sample on the manipulator can go through all stages of preparation via rotations and by movements on the z-axis, with little to no adjustments in x and y. This enables simpler and faster movement between relevant positions in the chamber, and between the preparation and analysis chambers. In light of these considerations, a logical shape was an extension of the spherical-type chamber, i.e. a cylinder, aligned on the same central axis as the analysis chamber Figure 3.3 demonstrates the overall system layout. The structure of the chamber can be seen in Figure 3.4, where the main ports are labelled. Using a cylindrical shape with a diameter of 260mm and length of 380mm allowed all of the important components to be incorporated. Crucially, both the OMBE source and ESI deposition port could be placed on the same side of the chamber, 120° and 90° from the vertical angle respectively. An OMBE source (and certain types of metal source) cannot be mounted horizontally or at an elevated angle, and so an additional constraint was found in maximising the number of ports in the lower hemi-cylinder. The ion source for argon sputtering is mounted vertically, sample heating is built into the manipulator, and the wobblestick is mounted opposite the ESI position with the loadlock vertical. With this setup, a sample can be introduced into the preparation chamber, cleaned, and receive a molecular deposition, all on a single axis with minimal z movement and rotation, reducing the time taken for a complete experiment. Sufficient space is also available for further components to be added at a later date, such as a gas doser or an additional OMBE source. Maintaining the flexibility for future expansion of the system was key to the initial design, especially in terms of the ESI and the overall comparison of different deposition techniques. Though factoring in extra space on a system intended to be compact and efficient can be problematic, the benefits proved substantial, as will be discussed at the end of this chapter.

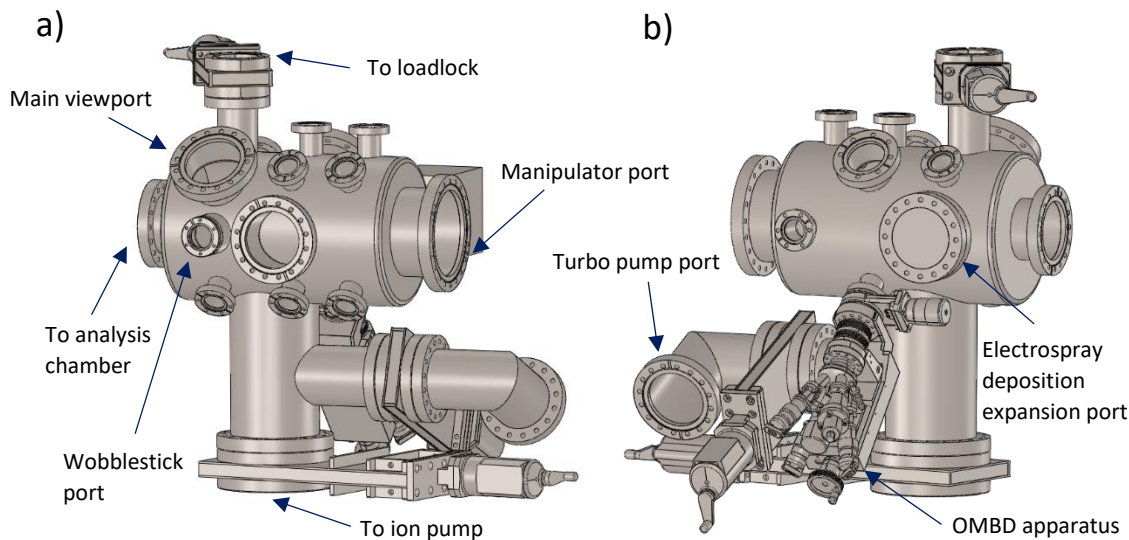


Figure 3.4. a) The preparation chamber, with pumps and other external components hidden for clarity. b) Rear view, with OMBD apparatus mounted.

The decision to place the loadlock vertically was somewhat unconventional, but greatly reduces the system footprint since the long sample transfer arm is moved into otherwise unused space. This arm uses a rack-and-pinion mechanism so it can be safely locked in place at any position, and the overall height of the system was tailored to ensure the arm was not impractically high. The loadlock chamber itself is of relatively simple structure, because the only major requirements for its design were the ability to load external samples, pump down to vacuum, and transfer the samples to the preparation chamber. As such, the chamber is essentially a CF40 cross piece with customised angles for the attached ports Figure 3.5. The access hatch and viewport are positioned for optimal loading and removal of samples, with the remaining non-vertical CF40 port hosting the gauge. A small turbomolecular pump can be mounted on the lateral CF63 port, leaving the final vertical ports for the transfer arm and gate valve. The transfer arm itself comprises a small garage of similar design to that of the analysis chamber, only with three sample storage spaces instead of four.

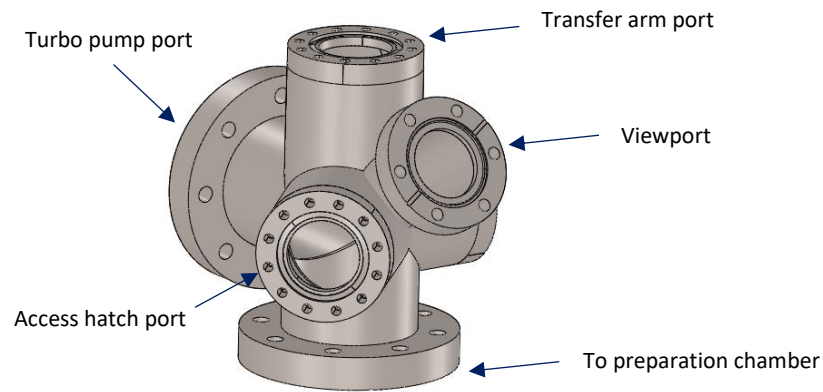


Figure 3.5. The compact vertical loadlock chamber.

The final major component designed was the manipulator head/sample stage. The external parts and moving parts of the manipulator as well as the electronic feedthroughs are standard VAb components, adapted to our requirements. Therefore, only the manipulator head needed a custom design, one which reflected the two types of molecular deposition planned. In particular, it is the electrospray deposition that imposes special requirements on the deposition stage, since some level of deceleration of the beam must occur to permit soft-landing, and the beam must be in some way focused onto or captured by the sample. The retardation of the beam is typically achieved with a bias applied to a grid or mesh, with steering and focusing of the beam on to the sample realised via biased plates with apertures. Building-in such functionality on the manipulator can cause problems for sample cleaning by sputtering, as it is important not to block the argon ion beam from reaching the full sample area. Furthermore, in an optimal setup for sputtering, the sample should be the closest object to the ion source, so that the surface is not contaminated by re-deposition of atoms sputtered off a material at higher elevation. It was therefore decided that the manipulator head would have two sample stages, one 'standard' stage to be used for sample sputtering, annealing and OMBE deposition, and one stage designed for electrospray deposition with the capacity to mount deceleration grids and focusing plates. This second stage would also feature sample heating (although with a smaller temperature range), to enable a variation in deposition temperature. In Figure 3.6 the resulting design of the manipulator head can be seen. Samples can be accessed in either position with the wobblestick of both the preparation and analysis chambers, and by rotation of the manipulator a deposition can be carried out by OMBE or electrospray as required.

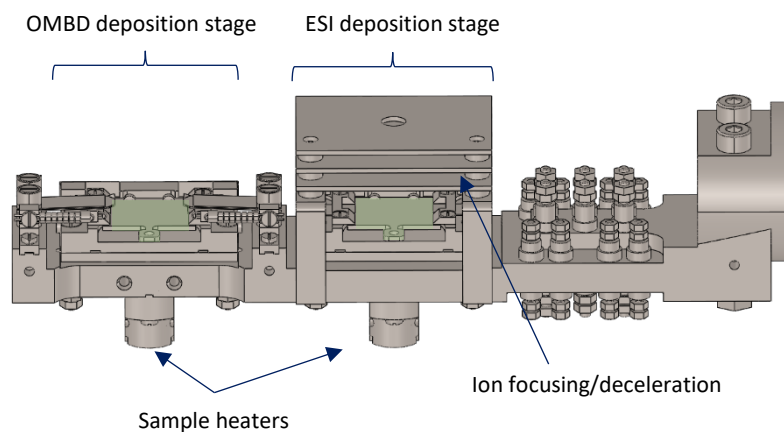


Figure 3.6. The manipulator head, viewed from the side accessed by the wobblesticks. Blank sample plates can be seen highlighted in green.

3.4 Support frame and baking tent design

With the main design phase complete, there remained the planning of a structural support frame for the system, and a baking setup to ensure that UHV conditions are achieved. A simple solution to the frame build was the use of aluminium strut profiles, which provide the necessary strength and support while offering excellent flexibility in terms of connectivity between parts. These profiles come in a range of cross-sectional areas (and can be cut to any length), and are easily joined together with a series of bolt connectors, angle connectors and t-bolts. Avoiding welding and other permanent fixings in this way means that the frame can be readily adapted to accommodate new components as the system expands.

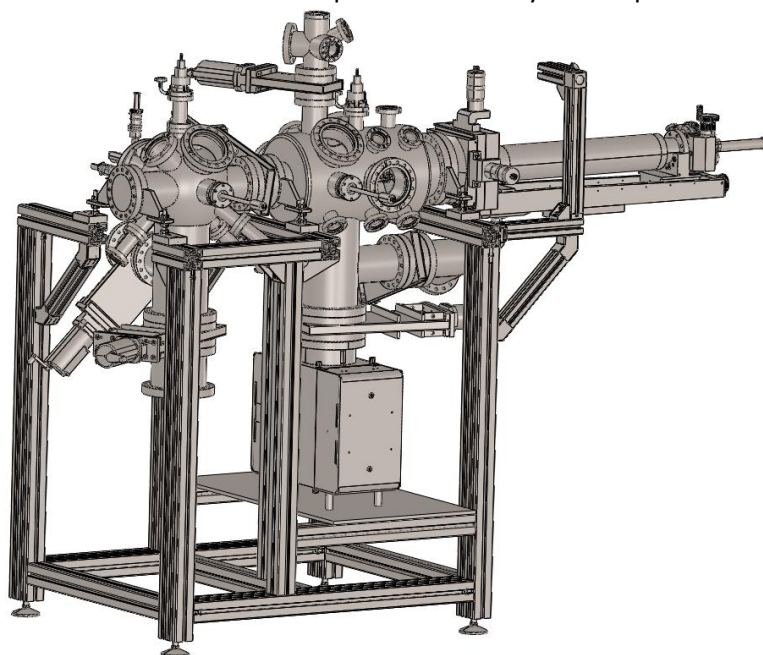


Figure 3.7. The support frame structure and complete set of chambers. The preparation chamber ion pump is shown to illustrate the role of the supporting plate.

Figure 3.7 shows the completed frame design and how it fits around the constructed vacuum system. The height selected is optimised so that wobblesticks and viewports are appropriately positioned, and to ensure enough space under the chambers for large ion pumps to be mounted. Any gaps in the frame are to allow access to important components and prevent ports from being blocked. A mock-up of a special support for the heavy load of the manipulator arm is highlighted in Figure 3.8a, which comprises a stiff spring under tension acting to oppose some of the moment the heavy manipulator applies about the mounting flange. Such considerations are important for a UHV system because the effect of the weight on the flange can open a small gap, one that cannot be seen but is sufficient to cause a leak that prevents UHV pressures from being maintained. Additional support is also provided for the large mass of the ion pump, by means of springs on a stainless steel plate bolted to the horizontal frame profiles Figure 3.8b. Finally, the overall shape of the frame should provide sufficient space around the vacuum chambers for a baking setup to be directly mounted, simplifying its design and potentially making a bake faster to set up in practice.

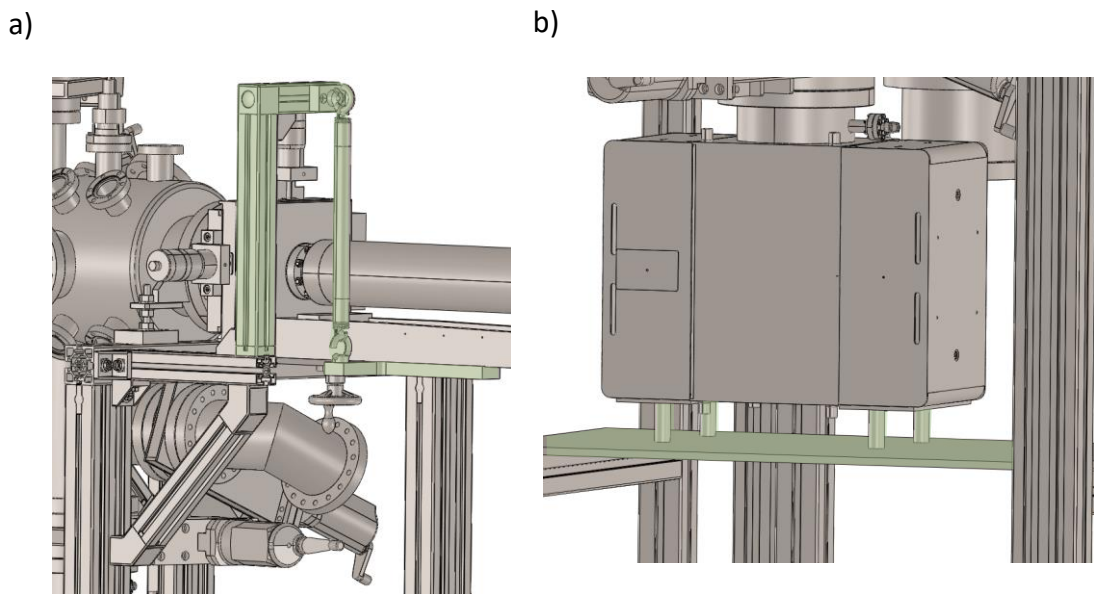


Figure 3.8. a) Frame-mounted support for the manipulator arm, highlighted in green. b) Steel plate and springs mounted under the ion pump to partition its heavy load, highlighted green.

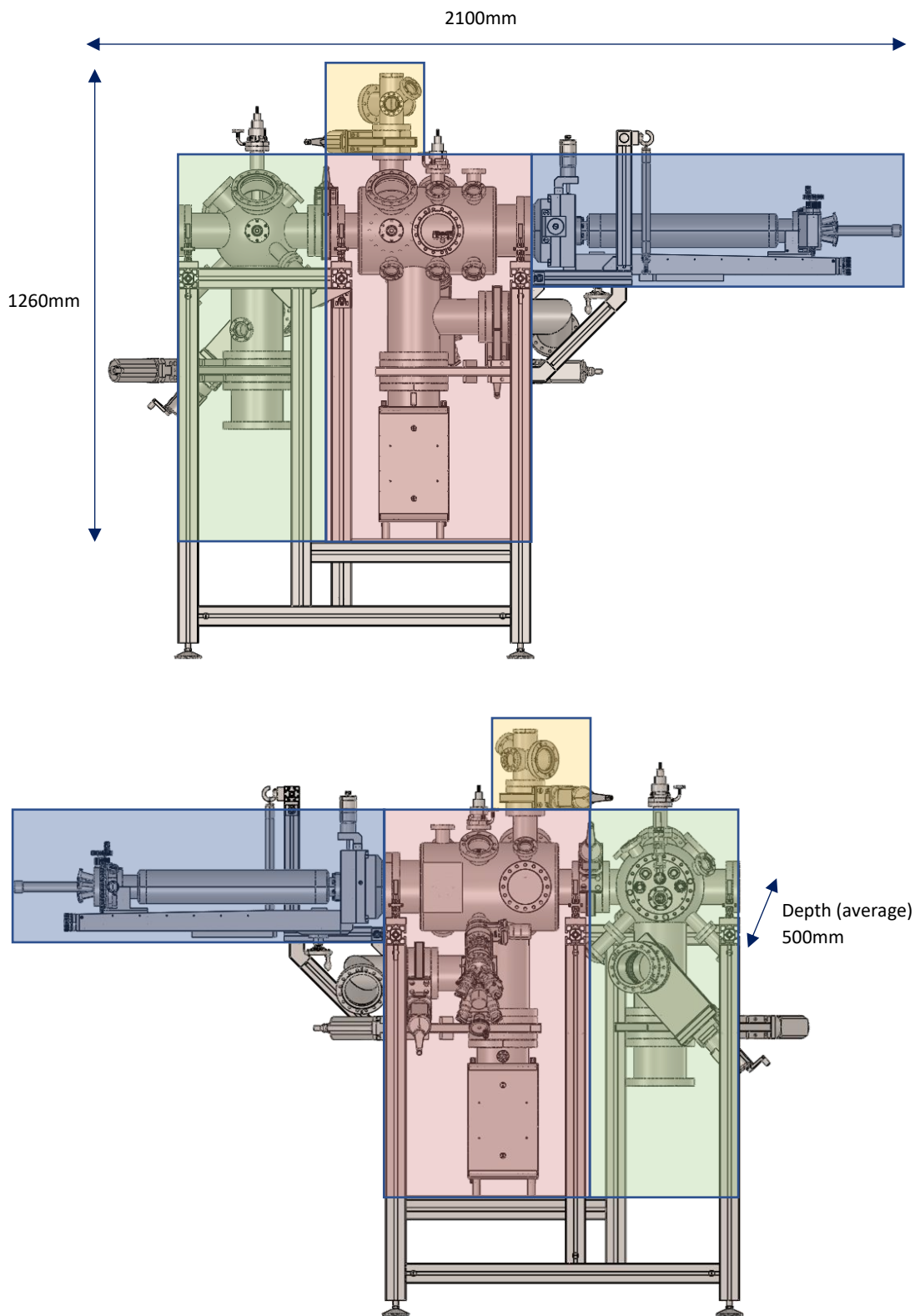


Figure 3.9. Side views of the full system, divided into major sections by colour. The analysis chamber is highlighted green, the preparation chamber red, the loadlock orange and the manipulator blue. Top: viewed from the 'front' side where the wobblesticks are accessed. Bottom: viewed from the 'back' side where the STM is mounted.

The complete system together with the frame is further illustrated in Figure 3.9. This was the final design produced before sending specifications to manufacturers and orders to suppliers. It is worth noting here that the typical style of ion pump (shown underneath the preparation chamber) was replaced for the analysis chamber by a much smaller pump at a late stage of designing the system (the smaller pump is not modelled). More specifically, it was decided that a combi non-evaporable getter (NEG) and small ion pump would be used. The NEG component is proficient at pumping most residual gases, and is especially suited for pumping H_2 , which is typically the largest component of the residual gas at UHV pressures. The small ion pump helps to deal with the inert gases that the NEG cannot handle. Since the analysis chamber should not regularly be exposed to either inert gases or high gas load in general, a combi pump of this kind is more than adequate to maintain UHV pressures, while the preparation chamber still requires the larger ion pump due to its more frequent exposure to argon sputter gas and higher pressures from the loadlock and pumping lines. The major advantage of substituting a combi pump for an ion pump is the greatly reduced size and weight, making the mounting easier and the load on the frame and chamber connection points lower.

The method chosen for baking the system was the use of a so-called 'tent', consisting of a flexible heat-resistant material (Nomex aramid) creating an enclosure, and two fan heaters to bring the system to approximately 120°C by heating the air to a uniform temperature. By using a relatively soft material in place of, for example, metal plate bake shields, it is easier to modify the baking setup in the future. Furthermore, the inherent flexibility can accommodate small changes in the vacuum system without the need for formal modifications. The facility for system expansion, in particular for the electrospray deposition source, was built into the tent design by means of small holes that are covered with Velcro-attached patches when not in use. An outline of the coverage to be provided by the tent is shown in Figure 3.10. The fan heaters are easily accommodated by bolting them to the frame profiles, and gaps are left in the tent for the heater placement. Additional gaps are found where components must be outside the bake, e.g. turbomolecular pumps. The loadlock chamber and manipulator are also outside of the tent to simplify its design, since these components are more easily baked with simple heating tapes.

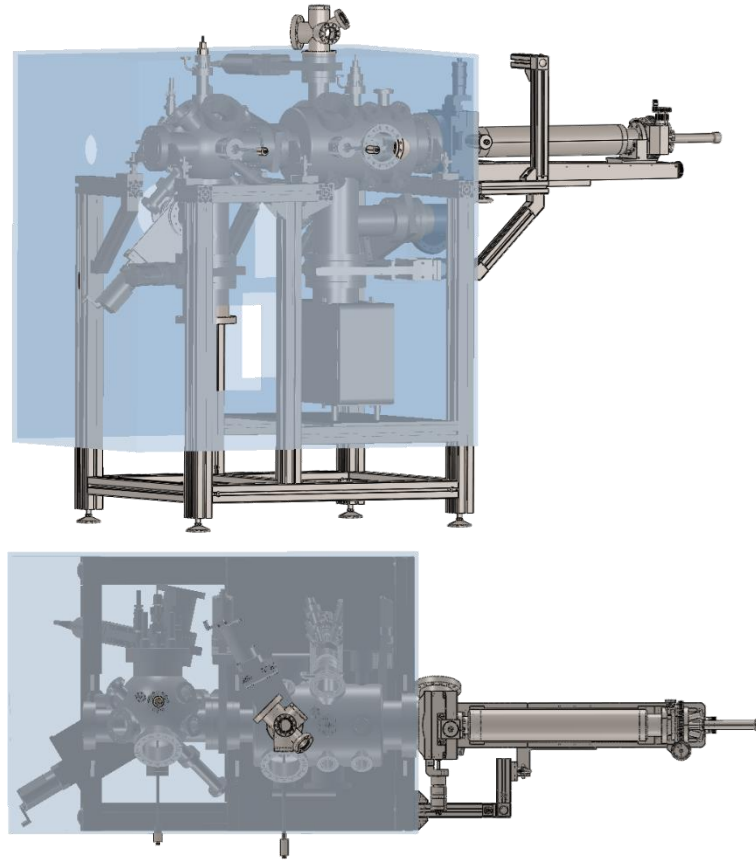


Figure 3.10. Side and overhead views of the system with the baking tent model in blue.

3.4 Final system build

Photographs of the constructed system can be found in Figure 3.11, and the completed baking tent (in isolation) is presented in Figure 3.12. The final setup of the system as-built was largely unchanged from the design phase, though a few changes were made to the design while in contact with manufacturers (and as such are undocumented in SolidWorks). Firstly, and most importantly, the overall height of the system was lowered, to simplify aspects of the frame and baking tent design without sacrificing usability of the system. This explains the slight difference in appearance of the complete setup in the photos of Figure 3.11, compared to the models of Figures 3.7 and 3.9. Other changes made to the final design were relatively minor technical changes based on manufacturer recommendations. Therefore overall the real system is a close match for the model, indicating that the design was realistic and functional. The design was also effective in meeting the ethos of being space-efficient while providing adequate room for the expansion required for the electrospray deposition source. The system's ease of use and sample turnover rate would

also prove to be optimal over the course of the experiments described in this thesis, due to a combination of the STM head chosen and design features of the chambers and sample transfer methods. Thus, the goals set out at the start of the process were met, and a new system for the investigation of different vacuum deposition techniques has been produced.

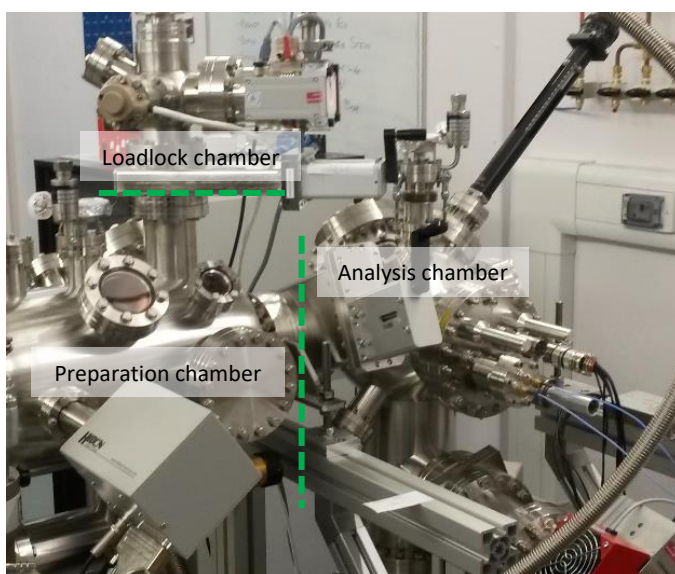
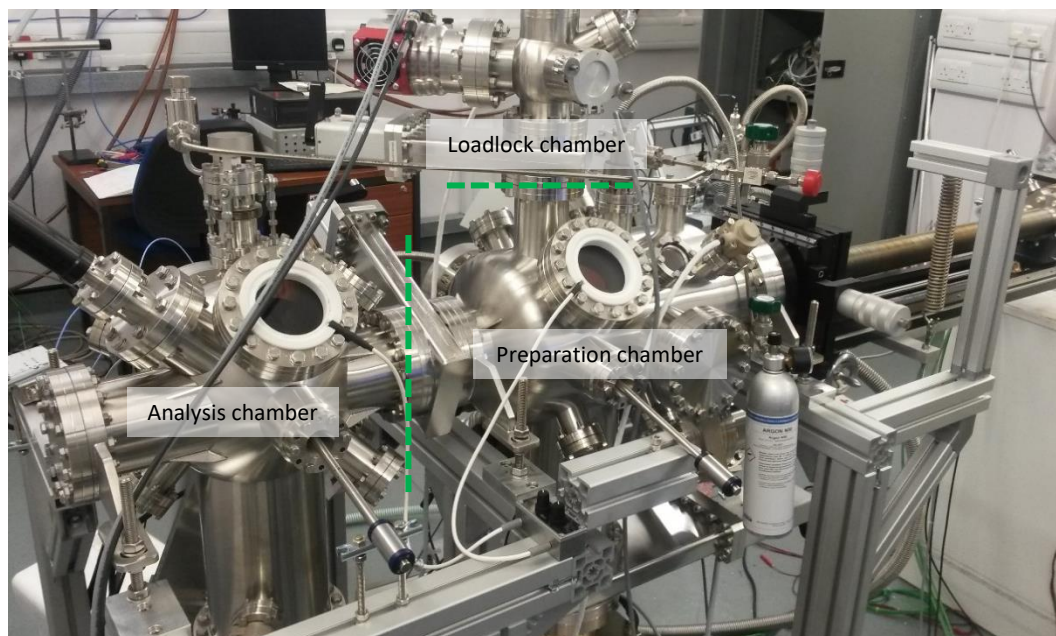


Figure 3.11. Photographs of the constructed system. Above: viewed from the ‘front’ side where the wobblesticks are accessed. Left: viewed from the ‘back’ side where the STM is mounted.



Figure 3.12. Photograph of the baking tent, viewed from the back (STM) side of the system.

Additionally, since the completion of the experiments contained in this thesis, the system has been expanded to incorporate not only the planned ESI deposition apparatus, but also a Molecular Spray modular ESI source (a simpler but quicker to use instrument than the in-house design), and a gas doser, which enables the deposition of volatile samples through a leak valve. Space still remains on the preparation chamber for the addition of a second OMBE source or a metal source, which would bring the total to 5 separate deposition techniques on a single system. There is also the scope for mounting deposition sources on the STM chamber. The current setup therefore serves to highlight the great flexibility built into the design, all of which was done without pre-existing diagrams of the additional deposition apparatus to work with. All of the deposition techniques see frequent use in the day-to-day operation of the system, whilst the STM itself continues to provide the same quality of data, thus illustrating the success of the multi-functional system as a whole.

Chapter 4: The sublimation of short peptides

4.1 Background

In most nanoscience and nanotechnology applications the most accurate technique available for transferring organic molecules onto a target substrate is OMBE in vacuum. As described in chapter 1 (“Introduction”), this simply involves thermal sublimation to generate gas-phase molecules, which pass through one or more small apertures in order to create a well-defined and oriented beam that can be directed towards a surface to grow a molecular film. This technique offers precise and reproducible control over the thickness and composition of organic thin films and, as such, is highly advantageous. In order to sublime a molecule for OMBE, the temperature in the crucible must be sufficiently high to result in the breaking of intermolecular bonds.

In many cases, an elevated temperature will inadvertently cause fragmentation of the molecules in question, due to the breaking of intramolecular bonds. This is particularly prevalent for large molecules or those with relatively weak internal bonds (e.g. coordinate/dative bonds),¹ which includes many biologically relevant systems, such as large peptides and proteins. However, since both the intermolecular and intramolecular bond-breaking are thermally-activated processes with an Arrhenius-type rate dependence, the outcome of a sublimation experiment will depend strongly on the conditions employed, in particular the relationship between the evaporation rate and the sublimation temperature chosen. Therefore, ultimately whether a molecular survives sublimation is strongly linked to the intended application of the process, as this directly influences the choice of sublimation conditions. With OMBE, the goal is typically to functionalise a surface through the creation of a thin film of a particular molecule or molecules. This requires a well-controlled sublimation and deposition process, which precludes the use of certain strategies such as flash annealing – where a very high temperature is applied but for a very brief period of time. The strategy applied in this thesis is instead one of using the minimum possible temperature that facilitates a measurable sublimation rate, adjusting deposition time as required. This approach enables the identification of the limits of the OMBE technique as a means of functionalising surfaces.

As discussed in chapter 1 (“Introduction”), relatively little is known about the precise limits of sublimation as a thin film sublimation technique, despite the importance of this issue for nanoscience. The concept of a limit itself is also difficult to define, since different types of molecules are not easily compared due to their varying structural features. However, gathering data for a specific class of noteworthy molecules would still be very instructive, and could act as a reference base for other compounds. Here, an effort to tackle this issue is undertaken, by conducting a study on the sublimability of simple peptides, primarily in relation to their size. The peptide class of molecules serves as an excellent model system, and are also attractive molecules for nanoscience in their own right, as detailed in chapter 1. While most amino acids have been reported to survive sublimation, relatively little data exists for larger peptides, especially beyond two and three residues in length. A systematic study of peptide sublimation as a function of length is, therefore, still lacking.

As briefly mentioned in chapter 1 (“Introduction”) and chapter 2 (“Experimental”), to determine if a molecule survives sublimation one must employ analytical techniques capable of directly identifying a molecule, such as mass spectrometry or NMR. Mass spectrometry was selected as the primary analytical technique for these sublimation experiments due to the low requirements for sample concentration, and the relative ease of use of the technique. Mass spectra for the pristine unsublimed material and the sublimed samples were compared in order to identify fragmentation. In addition, ‘theoretical’ m/z values were taken from the Bruker Data Analysis software corresponding to the molecular formulae of each peptide and fragment, to assist in identifying some of the major peaks. The primary instrument used for mass spectrometry experiments was the Bruker MicroTOF, though a Bruker Maxis II was also employed when higher resolution data was required (see chapter 2, “Experimental”, for additional details).

Two series of peptides were selected, based on the amino acids alanine and phenylalanine (see Figure 4.1). Alanine, with a methyl group side chain (Figure 4.1b), is the smallest chiral amino acid and therefore serves as a logical starting point for this investigation. Phenylalanine, with a larger and aromatic residue (Figure 4.1c), was chosen as the next step in side chain complexity that avoids strong secondary interactions (e.g. hydrogen bonding) whilst showing a more significant difference than simply adding length (e.g. valine). The two complete sequences analysed here comprise L-Alanine (A) through to ‘Penta-(L)-Alanine’ (AAAAA), and L-Phenylalanine (F) through to ‘Tetra-(L)-Phenylalanine’ (FFFF).

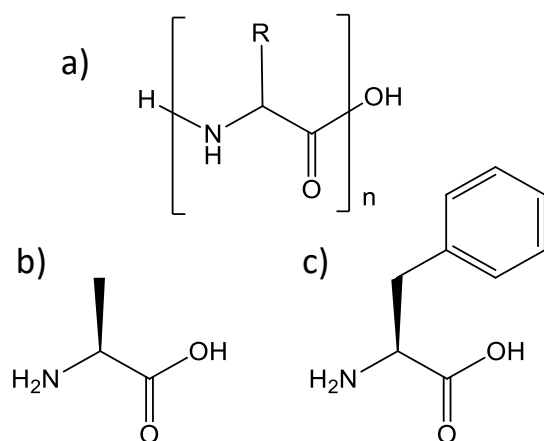


Figure 4.1. a) General structure of a peptide with n repeat units.
 b) Structure of L-Alanine
 c) Structure of L-Phenylalanine.

The results indicate that even peptides as short as only 4 or 5 repeat units can fragment when heated to their sublimation temperature. Fragmentation appears earlier for the phenylalanine series than for the alanine series, though a clear link between sublimation temperature and side chain complexity is not apparent. Also of note is that the observed fragmentation patterns do not necessarily seem to yield shorter peptides via clean amide bond cleavage, despite the prevailing wisdom that the peptide bond is the weakest and most likely to break^{2,3}. These results confirm the idea that sublimation is inherently flawed and limited as a deposition technique, meaning alternative strategies are required in order to functionalise surfaces with large and complex molecules.

4.2 Sublimation of the alanine series of peptides

The spectra shown in Figures 4.2-4.7 are used to mark the major peaks for each molecule and any key differences between data for unsublimed and sublimed samples. While the concentration of the species responsible for each peak plays a role in its height and area, the magnitude of the peak cannot be taken as a strict indicator of relative concentration. Precise ratios between peak areas depend on a number of factors including the conditions of the electrospray process, instrument tuning, and ionisability of the species under examination, and will typically vary from experiment to experiment, even between repeat experiments. Additionally, secondary details such as the proportion of sodiated and protonated peaks are also not inherently dependent on sublimation and/or fragmentation processes. As such, the focus of the analysis presented here is mainly on the presence or absence of certain relevant peaks, rather than their quantification.

4.2.1 L-Alanine

A minimum temperature of 423K for the sublimation of L-Alanine ($C_3H_7NO_2$) was ascertained according to the procedure described in section 2.2.2 (Experimental – sublimability tests). Mass spectra acquired for the sublimed material (Figure 4.2) featured a peak pertaining to the intact sodiated molecule ($[C_3H_7NO_2+Na]^+$, theoretical m/z 112.037, to be compared with the measured value of 112.039) and a peak that would fit a double sodiation ($[C_3H_6NO_2+2Na]^+$, theoretical m/z 134.019) as the strongest signals, as well as a weaker signal for the protonated molecule ($[C_3H_8NO_2]^+$, theoretical m/z 90.055, molecular ion/M+). The spectrum obtained compared favourably to the unsublimed sample, with the appearance of the same peaks and an absence of fragment peaks (i.e. below the m/z of the molecular ion), indicative that the molecule sublimed and reached the glass slide target intact. This is perhaps to be expected based on a number of literary studies of L-Alanine, which include implicit intact sublimation in the results, through indirect evidence such as RAIRS, STM and XPS.⁴⁻⁷

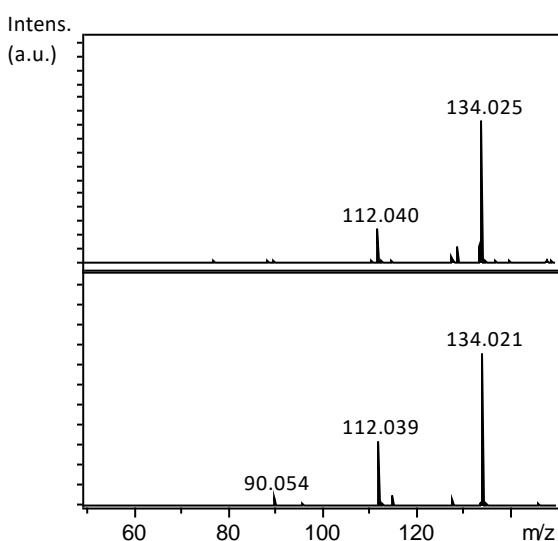


Figure 4.2. Mass spectra of [top] non-sublimed L-Alanine and [bottom] L-Alanine sublimed at 423K. Molecular ion occurs at $\sim m/z$ 90.

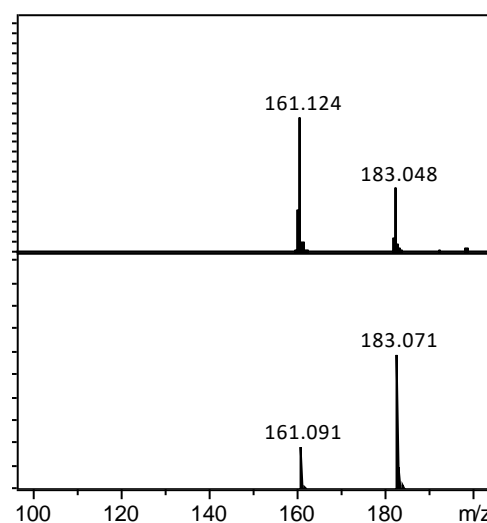


Figure 4.3. Mass spectra of [top] non-sublimed Di-L-Alanine and [bottom] Di-L-Alanine sublimed at 423K. Molecular ion occurs at $\sim m/z$ 161.

4.2.2 Di-(L)-Alanine

Di-(L)-Alanine ($C_6H_{12}N_2O_3$) was also successfully sublimed at 423K. Strong evidence that the molecule remained intact was found (Figure 4.3), with the principal sublimed peaks corresponding to the protonated molecule ($[C_6H_{13}N_2O_3]^+$, theoretical m/z 161.092) and

sodiated molecule ($[\text{C}_6\text{H}_{12}\text{N}_2\text{O}_3+\text{Na}]^+$, theoretical m/z 183.074), with no noticeable fragment peaks at lower mass. This is similar to the spectrum obtained for the pristine sample, displaying differences only in peak ratios and in the formation of the molecular dimer (data not shown). The pristine material generated peaks for a protonated dimer of Di-(L)-Alanine molecules ($[\text{C}_{12}\text{H}_{25}\text{N}_4\text{O}_6]^+$, theoretical m/z 321.177) and a sodiated dimer ($[\text{C}_{12}\text{H}_{24}\text{N}_4\text{O}_6+\text{Na}]^+$, theoretical m/z 343.159), which were only seen at trace levels in the sublimed material. We propose that the absence of dimers in the sublimed sample was due to a reduced concentration of the solution obtained from the slide wash, compared to one made up from the powdered sample. Thus it can be concluded that Di-(L)-Alanine can sublime intact, again consistent with the interpretation of STM and mass spectrometry data seen in the literature.⁸⁻¹⁰

4.2.3 Tri-(L)-Alanine

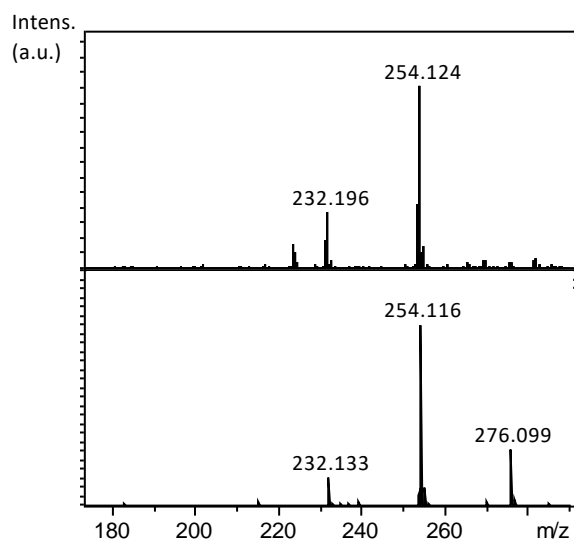


Figure 4.4. Mass spectra of [top] non-sublimed Tri-L-Alanine and [bottom] Tri-L-Alanine sublimed at 463K. Molecular ion occurs at $\sim m/z$ 232.

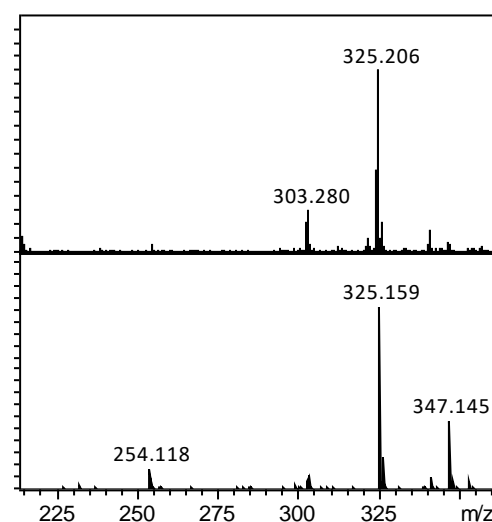


Figure 4.5. Mass spectra of [top] non-sublimed Tetra-L-Alanine and [bottom] Tetra-L-Alanine sublimed at 523K. Molecular ion occurs at $\sim m/z$ 303.

Tri-(L)-Alanine ($\text{C}_9\text{H}_{17}\text{N}_3\text{O}_4$) sublimed at a temperature of 463K. The results were similar to that of Di-(L)-Alanine, since also in this case the evidence points to an intact sublimation with some differences only in peak intensities to an unsublimed sample (Figure 4.4). The largest peak in the unsublimed case again corresponds to the sodiated intact molecule ($[\text{C}_9\text{H}_{17}\text{N}_3\text{O}_4+\text{Na}]^+$, theoretical m/z 254.111), with the molecular ion appearing at lower intensity ($[\text{C}_9\text{H}_{18}\text{N}_3\text{O}_4]^+$, theoretical m/z 232.129). In the sublimed sample, the ratio of sodiated to protonated was larger, and an additional peak indicating double sodiation also

became prominent ($[\text{C}_9\text{H}_{16}\text{N}_3\text{O}_4+2\text{Na}]^+$, theoretical m/z 276.093). Furthermore, an effect was again seen on the formation of dimers in the sublimed sample (data not shown), as the sodiated dimer signal ($[\text{C}_{18}\text{H}_{34}\text{N}_6\text{O}_8+\text{Na}]^+$, theoretical m/z 485.233) dropped dramatically, and the smaller protonated dimer peak ($[\text{C}_{18}\text{H}_{35}\text{N}_6\text{O}_8]^+$) dropped into the noise. This is likely due to the same proposed reasons as for Di-(L)-Alanine. It is also worth noting that in the unsublimed sample, a small peak is observed below the molecular ion peak, which is most likely due to an impurity. This peak disappears post-sublimation, meaning that the impurity has not been deposited. Such behaviour underpins the mechanism by which purification by sublimation can be achieved, as a target molecule and its contaminants will sublime at different temperatures and at different rates.

4.2.4 Tetra-(L)-Alanine

Tetra-(L)-Alanine ($\text{C}_{12}\text{H}_{22}\text{N}_4\text{O}_5$) was sublimed at 523K. The spectrum for the sublimed sample appeared broadly similar to that of the unsublimed material (Figure 4.5), retaining the major peaks for the molecular ion ($[\text{C}_{12}\text{H}_{23}\text{N}_4\text{O}_5]^+$, theoretical m/z 303.166) and the sodiated ion ($[\text{C}_{12}\text{H}_{22}\text{N}_4\text{O}_5+\text{Na}]^+$, theoretical m/z 325.148). Other peaks at higher m/z values remain small, though a peak at 347.145, which would fit a double sodiation, does grow in the post-sublimation sample. It is worth noting that even in the pristine, unsublimed material, the remaining peaks at m/z greater than the molecular ion are more noticeable compared to the spectra for shorter peptides, indicating the presence of some minor impurities in the pristine Tetra-(L)-Alanine sample. However, there were subtle differences in the sub-(molecular ion) region of the sublimed sample relative to the unsublimed one, indicating that some level of sample degradation may have started to occur. Sublimation introduced a substantial peak at $m/z \sim 254$, which was not present in the pristine sample and could correspond to the same sodiated species as seen in the spectra for Tri-(L)-Alanine. Other peaks can also be found at lower m/z , though these are much smaller and difficult to see in Figure 4.5. The only identifiable peaks are found at $m/z \sim 232$, which would correspond to protonated Tri-(L)-Alanine, and $\sim m/z$ 289, which would fit with a loss of a methyl group (i.e. the alanine side group). However, with intensities so close to the noise level, one cannot place a great deal of confidence in any such peak assignments. Overall, the presence of a major new peak that fits with data from Tri-(L)-Alanine, together with traces of other species below the molecular

ion m/z , suggests that Tetra-(L)-Alanine started to fragment, although the evidence is clear that the majority of the molecules sublimed intact.

4.2.5 Penta-(L)-Alanine

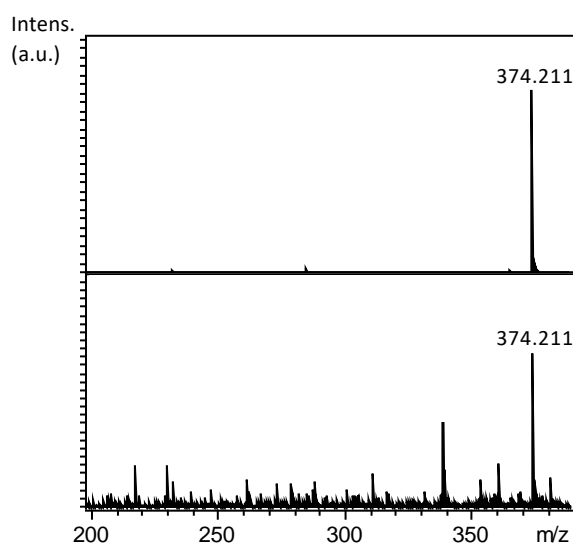


Figure 4.6. Mass spectra of [top] non-sublimed Penta-L-Alanine and [bottom] Penta-L-Alanine sublimed at 533K. Molecular ion occurs at $\sim m/z$ 374.

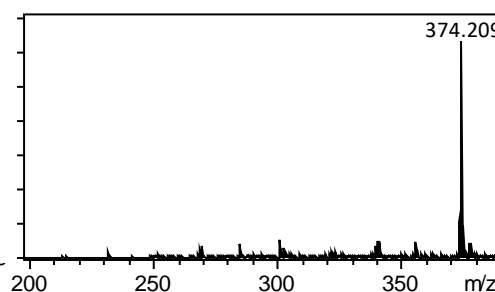


Figure 4.7. Mass spectrum of Penta-L-Alanine from a crucible heated to 533K.

Penta-(L)-Alanine ($C_{15}H_{27}N_5O_6$) was sublimed at 533K. A stark difference was seen between the unsublimed sample and the sublimed, featuring a greatly diminished signal-to-noise ratio for the molecular ion ($[C_{15}H_{28}N_5O_6]^+$, theoretical m/z 374.203), with numerous peaks at lower m/z . The unsublimed material (Figure 4.6) showed a dominant molecular ion peak, and any small impurities at lower m/z did not match or explain the data seen for the sublimed sample. A side point of interest is that the sodiated peak ($m/z \sim 396$) was almost entirely absent in both samples. Overall this points toward significant fragmentation of the molecule, albeit with some trace of the intact species. This would build upon the result for Tetra-(L)-Alanine, where some evidence of fragmentation was seen despite a largely intact sublimation. To further investigate this result, the material remaining in the crucible was dissolved and a mass spectrum taken. Here the molecular ion gave a strong signal and the spectrum was barely distinguishable from that of the unsublimed sample (Figure 4.7). This suggests that at 533K we are very much at the limit of fragmentation for Penta-(L)-Alanine, where only those molecules that sublime will fragment. The exploration and definition of such a limit has been the subject of considerable investigation at Warwick.¹¹

The conclusion of the Alanine series is therefore a markedly early stage of fragmentation, at a chain length of just 4 or 5 units, even with the simple and low molecular weight unit that alanine provides.

4.3 Sublimation of the phenylalanine series of peptides

4.3.1 L-Phenylalanine

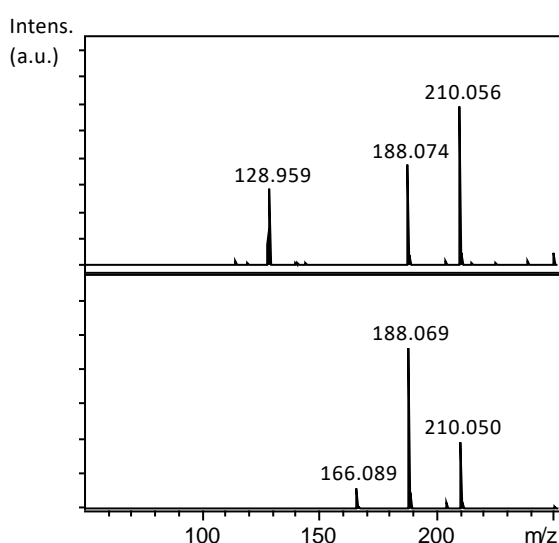


Figure 4.8. Mass spectra of [top] non-sublimed L-Phenylalanine and [bottom] L-Phenylalanine sublimed at 378K. Molecular ion occurs at $\sim m/z$ 166.

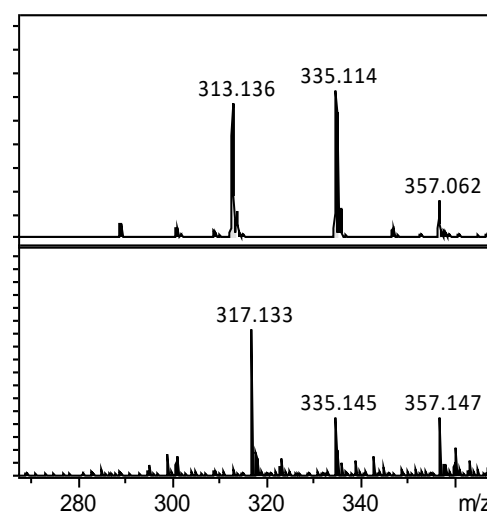


Figure 4.9. Mass spectra of [top] non-sublimed Di-L-Phenylalanine and [bottom] Di-L-Phenylalanine sublimed at 413K. Molecular ion occurs at $\sim m/z$ 313.

L-Phenylalanine ($C_9H_{11}NO_2$) was sublimed at a temperature of 378K. The sublimed and unsublimed samples yielded spectra with the same dominant peaks and no evidence of new low mass peaks as a result of sublimation (Figure 4.8). A prominent peak in both cases was the intact, sodiated molecule ($[C_9H_{11}NO_2+Na]^+$, theoretical m/z 188.068), with the peak that would fit a doubly sodiated species also showing strongly ($[C_9H_{10}NO_2+2Na]^+$, theoretical m/z 210.050). The signal for the protonated molecule was noticeably weaker, in fact being undetectable in the unsublimed sample ($[C_9H_{12}NO_2]^+$, theoretical m/z 166.086). The spectra obtained are quite clear, however, in their indication that L-Phenylalanine sublimed intact, which is again as expected based on literary evidence.¹²⁻¹⁴ The peak at $m/z \sim 129$ corresponded to an impurity in the unsublimed material, which is not reproduced in the sublimed sample, again demonstrating purification by sublimation.

4.3.2 Di-(L)-Phenylalanine

Di-(L)-Phenylalanine ($C_{18}H_{20}N_2O_3$) was sublimed at 413K, yielding a markedly different spectrum (Figure 4.9) with respect to the unsublimed material, with significant reductions in the peaks for the protonated molecule ($[C_{18}H_{21}N_2O_3]^+$, theoretical m/z 313.154) and sodiated molecule ($[C_{18}H_{20}N_2O_3+Na]^+$, theoretical m/z 335.137), though the peak corresponding to a double sodiation remained of comparable relative intensity ($[C_{18}H_{19}N_2O_3+2Na]^+$, theoretical m/z 357.119). Crucially, however, a new prominent peak emerged at m/z 317.133. Through a combination of NMR and high-resolution mass spectrometry, it was possible to identify this peak, in addition to a further small peak at $\sim m/z$ 295, as the result of a cyclisation reaction through which Di-(L)-Phenylalanine transforms into a six-membered ring, specifically a diketopiperazine. The peaks observed after sublimation therefore correspond to the protonated cyclised peptide ($[C_{18}H_{19}N_2O_2]^+$, theoretical m/z 295.144) and the sodiated cyclised peptide ($[C_{18}H_{18}N_2O_2+Na]^+$, theoretical m/z 317.105), though the former is only present at very low intensity. Other peaks are present at similar intensity to that at $m/z \sim 295$, but across the full m/z range, suggesting trace impurities or simply a low sample concentration. Fragmentation does not appear to have occurred, with Di-(L)-Phenylalanine instead exclusively cyclising or subliming intact. Subliming the Di-(L)-Phenylalanine without cyclisation proved challenging, with the lower temperature limits for both sublimation and cyclisation appearing close together. This issue has also arisen during further internal research into the limits of sublimation.¹¹

4.3.3 Tri-(L)-Phenylalanine

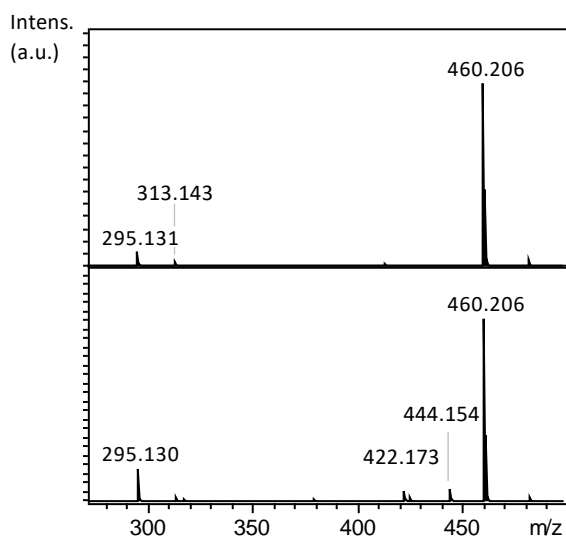


Figure 4.10. Mass spectra of [top] non-sublimed Tri-L-Phenylalanine and [bottom] Tri-L-Phenylalanine sublimed at 473K. Molecular ion occurs at $\sim m/z$ 460.

Tri-(L)-Phenylalanine ($C_{27}H_{29}N_3O_4$) was sublimed at 473K. The spectrum for the unsublimed sample (Figure 4.10) was already noteworthy due to the presence of small signals for the

protonated cyclised Di-(L)-Phenylalanine ($[C_{18}H_{19}N_2O_2]^+$, theoretical m/z 295.144) and linear Di-(L)-Phenylalanine ($[C_{18}H_{21}N_2O_3]^+$, theoretical m/z 313.154). The occurrence of these peaks in unsublimed material means that these species are likely the result of a minor synthetic by-product. The spectrum for the sublimed sample strongly resembled that of the unsublimed material, with the molecular ion appearing dominant ($[C_{27}H_{30}N_3O_4]^+$, theoretical m/z 460.223). The sublimed sample does, however, result in peaks that appear to be the result of fragmentation, at $\sim m/z$ 422 and 444. These species do not relate well to commonly seen fragments.¹⁵⁻¹⁷ Attempts were made to identify the peaks with higher resolution mass spectrometry but were not conclusive. Although a precise identification of these fragments goes beyond the scope of this work, their appearance only in the sublimed sample is a clear indication that Tri-(L)-Phenylalanine is partially degrading in the process of sublimation.

4.3.4 Tetra-(L)-Phenylalanine

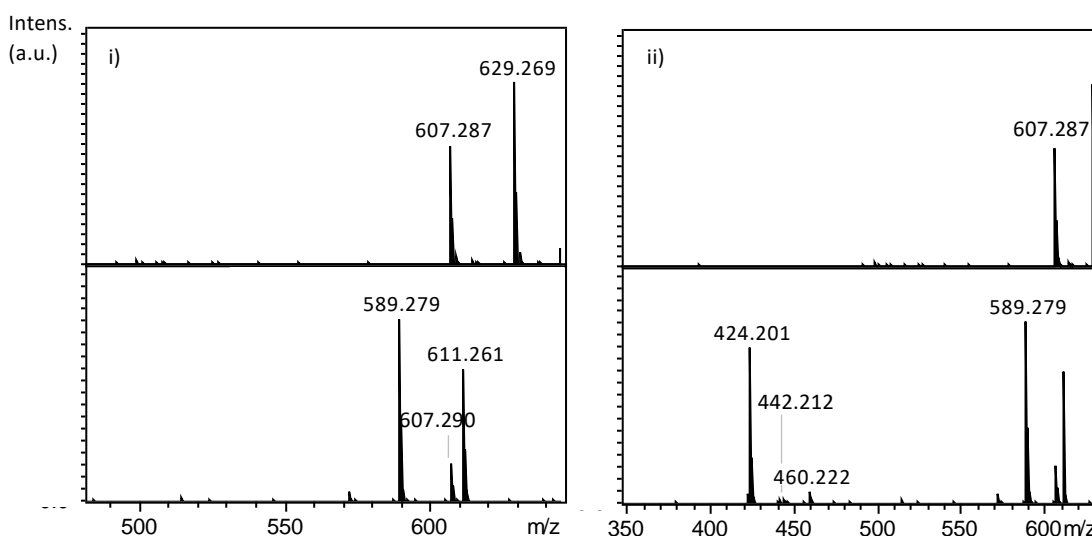


Figure 4.11. Mass spectra of [top] non-sublimed Tetra-L-Phenylalanine and [bottom] Tetra-L-Phenylalanine sublimed at 473K. i) Spectra featuring the group of peaks around the molecular ion, occurring at $\sim m/z$ 607. ii) Spectra focusing on the main fragment peaks.

Tetra-(L)-Phenylalanine ($C_{36}H_{38}N_4O_5$) sublimed after heating to 473K. A substantial difference was observed between spectra of the sublimed and unsublimed material. The dominant protonated ($[C_{36}H_{39}N_4O_5]^+$, theoretical m/z 607.292) and sodiated peaks ($[C_{36}H_{38}N_4O_5+Na]^+$, theoretical m/z 629.273) from the unsublimed material (Figure 4.11) were greatly diminished in the sublimed sample, instead being replaced by a number of fragment peaks. A peak was observed at $\sim m/z$ 460 that likely occurred as a result of Tri-(L)-Phenylalanine formation after

thermal degradation ($[\text{C}_{27}\text{H}_{30}\text{N}_3\text{O}_4]^+$, theoretical m/z 460.223). It therefore becomes easier, with the help of higher resolution data, to identify the peak at $m/z \sim 442$. While the peaks at $m/z \sim 424$ and 442 superficially appear similar to those seen for sublimed Tri-(L)-Phenylalanine (at $\sim m/z$ 422 and 444), the m/z difference of 2 for calibrated data makes it unlikely that the peaks are related. In fact, the peak at m/z 442.212 fits with a loss of water ($\sim m/z$ 18) from Tri-(L)-Phenylalanine, either from the linear form or as part of a cyclisation process ($[\text{C}_{27}\text{H}_{28}\text{N}_3\text{O}_3]^+$, theoretical m/z 442.213). The peak at $\sim m/z$ 424, however, remains unidentified. Peaks that can be attributed to the formation of Di-(L)-Phenylalanine and its cyclised derivatives were again observed, but these are not shown in Figure 4.11 for simplicity. Even more strikingly, there is evidence of cyclisation of the Tetra-(L)-Phenylalanine itself, which for such a long molecule is a statistical and entropic challenge. The resultant 12-membered ring, a cyclic tetrapeptide, is of significant value to macrocyclic chemistry,¹⁸ and its creation by this method could bypass otherwise complex synthetic strategies.¹⁹ Signals that would relate to cyclised ($[\text{C}_{36}\text{H}_{37}\text{N}_4\text{O}_4]^+$, theoretical m/z 589.281) and sodiated cyclised ($[\text{C}_{36}\text{H}_{36}\text{N}_4\text{O}_4+\text{Na}]^+$, theoretical m/z 611.263) Tetra-(L)-Phenylalanine were prevalent in the spectrum of the sublimed material. Together with the other fragmentation patterns discussed, it is apparent that Tetra-(L)-Phenylalanine is at least significantly changed or cyclised during the sublimation process, but is also fragmented to a considerable extent.

The conclusion of the Phenylalanine series is therefore an even earlier stage of fragmentation than for the alanine series, at a chain length of just 3 or 4 units. Additionally, a significant trait observed in the Phenylalanine series is that cyclisation appears to occur quite routinely under the influence of elevated temperature.

4.4 Conclusions

The overall outcome of the experiments is a rather early onset of fragmentation when attempting to thermally sublime short peptides. In the Alanine series, the sample degraded when the chain length reached 5 subunits, and for the Phenylalanine series fragmentation already began for 3 subunits and was significant for a 4-subunit peptide. Though these represent just two of many possible combinations of amino acids into peptides, the data gathered points strongly towards a low threshold to the breakdown of the sublimation technique for peptide deposition in vacuum.

We therefore put forward that the use of OMBE for creating functional molecular films from peptides is substantially limited by the tendency for these molecules to fragment. Variation in side chain nature evidently plays a role in the sublimation and fragmentation processes, due to their influence in determining the strength of the intermolecular forces. For example, phenylalanine residues might undergo pi-stacking interactions via the benzene rings, whereas alanine residues are limited strictly to van der Waals type bonds (outside of the peptide backbone common to both). According to the sublimation temperatures recorded here, and literary values for the ambient pressure melting points of alanine and phenylalanine (570K and 556K respectively),²⁰ it would be expected that alanine-based peptides have stronger intermolecular forces overall, due to the higher temperatures for phase transitions on average. This would likely be due to denser packing of the smaller alanine residues. However, in contrast to this, phenylalanine-based peptides are shown here to have an earlier onset of fragmentation with respect to chain length, which would also be an indicator of strong intermolecular bonding, arising from the aforementioned pi-stacking. Meanwhile, the intramolecular bonds of each molecule are expected to be of similar strength, since both peptide series have the same backbone, and their identifiable fragments tended to be of a similar nature – the loss of water or peptide subunits. Overall, therefore, the data obtained indicates a more complex interplay between intermolecular and intramolecular bonding, without a clear trend based on peptide side chain.

It is important, still, to note that despite their chemical differences, the two series studied feature very similar sublimation limits in terms of peptide length. It is expected that this is a quite general characteristic for other peptides, since it is unlikely that the variation caused by differing side chains would be so great as to result in much longer peptides subliming completely intact. Evidently an alternative strategy is required in order to bring peptides (and other thermolabile molecules) to a surface in vacuum intact. Indeed, the implicit knowledge of the restrictions of OMBE have driven a search for alternative deposition strategies in recent years. Perhaps the most promising new technique is electrospray deposition, which is adapted from soft ionisation sources in mass spectrometry, and has already been demonstrated as capable of handling larger molecules without fragmentation.²¹⁻²⁴

4.5 Addendum: additional peptides

Several other short peptides have been sublimed and tested by mass spectrometry that are not discussed in detail here. These were examined for additional, supporting evidence for the conclusions above, from a stock of peptides in-house. A brief summary is included for completion, in table 4.1 below.

Molecule	Sublimation temperature/K	Mass spectrometry comments
Gly-Leu	388	Sublimed intact
Gly-Gly-Leu	403	Partial fragmentation
Phe-Gly-Gly	408	Partial fragmentation

Table 4.1. Additional peptides whose sublimation was studied by the methods described in this chapter, with brief notes on the outcome of the experiment.

Furthermore, in the subsequent chapters of this thesis, the peptides L-Phe-D-Phe, D-Phe-L-Phe, L-Tyr-L-Tyr and L-Trp-L-Trp are deposited on metal surfaces and studied by STM. As a first step in this process, each is checked for its sublimation behaviour in the same manner as the other peptides of this chapter. The results of these experiments are presented in their respective chapters.

4.6 References

1. L. Grill, *J. Phys. Condens. Matter*, 2010, **22** (8), 084023-084036.
2. B. Paizs and S. Suhai, *Mass Spectrom. Rev.*, 2004, **24** (4), 508-548.
3. V. Wysocki, K. A. Resing, Q. Zhang and G. Cheng, *Methods*, 2005, **35**, 211-222.
4. J. Williams, S. Haq and R. Raval, *Surf. Sci.*, 1996, **268**, 303-309.
5. S.M. Barlow, S. Louafi, D. Le Roux, J. Williams, C. Muryn, S. Haq and R. Raval, *Surf. Sci.*, 2005, **590**, 243-263.
6. M. Mahapatra, L. Burkholder, S.P. Devarajan, A. Boscoboinik, M. Garvey, Y. Bai and W.T. Tysoe, *J. Phys. Chem. C*, 2015, **119**, 3556-3563.
7. F. Kling, M. Kittelmann and A. Kühnle, in *Imaging and manipulation of adsorbates using dynamic force microscopy*, ed. P. Moriarty and S. Gauthier, Springer, Cham, 2015, ch. 8, 119-129.
8. H. J. Svec and G. A. Junk, *J. Am. Chem. Soc.*, 1964, **86**, 2278-2282.
9. I. Stensgaard, *Surf. Sci. Lett.*, 2003, 545, L747-L752.
10. V. G. Badelin, E. Yu. Tyunina, A. V. Krasnov, V. V. Tyunina, N. I. Giricheva and A. V. Girichev, *Russ. J. Phys. Chem. A*, 2012, **86**, 457-462.
11. A. Price and G. Costantini, unpublished work.
12. D. Gross and G. Grodsky, *J. Am. Chem. Soc.*, 1955, **77**(6), 1678-1680.
13. M. Lingenfelder, PhD thesis, 2007, EPF Lausanne, Switzerland.
14. A. G. Thomas, W. R. Flavell, C. P. Chatwin, A. R. Kumarasinghe, S. M. Rayner, P. F. Kirkham, D. Tsoutsou, T. K. Johal and S. Patel, *Surf. Sci.*, 2007, **601**, 3828-3832.
15. R. M. Silverstein, G. C. Bassler and T. C. Morrill, *Spectrometric identification of organic compounds*, Wiley, Chichester, 1991.
16. F. W. McLafferty, *Interpretation of mass spectra*, 4th edn, University Scientific Books, Mill Valley, California, 1993.
17. The Spectral Database for Organic Compounds (SDBS), https://sdb.sdb.aist.go.jp/sdb/cgi-bin/cre_index.cgi, (accessed 2018).
18. B. K. W. Chung, C. J. White, C. C. G. Scully and A. K. Yudin, *Chem. Sci.*, 2016, **7**, 6662-6668.
19. K. A. Fairweather, N. Sayyadi, I. J. Luck, J. K. Clegg and K. A. Jolliffe, *Org. Lett.*, 2010, **12**, 3136-3139.
20. D. R. Lide, *CRC Handbook of Chemistry and Physics*, 88th end, CRC Press, Taylor & Francis, Boca Raton, Florida, 2007-2008.
21. V. N. Morozov and T. Y. Morozova, *Anal. Chem.*, 1999, **71** (7), 1415-1420.

22. S. Rauschenbach, F. L. Stadler, E. Lunedei, N. Malinowski, S. Koltsov, G. Costantini and K. Kern, *Small*, 2006, **2**, 540–547.
23. C. Hamann, R. Woltmann, I. P. Hong, N. Hauptmann, S. Karan and R. Berndt, *Rev. Sci. Instrum.*, 2011, **82**, 033903.
24. Z. Deng, N. Thontasen, N. Malinowski, G. Rinke, L. Harnau, S. Rauschenbach and K. Kern, *Nano Lett.*, 2012, **12**, 2452–2458.

Chapter 5: Chemical transformations of the Phe-Phe dipeptide

5.1 Background

As discussed in chapter 1 (“Introduction”), the Phe-Phe dipeptide has already generated some considerable interest, from its capability for assembling into functional nanotubes¹ to its potential role in amyloid plaque formation.²⁻⁴ Such properties are inherently tied to the self-assembly of the molecules, be it stacking into uniform tubes or as part of a more complex protein folding mechanism, respectively. Since this thesis is focussed on the potential of peptides for functionalising surfaces by self-assembly, the Phe-Phe dipeptide is therefore a prime candidate for investigation. Establishing the self-assembly behaviour of L-Phe-L-Phe in a 2D model system is a valuable step towards understanding the molecule’s properties, and can also serve as a foundation for the study of the self-assembly of short peptides on surfaces.

Considerable research into L-Phe-L-Phe on a Cu(110) surface has already been reported by Lingenfelder and co-workers,^{5,6} as well as co-deposition with terephthalic acid⁷ and investigations into the effects of changing the stereochemistry of the molecule⁸. At room temperature, the principal assembly pattern exhibited by L-Phe-L-Phe appeared to be short length chains of 2-10 units, whose direction on the surface was uniform until annealed to 400K, at which point a global re-orienting of the chains occurred.⁵ This transformation was attributed to a conformational change of the molecule. Chains were held together by intermolecular hydrogen bonding, between the carbonyl oxygen and amine hydrogen of adjacent molecules. At low temperature, small clusters of L-Phe-L-Phe could be observed, though annealing to room temperature immediately brought about the chain formation.⁵

However, as mentioned in chapter 4 (“The sublimation of short peptides”), it is very difficult to sublime L-Phe-L-Phe without causing it to cyclise, especially if one is not aware of such a possibility and seeking to avoid it. It is thus quite possible that an alternative explanation can be proposed for the observations of Lingenfelder et al, in that the cyclised molecule was deposited onto the surface, and responsible for the primary self-assembly motif. Subsequent annealing that led to a change in the self-assembly would then also have to be re-examined in light of this new theory. In this section, new data is presented that provides evidence in

support of the cyclic deposition theory, and that explains the transformation brought about by annealing.

L-Phe-L-Phe, Cyclo-(L-Phe-L-Phe) (cFF) and both 'singly' and 'doubly' dehydrogenated Cyclo-(L-Phe-L-Phe) (sdcFF and ddcFF) were studied via UHV STM at 77K (molecular structures in Figure 5.1). As noted in chapter 2 ("Experimental"), L-Phe-L-Phe was purchased from Sigma-Aldrich and used without prior purification before insertion into vacuum, while cFF, sdcFF and ddcFF were synthesised by Lona Alkhalaf of the Challis group at Warwick, using the method found in Ando et al.⁹ In addition to the STM data, surface XPS spectra for depositions of L-Phe-L-Phe, cFF and ddcFF were taken, to assist in the identification of the molecular species present, focusing particularly on the C 1s, N 1s and O 1s peaks.

The data obtained and presented in the following strongly agrees with the previous findings that L-Phe-L-Phe generally cyclises upon sublimation, as the cFF deposition reproduces the data from an experiment with L-Phe-L-Phe. Furthermore, the results of annealing experiments of both L-Phe-L-Phe and cFF are analogous to data obtained for deposited ddcFF, indicating that the cyclised molecule dehydrogenates on the surface when annealed, giving rise to the change in self-assembly pattern. In this way, a typically challenging synthesis of substituted 2,5-diketopiperazines^{9,10} is mimicked by a simple on-surface annealing.

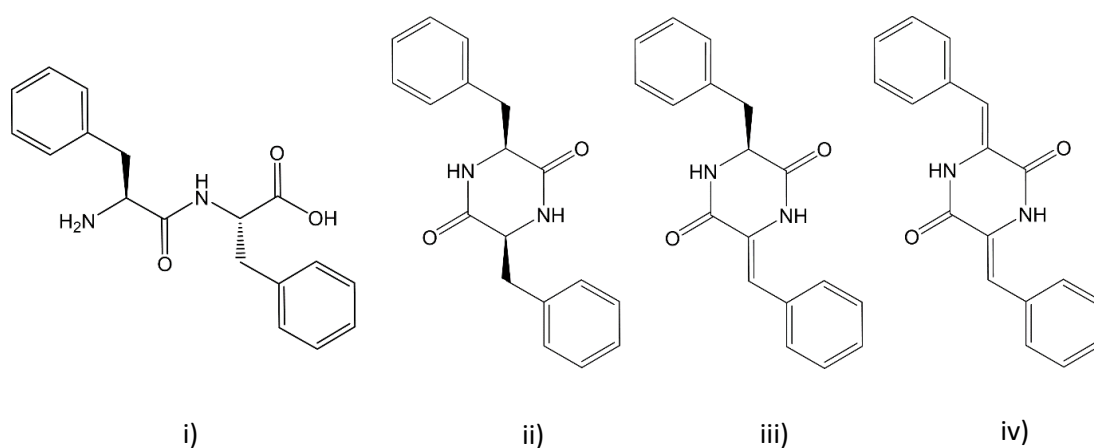


Figure 5.1. Molecular structures of i) L-Phe-L-Phe, ii) Cyclo-(L-Phe-L-Phe) or cFF, iii) singly dehydrogenated Cyclo-(L-Phe-L-Phe) or sdcFF, and iv) doubly dehydrogenated Cyclo-(L-Phe-L-Phe) or ddcFF.

5.2 Scanning tunnelling microscopy

5.2.1 L-Phe-L-Phe

After a UHV deposition of L-Phe-L-Phe at submonolayer coverage on a room temperature Cu(110) surface, STM imaging produced data consistent with that of Lingenfelder et al,^{5,8} showing some small clusters but mainly supramolecular chains of a single dominant orientation (Figure 5.2). This orientation is defined by a $49^\circ (\pm 2^\circ)$ angle (anticlockwise) to the $[1\bar{1}0]$ direction of the surface, with the molecules within the chain aligned at $73^\circ (\pm 2^\circ)$ (clockwise) to the $[1\bar{1}0]$ direction (Figure 5.3 demonstrates such measurements).

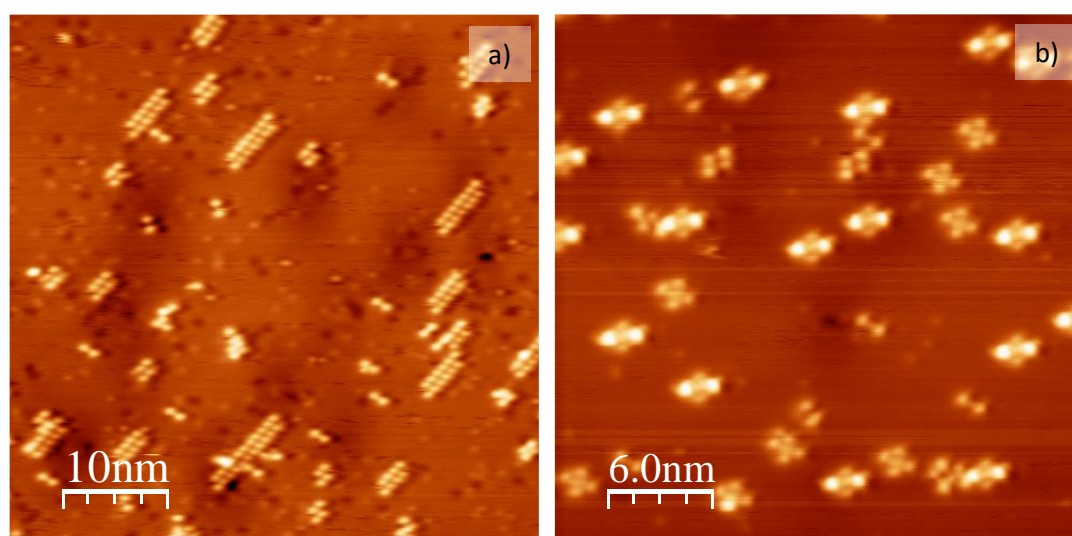


Figure 5.2. a) Typical STM image of a deposition of L-Phe-L-Phe on room temperature Cu(110), illustrating the chains and smaller clusters commonly observed. b) At low temperature (77K), the small clusters dominate, and chains are absent.

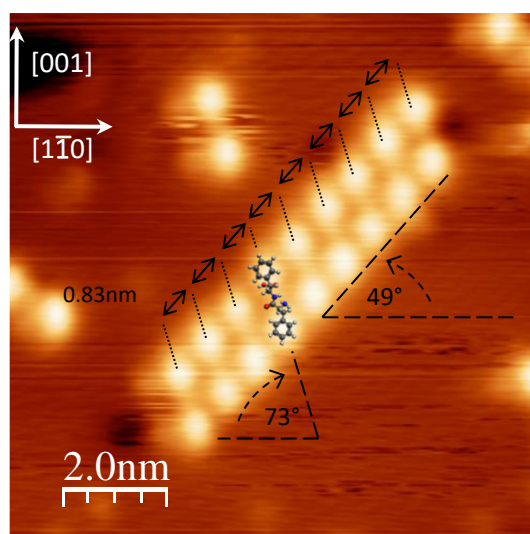


Figure 5.3. Analysis of the orientation of the molecular chains with respect to the $[1\bar{1}0]$ axis, and the orientation and periodicity of molecular features. A scaled model of L-Phe-L-Phe is superimposed for illustrative purposes.

The resolution within the chains appears to show molecules lying lengthways alongside one another, typically three to ten per chain at a periodicity of 0.83 ± 0.04 nm (see Figure 5.3), with the most distinct features being at either end of each molecule. Due to the prominence and symmetry of these features, they are assigned to the phenyl side chains of the peptide. Upon annealing to 400K the same transformation as reported by Lingenfelder et al⁵ is observed, by which the orientation of the chains changes substantially. Though at first the new chain orientation may appear to be mirrored about the [001] surface direction, in fact the chains are oriented at $72^\circ (\pm 2^\circ)$ (clockwise) from the $[1\bar{1}0]$ surface direction, with the molecules now aligned at $31^\circ (\pm 2^\circ)$ anticlockwise to the $[1\bar{1}0]$ plane at a periodicity of 0.69 ± 0.03 nm (Figure 5.4). These chains display more defects than those formed before annealing, whereby one or molecules is offset laterally, effectively reducing the range of molecules per continuous chain to three to six.

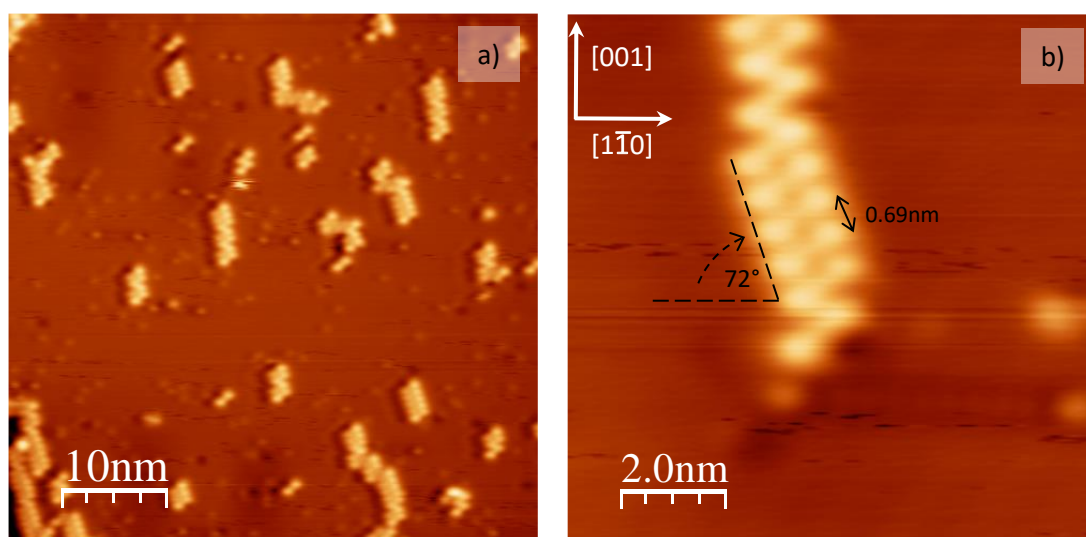


Figure 5.4. Appearance of a deposition of L-Phe-L-Phe after annealing to 400K. The new chain orientation with respect to the $[1\bar{1}0]$ axis is indicated. Note that some chains, as illustrated in b), feature defects with molecules offset from their nearest neighbours.

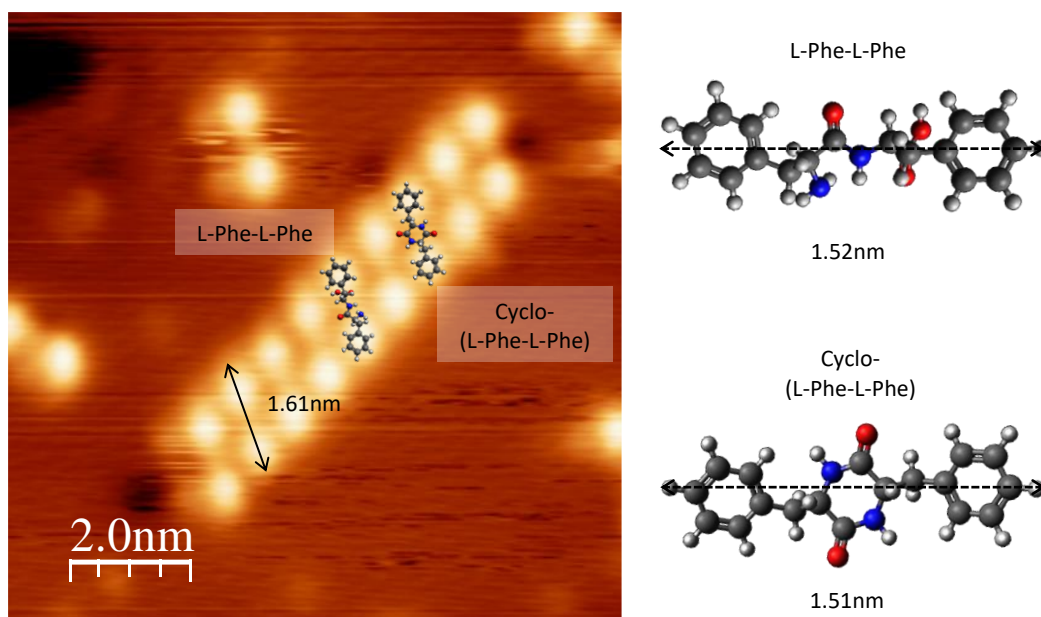


Figure 5.5. Comparison of the measured size (FWHM) of molecular features in the pre-anneal STM images with predicted lengths of L-Phe-L-Phe and Cyclo-(L-Phe-L-Phe) from gas-phased minimised Avogadro models. Scaled models of each molecule are also overlain onto the STM image for illustration.

Understanding the origin of the transformation described above first requires the nature of the deposited material to be ascertained, as it could be composed of L-Phe-L-Phe or, more likely, cFF (as discussed in chapter 4 (“The sublimation of short peptides”). Distinguishing between the linear and cyclised molecules is however not trivial based on the STM data alone. The phenyl side groups are prominent in the STM images, but there is little resolution of the structure of the central part of each molecule, which could have been helpful in determining whether the molecules are cyclised or not. Furthermore, the resolved length of what appears to be a single molecule pre-anneal is 1.61 ± 0.08 nm, which could correspond to both linear L-Phe-L-Phe (predicted 1.52 nm) and Cyclo-(L-Phe-L-Phe) (predicted 1.51 nm) (see Figure 5.5), given an appropriate conformation on the surface and the tip-convolution effect. The full-width half-maximum (FWHM) of STM signal intensity is used as a guideline for the edge of a molecule. Additionally, modelling the self-assembly pattern with either species (Figure 5.6) illustrates how both can reasonably fit within the chains. The model for L-Phe-L-Phe is reproduced from Lingenfelder et al.⁵

The STM data from this experiment is thus insufficient in isolation to either support or disprove the possibility of cyclisation before deposition. However, it is worth considering the on-surface transformation brought about by annealing in more detail. The change in the self-assembly pattern observed after annealing is universal across the surface, which is suggestive of a similarly significant change at the molecular level. Simple conformational differences can sometimes be observed through a distribution of states on the surface,

provided the energy of the states is close together, whereas here a single pattern is observed before annealing, and a different single pattern after annealing. Therefore, the two states recorded in this experiment must be separated by a substantial energy barrier. Furthermore, the transformation occurs always on annealing, and is not affected by surface coverage, unlike many systems where lateral pressures enforce a new self-assembly pattern.¹¹⁻¹⁶ Perhaps a better explanation here is that the molecules undergo an irreversible chemical change, which has a major impact on their bonding with the surface and their intermolecular interactions. Determining what chemical reaction could be occurring first requires certainty on the structure of the molecules as they are deposited. In particular, the simplest way to show that cyclisation has occurred is to deposit the cyclised molecule, cFF, and compare the STM data obtained. This experiment is presented in the following section.

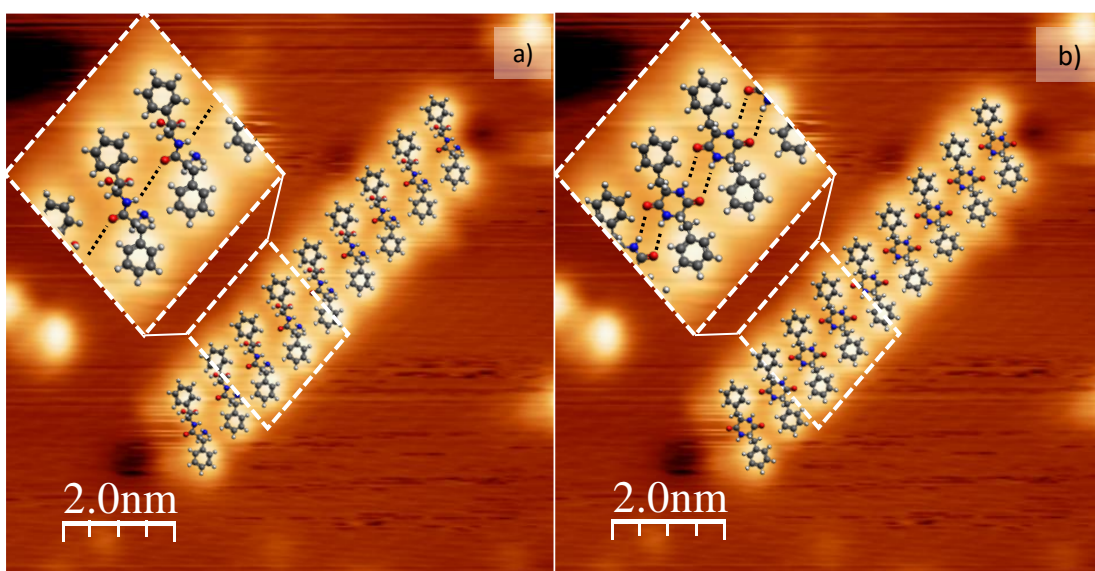


Figure 5.6. Models of both L-Phe-L-Phe (a) and Cyclo-(L-Phe-L-Phe) (b) overlaid onto the original self-assembly pattern. Potential hydrogen bonding is indicated with black dashed lines. Inset images are approximately 2.2 nm x 2.2 nm.

5.2.2 Cyclo-(L-Phe-L-Phe) – cFF

cFF was deposited at comparable coverage to L-Phe-L-Phe on a room temperature Cu(110) surface. Typical STM data obtained is represented in Figure 5.7. As subsequently illustrated in Figure 5.8, the similarity between the self-assembly of cFF and what is nominally L-Phe-L-Phe is striking. Small differences in molecular size and angle are apparent, but this can be accounted for by differing tip conditions and a degree of drift in the cFF data. Unidirectional chains are observed that are oriented at $51^\circ (\pm 2^\circ)$ (anticlockwise) with respect to the $[1\bar{1}0]$

substrate direction, analogous to the L-Phe-L-Phe deposition experiment, and the images feature a similar resolution of the prominent phenyl side groups within each molecule.

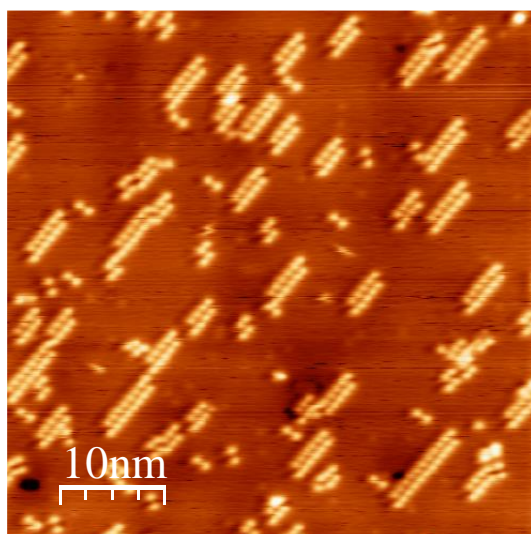


Figure 5.7. Typical STM image of a deposition of cFF on room temperature Cu(110).

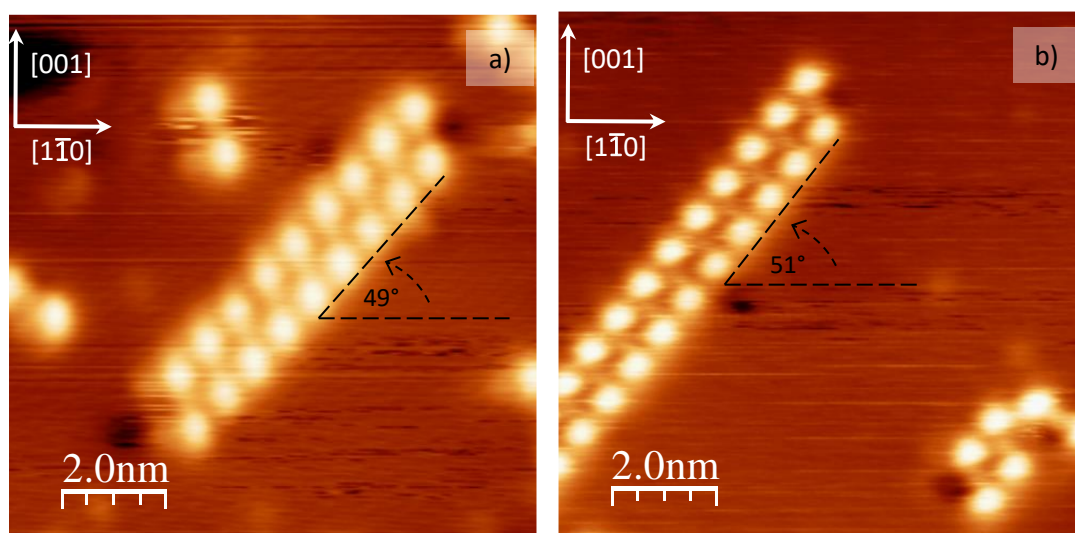


Figure 5.8. A comparison of the chains observed for depositions of a) L-Phe-L-Phe and b) cFF. The chain orientations are also labelled with respect to the $[1\bar{1}0]$ axis of the surface.

The average size of each molecule (1.59 ± 0.08 nm, Figure 5.9) and the typical lengths of the chains (three to ten monomer units, in-chain periodicity 0.79 ± 0.04 nm) also correlates strongly with the L-Phe-L-Phe data. Furthermore, upon annealing to 400K, the transition to a different self-assembly pattern is reproduced, with chains now oriented at $70^\circ (\pm 2^\circ)$ (clockwise) from the $[1\bar{1}0]$ direction (Figure 5.10). Table 5.1 provides a summary of the key parameters measured, for a direct comparison of the two depositions.

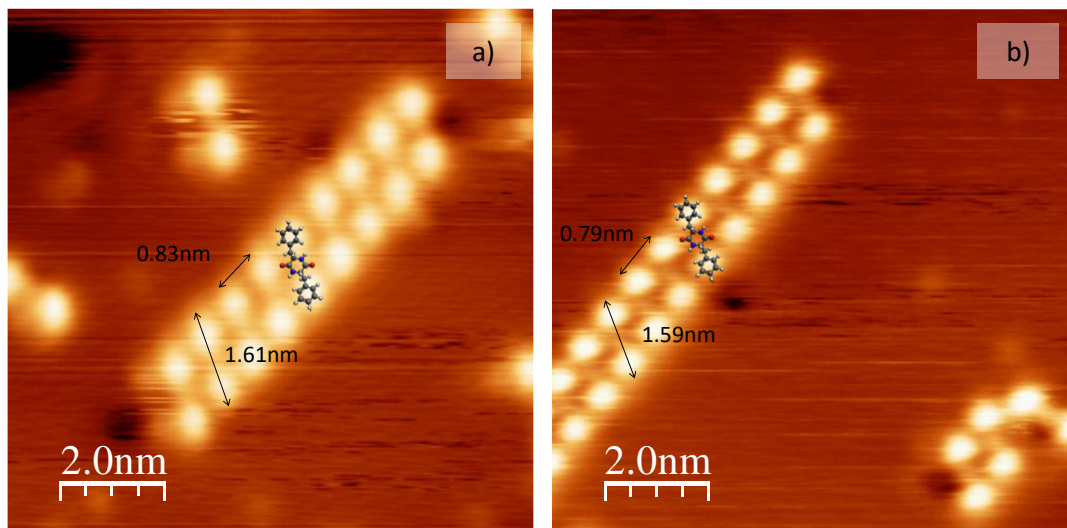


Figure 5.9. Comparison of the key dimensions of molecular features in STM images from depositions of a) L-Phe-L-Phe and b) cFF. Scaled models of cFF are overlain for illustration.

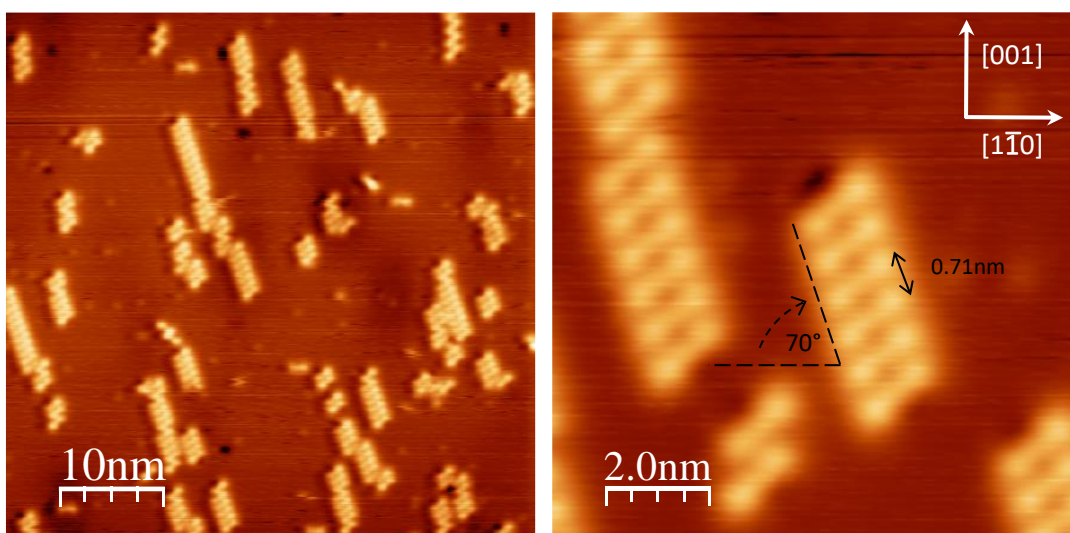


Figure 5.10. STM images from a deposition of cFF annealed to 400K. The new chain orientation is indicated, and similar defects to the annealed deposition of L-Phe-L-Phe can be observed.

The natural conclusion from the highly congruent L-Phe-L-Phe and cFF sets of data is that they are in fact corresponding to the same molecular species on the surface; that is, the linear FF molecule cyclises to cFF when heated in the crucible, and thus adsorbs and assembles on Cu(110) in an identical fashion to the synthesised cFF molecule. Alternatively, it is theoretically possible that the cyclisation occurs on the Cu(110) surface after deposition; however, cyclisation has already been shown via mass spectrometry to be an almost certain

outcome of any sublimation of L-Phe-L-Phe (see chapter 4, “The sublimation of short peptides”), which makes the latter a much more compelling argument.

Data obtained from a low temperature (130K) deposition further support this hypothesis, and images from such an experiment are presented in Figure 5.11. Depositing on a sample at 130K, and subsequently scanning at 77K, reduces the thermal motion of the adsorbed molecules, and greatly decreases the likelihood of any on-surface reaction with an activation barrier. At this temperature, only small clusters are observed (fig. 11a), and these are of identical size and shape to those recorded in a low temperature experiment with L-Phe-L-Phe (fig. 11b). A gentle annealing to 325K brings about total conversion to the unidirectional chains described in Figures 5.7 and 5.8, completing the comparison between the two depositions.

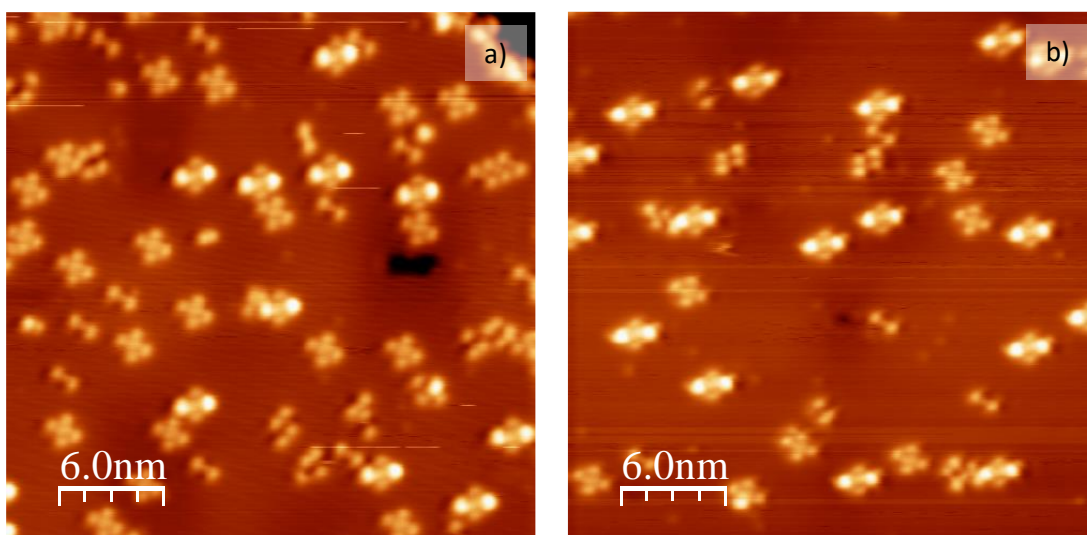


Figure 5.11. a) STM image from a low temperature (77K) experiment with cFF on Cu(110), illustrating the clusters observed. b) Low temperature image from a deposition of L-Phe-L-Phe, reproduced from Figure 5.2 for comparison.

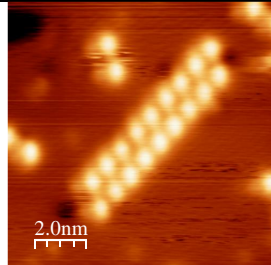
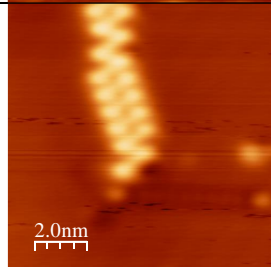
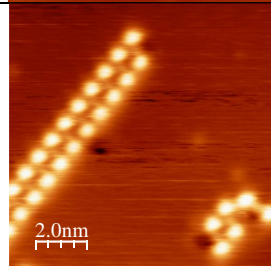
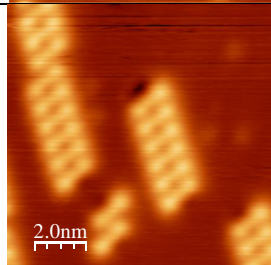
Experiment	Sample image	Molecule length	Molecule angle to [110] plane	Chain angle to [110] plane	Periodicity
L-Phe-L-Phe		1.61 ±0.08 nm	+73° ±2°	-49° ±2°	0.83 ±0.04 nm
L-Phe-L-Phe annealing		1.81 ±0.08 nm	-38° ±2°	+72° ±2°	0.69 ±0.03 nm
cFF		1.59 ±0.08 nm	+71° ±2°	+51° ±2°	0.79 ±0.04 nm
cFF annealing		1.80 ±0.08 nm	-39° ±2°	+70° ±2°	0.71 ±0.03 nm

Table 5.1. Key parameters from depositions of both L-Phe-L-Phe and cFF, for direct comparison.

In light of the findings of the cFF experiments, the published description of L-Phe-L-Phe on Cu(110) ought to be reconsidered in the context of cFF molecules being present instead. The first step is to examine how cFF might self-assemble into chains, followed by the effect of annealing on this assembly. Figure 5.12 shows a possible arrangement of the cFF molecules within each chain, suggesting that hydrogen bonding between adjacent molecules might be possible. The hydrogen bonds indicated in Figure 5.12 would be up to 3Å in length, which is in the outer range of relatively weak hydrogen bonds. There is no universal definition of a hydrogen bond length, but the upper limits quoted in the literature can range anywhere from 2.5Å to 5Å.¹⁷⁻¹⁹ Furthermore, the hydrogen bonds formed by peptides are typically not

amongst the strongest category of hydrogen bonds.¹⁷ It therefore seems feasible that hydrogen bonds might form in the self-assembly of cFF, albeit relatively weak ones. This description of the assembly differs from that proposed for L-Phe-L-Phe⁵ in terms of the number of hydrogen bonds and their length, but nonetheless would serve well as an explanation for the chains observed. The cFF molecules organise into isolated 1D chains without clustering into larger compact 2D islands, even when increasing the molecular coverage (see Figure 5.13). This evident avoidance of 2D agglomeration most probably indicates a repulsive interaction between molecules, perhaps due to a charging effect. A balance between short range attractive forces (e.g. van der Waals or hydrogen bonds) and long-range repulsive forces (e.g. Coulombic repulsions) has been shown in the literature to drive the formation of molecular chains and small islands in preference to larger assemblies.²⁰⁻²¹ Since the cyclic molecules deposited here are neutral, this effect must develop post-deposition, for example as a result of charge transfer^{22,23}, amide deprotonation, or dipolar repulsions.²⁴⁻²⁷ It is not possible with the current data to establish the precise cause of the repulsive interaction, and so further investigation would be required to examine this phenomenon further.

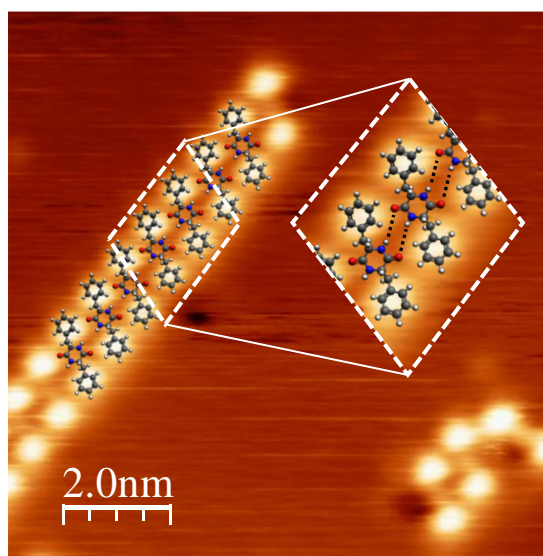


Figure 5.12. Models of cFF overlaid onto the self-assembly pattern of cFF on Cu(110). Potential hydrogen bonding is indicated with black dashed lines. Inset image is approximately 2.0 nm x 2.2 nm.

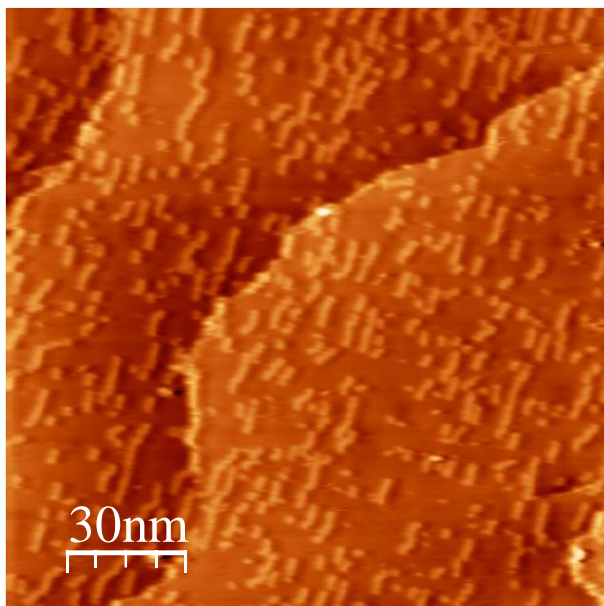


Figure 5.13. Even as coverage is increased, cFF on Cu(110) resists island formation in favour of chains.

The on-surface transformation that occurs after surface annealing to 400K needs to also be reconsidered, in terms of cFF as the starting material. cFF contains three 6-membered rings, two of which are aromatic, and no longer has exposed amine or carboxylic acid functional groups. As such, the molecule appears generally quite stable and has limited reactivity. However, due to the highly-ordered nature of the assembly post-annealing, it also would be very unlikely that the molecules have simply thermally fragmented, and so a more consistent reaction path must be followed. One possibility is that a dehydrogenation occurs across the only aliphatic carbon atoms, which are indicated in Figure 5.14. This process produces an alkene group, or two if both sides of the molecule dehydrogenate simultaneously (this is explored further in the subsequent section, 5.2.3). The dehydrogenated molecule, also shown in Figure 5.14, would have a significantly different conformation to cFF, due to the now sp^2 hybridised carbon atoms of the alkenes and the loss of rotational flexibility about the C=C bonds. Such a change in conformation would result in a different mode of binding to the surface, and different intermolecular interactions, thus possibly explaining the transformation in the self-assembly observed in the STM as a result.

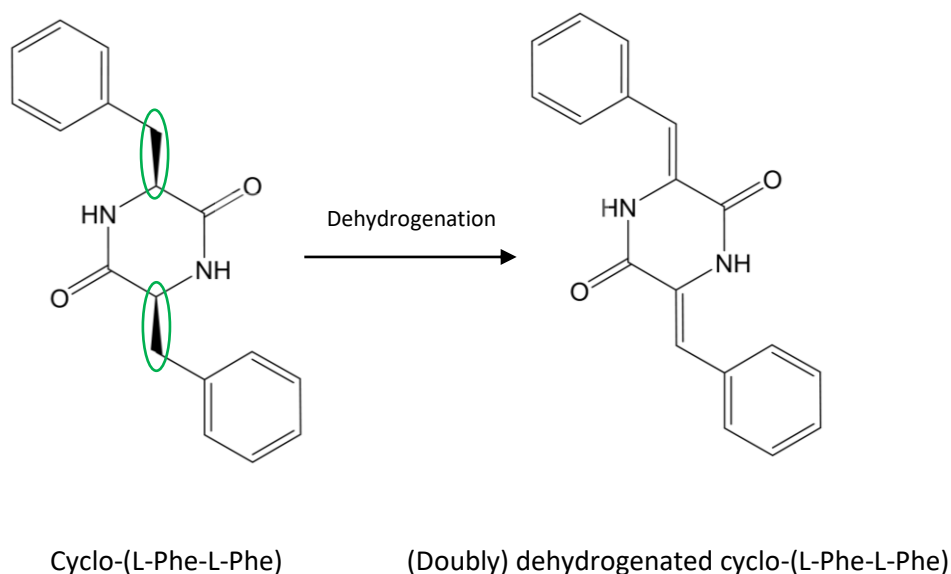


Figure 5.14. The molecular structures of cFF and ddcFF, with the location of the potential dehydrogenation reaction highlighted.

Additionally, in contrast to cFF, the resulting molecule would be planar (Figure 5.15), which would be recognisable in STM data – indeed, in Figure 5.16 the difference in the apparent height profiles across images from before and after annealing a deposition of cFF can be clearly seen. To definitively prove this theory, however, the best strategy is to directly deposit the dehydrogenated molecule and to compare the resulting STM data with those acquired after the 400K annealing of cFF. To this end, both the singly and doubly dehydrogenated cFF molecules (sdcFF and ddcFF) were synthesised, deposited on Cu(110), and scanned by STM.

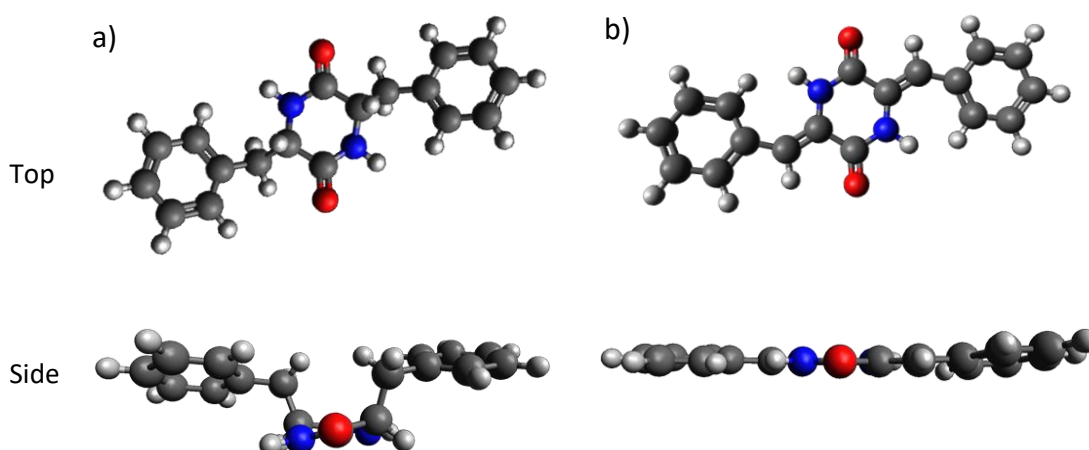


Figure 5.15. Gas-phase models of a) cFF, and b), ddcFF, demonstrating the difference in conformation between the two, especially from a side-view.

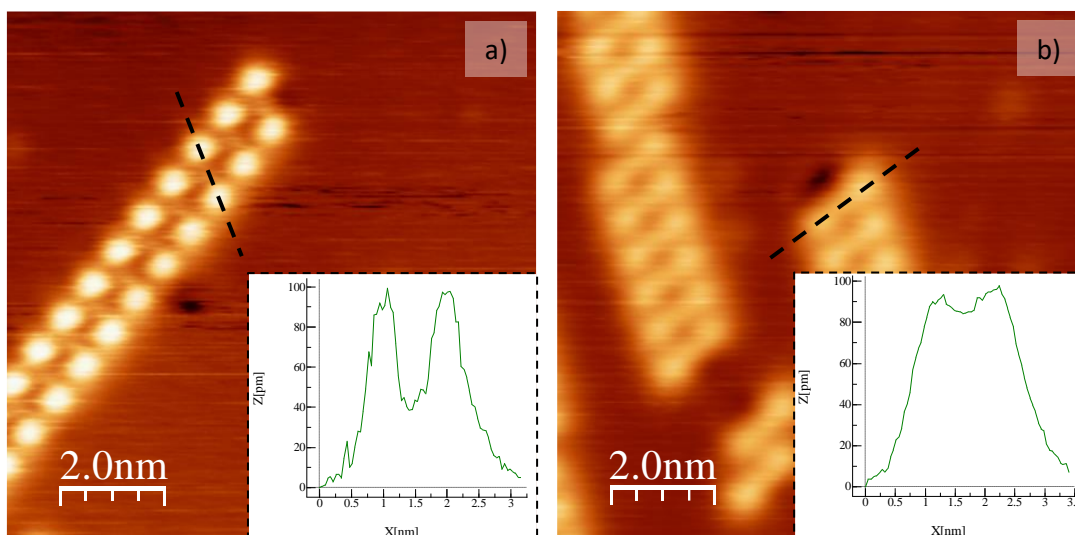


Figure 5.16. A comparison of STM data from a deposition of cFF, a) before annealing, and b) after annealing. The difference in contrast across a molecule is noticeable, and is highlighted with line profiles (dashed lines). Z(pm) values broadly correlate with molecular height.

5.2.3 Dehydrogenated Cyclo-(L-Phe-L-Phe)

A deposition of ddcFF on a room temperature Cu(110) surface gives rise to a highly similar self-assembly network to the 400K annealed experiments described above, with the same molecular features and dimensions. ddcFF displays two mirror symmetric orientations on the surface, both of which feature molecules of the same appearance and height profiles as annealed cFF, and one of which is a match in terms of molecular orientation. Figure 5.17 illustrates typical data from the ddcFF experiment, and table 5.2 provides a comparison between ddcFF and annealed cFF.

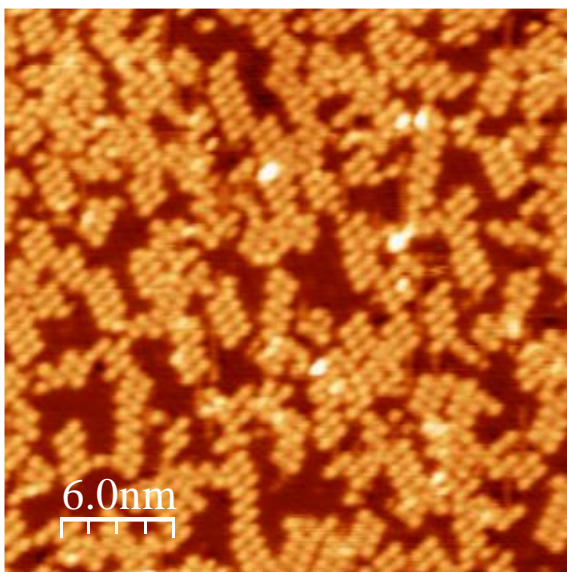


Figure 5.17. Typical STM image from a deposition of ddcFF on Cu(110) at room temperature.

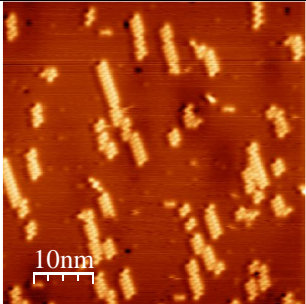
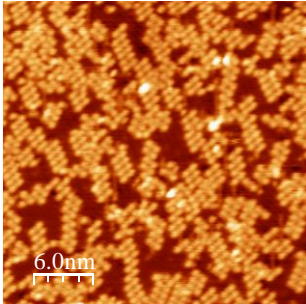
Experiment	Sample image	Molecule length	Molecule angle to [110] plane	Chain angle to [110] plane	Periodicity
cFF annealing		1.80 ±0.08 nm	-39° ±2°	+70° ±2°	0.71 ±0.03 nm
ddcFF deposition		1.82 ±0.08 nm	+39° /-45° ±2°	+68° /-70° ±2°	0.78 ±0.04 nm

Table 5.2. Comparison of STM parameters from an annealed deposition of cFF, and a deposition of ddcFF.

It is clear from examining these two sets of data that they represent the same molecule, and that cFF must indeed dehydrogenate on the surface during annealing. This confirms the theory described above and completes the picture of the thermal transformations of the

L-Phe-L-Phe dipeptide, but is also of considerable interest in its own right. In fact, this simple on-surface transformation brought about by annealing effectively replaces a multi-step synthesis,^{9,10} and offers complete conversion of the starting material to product. The scale of this process is so far quite small, but its simplicity and reliability are attractive qualities for any potential application. Furthermore, the production of dehydrogenated diketopiperazines is a process known to occur enzymatically in nature; including, for example, the biosynthesis of albonoursin.²⁸ Albonoursin is an antibacterial compound synthesised by some strains of *Streptomyces*, and is equivalent to a Phe-Leu dipeptide that has been cyclised and dehydrogenated, i.e. “ddcFL”. This molecule is very similar to ddcFF, and serves to highlight the biological relevance and potential impact of the method for producing ddcFF discovered here.

As mentioned earlier, a key difference between ddcFF and cFF experiments is the presence of two orientations for the as-deposited ddcFF molecules, whereas only one exists for those generated by annealing of cFF. These two orientations produce chains that appear to be mirror images of one another, at $70^\circ (\pm 2^\circ)$ clockwise and $69^\circ (\pm 2^\circ)$ anticlockwise from the $[1\bar{1}0]$ direction. The two orientations are equally prevalent, and as such must correspond to two states that are energetically equivalent. Therefore, it is apparent that the molecules are differentiated by a pseudo-stereochemical effect, meaning that the prochiral ddcFF molecules are bound to the surface in non-equivalent mirror image conformations (Figure 5.18). The molecule-surface interactions create a barrier to the ‘flipping’ of the molecules, and so the two conformations do not interconvert. However, both are equally likely to be generated from the landing of ddcFF from the molecular beam, hence the 50:50 ratio observed.

Once adsorbed, the two species phase-separate based on their stereochemistry, only forming intermolecular bonds with molecules of the same landing conformation, thus giving rise to the two kinds of chiral chain observed. This type of racemic supramolecular assembly is often observed in the literature.²⁹⁻³⁰

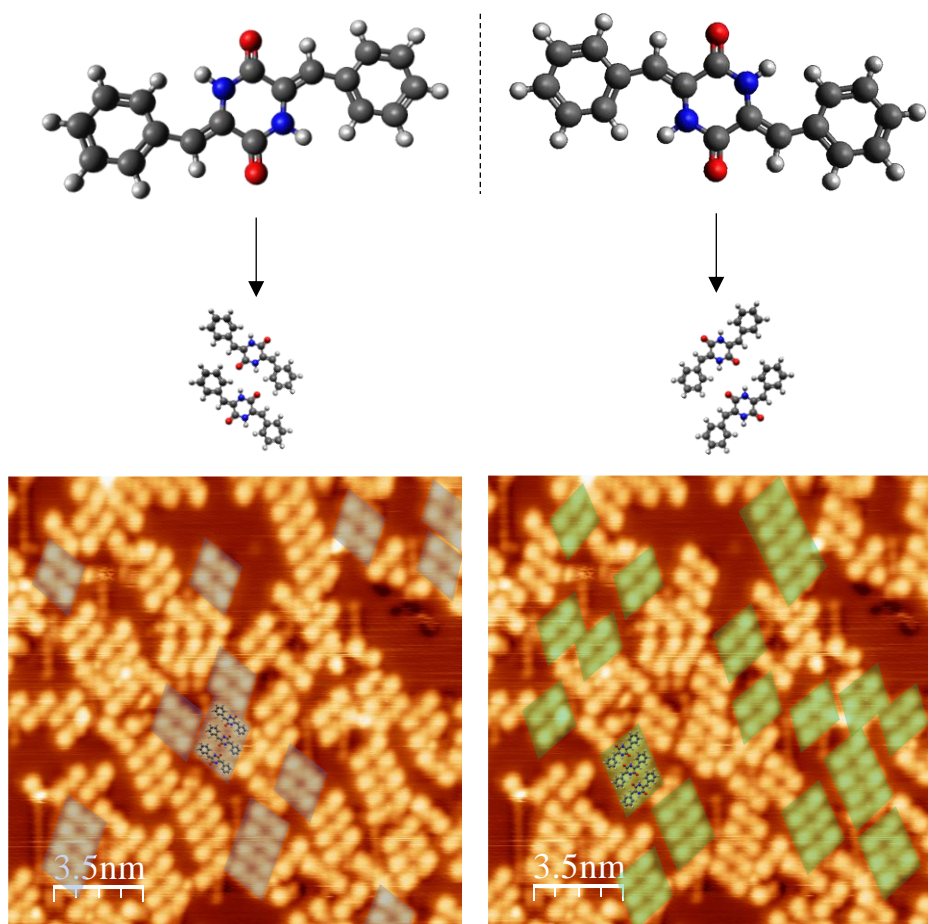


Figure 5.18. a) Models of two non-equivalent mirror image conformations of ddcFF, and how these might form mirror-image assemblies. b) Overlay of assembly models onto an STM image, demonstrating the equal prevalence of both conformations and therefore modes of assembly.

While the appearance of two self-assembly phases from deposited ddcFF can therefore be considered unsurprising, the contrast with the ddcFF molecules generated on-surface is striking. In the experiments with cFF, annealing brought about dehydrogenation but resulted in only a single phase of molecules, i.e. manifesting the unusual situation of an enantiomerically pure supramolecular arrangement formed from a prochiral molecule. This occurs because cFF is chiral, and, as described above (sections 5.2.1 and 5.2.2), adsorbs in a single preferred conformation resulting in chains of uniform orientation. This selectivity must have been preserved in the dehydrogenation process, in which the chiral cFF molecules were converted into the prochiral ddcFF molecules, in order to give a single phase post-anneal. In theory, the pro-chirality of the product could mix or ‘scramble’ with respect to the surface, if the thermal energy was sufficient to enable absorbed molecules to flip over, but this evidently does not occur as evidenced by the STM data. Thus, while the deposition of a prochiral molecule such as ddcFF normally results in a heterochiral surface, a homochiral surface can still be created with the same molecule via its generation during an on-surface

reaction. This highly unusual result could have significant impact in attempts to create a homochiral surface from a non-chiral molecule, for example for catalytic applications, and has connections with studies of molecules with helical chirality by Stetsovych et al.³¹ Stetsovych et al. demonstrated a similar principle of controlling the surface chirality of prochiral molecules by generating them from an on-surface reaction. Where this study used polycyclic aromatic compounds, however, we have used simple diketopiperazines created from biologically relevant peptides, thus considerably expanding the scope and therefore impact of this on-surface synthetic approach.

The STM data for ddcFF provide clear evidence of the on-surface dehydrogenation of cFF but cannot offer a description of how dehydrogenation occurs. In particular, they do not tell us whether the dehydrogenation of the two aliphatic carbon atoms occurs simultaneously or sequentially, whether the two alkene groups are formed at the same time or not. In fact, it is possible that the singly dehydrogenated species, sdcFF, is at some stage stable on the surface and even imaged in the STM. In order to ascertain whether or not this could be the case, experiments were carried out with sdcFF also, deposited on a low temperature (~130K) Cu(110) surface. In subsequent low temperature (77K) scans, the molecule is imaged as asymmetrical clusters and isolated species, reflecting its asymmetrical nature due to the single alkene present (Figure 5.19). These clusters appear to be irregular and are most likely kinetically trapped by the low thermal energy at 140K. Annealing to room temperature results in a re-occurrence of the chains observed for ddcFF, with STM images similar to those shown in Figure 5.18. It is proposed that, at variance with cFF, sdcFF is highly reactive on a Cu(110) surface, and thus only stable at low temperatures. At room temperature the second dehydrogenation occurs immediately, likely facilitated by the planar side of the molecule that brings the remaining aliphatic group in close proximity to the surface, thereby potentially lowering the activation energy for the reaction. A consequence of this conclusion is that the annealing of cFF to 400K must result in both dehydrogenation reactions occurring simultaneously, due to the fact that the sdcFF species is unstable even at the lower temperature of 300K.

It should be noted that in the original studies of L-Phe-L-Phe by Lingenfelder et al., some images were identified as illustrating an additional phase of the self-assembly, apparently caused by further annealing to 450K (see Figure 5.20, from Lingenfelder⁵). However, this was not reproduced by annealing alone in any of the experiments conducted here, leading us to

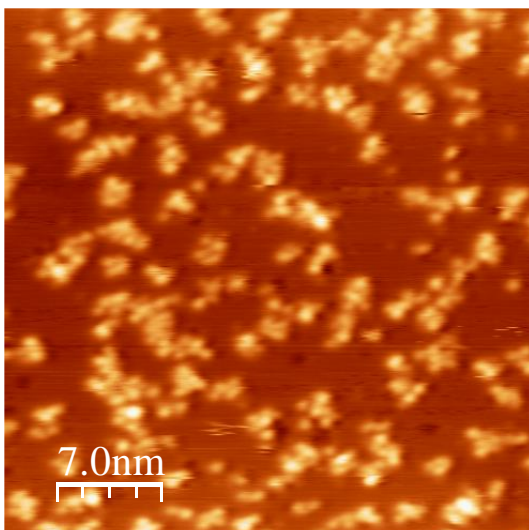


Figure 5.19. Irregular and asymmetrical clusters from a deposition of sdcFF on a low temperature (140K) Cu(110) surface.

believe that this phase is not the result of a further chemical reaction, but in fact a re-organisation of the assembly as a result of higher molecular coverage. When coverage of ddcFF was increased above a full monolayer, followed by an anneal to 400K to remove overlayer material, the molecules were seen to assemble into a more densely packed phase with a brickwork pattern (Figure 5.21). This pattern is comparable with the final phase reported by Lingenfelder, taking into consideration that as-deposited ddcFF has two mirror-symmetric self-assembly patterns compared to one for annealed cFF.

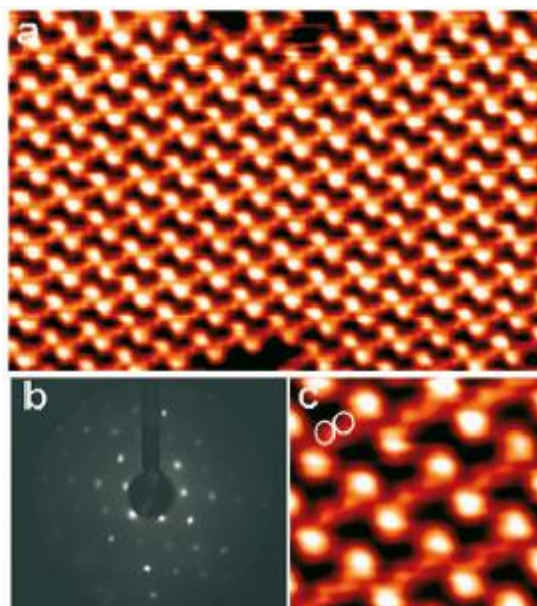


Figure 5.20. High coverage of molecules adsorbed on Cu(110) and annealed to 450K, from a proposed deposition of L-Phe-L-Phe. As reproduced from Lingenfelder⁵. a) 15 x 10.4 nm STM image, b) LEED pattern, c) 5 x 4 nm high resolution STM image.

Therefore, it is put forward that such a phase is only seen when forced by coverage. Indeed, the ddcFF chains were observed to resist island formation in the same manner as cFF when coverage was slowly increased, and annealing had no effect on this tendency. Only a greatly increased coverage followed by annealing, as described above, brings about the brickwork phase. As the coverage approaches a complete monolayer, a lateral pressure is exerted on the assembly by the addition of further molecules. This can cause a change in the way in which individual molecules adsorb to the surface and form intermolecular bonds, even though locally this causes deviation from the optimal bonding configuration, since the global energy is minimised by a denser packing of molecules.

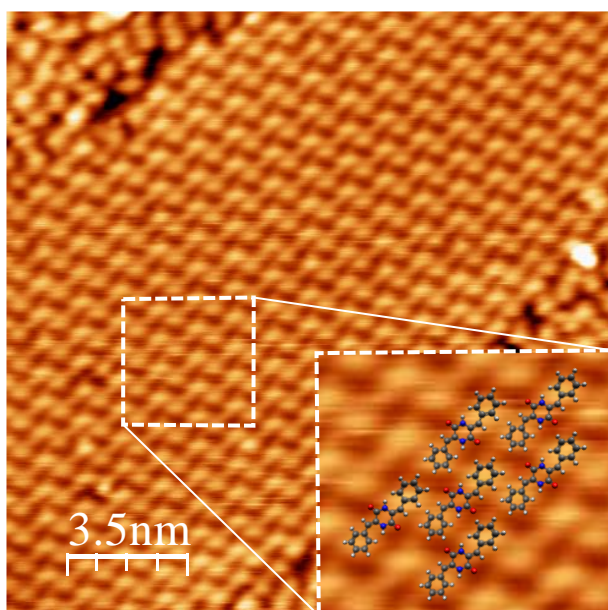


Figure 5.21. Brickwork pattern of ddcFF molecules on Cu(110), only observed at high coverage. Overlaid models indicate how the molecules might be arranged in order to produce such an assembly.

In summary, the high degree of similarity between STM data sets from different experiments has enabled the identification of two key reactions of the L-Phe-L-Phe dipeptide. First, the dipeptide cyclises when heated in a crucible, as evidenced by the matching data for depositions from crucibles of cFF and what was originally L-Phe-L-Phe. Secondly, the cFF molecules are shown to dehydrogenate into ddcFF when annealed on the Cu(110) surface, due to the strong similarity with data from as-deposited ddcFF. The chirality of the supramolecular self-assembly of ddcFF is also shown to depend on the method by which it arrives on the surface, since annealed cFF gives a single chain orientation whereas as-deposited ddcFF results in two mirror-image configurations. However, despite the substantial evidence presented by the STM data, the only way to be certain of the above conclusions is to use a chemically-sensitive technique to distinguish between different molecular species in a more precise way. For this reason, XPS was employed as a

complementary technique to STM, with a focus on C 1s, N 1s and O 1s spectra as reported below.

5.3 X-Ray Photoelectron Spectroscopy

As noted in chapter 2 (“Experimental), XPS experiments were carried out in the UHV XPS system of Warwick’s Interdepartmental Photoemission facility. Analogous conditions to the STM experiments were used to deposit molecules from crucibles of L-Phe-L-Phe, cFF and ddcFF on to a Cu(110) surface. The XPS data is presented below starting with ddcFF, since this molecule is the expected end point of each experiment and must be identified first. Subsequently, the structures of the other species can be studied, and the effects of the annealing process tracked in comparison to the pristine ddcFF sample.

As discussed in chapter 2, the XPS experiments presented in this chapter were calibrated with respect to the substrate Cu 2p_{3/2} peak, at binding energy 932.6eV.³² A Shirley-type background subtraction was applied across all peaks, with fittings performed by using a combination of Gaussian and Lorentzian functions, typically the GL(30) mix. Additional technical details can be found in chapter 2.

5.3.1 Dehydrogenated Cyclo-(L-Phe-L-Phe)

The ddcFF molecule is highly symmetrical in terms of the functional groups present (see Figure 5.1) and as such the resultant XPS spectra (Figure 5.22) are relatively simple to interpret due to a small number of distinct peaks. The N 1s and O 1s spectra both feature a single peak, at 398.3eV and 530.8eV, respectively. The best fit to the C 1s spectrum indicates that it is comprised of three peaks, at 284.7, 286.5 and 288.1 eV. A stoichiometry calculation gives a ratio of carbon atoms of 10:2:1 across the respective peaks, which matches reasonably well with a predicted 12:4:2. The largest peak at 284.7eV represents the 12 isoelectronic aromatic carbons, with the 286.5eV peak corresponding to 4 aliphatic carbon atoms that are closer to heteroatoms. The smallest peak, at the highest binding energy of 288.1eV, corresponds to carbons in a C=O bond. The discrepancies in precise peak ratios are likely a result of the higher binding energy peaks being less well-defined and having weaker signals. Furthermore, stoichiometric calculations from XPS are always approximate due to a range of factors that affect the peak height, rather than solely the density of scatterers

present.³³ The C1s peaks recorded do correlate well with literature values, in particular for aromatic^{32,34,35} and carbonyl carbons.^{32,34} The N 1s and O 1s spectra are rather simpler to interpret. The single peak for N 1s is a direct result of the symmetry and planarity of the molecule, meaning that both nitrogen atoms are in identical chemical environments. In this case, the peak at 398.3eV is a close match for nitrogen atoms deemed to be strongly bound to the Cu(110) surface, as reported in other XPS studies of peptides.³⁶⁻³⁸ A similar argument applies for the oxygen atoms also, with a single peak in the O 1s spectrum at 530.8eV that is comparable with other peptide carbonyl oxygen atoms.^{35,37,39} Annealing experiments on the ddcFF sample had no discernible effect, until the signal intensity began to decrease across all spectra past approximately 500K. This uniform decrease is indicative of the desorption of molecules from the surface. By 550K, the signals had completely disappeared, due to the complete desorption of all molecules.

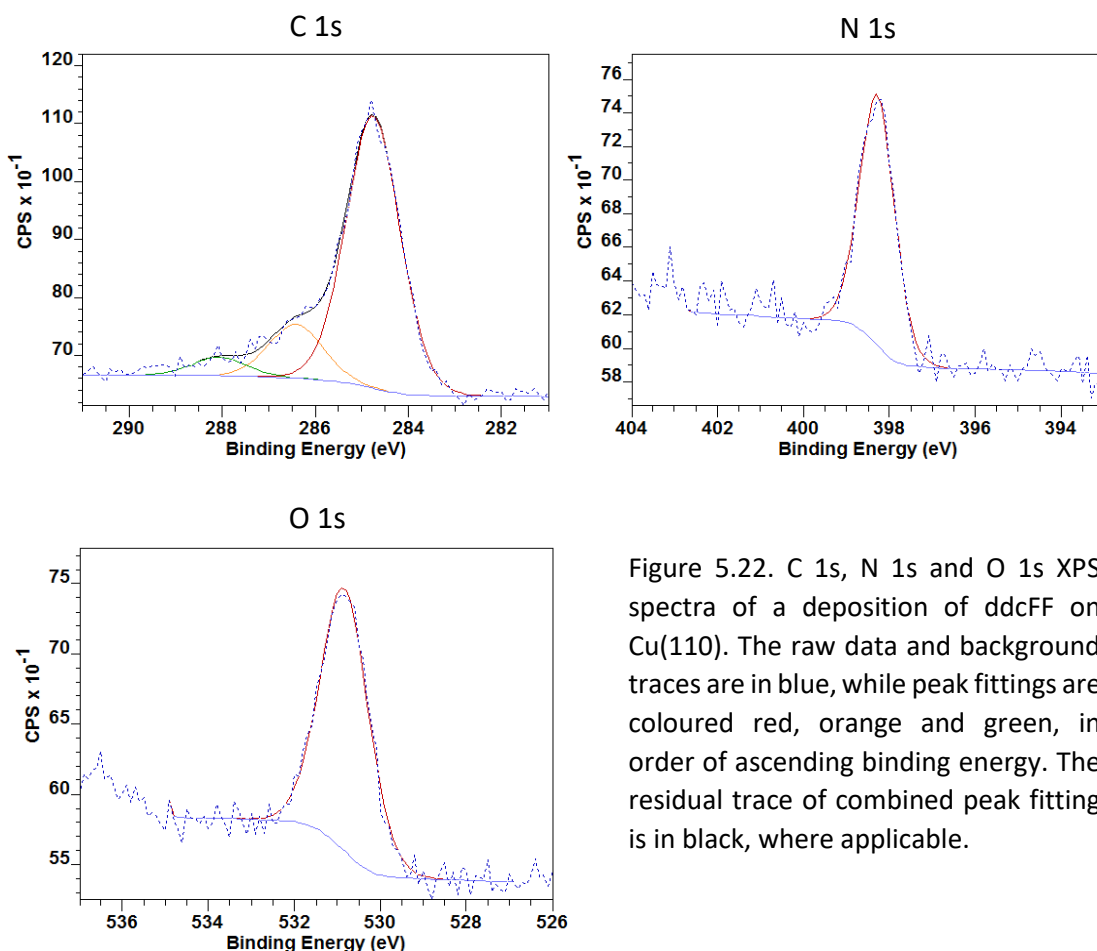


Figure 5.22. C 1s, N 1s and O 1s XPS spectra of a deposition of ddcFF on Cu(110). The raw data and background traces are in blue, while peak fittings are coloured red, orange and green, in order of ascending binding energy. The residual trace of combined peak fitting is in black, where applicable.

5.3.2 Cyclo-(L-Phe-L-Phe)

XPS of cFF revealed C 1s and O 1s spectra largely similar to the ddcFF, but a markedly different N 1s spectrum, with the addition of a secondary peak (Figure 5.23). The C 1s features three peaks – at 285.0, 286.5 and 288.1eV. The first of these peaks has a small shift of 0.3eV compared to the ddcFF data, but the remaining peaks have a shift too small to be resolved, if any. A single O 1s peak is identified at 531.3eV, a shift of 0.5eV from ddcFF. Therefore, neither the C 1s nor O 1s spectra for cFF are substantially changed from those of ddcFF, and as such, the difference in the N 1s spectrum is the key factor in distinguishing between the two molecules.

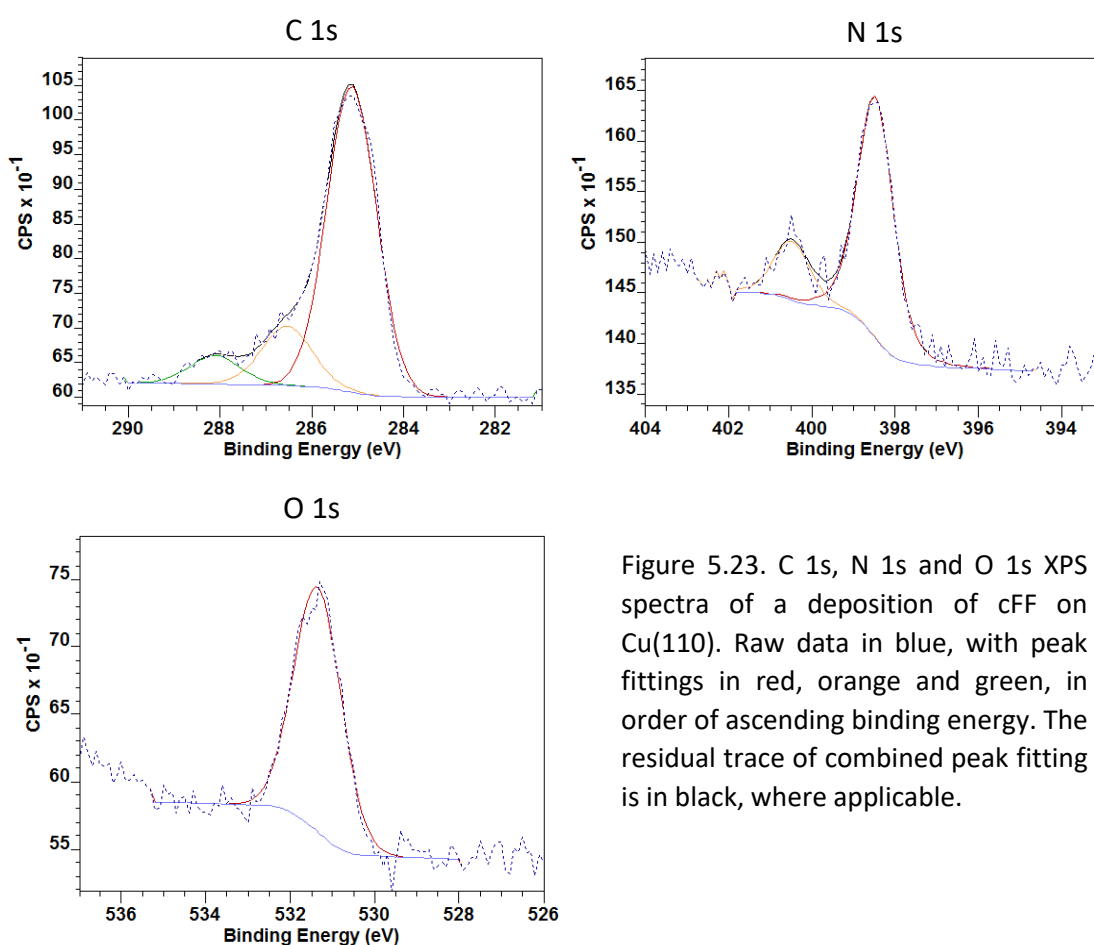


Figure 5.23. C 1s, N 1s and O 1s XPS spectra of a deposition of cFF on Cu(110). Raw data in blue, with peak fittings in red, orange and green, in order of ascending binding energy. The residual trace of combined peak fitting is in black, where applicable.

Two peaks are evident at 398.5eV and 400.5eV, a 2eV separation, with the former having approximately four times the area of the latter. The cFF molecule is also highly symmetrical, and so the appearance of a second N 1s peak is perhaps surprising. One significant difference between cFF and ddcFF that could contribute to the occurrence of two N 1s peaks is that cFF has increased conformational flexibility, potentially allowing different bonding modes to develop. The sp³ carbon atoms still present in cFF offer significant rotational flexibility to the

side groups, as well as permitting the diketopiperazine ring to buckle slightly, moving away from a flat configuration. These small conformational variations may be significant enough that alternative molecule-surface and intermolecular interactions arise. In particular, the new peak at 400.5eV corresponds well to a typical peptidic nitrogen atom, one that is not strongly bound to the surface.³⁵⁻³⁹ The larger peak at 398.5eV is shifted by only 0.2eV from the ddcFF data, and thus represents nitrogen atoms bound more strongly to the surface in the same vein. According to reports on peptides and cyclic peptides in the XPS literature, the occurrence of two N 1s peaks in this way is quite common.³⁶⁻³⁹ It has been suggested that even within individual molecules, one nitrogen atom can be essentially chemisorbed to the surface while the other interacts with the surface more weakly. Alternatively, it may be the case that some molecules bind strongly across both nitrogen atoms, whereas others are entirely in the weakly bound state. In either case, the STM data for cFF did not show any obvious distinction between molecules, nor within individual molecules, and so the differences observed in the XPS must be too subtle to detect in this way. The phenomenon observed in the N 1s spectrum here is known to be strongly coverage dependent,^{36,40} which will be explored further in the L-Phe-L-Phe experiment (see below) and used to guide the analysis of the N 1s spectra.

Upon annealing to 400K, the spectra become near indistinguishable from those of the original ddcFF experiment (Figure 5.24). The N 1s returns to a single peak at 398.3eV, while any small shifts previously displayed in the C 1s and O 1s spectra are reversed. The C 1s peaks now fall at 284.7eV, 286.4eV and 288.2eV, and O 1s at 530.8eV. This result clearly substantiates the theory proposed from the STM data, which is that the molecules have dehydrogenated due to the annealing on the surface, and that there is no practical difference between the resulting adlayer and a deposition of pristine ddcFF.

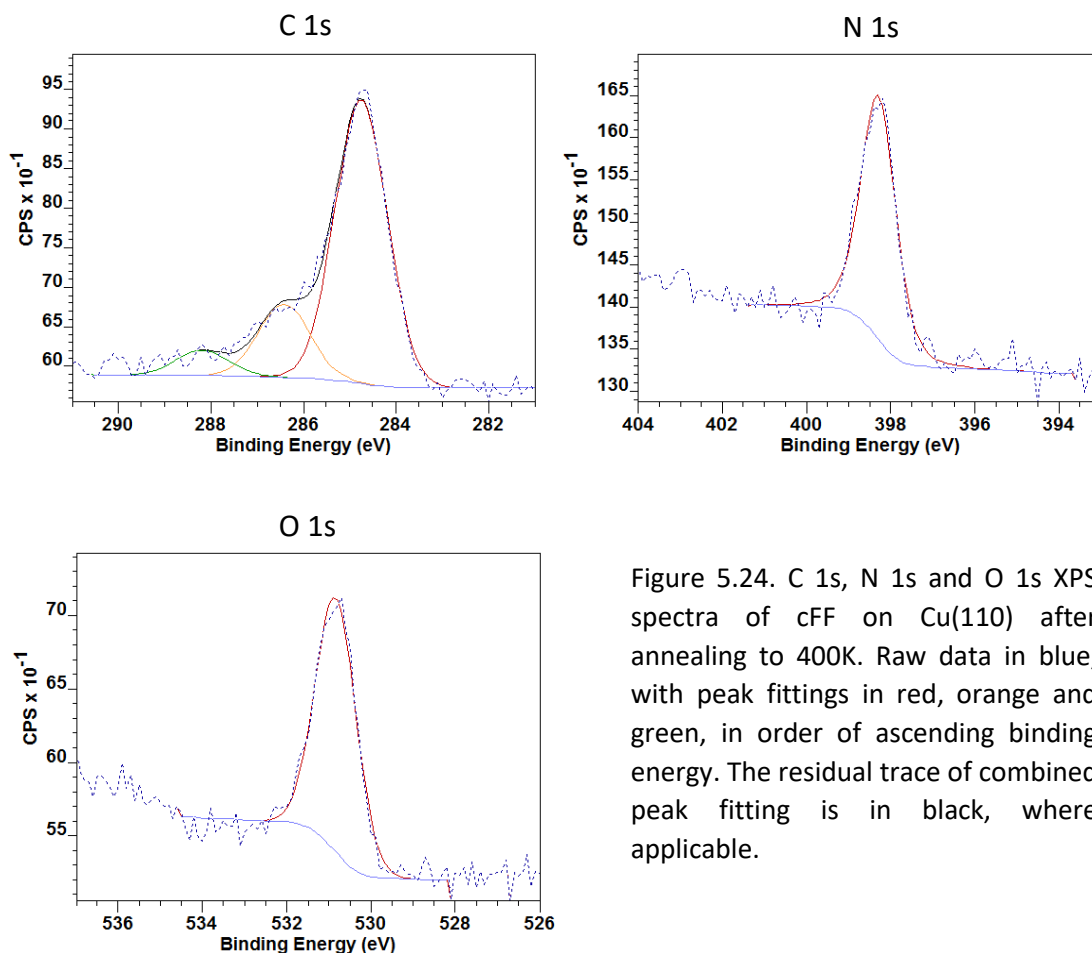


Figure 5.24. C 1s, N 1s and O 1s XPS spectra of cFF on Cu(110) after annealing to 400K. Raw data in blue, with peak fittings in red, orange and green, in order of ascending binding energy. The residual trace of combined peak fitting is in black, where applicable.

5.3.3 L-Phe-L-Phe

As has already been discussed, L-Phe-L-Phe is almost certainly deposited as cFF, and this is immediately apparent when studying the XPS data in Figure 5.25. In the C 1s spectrum are three peaks at 285.1eV, 286.4eV and 288.1eV; in the N 1s are two peaks at 398.6eV and 400.3 eV; and the O 1s has a single peak at 531.5eV. These peaks feature only very small shifts from the cFF data set, with the only major difference being the ratio between the two N 1s peaks. The larger peak in terms of area remains the one at lower binding energy, which corresponds to the strongly bound nitrogen atoms, but the higher binding energy peak is substantially larger than in the cFF experiment. This is attributed to a coverage effect, as the overall increased XPS signal strength from this experiment in comparison to the cFF experiment suggests more molecules are present on the surface (in this instance, the higher coverage was unintentional). This interpretation is supported by the work of Méthivier *et al*³⁶ and Feyer *et al*⁴⁰, where coverage was intentionally increased and caused a rise in the higher binding energy peak.

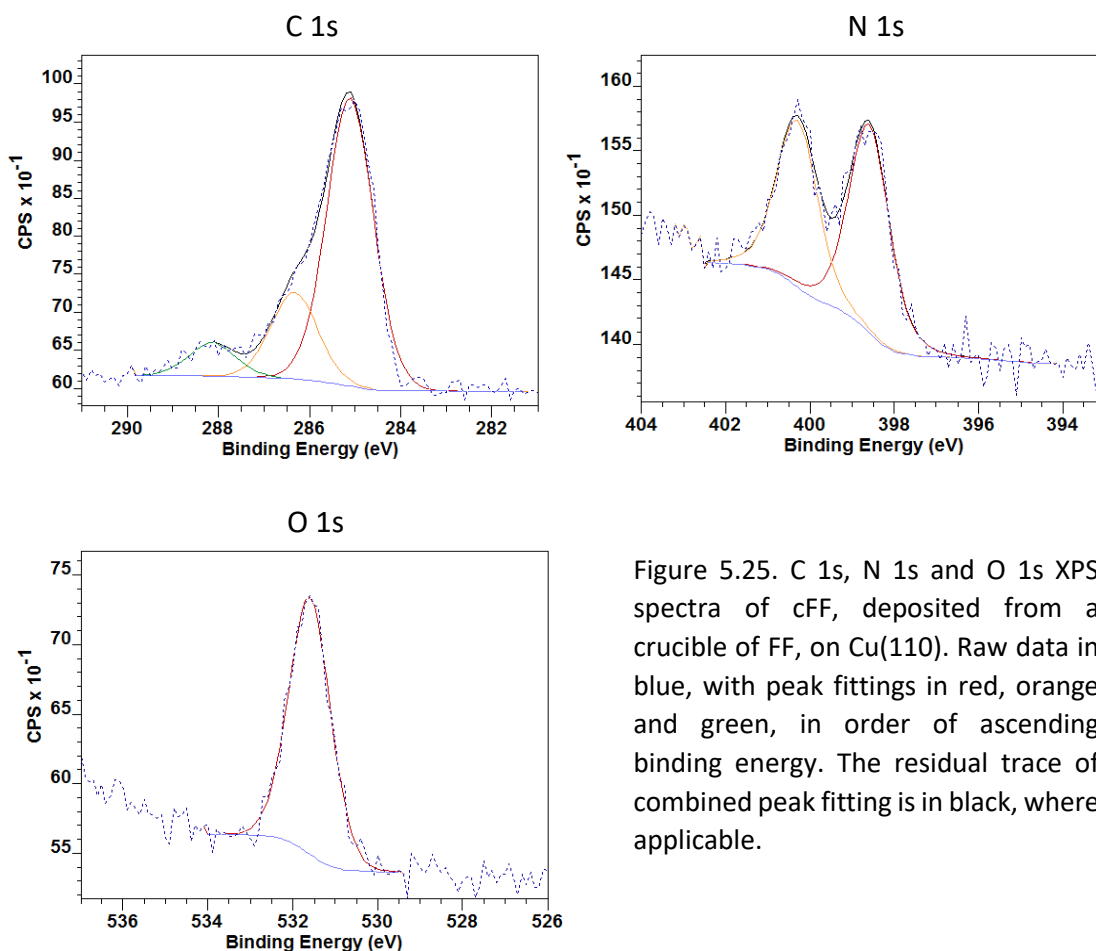


Figure 5.25. C 1s, N 1s and O 1s XPS spectra of cFF, deposited from a crucible of FF, on Cu(110). Raw data in blue, with peak fittings in red, orange and green, in order of ascending binding energy. The residual trace of combined peak fitting is in black, where applicable.

In order to verify this hypothesis, a second independent deposition was carried out at a greater exposure time, the results of which are presented in Figure 5.26. The C 1s spectrum contains peaks at 285.2eV, 286.5eV and 288.2eV; the N 1s two peaks at 398.6eV and 400.3eV; and the O 1s a single peak at 531.5eV. These peak positions are all very similar to the first deposition of L-Phe-L-Phe and, by extension, to that of cFF, but the nitrogen peak ratio has increased even further. The higher binding energy peak now exceeds the area of the lower binding energy peak, indicating that weakly bound nitrogen species now dominate the surface.

Based on the XPS data for the three depositions of cFF, a theory can be proposed to explain the molecular interactions that are responsible for the N 1s spectra. The peak assignments fit well to literary descriptions of nitrogen atoms strongly and weakly bound to the surface, but it must be considered why two different binding modes should occur, and why they should change with coverage. In the STM data, the only distinguishable difference between the molecules is their position in the chains, or indeed outside of a chain altogether. A logical possibility then is that the molecules are bound to the surface via different interactions depending on their position in relation to the self-assembled chains (or rather, the bonding

is what determines their self-assembly). In this case, the dominant mode of molecule-surface interaction involves strongly bound nitrogen atoms, and the peak in the XPS that represents this state decreases with increasing coverage. The corresponding change observed in the self-assembly is a shift towards more densely-packed chains, with fewer isolated molecules and chain ends. Therefore, it is proposed that isolated molecules and those at the ends of chains contribute to the strongly bound nitrogen peak, and their reduction in relative frequency with coverage causes the change in peak heights observed. However, the relative size of the strongly bound N 1s peak is too large to correspond to these species alone, since statistically most molecules appear within the chains rather than at the ends. Therefore, it may also be the case that, as suggested in the literature,³⁷ one nitrogen atom from each molecule within the chains is strongly bound to the surface, while the other is weakly bound. The sum of these atoms and those in isolated or chain-end molecules would give rise to the large XPS peak observed, and would explain why the peak shrinks with coverage but does not completely disappear. However, further experiments on the effects of coverage and the self-assembly of cFF would be required to validate this theory, as will be discussed in the conclusion below.

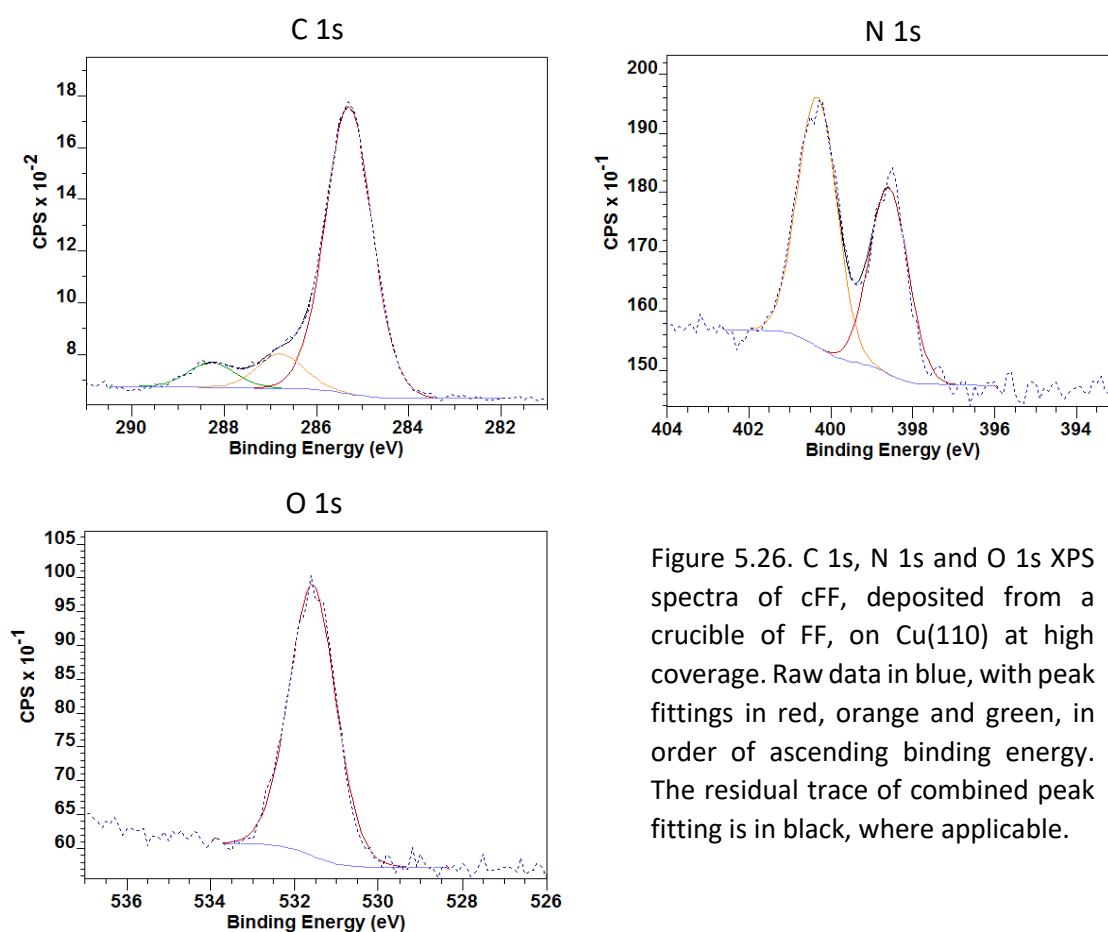


Figure 5.26. C 1s, N 1s and O 1s XPS spectra of cFF, deposited from a crucible of FF, on Cu(110) at high coverage. Raw data in blue, with peak fittings in red, orange and green, in order of ascending binding energy. The residual trace of combined peak fitting is in black, where applicable.

Upon mild annealing of both depositions to 325K, there is a decrease in intensity of the higher binding energy peak, reversing the trend described previously, which may indicate decreasing coverage. The C 1s and O 1s spectra are not significantly affected. Further annealing to 400K again brings about the dehydrogenation of the cyclic molecules, resulting in spectra akin to the ddcFF experiment. Due to the unusually high coverage of the second deposition, a higher annealing temperature of 450K was required to fully convert the system to the dehydrogenated form, though it is likely this could also have been achieved by simply increasing the duration of the anneal at 400K.

The combined sets of XPS spectra clearly demonstrate that not only is L-Phe-L-Phe deposited as a cyclic rather than linear molecule, but that this cyclic molecule readily dehydrogenates upon annealing the Cu(110) surface to 400K. The dehydrogenation process was shown to occur in three separate experiments and as such is highly reproducible, and the outcome is indistinguishable by XPS from a pristine ddcFF deposition.

5.4 Concluding remarks

In conclusion, the self-assembly on the Cu(110) surface of the L-Phe-L-Phe dipeptide and its synthetic derivatives, Cyclo-(L-Phe-L-Phe) and dehydrogenated Cyclo-(L-Phe-L-Phe), has been described using low temperature STM and XPS experiments. A comparison of the data across experiments proves that L-Phe-L-Phe cyclises upon heating and deposits as cFF, and that cFF dehydrogenates to ddcFF when annealed on the surface. These transformations of the L-Phe-L-Phe dipeptide are of significant interest due to their relevance to biological systems, chemical synthesis, and surface chirality.

The similarity of the ddcFF molecule to the natural antibacterial compound albonoursin has been highlighted, demonstrating the close link between the simple thermal transformations illustrated here and real-world enzymatic processes. A number of other dehydrogenated diketopiperazines have also been shown in the literature to be the product of enzyme-based biosynthesis,^{10,41} opening up a substantial pool of molecules that could be tested for similar on-surface behaviour to cFF. Mimicking the reactions of enzymes typically involves complex synthetic pathways,^{9,10} and will inherently have an incomplete yield including unintended products and leftover starting materials or intermediates. The processes described in this chapter are small in scale but offer a straightforward and direct route to a dehydrogenated diketopiperazine, starting from the DKP itself or even a linear dipeptide. Of additional

significance is that the deposition of ddcFF produces a racemic surface due to the molecule's prochiral nature, whereas dehydrogenating a deposition of cFF – which is chiral – via surface annealing results in a homochiral surface consisting of a single species on the surface. The creation of a chiral surface from a prochiral molecule has potentially broad impact, and thus far had not been demonstrated with molecules of biological relevance such as peptides. In addition, the procedure for generating this chiral surface is simple and reproducible. Therefore, it becomes of great interest to explore similar molecules to identify if such a phenomenon could be more general, especially given that peptides are a generally inexpensive and readily available starting material. A logical starting point for such studies would be peptides structurally similar to L-Phe-L-Phe, i.e. dipeptides with aromatic but weakly interacting side chains. Experiments with examples of such molecules are presented in the subsequent chapter (chapter 6, “Self-assembly of aromatic dipeptides on metal surfaces”).

In order to draw further conclusions from the studies of cFF and ddcFF, additional experiments could be conducted. In particular, a better understanding of the N 1s XPS spectrum could be established by further variation of the coverage of cFF on Cu(110), broadening the range of coverages so that the trend in peak heights can be more clearly observed. The new data would help to establish whether the theory on the source of the strongly and weakly bound nitrogen atoms is accurate, but would ideally need to be combined with STM experiments conducted on the same sample/in the same system. The two sets of data would be complementary, and would allow for a more direct evaluation of the number of molecules within chains compared to those at the ends or isolated. XPS data on a very low coverage deposition would be especially informative, since the number of chains formed is minimised, meaning that the strongly bound N 1s peak may completely dominate.

5.5 References

1. M. Reches and E. Gazit, *Science*, 2003, **300**, 625–627.
2. E. Gazit, *FASEB J.*, 2002, **16**, 77-83.
3. C. H. Görbitz, *Chem. Commun.*, 2006, **22**, 2332-2334.
4. R. Cukalevski, B. Boland, B. Frohm, E. Thulin, D. Walsh and S. Linse, *ACS Chem. Neurosci.*, 2012, **3** (12), 1008-1016.
5. M. Lingenfelder, PhD thesis, 2007, EPF Lausanne, Switzerland.
6. G. Tomba, M. Lingenfelder, G. Costantini, K. Kern, F. Klappenberger, J. V. Barth, L. C. Ciacchi and A. De Vita, *J. Phys. Chem. A*, 2007, **111**, 12740-12748.
7. Y. Wang, M. Lingenfelder, T. Classen, G. Costantini and K. Kern, *J. Am. Chem. Soc.*, 2007, **129**, 15742-15743.
8. M. Lingenfelder, G. Tomba, G. Costantini, L. C. Ciacchi, A. De Vita and K. Kern, *Angew. Chem. Int. Ed.*, 2007, **46**, 4492-4495.
9. S. Ando, A. L. Grote and K. Koide, *J. Org. Chem.*, 2011, **76**, 1155–1158.
10. A. D. Borthwick, *Chem. Rev.*, 2012, **112** (7), 3641-3716.
11. Y. Wang, S. Fabris, T. W. White, F. Pagliuca, P. Moras, M. Papagno, D. Topwal, P. Sheverdyeva, C. Carbone, M. Lingenfelder, T. Classen, K. Kern and G. Costantini, *Chem. Commun.*, 2012, **48**, 534–536.
12. J. M. Lehn, *Angew. Chem. Int. Ed.*, 1988, **27** (1), 89-112.
13. J. V. Barth, G. Costantini and K. Kern, *Nature*, 2005, **437**, 671–679.
14. K. S. Mali and S. de Feyter, *Philos. Trans. R. Soc. London, Ser. A*, 2013, **371** (2000), DOI: 10.1098/rsta.2012.0304.
15. A. Kumar, K. Banerjee and P. Liljeroth, *Nanotechnology*, 2017, **28**, 082001-082046.
16. L. Sosa-Vargas, E. Kim and A. J. Attias, *Mater. Horiz.*, 2017, **4**, 570-583.
17. G.A. Jeffrey, *An introduction to hydrogen bonding*, Oxford University Press, Oxford, 1997.
18. E. N. Baker and R. E. Hubbard, *Prog. Biophys. Mol. Biol.*, 1984, **44**, 97-179.
19. W. Kabsch and C. Sander, *Biopolymers*, 1983, **22**, 2577-2637.
20. A. Della Pia, M. Riello, A. Floris, D. Stassen, T. S. Jones, D. Bonifazi, A. De Vita and G. Costantini, *ACS Nano*, 2014, **8**, 12356–12364.
21. M. Seul and D. Andelman, *Science*, 1995, **267**, 476.
22. A. Ferretti et al., *Phys. Rev. Lett.*, 2007, **99**, 046802.
23. F. Bussolotti and R. Friedlein, *Phys. Rev. B*, 2010, **81**, 115457.

24. T. Yokoyama, S. Yokoyama, T. Kamikado, and S. Mashiko, *J. Chem. Phys.*, 2001, **115**, 3814.
25. X. Guo, Z. Dong, and D. Fujita, *Thin Solid Films*, 2008, **516**, 2407.
26. X. L. Guo et al., *Nanotechnology*, 2004, **15**, S402.
27. W. Deng et al., *J. Chem. Phys.*, 2002, **117**, 4995.
28. H. Kanzaki, D. Imura, T. Nitoda and K. Kawazu, *J. Mol. Catal. B Enzym.*, 1999, **6**, 265-270.
29. R. Raval, *Chem. Soc. Rev.*, 2009, **38**, 707-721.
30. K.-H. Ernst, *Phys. Status Solidi B*, 2012, **249**, 2057–2088.
31. O. Stetsovych, M. Švec, J. Vacek, J. V. Chocholoušová, A. Jančařík, J. Rybáček, K. Kosmider, I. G. Stará, P. Jelínek and I. Starý, *Nature Chem.*, 2016, **9**, 213–218.
32. A. V. Naumkin, A. Kraut-Vass, S. W. Gaarenstroom and C. J. Powell, NIST Standard Reference Database 20 (Version 4.1), <https://srdata.nist.gov/xps/>, 2012 (accessed 2018).
33. M. P. Seah, “The quantitative analysis of surfaces by XPS: A review”, *Surf. Interface Anal.*, 1980, **2** (6), 222-239.
34. N. Graf, E. Yegen, T. Gross, A. Lippitz, W. Weigel, S. Krakert, A. Terfort and W. E. S. Unger, *Surf. Sci.*, 2009, **603**, 2849–2860.
35. Y. Zubavichus, M. Zharnikov, A. Shaporenko, O. Fuchs, L. Weinhardt, C. Heske, E. Umbach, J. D. Denlinger and M. Grunze, *J. Phys. Chem. A*, 2004, **108** (20), 4557-4565.
36. C. Méthivier, V. Lebec, J. Landoulsi and C.-M. Pradier, *J. Phys. Chem. C*, 2011, **115**, 4041–4046.
37. O. Plekan, V. Feyer, S. Ptasińska, N. Tsud and K. C. Prince, *Phys. Chem. Chem. Phys.*, 2014, **16**, 6657.
38. C. Méthivier, V. Humblot and C.-M. Pradier, *J. Phys. Chem. C*, 2016, **120**, 27364–27368.
39. A. P. W. Arachchilage, F. Wang, V. Feyer, O. Plekan and K. C. Prince, *J. Chem. Phys.*, 2010, **133**, 174319.
40. V. Feyer, O. Plekan, N. Tsud, V. Cháb, V. Matolín and K. C. Prince, *Langmuir*, 2010, **26**, 8606–8613.
41. H. Kanzaki, S. Yanagisawa, K. Kanoh and T. Nitoda, *J. Antibiot.*, 2002, **55** (12), 1042-1047.

Chapter 6: Self-assembly of aromatic dipeptides on metal surfaces

6.1 Self-assembly of D-Phe-L-Phe and L-Phe-D-Phe on metal surfaces

6.1.1 Background

As part of the investigations into ddcFF and its self-assembly behaviour on a Cu(110) surface, it was discovered that the resultant stereochemistry on the surface could be controlled depending on whether the molecule was deposited by OMBE or generated through an on-surface reaction. The generation of ddcFF, an inherently prochiral molecule, occurred on Cu(110) via a dehydrogenation reaction of cFF, a chiral molecule. It is therefore of interest to study the effect of the stereochemistry of the starting material on its self-assembly, and the knock-on effect to on-surface reactions and the self-assembly of the products. The enantiomer of FF (LFLF), i.e. D-Phe-D-Phe (DFDF), has already been reported to self-assemble in a way that mirrors FF on Cu(110),¹⁻³ including after annealing to 400K. To further explore this behaviour, the diastereomers of FF, namely D-Phe-L-Phe (DFLF) and L-Phe-D-Phe (LFDF), were selected for study by STM on Cu(110) and Au(111). A sublimation test was carried out as the first stage of this experiment, to establish if the behaviour of these molecules is comparable to FF when heated in vacuum. Subsequent STM data was examined in light of this test, and again compared to the outcome of experiments with FF. The combined results highlight a simple but highly valuable method for controlling surface chirality arising from the adsorption of a prochiral molecule.

6.1.2 Sublimation of DFLF and LFDF

DFLF and LFDF were sublimed in HV conditions on to glass substrates, and the resulting deposited material tested by ESI mass spectrometry in methanol, as described in chapter 2 ("Experimental"). The sublimation temperature used was 415K in both cases. A single significant peak was observed for both samples, at m/z 317.1 (Figure 6.1), which corresponds to the cyclised molecule with a sodium adduct as described for FF in chapter 5 ("Chemical transformations of the Phe-Phe dipeptide").

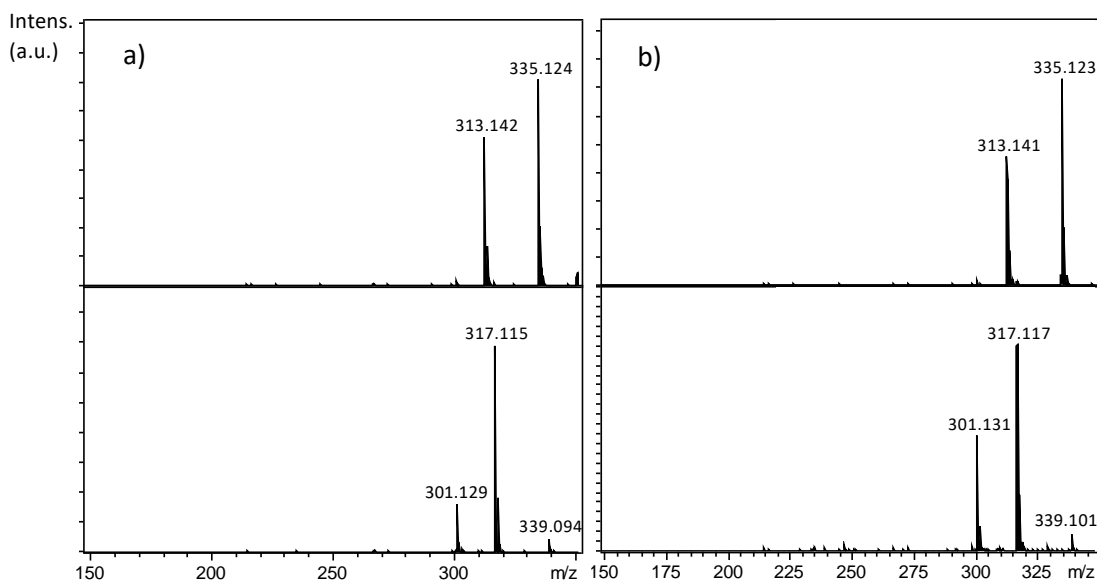


Figure 6.1. Mass spectra of a) DFLF and b) LFDF. In each set, the top spectra correspond to the non-sublimed molecules while the bottom spectra are from the sublimed material. The molecular ion in both cases occurs at $\sim m/z$ 313. The lack of peaks below m/z 300 illustrates that fragmentation does not occur. The peak at m/z 301.1 is a common plasticiser.

A much smaller peak at m/z 339.1 would fit with a second sodiation, while the peak at m/z 301.1 is from a common plasticiser contaminant. The pristine, non-cyclised samples showed peaks for the protonated linear molecule, at m/z 313.1, and the sodiated linear molecule at m/z 335.1 ($M+Na$), with no evidence of the cyclised species. Therefore it is apparent that both diastereomers cyclise upon thermal sublimation, echoing the behaviour of L-Phe-L-Phe. It should be noted that, after cyclisation, the two diastereomers acquire exactly the same structure, losing their stereochemical history and becoming the same molecule (see Figure 6.2). This is due to the amide bond formed by the former N and C termini of the peptide, creating symmetry in the cyclised molecule not present in the linear species. Therefore, assuming the same conditions in both crucibles, any deposition for STM sample preparation by OMBE should be expected to generate the same adlayer, composed of the same cyclic molecule, cFF(L/D). To confirm this outcome, depositions for STM were carried out from both crucibles and compared. In general, it was indeed found to be the case that both depositions yielded the same result, confirming that the same molecule was deposited. Therefore, the STM data is discussed in terms of a unified dataset. In the particular case of Cu(110), one crucible provided a somewhat cleaner deposition that was easier to scan in the STM, but this is likely the result of subtle differences in crucible parameters, and/or slightly higher sample purity.

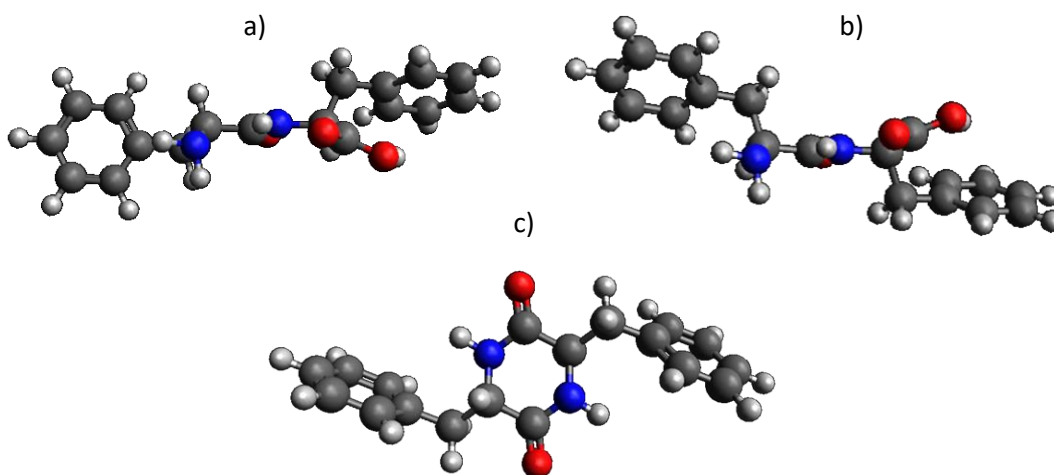


Figure 6.2. Molecular models of a) DFLF, b) LFDF, and c) cFF(L/D). Though the linear molecules are enantiomers, the cyclised product cFF(L/D) is the same in each case, since the N and C termini have formed an amide bond indistinguishable from the existing “peptide bond”. cFF(L/D) therefore always has one L and one D stereocentre.

6.1.3 Self-assembly of cFF(L/D) on Cu(110)

While one could have expected that the deposition of cFF(L/D) on Cu(110) would yield the same results to those of cFF, it did not prove to be the case. At submonolayer coverages, the molecules appeared to be too mobile to image, as no stable scans could be obtained at room temperature. Increasing the coverage to >1 monolayer followed by annealing enabled the deposited material to be imaged. It seems that a significant proportion of contaminant reaches the surface, despite the mass spectra appearing relatively clean. Alternatively, it could be the case that the molecules partially degrade upon sublimation from the OMBE source, since the conditions may be slightly different from the test chamber used for the mass spectrometry experiment.

Initial high coverage depositions of cFF(L/D) on Cu(110) resulted in poorly resolved images of the first layer, due to mobile and disordered material in the overlayer. However, even under these conditions, it was apparent that molecules were ordered into islands in the first layer. Annealing (to 400K) enabled imaging of the first layer due to desorption of the overlayer, and revealed a result similar to that of dehydrogenated cFF at high coverage (see chapter 5, section 5.2.3). Figure 6.3 illustrates the types of images obtained after annealing the high coverage deposition of cFF(L/D). Patches of ordered molecules can be observed, ranging in size from only a few molecules in length and breadth (approx. 2 nm) to larger islands of 10 nm or more in a given direction. Within these islands, the rows of molecules are offset from their neighbours in an ABA fashion, with a lengthways periodicity of 1.84 ± 0.07 nm and a breadthways periodicity of 0.65 ± 0.01 nm. The gaps between islands are not bare surface but seem to be filled by disordered material, which is not well resolved and so is difficult to directly identify, likely the result of contaminants or minor fragments. The resemblance of the assembly to the high coverage phase of ddcFF however suggests that the behaviour of the two molecules could indeed be analogous, meaning that cFF(L/D) can also dehydrogenate with annealing on Cu(110). Thus, while some impurities may be present, it would still be highly valuable to analyse the data gathered for cFF(L/D). Annealing to higher temperatures is known to degrade films generated from cFF, and so further annealing was avoided in this experiment.

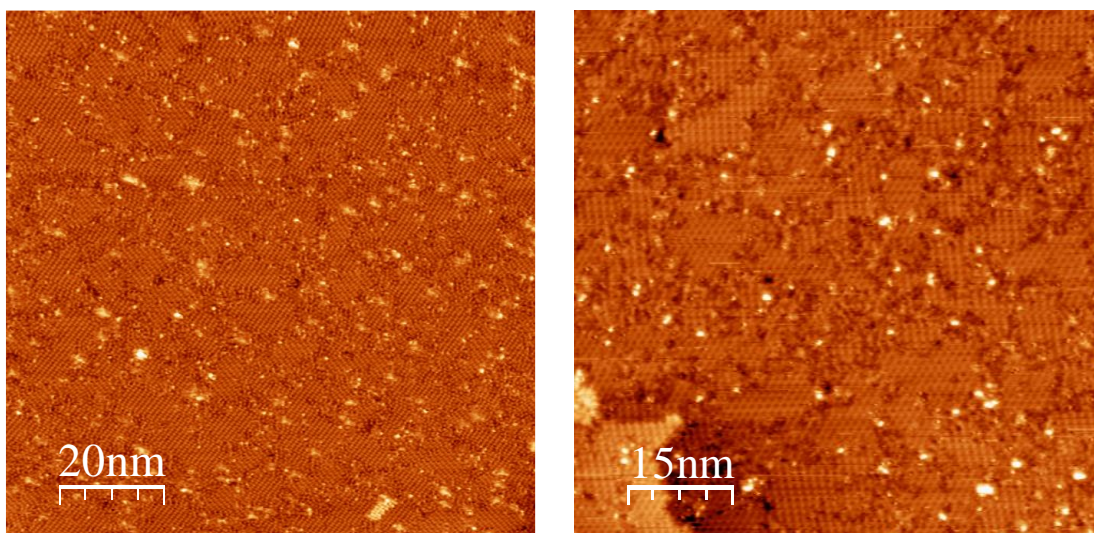


Figure 6.3. High coverage deposition of cFF(L/D) on Cu(110) annealed to 400K. A number of small islands containing ordered molecules are observed, with disordered material in the gaps between islands.

Though the molecules are arranged into numerous smaller patches as in Figure 6.3, it can be shown that only two molecular orientations are found within, always assembled into

homogeneous islands. Figure 6.4 provides smaller scale images in which the distinction between the two molecular orientations, and therefore types of islands, can be observed. It is also demonstrated that these two orientations are mirror images of one another about the known position of the $[1\bar{1}0]$ plane. Figure 6.5 shows the distribution of the islands of each type within a 50 nm x 50 nm scan area, which is in line with the proportion of approximately 50:50 recorded globally across the sample. A logical conclusion therefore is that the deposited molecule exists as two distinct, mirror-image species on the Cu(110) surface, that each have a specific and mirrored surface binding site.

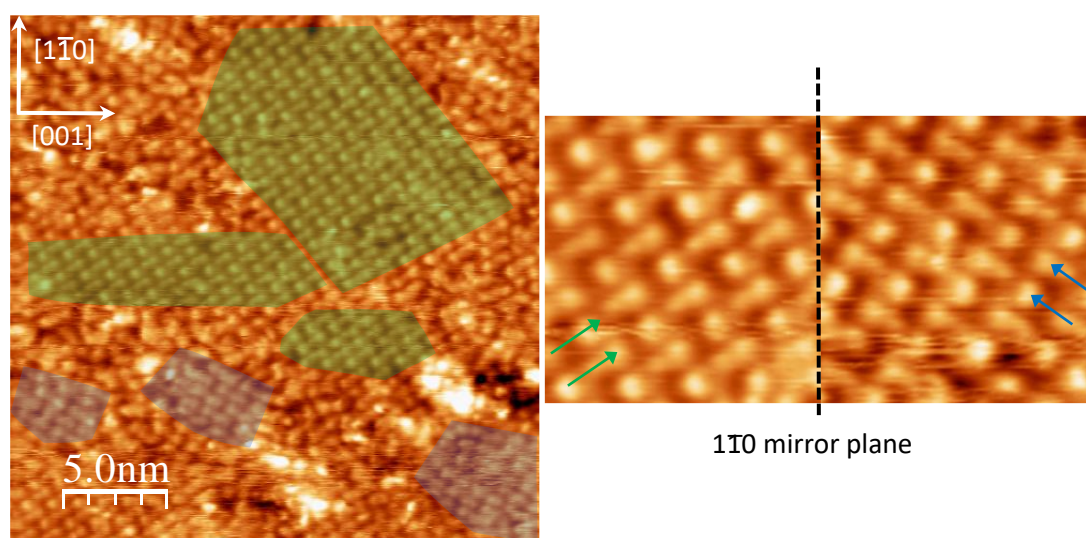


Figure 6.4. The two types of molecular island of cFF(L/D) on Cu(110), more clearly distinguished at a smaller image scale. Left: Island types indicated in green and blue. Right: the two islands types are shown to be mirror images of one another about the $[1\bar{1}0]$ plane (image size 5 nm x 5 nm).

As discussed above, cFF is known to dehydrogenate on a Cu(110) surface upon annealing to 400K, so under the conditions of the cFF(L/D) experiment, the same outcome could be expected. The product of this dehydrogenation is in both cases the same molecule, but is discussed here as separate species in the context of on-surface conformations and method of generation. Therefore, ddcFF(L/D) represents the dehydrogenation product of cFF(L/D), whereas ddcFF is the dehydrogenation product of cFF (chapter 5). The generation of ddcFF by on-surface annealing notably resulted in a single molecular orientation, in keeping with the single conformer of the chiral cFF deposited (see chapter 5, section 5.2.3). However, the generation of ddcFF(L/D) by on-surface annealing has produced two orientations, more akin to a direct deposition of the molecule. Thus, a significant difference is found between the behaviour of a deposition of cFF and cFF(L/D). The most likely explanations for this difference

are either that the surface has a certain selectivity for a particular landing conformation of the cyclic peptides, or that during the dehydrogenation reaction particular conformations of product are favoured. While a model of cFF in vacuo is highly contoured, cFF(L/D) is much flatter, and symmetric about the plane of the central diketopiperazine ring (Figure 6.6). As such, inverting the conformation of cFF on Cu(110) has a major impact on the energetics of its adsorption, for both the LL and DD isomers (cf. Tyr-Tyr on Au(111), chapter 6.2). In contrast, there may be very little effect of inverting the conformation of the flatter cFF(L/D) molecule. Consequently, a Boltzmann-distribution of the conformational states for cFF(L/D) molecule. Consequently, a Boltzmann-distribution of the conformational states for cFF(L/D) could be expected to give a close to 50:50 ratio, meaning that subsequent dehydrogenation on-surface would result in the same distribution, but of ddcFF(L/D).

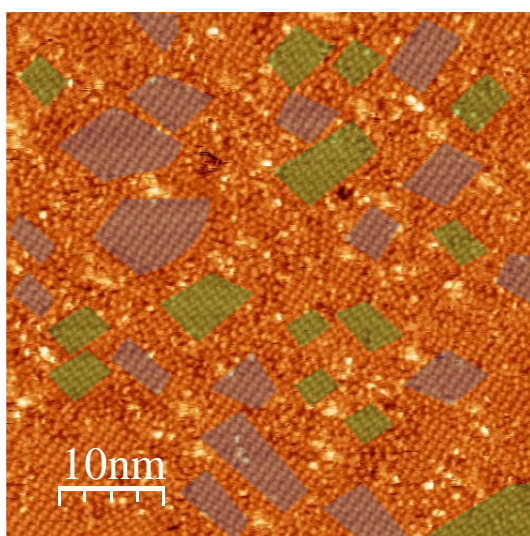


Figure 6.5. Analysis of the distribution of cFF(L/D) island types on Cu(110). Across the surface an approximate 50:50 ratio is found.

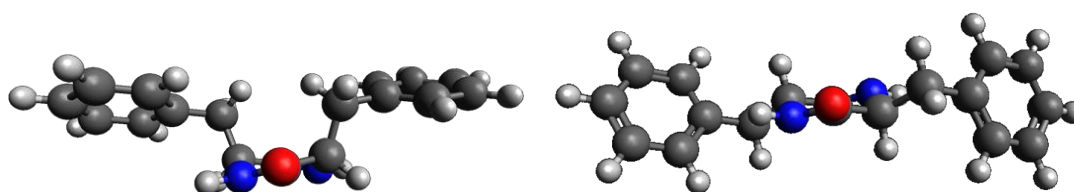


Figure 6.6. Molecular models of cFF (left) and cFF(L/D) (right), viewed along the plane of the central ring. The differences at the chiral centres causes a different conformation to arise as the lowest energy structure.

A comparison can be directly drawn between the STM data for ddcFF(L/D) and ddcFF at high coverage, to support the above conclusion. As described in chapter 5, ddcFF could be forced into a high coverage phase, forming islands of two distinct orientations of molecules, similar to those of ddcFF(L/D). In Figure 6.7, the orientation of molecules within islands of high coverage ddcFF is compared to ddcFF(L/D), with respect to previously ascertained surface directions in both cases. These orientations are within 5 degrees of one another for both types of islands, an error that could feasibly arise from the different scanning conditions of

the two instruments involved. It is therefore reasonable to state that the two orientations seen for a high coverage of ddcFF(L/D) match those of high coverage ddcFF. By extension, a single orientation from these two would be expected for ddcFF generated instead by on-surface annealing.

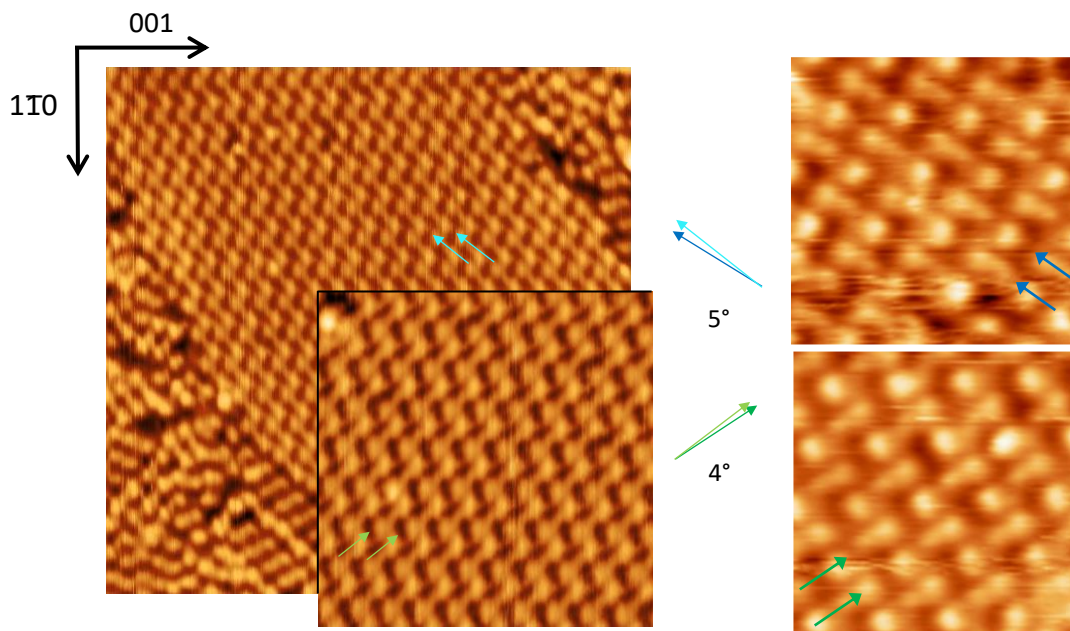


Figure 6.7. Comparison of the molecular orientations of ddcFF (left) and ddcFF(L/D) (right) on Cu(110). The difference between the orientations is only a few degrees in each case. ddcFF image scales: 18.5 nm x 18.5 nm, inset 9.2 nm x 9.2 nm. ddcFF(L/D) image scale: image size 5 nm x 5 nm.

Figure 6.8 illustrates how the dehydrogenated molecules self-assemble into the islands observed, in the same fashion as described in chapter 5 (section 5.2.3). A scaled molecular model of ddcFF(L/D) correlates well to the two-lobed features observed, and builds into a series of molecular rows. As discussed in chapter 5, this arrangement appears to be forced by coverage, forgoing optimal intermolecular interactions in favour of the most space-efficient packing possible.

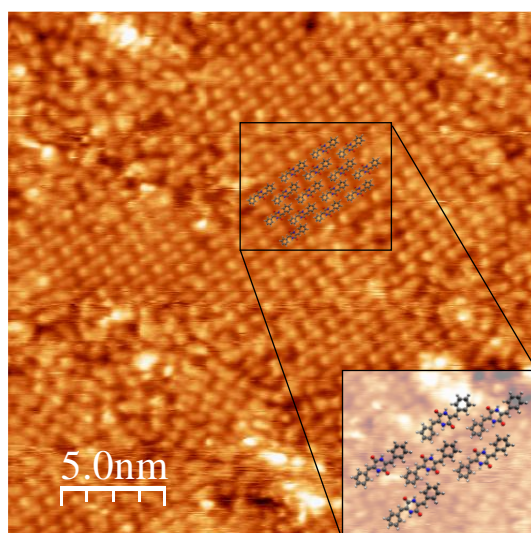


Figure 6.8. Proposed self-assembly pattern of ddcFF(L/D) molecules on Cu(110), enforced by the high coverage.

In summary, cFF(L/D) did not prove possible to image on Cu(110) at sub-monolayer coverages, in contrast to cFF. This could be caused by a purity issue with the deposited material, or by the different stereochemistry affecting the strength of molecule-surface interactions. At high coverages of cFF(L/D), molecules appear to assemble into islands, which upon annealing to 400K bear a strong resemblance to data for ddcFF at high coverage. Examining the molecular orientation within these islands indicates that cFF(L/D) does indeed exhibit the same dehydrogenation behaviour as cFF, but yields two mirror-image species on the surface instead of one. Analysis of the conformation of cFF(L/D) in vacuo suggests that the conformation of the molecule on Cu(110) is much less selective than that of cFF, and as such generates an approximate 50:50 ratio of conformers on the surface. The dehydrogenation process then preserves this ratio to give the result observed.

The results of the cFF and cFF(L/D) experiments clearly demonstrate multiple pathways to obtaining ddcFF on a Cu(110) surface – by direct deposition, by annealing a deposition of cFF(LL), by annealing a deposition of cFF(DD), by annealing a (cold) deposition of sdcFF(LL), and by annealing a deposition of cFF(L/D). The data shows that the method chosen has a direct effect on the resultant assembly of ddcFF molecules, since although ddcFF is only prochiral, the surface chirality can effectively be selected for through the choice of the initially deposited material, which in 4 of the 5 listed cases is chiral. A generalised method for control over the chirality of a surface-prochiral molecule system is a significant goal in surface science,⁴⁻⁶ and as such the results presented here could have considerable impact if shown to be a more general feature of cyclised peptides.

6.1.4 Self-assembly of cFF(L/D) on Au(111)

The dehydrogenation reaction occurring on Cu(110) is evidently affected by the surface itself, at least in the sense of conformational selection, though it is possible the surface plays a more complex role. It was therefore deemed of great interest to study the interaction of cFF(L/D) on a less-interacting substrate, in this case Au(111). Additionally, Au(111) does not adsorb the common Cu(110) contaminants of oxygen or water under ambient conditions.⁷⁻⁸

Submonolayer depositions produced stable assemblies of large islands (often in excess of 100 x 100 nm), which could be scanned without issue unlike on Cu(110). Furthermore, impurities or contaminants did not appear as significant issues on the Au(111) surface, and the islands were imaged largely without defects. Figure 6.9 summarises the STM data for such a deposition. A clear overall trend can be seen, in that the molecules not only self-assemble exclusively into islands, but do so always in the same paired row fashion. Variations in the precise appearance of the molecular features is quite common due to changes in the tip, but there are always two 'types' of bright feature, assembled into alternating rows. A number of orientations of these islands are recorded across the surface, which do not appear to have a recognisable trend in terms of alignment with the herringbone reconstruction (and therefore the surface orientation). It is thus proposed that the molecular assembly is non-commensurate with the surface, and is not driven by specific surface binding sites as the Cu(110) assembly is.

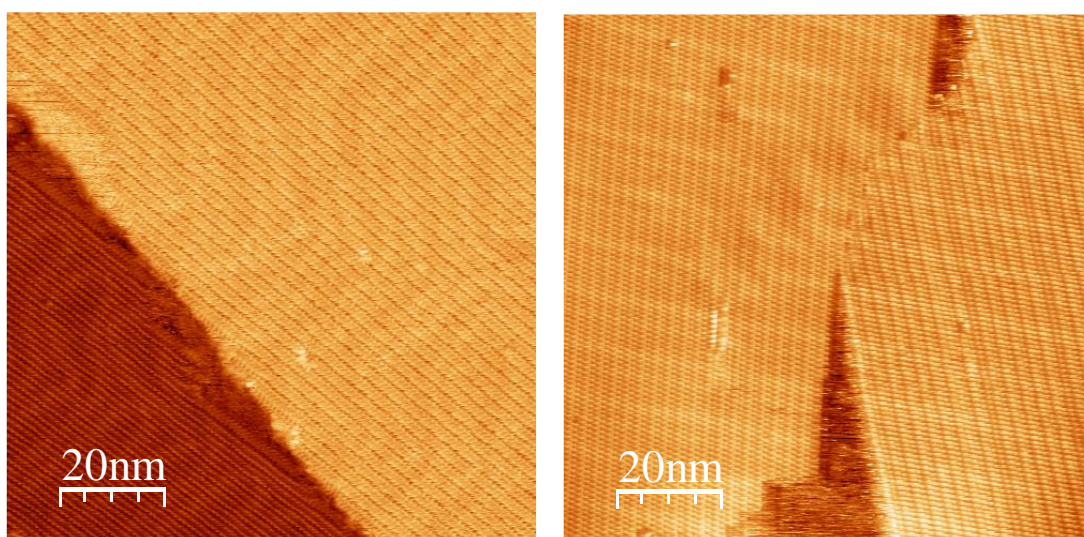


Figure 6.9. Large islands of self-assembled cFF(L/D) molecules on Au(111) oriented in various directions.

Since the molecular features were recorded with a variety of appearances, a closer analysis is essential. An example image used for such an analysis is shown in Figure 6.10. Using the shape and orientation of the bright features as a guide, models of the cyclised species cFF(L/D) can be overlain, identifying the bright features as corresponding to the phenyl side groups. In some images, such as in Figure 6.10a, a fainter feature is resolved that connects a pair of bright lobes, which is believed to correspond to the central diketopiperazine ring. As such, the molecules are described as lying alongside one another to form chains breadthways, and these chains pack together with an offset to form islands. The scaled models fit well with the recorded sizes of molecular features (1.85 ± 0.06 nm x 0.67 ± 0.01

nm) periodicity), and a potential intermolecular interaction between oxygen and an adjacent H-C bond can be identified. A formal hydrogen bond could be made between neighbouring molecules if oriented as in Figure 6.10b, but the shape of the features imaged does not well match the molecular orientation required. While an STM image alone cannot truly determine molecular structure and conformation, without complementary data a theory has to be built based on the information available. The proposed assembly pattern works well with the data across a range of island orientations and molecular appearances, but notably requires a specific conformation of the molecule on the surface. As discussed for the Cu(110) data, a surface could select for one of two mirror-image conformers, though this did not seem to occur for the relatively flat cFF(L/D) molecule (in comparison to cFF). Given that a Au(111) surface would typically have lower molecule-surface interactions than Cu(110),⁷⁻¹² it seems unlikely that only one conformation should be found here when two were observed on Cu(110). However, models of the molecule in a mirror-image conformation to that illustrated in Figure 6.10a suffer the same issue as the aforementioned attempt at creating hydrogen bonding, and do not well match the images. Therefore, it is suggested that both conformers are present on the surface, but only one may form stable assemblies at room temperature and is imaged exclusively under these conditions. While it is not apparent why this should be the case, this theory gains weight in light of a similar result for Cyclo-(Tyr-Tyr) presented in chapter 6.2 (“Self-assembly of L-Tyr-L-Tyr on metal surfaces”), which itself is supported by DFT and MD calculations.

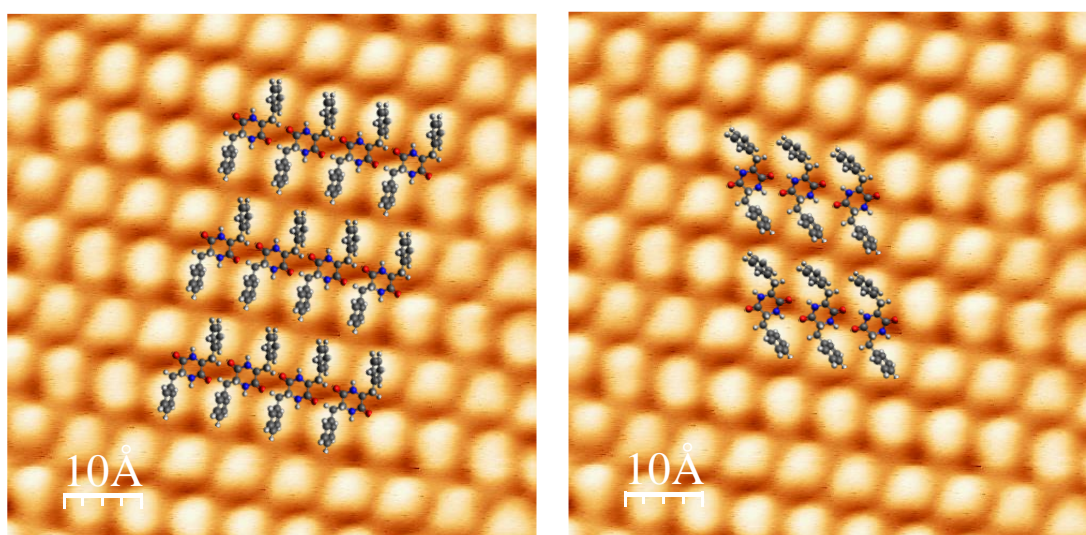


Figure 6.10. a) Proposed self-assembly model for cFF(L/D) on Au(111), b) A suggestion for how cFF molecules could theoretically hydrogen bond on Au(111), though such an assembly is a poor match for the resolved features in the STM image.

A question remains, however, as to why the molecules do not pack more closely together, possibly even interdigitating if the phenyl rings remain oriented as per the model once landed. This cannot be definitively answered by STM alone, but it can be postulated that the phenyl side groups do twist to become flatter with respect to the central ring, in order to maximise molecule-surface interactions. This would prevent interdigitation, but would be expected to cause a flatter STM profile more akin to that of ddcFF. Therefore this question remains somewhat open.

In summary, on Au(111) the cFF(L/D) molecules arrange themselves into offset chains packed into islands, but unlike ddcFF(L/D) on Cu(110), the orientation of the islands is highly variable, indicating a weaker surface registry. At present, there is not a published study of cFF on Au(111) with which to compare this result. Since the STM data could be explained well through the use of a model of cFF(L/D), it remained to be examined how the product of dehydrogenation, ddcFF(L/D) would behave on a gold surface. As such, the deposition of cFF(L/D) was annealed in an effort to bring about dehydrogenation. It was found that while annealing to 375K had no effect, further annealing to 425K largely destroyed the existing assembly, causing molecules to degrade and/or evaporate. It is concluded therefore that cFF(L/D) does not dehydrogenate on a Au(111) surface, since the activation barrier is too high relative to that of evaporation. This presents an additional contrast to the behaviour on Cu(110).

6.1.5 Concluding remarks

The study of LFDF and DFLF completes the set of stereoisomers of the FF peptide, and allows a clearer picture of the reactions and self-assembly of this molecule to emerge. Both LFDF and DFLF thermally cyclise to the same product (cFF(L/D)), which itself is a distinct molecule from cyclised LFLF and DFDF, and so three unique cases can be broadly considered. Though it was not possible to directly image cFF(L/D) on Cu(110), it could be shown that the same on-surface behaviour as for cFF occurs, in that the molecule dehydrogenates upon annealing the surface to 400K. At high coverage, the self-assembly behaviour of ddcFF(L/D) appears to be the same as that reported by Lingenfelder et al¹ and also at Warwick (chapter 5), with molecules packing into dense islands. A contrast is however seen with the experiments with cFF, as two molecular orientations are found for ddcFF(L/D) in contrast to one. It is believed that this difference arises due to the conformation of the cyclised species, with cFF(L/D)

presenting a flatter molecular geometry to the surface, and so a specific landing conformer is not selected for. It is also possible that the dehydrogenation reaction mechanism itself is the source of the selectivity, or lack thereof, rather than the initial landing of the molecules. On Au(111), cFF(L/D) molecules pack into uniform islands in various orientations, in a consistent but non-commensurate assembly. In contrast to experiments on Cu(110), annealing cFF(L/D) on Au(111) does not appear to result in dehydrogenation of the molecules, which simply degrade or evaporate from the surface once a high enough temperature is reached. Thus the behaviour of the FF dipeptide can be seen to be quite general across its stereoisomers, but quite specific with respect to the surface required to facilitate the dehydrogenation process. This on-surface transformation creates a product whose surface adsorption and assembly is intrinsically tied to the stereochemistry of the starting material, in contrast to a direct deposition of that product. This bears interesting implications for efforts to create controlled 2D assemblies from prochiral molecules.

6.1.6 References

1. M. Lingenfelder, PhD thesis, 2007, EPF Lausanne, Switzerland.
2. M. Lingenfelder, G. Tomba, G. Costantini, L. Colombi Ciacchi, A. De Vita and K. Kern, *Angew. Chem. Int. Ed.*, 2007, **46**, 4492–4495.
3. G. Tomba, M. Lingenfelder, G. Costantini, K. Kern, F. Klappenberger, J. V. Barth, L. C. Ciacchi and A. De Vita, *J. Phys. Chem. A*, 2007, **111**, 12740–12748.
4. K.-H. Ernst, *Phys. Status Solidi B*, 2012, **249**, 2057–2088.
5. R. Raval, *Chem. Soc. Rev.*, 2009, **38**, 707–721.
6. D.B. Amabilino, *Chirality at the Nanoscale*, Wiley-VCH, Weinheim, Germany, 2009.
7. B.M.W. Trapnell, *Proc. Royal Soc. Lond.*, 1953, **A218**, 566.
8. R.R. Ford and J. Pritchard, *Chem. Commun.*, 1968, 362–363.
9. J. V. Barth, G. Costantini and K. Kern, *Nature*, 2005, **437**, 671–679.
10. K. S. Mali and S. de Feyter, *Philos. Trans. R. Soc. London, Ser. A*, 2013, **371** (2000), DOI: 10.1098/rsta.2012.0304.
11. A. Kumar, K. Banerjee and P. Liljeroth, *Nanotechnology*, 2017, **28**, 082001–082046.
12. L. Sosa-Vargas, E. Kim and A. J. Attias, *Mater. Horiz.*, 2017, **4**, 570–583.

6.2 Self-assembly of L-Tyr-L-Tyr on metal surfaces

6.2.1 Background

The chemical transformations of the L-Phe-L-Phe dipeptide identified in chapter 4 and 5 have considerable potential for surface science, due to the discussed implications for stereochemical control, as well as the synthetic processes that may be bypassed via simple thermal activation. If the processes that underpin this behaviour, thus far unreported in the literature, could be more deeply understood or found to be more general, the impact of these discoveries could be even broader. A logical starting point would be to explore other short peptides with a similar structure and functionality to L-Phe-L-Phe. The sublimation data in chapter 4 already indicates that cyclisation is not general to all short peptides, though the list of molecules studied is far from exhaustive. Additionally, a small number of peptides have already been studied by STM (chapter 1.5), including Ala-Ala,¹ Gly-Pro-Glu²⁻⁴ and Lys-Phe-Phe-Glu.⁵ In these literary reports, there is not an explicit recognition that a chemical change other than fragmentation might occur during sublimation, and as such the possibility that a modified species might deposit on a surface is not addressed. Therefore, the data presented does not prove that cyclisation is not possible for these molecules. Furthermore, the potential for an on-surface thermal transformation, similar to that of cFF, is not considered. However, analysis of the data under the assumption of linear, intact molecules did provide logical and reasonable conclusions, which would suggest neither cyclisation nor dehydrogenation had occurred.

In order to explore how widespread the reactions of Phe-Phe might be, the most logical approach is to use another dipeptide that is as closely related in structure as possible, which is easily identified as L-Tyr-L-Tyr (YY) and its diketopiperazine (DKP) analogue, Cyclo-(L-Tyr-L-Tyr) (or cYY) (see Figure 6.2.1). L-Tyr-L-Tyr is structurally identical to L-Phe-L-Phe

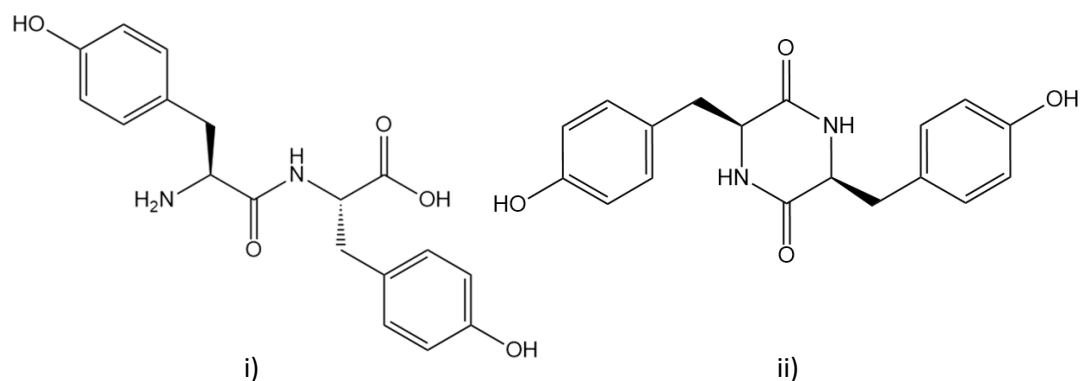


Figure 6.2.1. Molecular structures of i) L-Tyr-L-Tyr, and ii) Cyclo-(L-Tyr-L-Tyr).

apart from the addition of a para-substituted alcohol group on each benzene ring in the side chains.

In this chapter, first the sublimation of L-Tyr-L-Tyr is investigated, and then its deposition on to Cu(110) and Au(111) surfaces and study by STM. The data suggested similar behaviour to L-Phe-L-Phe, with thermal cyclisation occurring in the OMBE crucible, and chain formation post-deposition on to Cu(110). Annealing experiments resulted in an analogous transformation of the molecule and resultant assembly due to dehydrogenation, with a modified assembly pattern as a result of the hydroxy groups present in each Tyr residue. Data for the Au(111) deposition also bears resemblance to the experiments on Cu(110), featuring a major change in the self-assembly following surface annealing. Of particular interest on Au(111) is evidence for an adatom-mediated assembly, which has so far not been observed in the literature without molecular deprotonation or the use of thiols. These conclusions are supported by extensive DFT and MD simulations, as well as C 1s, N 1s and O 1s XPS data for a deposition on Au(111).

6.2.2 Sublimation of L-Tyr-L-Tyr

L-Tyr-L-Tyr was sublimed in HV conditions on to a glass substrate, and the resulting film dissolved and tested by ESI mass spectrometry in methanol, as described in chapter 2.2.2. The sublimation temperature used was 515K. The resulting mass spectrum (Figure 6.2.2) conclusively proved that YY cyclises upon sublimation, in the same fashion as L-Phe-L-Phe⁶ (see also chapter 4, “The sublimation of short peptides”). The largest peak observed was at

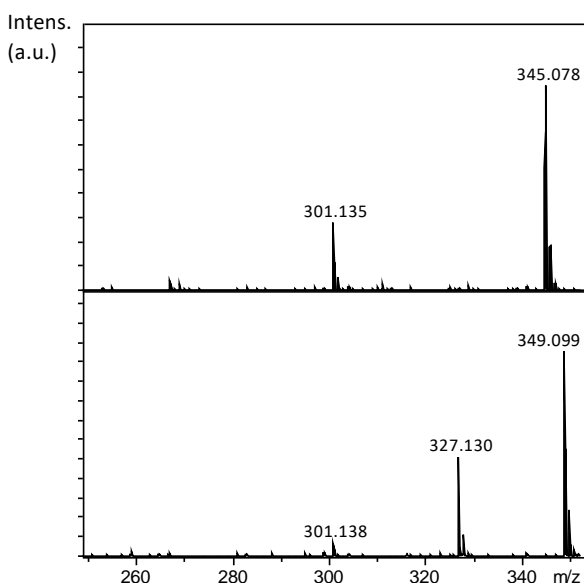


Figure 6.2.2. Mass spectra of [top] non-sublimed L-Tyr-L-Tyr and [bottom] L-Tyr-L-Tyr sublimed at 515K. Molecular ion occurs at $\sim m/z$ 345.

m/z 349.1, which is 4 Da above the expected protonated molecular ion peak for YY at 345.1. An additional peak is seen at m/z 327.1, 18 Da below the molecular ion. As for FF, there is no sensible adduct to YY that could account for a mass difference of 4, and so the molecule has clearly undergone a chemical transformation. The best fit for the mass difference is a loss of water due to cyclisation (-18 m/z , giving the m/z 327.1 peak) followed by the coordination of a sodium ion in place of a proton (+22 m/z). This conclusion is supported by extensive evidence of cyclisation for FF which, as already mentioned, is a structurally highly similar molecule to YY. Since the molecular ion peak for YY is also not observed at all, it is apparent that complete cyclisation of the sample has occurred, and any deposition for STM or XPS sample preparation should give an adlayer entirely composed of cYY. The final peak at 301.1, found in both pristine and sublimed YY, is the result of a common plasticiser.

Therefore, since the deposition of cYY was anticipated as the main outcome of any OMBE experiment, a crucible of molecules was first intentionally cyclised to cYY by heating, thus ensuring the deposited material is free from any residual linear YY.

6.2.3 Self-assembly of Cyclo-(L-Tyr-L-Tyr) on Gold (111): Scanning Tunnelling Microscopy

A submonolayer deposition of cYY at room temperature on Au(111) yielded STM data as exemplified in Figure 6.2.3. The molecules are imaged exclusively within ordered islands, often in excess of 100 x 100 nm in size, and occasionally in disordered regions on the edges

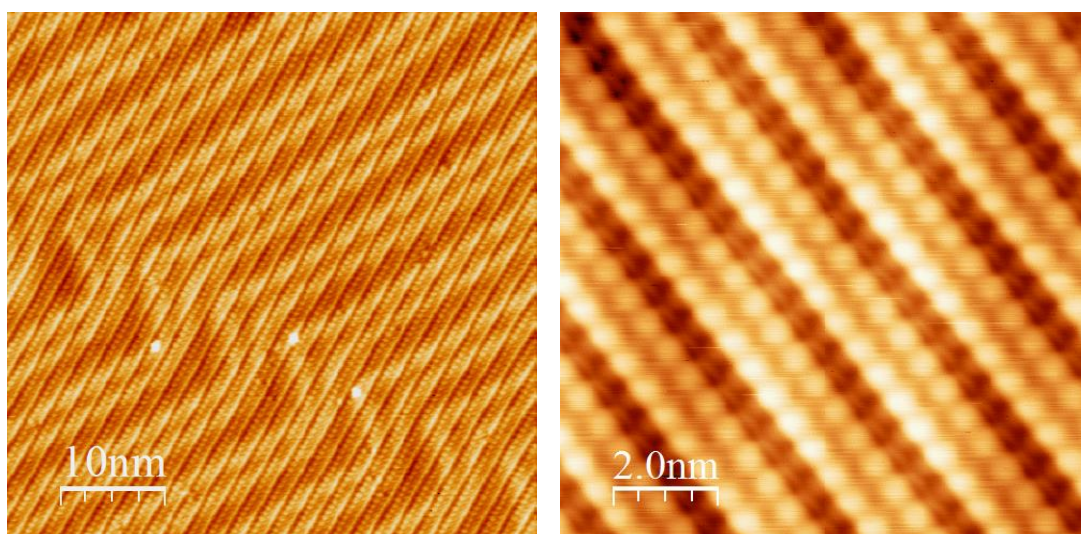


Figure 6.2.3. Typical STM images from a deposition of cYY on Au(111). Molecules are only imaged within ordered islands such as these, in a range of orientations across the surface.

of these islands. When not stabilised in two dimensions by intermolecular forces, the molecules are highly mobile across the gold surface and cannot be imaged at room temperature. This is illustrated in Figure 6.2.4, where molecules are observed constantly adding to and leaving from an island edge, demonstrated here across a time period of 180s. Such behaviour is evidence of a weak interaction between the cYY and the surface, resulting in a relatively flat adsorption potential energy surface such that molecular diffusion has a low activation barrier. Within each island, the molecular orientation and appearance is uniform (though a number of orientations are observed across the whole surface, see Figure 6.2.5). The average periodicity of the molecules is 0.63 ± 0.01 nm in the direction of the chain growth (“breadthways”) and 1.84 ± 0.09 nm perpendicular to the chains (“lengthways”), across all 3 major island orientations. A degree of submolecular resolution is found, with what appears to be the phenol groups in the side chains imaged as bright protrusions relative to the central diketopiperazine ring. Data from island edges confirmed that the bright protrusions are the ‘edge’ of the molecules when ordered in this fashion. The bright protrusions are not of uniform intensity, which is partly explained by the effect of the underlying herringbone reconstruction, but could also reflect a small difference in height due to the molecular conformation.

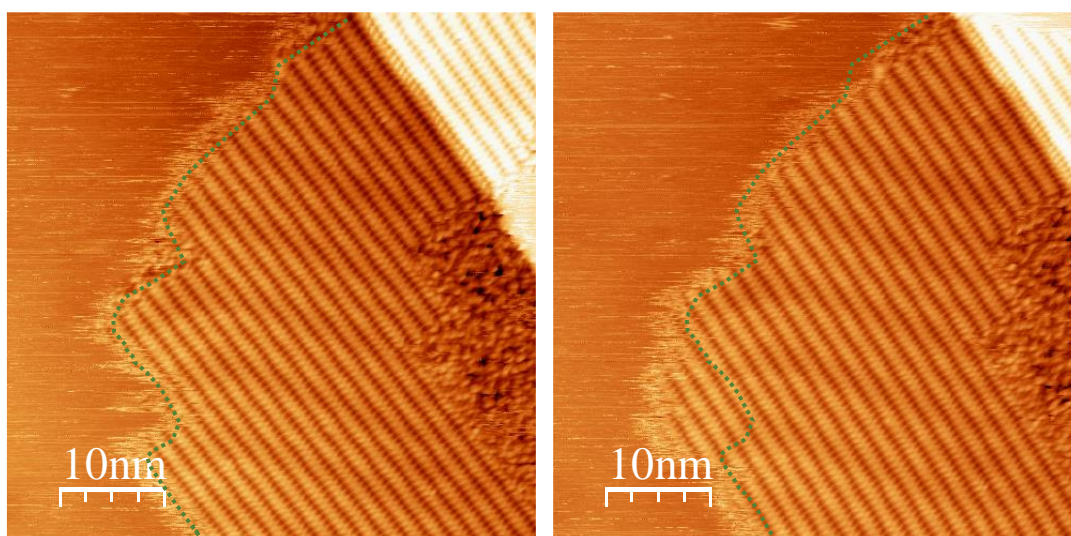


Figure 6.2.4. Sequential STM images of cYY on Au(111), with a time difference of approximately 180s. The outline of the original island in green illustrates the change that occurs between the two images.

As mentioned, different orientations for chains within the islands were observed across the surface. Using the herringbone reconstruction of the Au(111) surface as an indicator of the principal surface directions ($[1\bar{1}0]$, $[01\bar{1}]$ and $[\bar{1}01]$), it is possible to perform a statistical

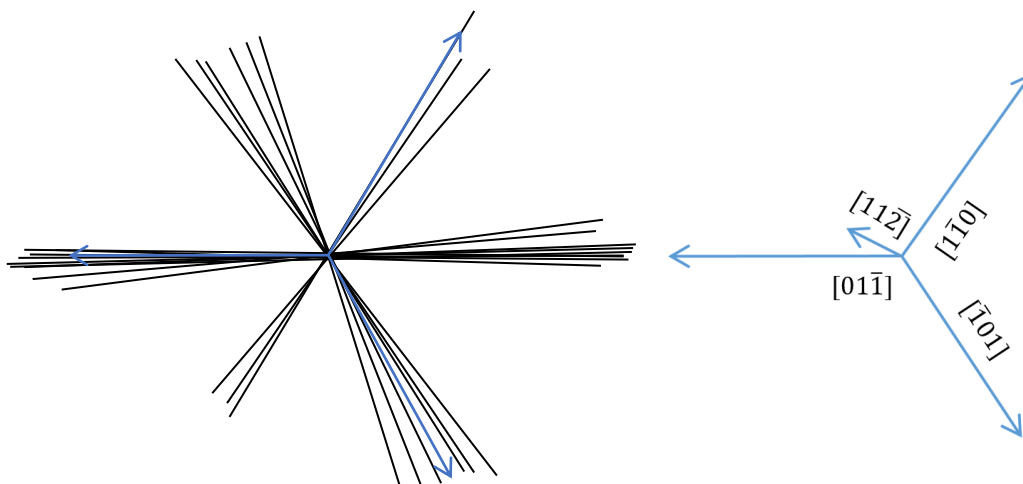


Figure 6.2.5. Sampling the orientation of recorded islands, and plotting against the three surface orientations of the Au(111) surface underneath. The long axis of the gold herringbone, $[11\bar{2}]$, is also indicated.

analysis of the alignment of the molecular chains/islands with respect to these axes. A summary of such an analysis is presented in Figure 6.2.5. It is clear that the vast majority of islands grow at angles very close to the primary surface directions, with a small variation of $\pm 10^\circ$ or less, which can most likely be attributed to artefacts of the imaging process such as thermal drift and scanner creep. This indicates that the molecule-surface interaction is substantial enough to influence the self-assembly pattern, although evidently not so significant as to inhibit the high mobility of the molecules on the surface at room temperature. This particular aspect of the assembly is in fact quite common for molecular species adsorbed on metal surfaces.⁷ Additionally, while the surface axes seem to guide the island growth directions, the herringbone reconstruction itself does not directly perturb the assembly, and periodicity statistics remain consistent across a range of local environments. A small number of islands did not appear to have grown along the surface directions at all (approximately 60° deviation), though these were all imaged in the same macroscopic region within a single day, and as such represent a minor anomaly rather than a more general growth pattern. Since this occurrence was rare and seemingly localised, it is proposed that these islands represent a disfavoured assembly, the product of nucleation at a defect or grain boundary. It is possible that once an island is seeded at such a site, it continues to grow in the same direction even over a change in surface orientation. Such changes are more common on a gold on mica substrate than a single crystal, with the average grain size being on the order of 5 to $10\mu\text{m}$.

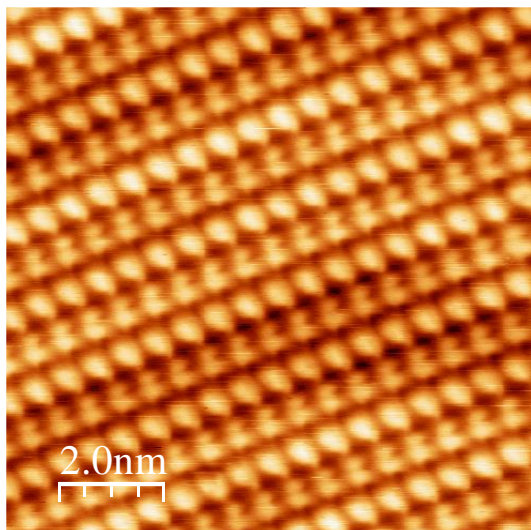


Figure 6.2.6. A unique phase of cYY molecules self-assembled on Au(111). The lateral packing of chains is noticeably denser than the vast majority of data, as exemplified in Figure 6.2.3.

An even rarer case in the self-assembly of cYY was a more densely packed phase, with a near identical breadthways periodicity (0.62 nm) but shorter lengthways periodicity (1.56 nm), as shown in Figure 6.2.6. This island was the only one of its kind recorded, and appears to show a case where the cYY molecules can sit closer to one another than in the dominant islands imaged. However, while a denser packing of the molecules is possible, it is evidently strongly disfavoured in comparison to the predominant self-assembly motif. The fact that the wider-spaced chains are preferred suggests that more than simple intermolecular interactions must be involved in stabilising this phase, as this would typically give rise to very compact islands. The origin of the observed spacing is investigated further below.

A model for the molecular conformation and self-assembly pattern of the major island types can be proposed, as detailed in Figure 6.2.7, through the use of the averaged periodicity measurements and several key observations. Firstly, the appearance of the central diketopiperazine ring as a relatively dark feature could be evidence of the overall molecular conformation, or it could arise from the electron density of the aromatic systems in the phenol groups. However, the apparent C_{2v} symmetry of each molecular feature can help provide insight into its conformation, as can the preferred positions of nearest neighbours. Each molecule lies alongside its nearest neighbour with no offset, forming a straight chain in the breadthways direction. In the lengthways direction, neighbouring molecules are offset by half a molecular width, creating an AB staggered pattern of the chains within the islands. Finally, the proposed conformation in Figure 6.2.7 was inspired by a number of studies into cyclic peptides⁸⁻²⁰ (see also chapter 2.2.4), and energetically minimised using the Avogadro software.

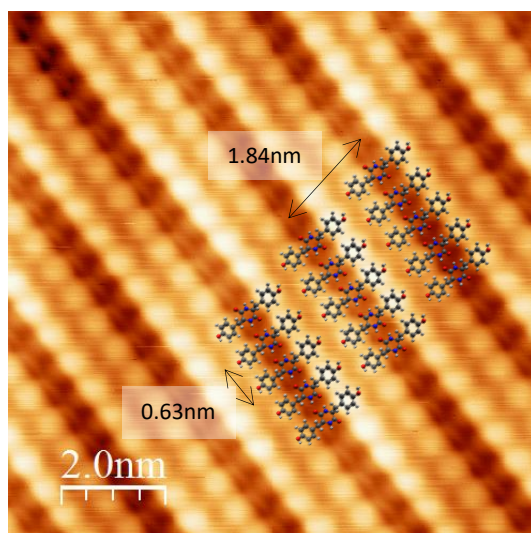


Figure 6.2.7. Models of cYY overlaid on to the self-assembly pattern on Au(111), with key dimensions labelled. The gap between adjacent offset chains of molecules is apparent.

Assuming the molecular conformation as proposed (or one similar), the central ring of each cYY sits on the surface in such a way that N-H and C=O groups on adjacent molecules come into close proximity, permitting a total of four hydrogen bonds per molecule (see Figure 6.2.8). This provides a substantial energetic benefit to 1D aggregation, and explains the stability of a chain-type assembly despite the intrinsic mobility of cYY on Au(111). In the second, lengthways, direction however, the measured periodicity of 1.84 nm is larger than might be expected based on, for example, a hydrogen bonding model, and translates in the model as a 0.33 nm separation between the hydroxyl groups of the neighbouring molecules. This distance is at the extreme limit of recorded hydrogen bonds,²¹⁻²³ and it seems unlikely that such an interaction drives the assembly in this direction, as the molecules could simply pack closer for stronger hydrogen bonding. It is not immediately clear why such a gap exists

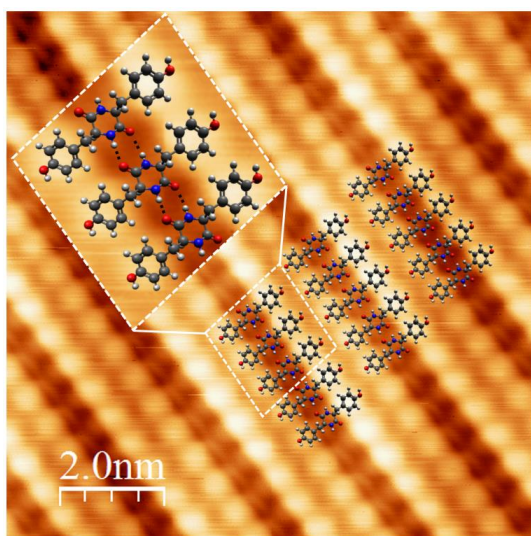


Figure 6.2.8. Enlarged view of the assembly of cYY on Au(111). Potential hydrogen bonding is indicated with black dashed lines. Inset image is approximately 2 nm x 2 nm.

between the molecules, other than perhaps an enforced commensurability with the substrate below, or a small repulsive force preventing perfect aggregation.^{24,25} The former argument did not hold weight upon further investigation, while the latter would require the presence or formation of a charge or dipole, which there is not direct evidence for here. In many cases, intermolecular repulsions on surfaces lead to more substantial separation of 1D chains.²⁴ An alternative hypothesis is that the hydroxyl groups on the phenol rings are bonding to gold adatoms, with the AB offset providing the most efficient packing and coordination of each adatom. This would be highly unusual on a Au(111) surface, where adatom-mediated assemblies are rare^{26,27} without deprotonation, or in the case of molecular species that bind more strongly to gold atoms, such as thiols.²⁸⁻³⁰ The possibility of adatom coordination, with or without deprotonation, is explored further through the use of XPS data, DFT calculation, and MD simulations in subsequent sections (6.2.4 and 6.2.5).

In some cases, the molecules are imaged with a different contrast to the above description, whereby the central ring becomes even less prominent and the phenol rings display slight changes in appearance. The overall symmetry of the cYY is maintained however, and the periodicity of each assembly is always the same within a small statistical error (1.84 ± 0.09 nm). It is therefore straightforward to attribute these differing appearances to effects of the tip, whose condition changes particularly frequently when scanning molecules that are mobile on the surface in question. Indeed, in some situations there was even a change in contrast of the molecules mid-scan, which is clear proof that the effect is not based in a chemical change of the molecules.

An additional important consideration about the conformation of the cYY molecules is their orientation as they land on the surface from the molecular beam. Since cYY is a chiral molecule, the conformation used in Figures 6.2.7 and 6.2.8 is not identical to a conformer that is flipped relative to the surface, i.e. rotated about an axis parallel to the surface, as demonstrated in Figure 6.2.9. The number of atom-surface interactions for an adsorbed molecule that would need to be broken simultaneously to bring about a complete flip of the molecule creates a prohibitively large energy barrier for the process, thus creating two surface conformers that are distinct and cannot interconvert. These can be considered as the “up” and “down” conformers depending on the height of the central ring with respect to the gold surface (see Figure 6.2.9). The model used in Figure 6.2.7 uses molecules all in a single landing orientation (“down”) based on the fact this conformer best fit the images, including the facility for hydrogen bonding. If the model is correct, it may be the case that a

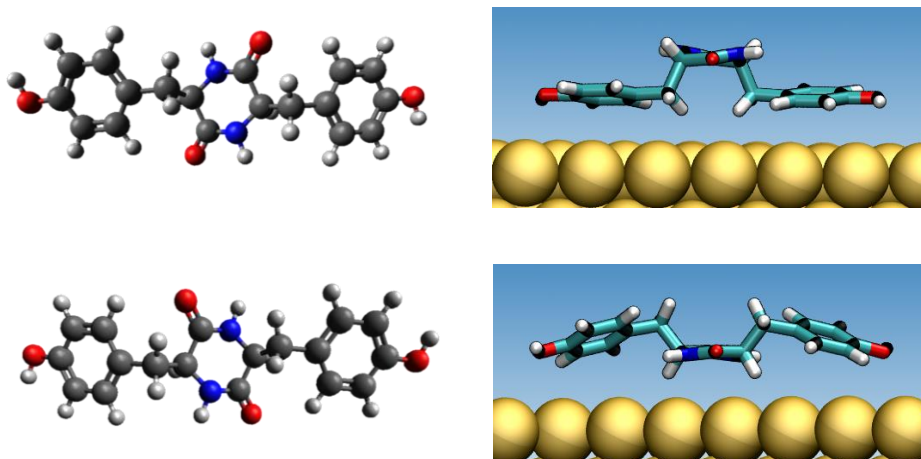


Figure 6.2.9. Top-down view of mirror-image models of cYY, alongside potential landing conformations on the surface (adapted from DFT, see Figure 6.2.10). The non-equivalent nature of these “flipped” conformers with respect to the surface is apparent.

particular landing orientation for the molecule is favoured by the surface, and as such a form of selection is imposed. DFT calculations and MD simulations were used to assess the validity of this model and resultant conclusion.

6.2.4 Self-assembly of Cyclo-(L-Tyr-L-Tyr) on Gold (111): Density Functional Theory and Molecular Dynamics

Computational work on the self-assembly of cYY on Au(111) was composed of two main parts: DFT geometry optimisations and energy calculations, to provide precise thermodynamic information about single molecule and dimer conformations; and MD simulations of clusters of molecules to simulate the self-assembly process, with and without adatom involvement. Plane-wave DFT calculations were performed using the revPBE-vdW-DF functional, which has previously been used to determine the adsorption energy of non-covalently adsorbed molecules to the Au(111) surface, with close agreement with experiment.³¹⁻³⁸ The gold surface was modelled as an as cut (111) slab four atomic layers thick, with a surface area scaled depending on the size of the system so as to minimise adsorbate-adsorbate interactions. MD simulations used the GoIP-CHARMM force field, a polarisable force field specifically designed for use with peptides and proteins at gold interfaces.³⁹ The value of this force field was reinforced by extensive comparison of data outputs with DFT, exemplified in Figure 6.2.10. A close match for the results of DFT on the single-molecule and dimer scale allowed the larger MD simulations cells to be analysed

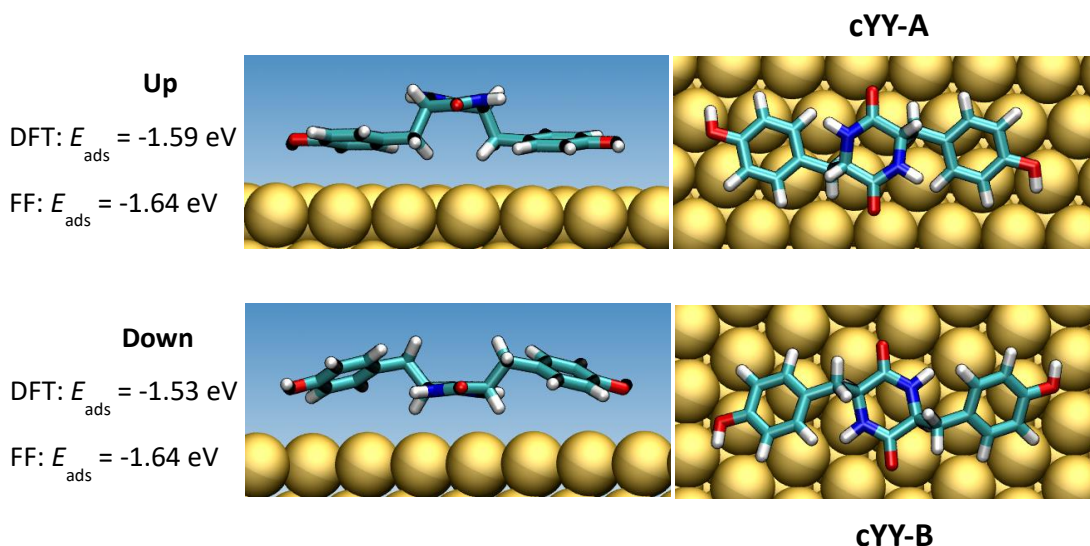


Figure 6.2.10. A comparison of the two landing conformations of cYY on Au(111). The adsorption of the “up” and “down” conformations are modelled, giving rise to the on-surface conformers “A” and “B”. The results of energy minimisation calculations by both DFT and the GoIP-CHARMM Force Field (FF) are also shown.

with greater confidence. Typically, groups of molecules were defined and simulated for 10ns, using periodic boundary conditions, on a gold slab five atomic layers thick.

From a range of conformational inputs, DFT geometry optimisations readily identified two principal surface conformers for the cYY molecule, which correspond to the up and down conformers previously described. Once adsorbed to the surface, the conformation of these species adapts in order to maximise intermolecular interactions and minimise the overall energy adsorption energy. The resulting similar but new conformers are henceforth referred to as cYY-A (originally from the up conformer) and cYY-B (originally from the down conformer), as illustrated in Figure 6.2.10). A smooth potential energy surface across the gold interface is found, with adsorption site having little effect on the adsorption energy of a molecule, which indicates that the surface registry is not influential on the self-assembly process. The adsorption energy calculations show that the two modes of binding to the surface are almost isoenergetic (a difference of only 0.06eV in the DFT), which would indicate they should be represented equally on the surface experimentally. Further calculations on dimers of each conformer were carried out, as illustrated in Figure 6.2.11 (larger scale calculations of chains were, at present, of computational expense beyond the scope of the project). These calculations also indicate that the formation of dimeric hydrogen bonds is favoured for both surface conformers, which by extension suggests that longer chains can indeed be formed. These results appear to be in contrast to the STM data obtained. While it is possible that both conformers have the same appearance in the STM,

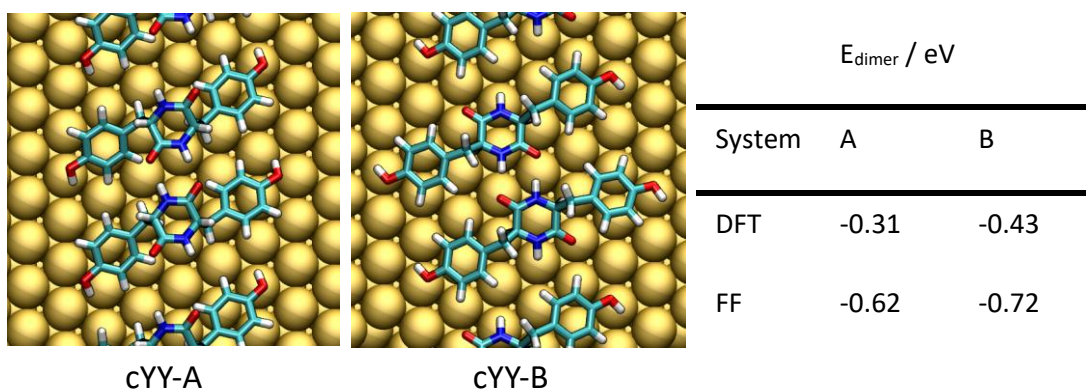


Figure 6.2.11. DFT Models of dimers of cYY in both surface conformations, to evaluate the energy gain from hydrogen bond formation. While DFT and FF energy calculations differ from one another, the overall result clearly indicates both species should form stable on-surface hydrogen bonds, cYY-B slightly more favourably.

this seems highly unlikely, especially considering the differences in molecular shape and topography between the up and down models. However, information on the larger scale self-assembly from MD simulations can provide an explanation for this apparent dichotomy between STM data and DFT.

Clusters of sixteen molecules were simulated by MD for both the A and B configurations, at temperatures of 300K and 450K. In all cases, the molecules were pre-ordered in a fashion similar to the proposed model from STM, and their dynamics observed over time to determine the stability of the assemblies and whether they began to grow. The assembly of cYY-B molecules was stable at 300K and 450K, and the chains also began to grow in the same direction as observed in the STM data. On the other hand, the cYY-A assembly was unstable at 450K, with the chains falling apart into more randomised molecular orientations. Furthermore, at 300K the chains even showed some growth perpendicular to the chain direction seen with the STM. Therefore, while cYY-A and B are both stable conformers of the isolated molecule on Au(111), MD simulations indicate only cYY-B, the “down” conformer, forms stable islands comparable to experimental data. Additionally, the simulations at elevated temperatures indicated a small number of molecules were able to flip over, meaning a switch between the A and B conformers occurs under these conditions, despite the surface pinning effect. This provides a mechanism by which surface conformers can interconvert, removing the requirement for a preferential landing conformer in the explanation of the STM data. This will bear a strong relevance to the experimental data for the annealed, dehydrogenated molecule in (section 6.2.6). These results help to resolve the apparent differences between theory and experiment. Both conformers may indeed land on

the surface, but only one is stably imaged at room temperature, a theory which also gains further traction in light of subsequent data on the annealed cYY.

A statistical analysis of the MD simulations provides a quantitative comparison of the self-assembly models with the STM data (Figure 6.2.12). For this purpose, we employed 2-dimensional radial distribution function ($g(r)$) calculations, which in essence output the probability of finding a molecule (or “particle”) at distance “ r ” from a given molecule. These calculations involve plotting the distances of all possible molecule pairs into a histogram, before normalising this histogram with respect to a model fluid. In this way, meaningful intermolecular distances are readily identified. The values on the x-axis of the graph in Figure 6.2.12 indicate the distances between a given point in a molecule and the next occurrence of the same point in any direction. The radial distribution function can be used directly to compare to the average experimental periodicities established by STM. The shortest distance at which a peak is found in the $g(r)$ corresponds to the nearest neighbour

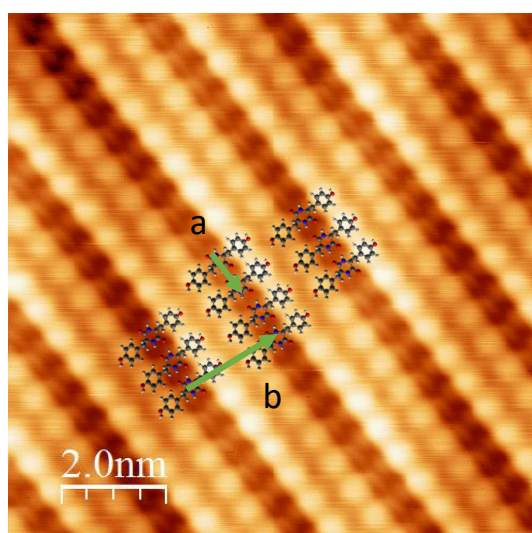
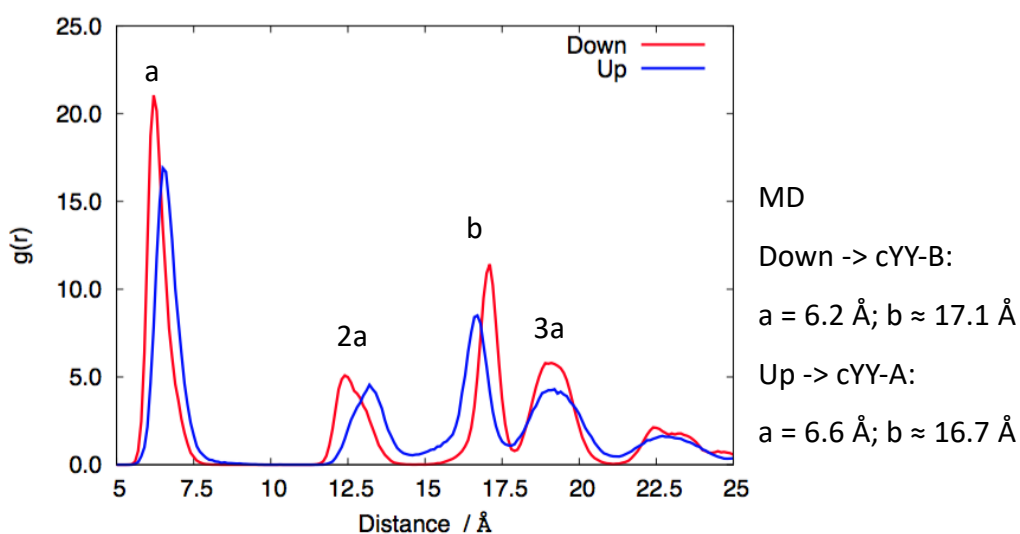


Figure 6.2.12. Comparison of experimental cYY periodicity data with values obtained from a radial distribution function performed on MD simulations.

STM

$$a = 6.3\text{\AA} \text{ (st. dev. } 0.14)$$

$$b = 18.4\text{\AA} \text{ (st. dev. } 0.92)$$



separation in the direction of the chain growth. The next $g(r)$ peak is in fact due to the next nearest neighbour in the same direction, due to the function's search for the same point within a molecule. The third peak represents the nearest neighbours separation in the lengthways direction of the molecule. From these distances, it is again apparent that cYY-B, from the "down" configuration, creates a better reproduction of the islands recorded by experiment, since there is a very close match for the periodicity in the chain direction. However, neither cYY-A or B reproduce the separation in the perpendicular (or lengthways) direction, instead yielding distances approximately 10% shorter. This indicates that simple hydrogen-bonding and van der Waals forces cannot be solely responsible for the experimentally observed longer periodicity as, with only such interactions involved, the molecules tend towards a closer packing density. Therefore, DFT and MD were also used to evaluate the possibility repulsive interactions mediate the assembly, as a result of alcohol group deprotonation, or that adatom coordination is responsible for the increased molecular separation, with or without a deprotonation occurring.

A two-part computational study was thus employed to evaluate these theories. The first step consisted of exploratory MD simulations, again using a sixteen molecule pre-ordered set, to observe the changes that might be caused to the self-assembly pattern by alcohol group deprotonation. Two scenarios were considered, both involving deprotonation, but one with residual charge localised on the molecules while the other featured neutral molecules (Figure 6.2.13).

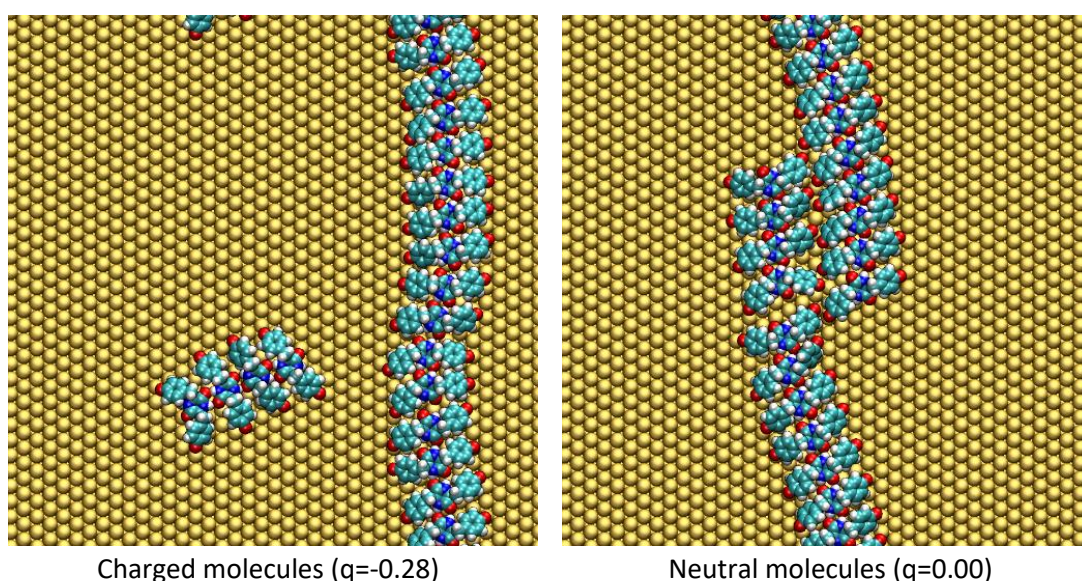


Figure 6.2.13. Images obtained from MD simulations of charged and neutral deprotonated cYY molecules in chains on Au(111). The results cannot reproduce the STM data, but do demonstrate the repulsion between, but not within, charged molecular chains.

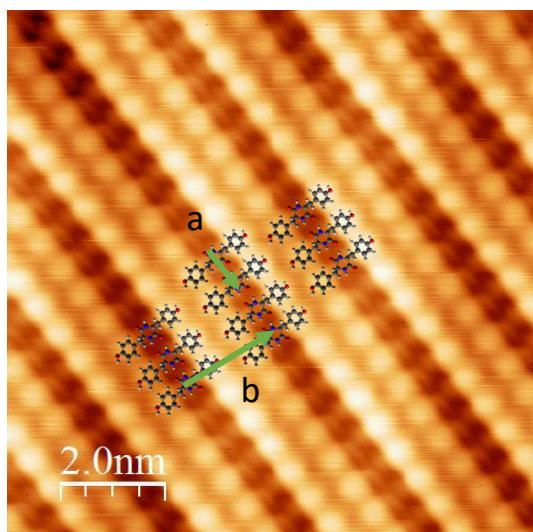
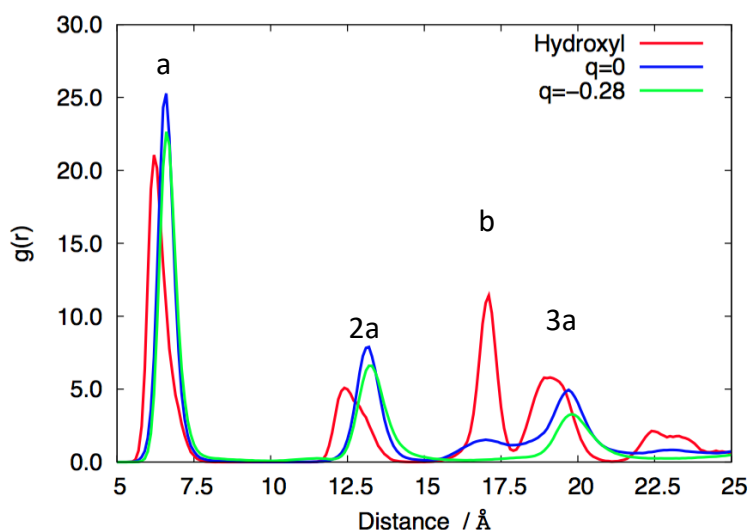


Figure 6.2.14. Comparison of experimental cYY periodicity data with a radial distribution function of MD simulations of molecules in different charge states.

STM

$$a = 6.3 \text{ \AA} \text{ (st. dev. 0.14)}$$

$$b = 18.4 \text{ \AA} \text{ (st. dev. 0.92)}$$



MD

Hydroxyl:

$$a = 6.2 \text{ \AA}; b \approx 17.1 \text{ \AA}$$

$$q = 0.0:$$

$$a = 6.6 \text{ \AA}; b \approx 17 \text{ \AA}$$

$$q = -0.28:$$

$$a = 6.6 \text{ \AA}; b = \text{N/A}$$

The negatively charged species only formed isolated chains, indicating that repulsive energy terms do indeed force chains apart, though the effect here is evidently too large to match the experimental data. Similarly, these results show that even deprotonation without considering charge effects does not explain the assembly behaviour of cYY, since the chains remain close together. An analysis of the radial distribution function supports this analysis (Figure 6.2.14), as there is no noticeable improvement in the spacing of the chains compared to experiment.

The second part of evaluating the deprotonation model was to employ DFT to infer whether a deprotonation of a cYY molecule, and subsequent coordination to two Au adatoms, was thermodynamically favourable. A supercell was created that included two adatoms and a single cYY molecule, either with the alcohol protons detached (and adsorbed at a favourable Au surface site) or in the normal state bonded to oxygen (see

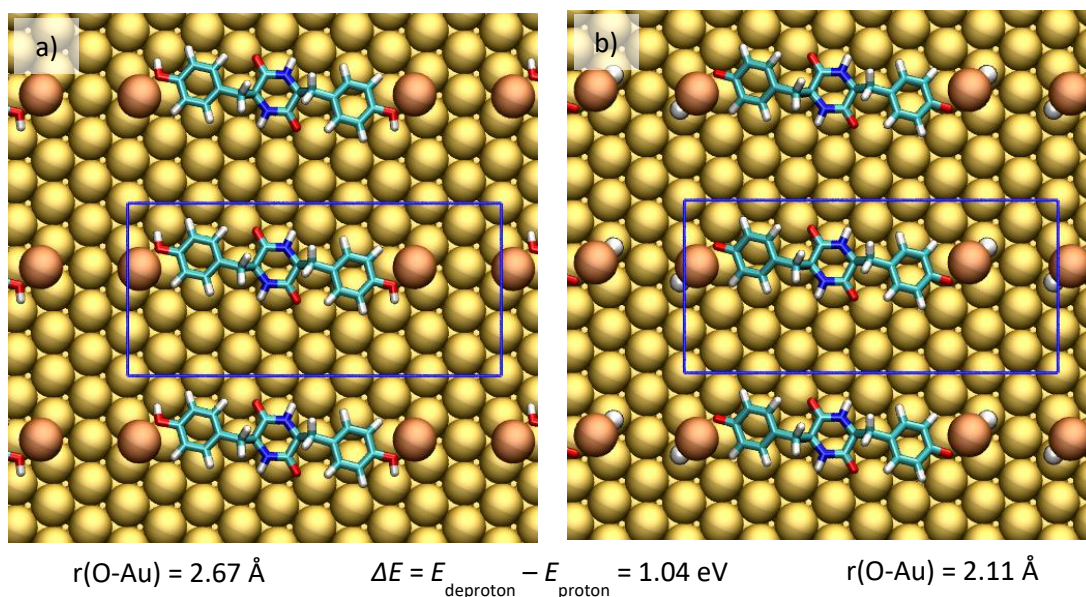


Figure 6.2.15. DFT models of a single cYY molecule on Au(111), with two gold adatoms. a) An unmodified, protonated cYY molecule. b) A doubly deprotonated molecule, with H atoms bonded independently to the adatoms. The energy minima of these systems were used to calculate the displayed energy cost of the on-surface deprotonation.

Figure 6.2.15). Both species were capable of bonding with the adatoms via the oxygen atoms of the alkoxy groups, though the O-Au distance was shorter for the deprotonated system suggesting a stronger interaction. Any difference in energy between these two bonds is however not sufficient to compensate for the loss of an O-H bond, as the overall minimised energy for each system puts the deprotonated case 1.04eV higher in energy. This is a substantial disparity and, as such, it is highly unlikely that the cYY molecules deprotonate in order to coordinate with adatoms. Nevertheless, it remains a possibility that adatoms are involved in the self-assembly of cYY without deprotonation occurring.

The final conclusion of the DFT and MD is that the self-assembly pattern observed in the STM can be explained as a product of cYY molecules in a single specific conformation lying alongside one another for optimal hydrogen bonding interactions, with the separation of the resultant chains most likely the product of bonding between gold adatoms and hydroxy groups in the cYY side groups, which do not deprotonate under the conditions employed for the STM experiments.

6.2.5 Self-assembly of Cyclo-(L-Tyr-L-Tyr) on Gold (111): X-Ray Photoelectron Spectroscopy

Using the same preparation methods as for the STM data, cYY was deposited on a Au(111) single crystal. As discussed in chapter 2 (“Experimental”), the XPS experiments presented in this chapter were calibrated with respect to the substrate Au $4f_{7/2}$ peak at binding energy 84.0eV.⁴⁰ A Shirley-type background subtraction was applied across all the peaks, with fittings performed by using a combination of Gaussian and Lorentzian functions, typically the GL(30) mix.

In order to support the conclusion of the simulations, it was important to discover whether any evidence for deprotonation of the cYY could be found. The position of the peaks in the O 1s spectrum is the most reliable way to assess this possibility, because a substantial shift in binding energy is anticipated between signals for an OH group and the deprotonated O⁻.⁴⁰ The O 1s spectrum of a protonated cYY should yield two peaks, one representing the carbonyl oxygens at approximately 531.1eV⁴¹⁻⁴³ and another for the phenolic oxygens at approximately 532.7eV,^{41,44} theoretically of equal area due to the 1:1 stoichiometric ratio. Deprotonation of the alcohol groups would cause a reduction in the C-OH peak and the growing in of a C-O⁻ peak at lower binding energy, which would very likely overlap with the C=O signal. Due to the highly regular self-assembly displayed by cYY and the inherent symmetry of the molecule, it would be logical to assume that if one phenol group can deprotonate, then both can do so. Therefore, a deprotonated system could even appear as a single peak, centred on 531.1eV. The XPS data gathered for cYY are summarised in Figure 6.2.16. Deviation from the deprotonation scenario is immediately apparent, as there are two significant peaks with a 1.4eV separation in the O 1s spectrum, though they are not well resolved from one another, which is possibly indicative of a smaller third peak between them. Models for two and three peaks within the spectrum were made, and although a 2-peak fit (as in Figure 6.2.16) works well, a 3-peak fit also seems viable. However, if the areas under the three peak set are restricted so that the C=O signal is equal to the sum of the other two, thus enforcing the known stoichiometry, the fit becomes substantially worse. This suggests that, if a third peak is present, it is not due to a deprotonation effect. Overall the O 1s data set refutes the notion that the alcohol groups deprotonate, as the observed spectrum of two major peaks of similar size is a reasonable match for protonated cYY, and conversely a poor match for deprotonated molecules. Using a two-peak fit, the signal for C=O is centred at 531.3eV, and the signal for C-OH at 532.7eV. These values are in good agreement with

those reported in the literature,^{20,41-44} with particular attention drawn to studies of other cyclic peptides.^{20,42,43}

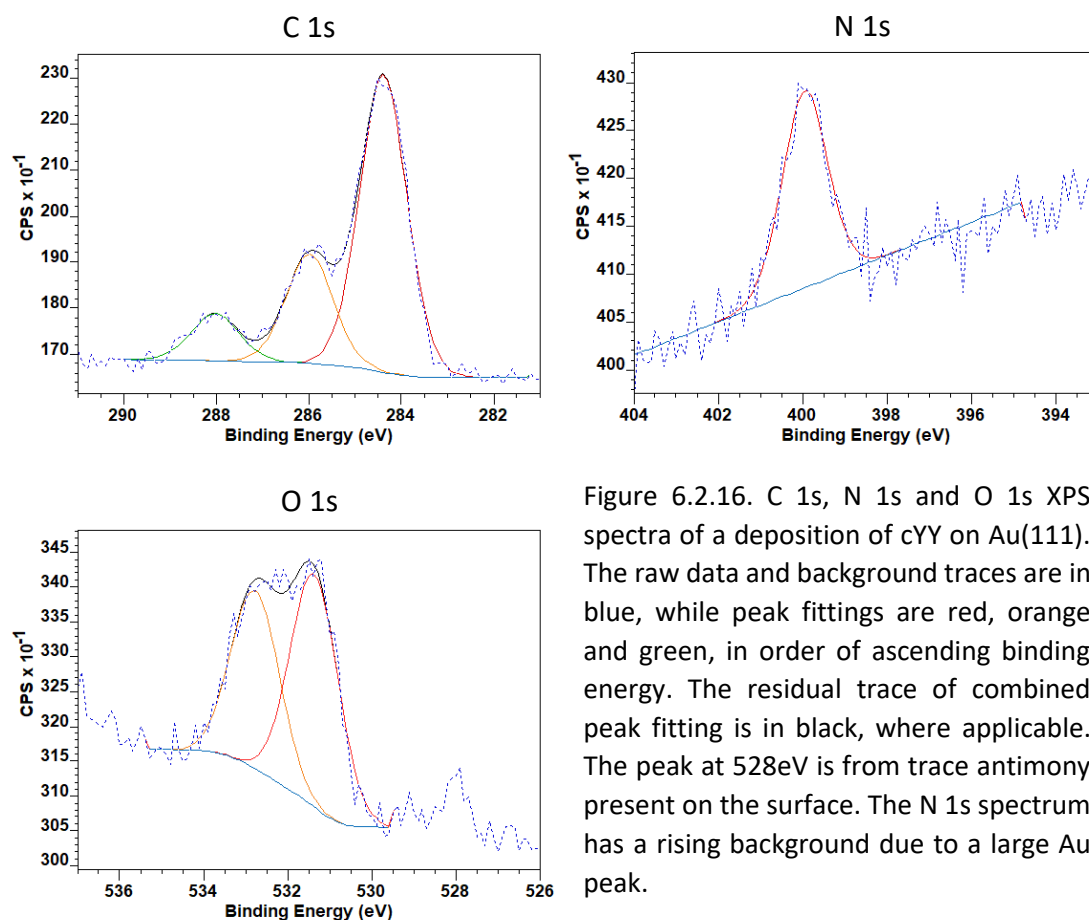


Figure 6.2.16. C 1s, N 1s and O 1s XPS spectra of a deposition of cYY on Au(111). The raw data and background traces are in blue, while peak fittings are red, orange and green, in order of ascending binding energy. The residual trace of combined peak fitting is in black, where applicable. The peak at 528eV is from trace antimony present on the surface. The N 1s spectrum has a rising background due to a large Au peak.

The C 1s and N 1s spectra, also presented in Figure 6.2.16, are simpler to interpret but of less direct bearing on the protonation state of the molecule. Thus, these spectra act as a confirmation that the cyclic molecule has indeed been deposited, enabling further confidence in conclusions drawn from the O 1s data, but cannot directly identify alcohol deprotonation. The C 1s spectrum contains three distinct peaks, at 284.4eV, 286.0eV and 288.0 eV. The largest peak by a considerable margin is at the lowest binding energy of 284.4eV, and must arise from aliphatic and aromatic carbons that are not bound to heteroatoms.^{40,41,45} The smallest peak, at the highest binding energy of 288.0eV, corresponds to carbon signals strongly shifted by a carbon-oxygen double bond in the diketopiperazine ring.^{40,45} The intermediate peak at 286.0eV represents the remaining carbon atoms, those adjacent to heteroatoms but not forming double bonds, and so with binding energies shifted upward but not as high as the carbonyl carbons.^{40,46} A stoichiometry calculation based on the

areas under the peaks yields a ratio of 12 : 4.4 : 1.9, a close match for a predicted stoichiometry of 12 C-C/C-H : 4 C-N/C-O : 2 C=O. Additionally, the C 1s spectrum bears a strong resemblance to prior work on the analogous molecule cFF (see chapter 5.3.2), but features better resolved peaks. The N 1s spectrum contains only a single peak, as there is only a single chemical environment for the nitrogen atoms in the symmetrical diketopiperazine ring. The peak position at 399.9eV correlates well with XPS studies of other peptides,^{2,41-43,47} again confirming the structure identification of cYY. In contrast to studies on cFF on Cu(110) (chapter 5.3.2), different binding modes of the nitrogen to the metal surface were not observed for cYY on Au(111). This is most likely due to a weaker interaction in general between the cYY molecules and a Au(111) surface, as evidenced by the small upshift in binding energy compared to cFF on Cu(110). Additionally, the hydroxyl groups of the cYY may have a 'pinning' effect on the conformation of the molecule due to interactions with adatoms as we have proposed, enforcing the planarity of the molecule and reducing the capability for different binding modes.

In summary, the XPS data for cYY/Au(111) confirm its structure as deposited on the surface, and bear several similarities to earlier work on cFF. Furthermore, deprotonation of the molecule is shown to not occur, based particularly on the O 1s data. Therefore the XPS experiments support the simulations in the conclusion that any adatom coordination by the molecule does not occur via alcohol deprotonation.

6.2.6 Effect of annealing on the self-assembly of Cyclo-(L-Tyr-L-Tyr) on Gold (111): Scanning Tunnelling Microscopy

Annealing a deposition of cYY on Au(111) to 475K brought about a major transformation in the appearance of the molecules and their self-assembly (Figure 6.2.17). Individual molecules display a more uniform internal contrast, suggesting a flatter conformation, and are arranged in a criss-cross type pattern within large islands. This pattern is comprised of molecules in two distinct orientations in a 50:50 ratio, which are rotated approximately 90° from one another. Unlike the as-deposited cYY data, imaging conditions are stable and consistent, which assists with detailed analysis (*vide infra*). The islands formed are much larger than the pre-anneal assembly, the largest extending at least 500 nm in a given direction, and are completely uniform throughout, save for occasional defects. Furthermore, islands are frequently imaged with the Au(111) herringbone reconstruction visible

underneath without any noticeable perturbation to the assembly. Given the prevalence of the dominant pre-anneal assembly, and supporting data for its structure

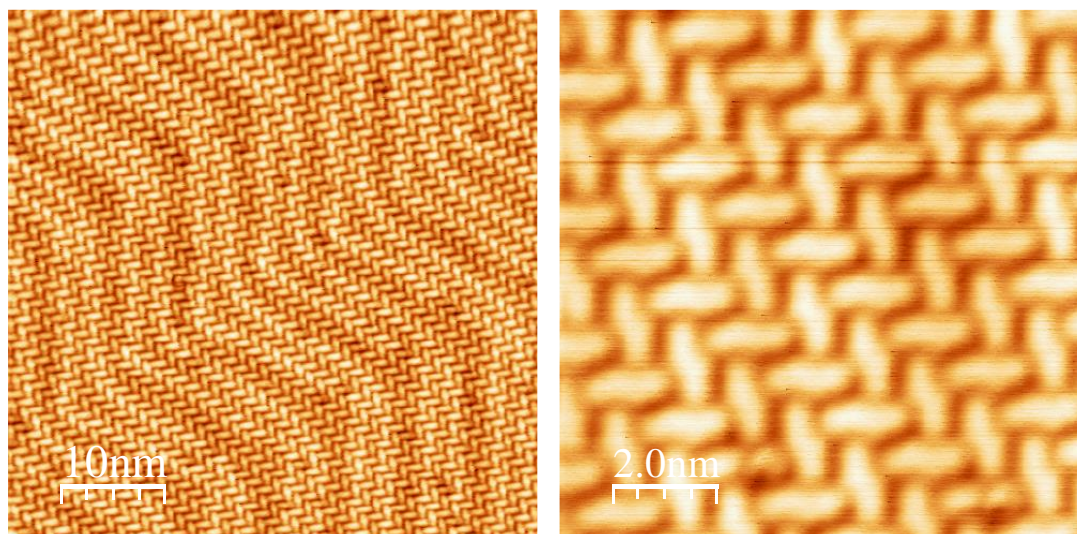


Figure 6.2.17. Typical STM images from a deposition of cYY on Au(111) annealed to 475K. Molecules are imaged exclusively in islands of this type, in a single orientation across the surface.

from simulations, it is unlikely that such a significant change is the result of simply finding a different thermodynamically favoured conformation of the same molecule, or a new intermolecular bonding motif. A logical hypothesis is that the annealing has brought about some chemical change in the cYY, and it is proposed that this is a dehydrogenation reaction comparable to that observed for cFF on Cu(110) (see chapter 5). The product of this process would be dehydrogenated cYY (ddcYY), as illustrated in (Figure 6.2.18). A more direct comparison to cFF on Cu(110) is presented later (section 6.2.11).

As discussed in chapter 5 (“Chemical transformations of the Phe-Phe dipeptide”), the molecular species generated by a dehydrogenation reaction will tend to adopt a flatter conformation due to the reduced degrees of rotational freedom about the double bonds. A flatter molecule explains the reduced contrast, or ‘smooth’ appearance, of the features imaged in the STM post-annealing. This change in conformation also inevitably has an

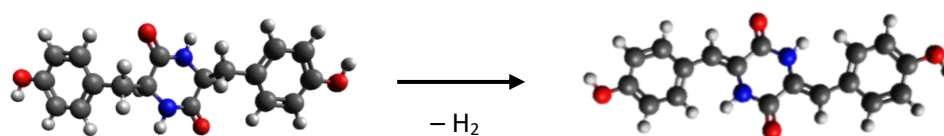


Figure 6.2.18. The dehydrogenation of cYY into ddcYY. Hydrogen atoms are lost across the alkyl carbons, creating an alkene group between each phenol group and the central diketopiperazine ring.

effect on the thermodynamically favoured packing motif, as intermolecular bonds might form at different positions on the molecule and at different angles. Molecule-surface interactions are also affected by the molecule being flatter, becoming stronger due to a greater overlap of the molecular orbitals with surface states of the metal. This can, in turn, have a secondary effect on intermolecular forces, and also means that molecular positions are expected to be more stable, i.e. the molecules will be less mobile on the surface. Due to the interplay of these factors, a significant change in the self-assembly pattern can result, as observed between cYY and ddcYY (see Figures 6.2.3 and 6.2.17).

The identification of a single molecule within the islands is easier than for the original deposition, due to the higher stability of the edges of the islands. Nevertheless, Figure 6.2.19 illustrates molecules adding to and leaving an island showing that some level of mobility over the surface remains. Closer inspection of the two orientations, especially in higher resolution images, reveals that their shape and internal contrast are actually distinct from one another, as displayed in Figure 6.2.20. The two shapes can be broadly described as “S” and “Z” shape, and these designations will be useful later when assigning a molecular structure to each feature. The differences in imaging the two species are consistent across multiple scans and several areas of the surface, and are independent of the orientation of the island with respect to the scan direction. Such regularity suggests a chemical reason behind the appearances, rather than simply random variations. Two possible explanations for this phenomenon are suggested, based on earlier discussion of the landing conformation of the cYY molecules. The first is that all molecules landed in a single, preferential conformation, and dehydrogenated on annealing into two energetically equivalent products, resulting in similar but distinct species that assemble in the criss-cross pattern observed.

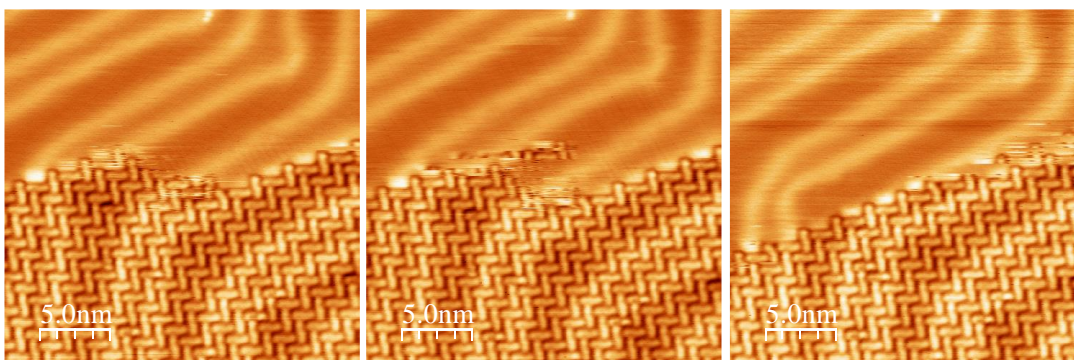


Figure 6.2.19. Sequential images of an island edge of annealed cYY on Au(111), illustrating the reversibility of the molecular interactions occurring at room temperature. Approximately 90s have passed between adjacent images.

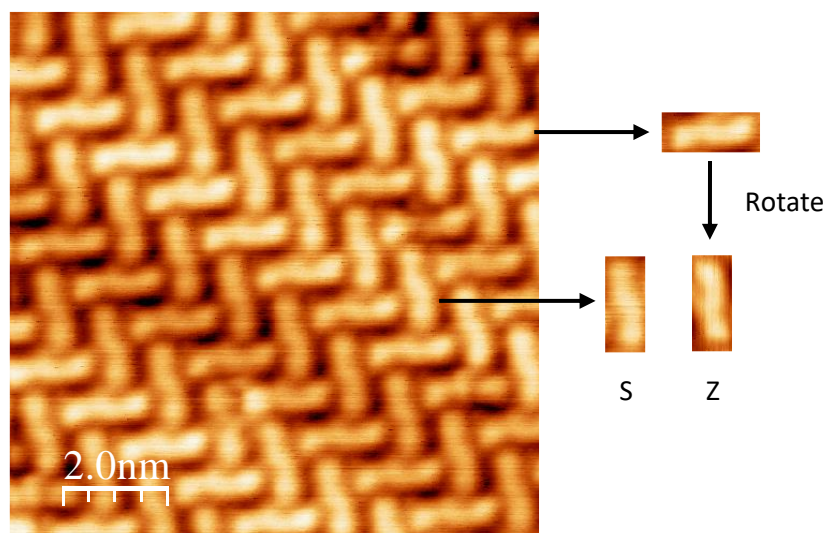


Figure 6.2.20. Illustration of the “S” and “Z” type of molecular features observed in the assembly of annealed cYY on Au(111). These features are recognisable across the surface.

Alternatively, the cYY molecules may have landed as two isoenergetic conformers and dehydrogenated on annealing via a single favoured mechanism, producing two species based on the initial landing. The increased dimensions of the annealed islands provide evidence for the second theory, as the observable molecular coverage is also increased by this phenomenon. Additionally, DFT and MD calculations for cYY indicated that the second theory is the more likely, as both landing conformations are shown to be isoenergetic but only one forms stable islands. It remains of interest to investigate the dehydrogenated molecule itself by means of simulations, however, in order to complete the picture. A provisional model of how the dehydrogenated molecules might form a hydrogen-bonded assembly is presented in Figure 6.2.21.

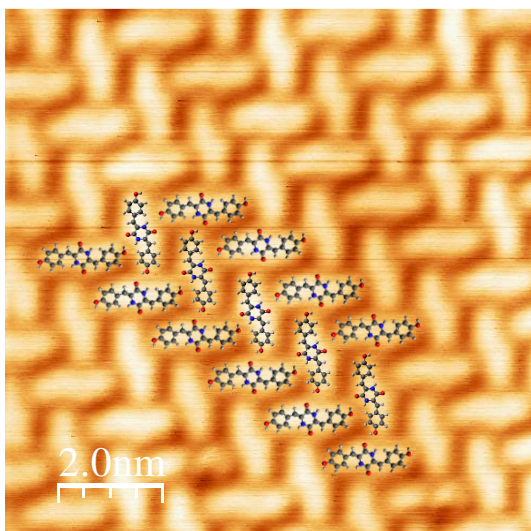


Figure 6.2.21. Overlaid models of ddcYY on the annealed assembly, demonstrating how the two types of ddcYY adsorption might give rise to the pattern observed, via a hydrogen-bonded network.

A question naturally arises concerning gold adatoms, since they are believed to be involved in the assembly of the cyclic molecule, but not for the dehydrogenated molecule. Unlike cYY, ddcYY packs together closely in all directions, enabling hydrogen bonding over reasonable distances and without requiring additional reasoning for the observed periodicity. The question is therefore why this should be the case, as the dehydrogenated species still possesses the hydroxyl residues capable of bonding to the adatoms. It is reasonable to suggest that the flatter and conformationally restricted ddcYY molecule forms stronger and more stable molecule-surface and intermolecular bonds than cYY, both of which reduce the energetic gain of coordinating an adatom. It is possible that this shifts the overall dominant phase away from adatom coordination towards a purely molecular island as observed. However, a more detailed consideration of the energetics of these processes is not presented here.

6.2.7 Effect of annealing on the self-assembly of Cyclo-(L-Tyr-L-Tyr) on Gold (111): Density Functional Theory and Molecular Dynamics

DFT and MD studies were performed to support the experimental data for annealed cYY, by modelling the adsorption and assembly of the dehydrogenated molecule (ddcYY). The same methods and parameters were used as described for cYY.

For each landing configuration of the cYY molecules (A and B as illustrated in Figure 6.2.10 earlier), there are in theory four possible dehydrogenation products depending on the

stereochemistry of the bi-alkene product. However, the large aryl side chains will inevitably prefer to adopt an “E” stereochemistry, with respect to one another across the central ring-alkene plane, due to their steric bulk. This reduces the number of viable stereoisomers to two, which are differentiated by the proximity of the aryl C-H to either the H-N or O=C of the central ring. DFT calculations of isolated molecules of ddcYY in the two conformations were performed both on the Au(111) surface and in vacuo. Only the results for the dehydrogenated analogue of cYY-B are presented in Figure 6.2.22 for simplicity, but cYY-A and B gave the same result, as described in the following. In vacuo and on the gold surface, the dehydrogenation product with aryl C-H and DKP H-N in close proximity is strongly favoured (Figure 6.2.22, species “X”), by an average of 0.30eV. The van der Waals radii of two hydrogen atoms clash much less in species X than that of a hydrogen and an oxygen in species Y, and this difference is so significant that the disfavoured configuration Y in fact

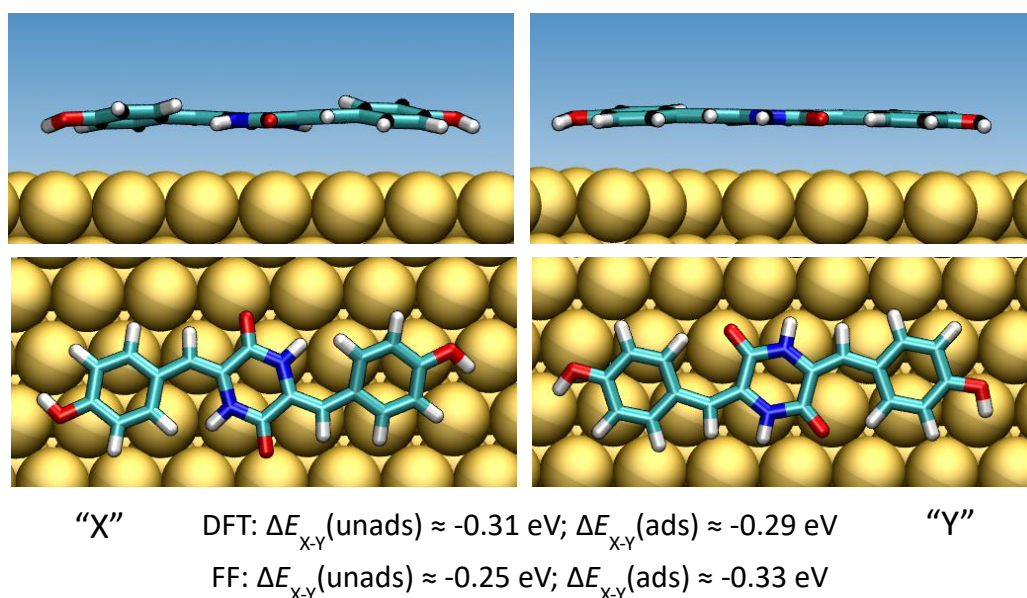


Figure 6.2.22. DFT models of the 2 viable stereoisomers of ddcYY on Au(111), in side and top-down views. DFT and GoIP-CHARMM Force Field (FF) calculations of the energy difference between the two adsorbed isomers are also presented, indicating the greater stability of the “X” species.

has an induced strain in the carbon bond angles in order to minimise the effect. Due to this large energy difference, the dehydrogenation reaction will likely result in the production of the favoured product X. Therefore, the DFT strongly supports the theory that the cYY molecule can land in two different conformations, but dehydrogenates via a single specific mechanism to leave two species on the surface based only on the initial landing. These two species would then be responsible for the S and Z molecular shapes seen in the STM, as

displayed in Figure 6.2.23. A final point of interest from the DFT is that the potential energy surface for adsorption was again found to be quite flat, meaning the molecules do not have a preferential binding site until constrained by the 2D self-assembly.

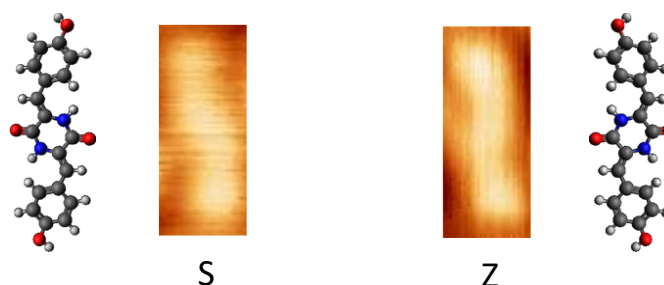


Figure 6.2.23. Gas phase models of the two adsorption modes of ddcYY, adjacent to archetypal S and Z molecular features from STM data on Au(111). The shape of each model broadly correlates to the shape of the STM features.

A potential issue with the above description is that the two dehydrogenated molecules are present in the STM images always in an approximate 50:50 ratio (see Figure 6.2.17), but the pre-anneal images of cYY show uniform molecular appearance (see Figures 6.2.3-4). This apparent change in stereoisomer distribution can potentially be resolved by considering two factors, firstly that a number of cYY molecules were known to be very mobile on the surface. It could be the case that these correspond to the conformer shown by earlier MD to be unable to form stable islands, and as such are difficult to image. Secondly, the MD showed that a small number of molecules could flip over at elevated temperatures. During room temperature scans this process would not occur, but after annealing to 475K, it is reasonable to suggest that this process could have helped to equalise the ratio of stereoisomers present on the surface, if such an imbalance existed for the cYY molecules.

MD simulations also supported the above theory, as well as directly providing evidence that the dehydrogenation has in fact occurred. When a pre-ordered cluster of a 50:50 mix of S and Z dehydrogenated molecules is simulated at 450K, the assembly is stable and retains a strong resemblance to the criss-cross pattern of the STM data (Figure 6.2.24). The major driving force for the assembly appears to be the capability for extensive hydrogen bonding, between the C=O groups on the DKP ring and O-H on neighbouring molecules, and vice versa between the O-H groups on a given molecule and C=O on (different) neighbours. This collection of four hydrogen bonds per molecule has a greatly stabilising effect on the assembly. The radial distribution function for this outcome yields distances in good agreement with STM periodicities, as illustrated in Figure 6.2.25.

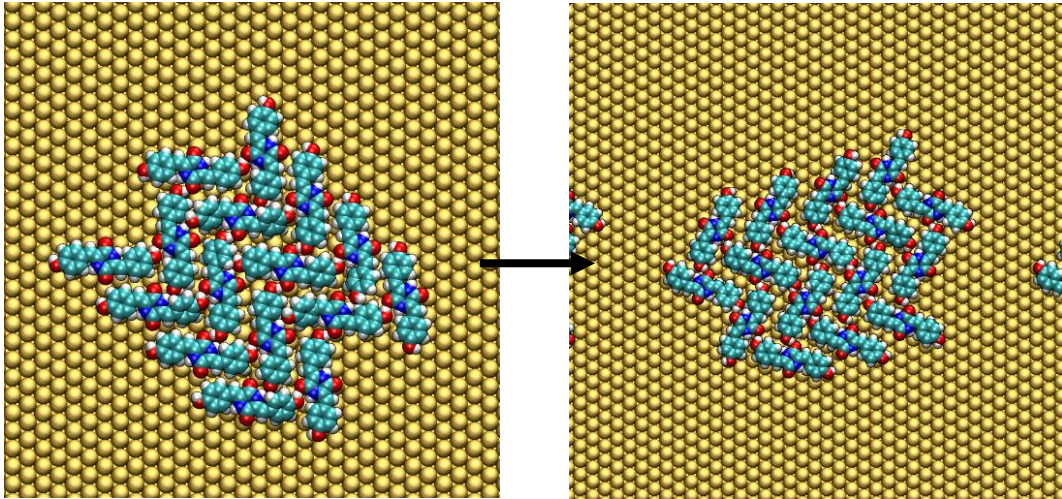


Figure 6.2.24. The progression of an MD simulation of 16 ddcYY molecules, 8 each of the S and Z-type species. The pre-ordered cluster remains stable at 450 K. Cell size $76 \times 79 \text{ \AA}^2$.

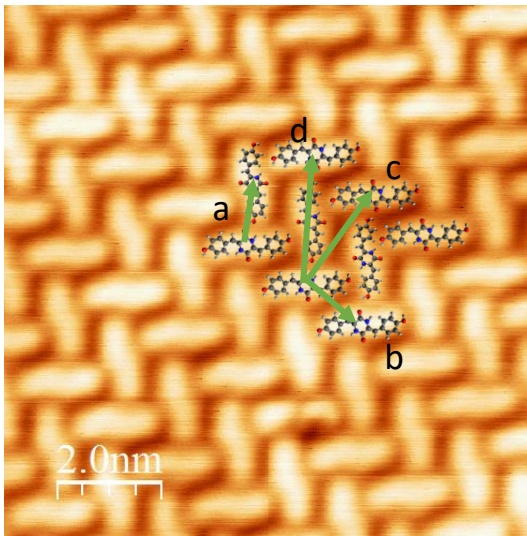


Figure 6.2.25. Comparison of experimental ddcYY periodicity data with a radial distribution function from MD simulations.

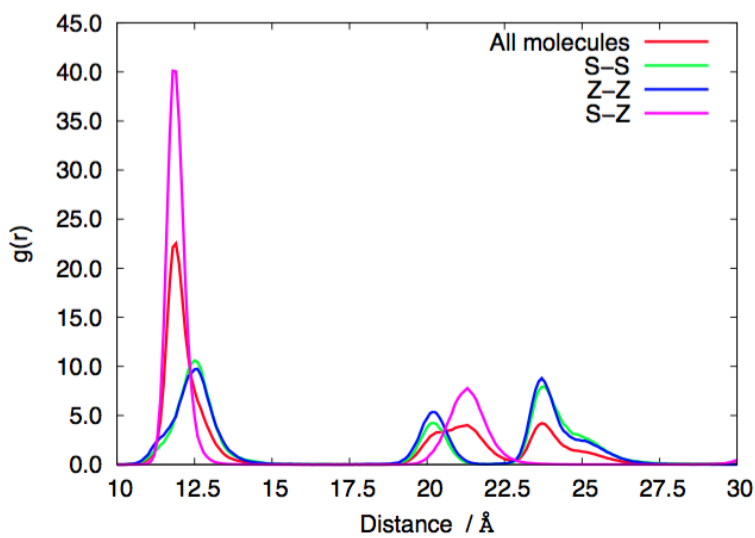
STM

$$a = 12.5 \text{ \AA} (0.38)$$

$$b = 13.2 \text{ \AA} (0.06)$$

$$c = 20.8 \text{ \AA} (0.45)$$

$$d = 24.8 \text{ \AA} (0.69)$$



MD

$$a = 11.9 \text{ \AA}$$

$$b = 12.6 \text{ \AA}$$

$$c = 20.2 \text{ \AA}$$

$$d \approx 24.1 \text{ \AA}$$

All recorded values are within 5% of experimental data, demonstrating the fidelity of the proposed model. Clusters of either S or Z molecules alone, theoretically arising from a single conformer cYY-A or B, are unstable at elevated temperatures. Though the structural differences between these species are subtle, they are significant enough to disrupt the hydrogen bonding described for the stable assembly. All of this together is a clear indication not only that the dehydrogenation has taken place after annealing, but that the explanation for the appearance of the STM images is sound.

Based on the computational models, an improved overlay of the self-assembly is presented in Figure 6.2.26. The conclusions of these simulations do not however provide any commentary on why the islands and the molecules within are exclusively imaged with a single global orientation, even across multiple scanning sessions. Even factoring in the aforementioned flat potential energy surface suggesting low surface registry, one would at least expect some random variation in the direction of the islands. If the surface registry is stronger than anticipated, then one instead expects a threefold symmetry in line with the primary axes of the surface. An explanation for this phenomenon is not immediately apparent. One possibility is that a single vast island has formed, but this would be very unlikely given the inevitable surface orientation boundaries that such an island would have to cross, without any perturbation. It seems more likely that the islands are indeed very large, but present in three major orientations. For the experiments described here, then, all of the high-quality images must be from a similar region of the surface, and so by chance only a single island type has been imaged. Further experiments would be required in order to assess this reasoning, or elucidate whether another may be involved.

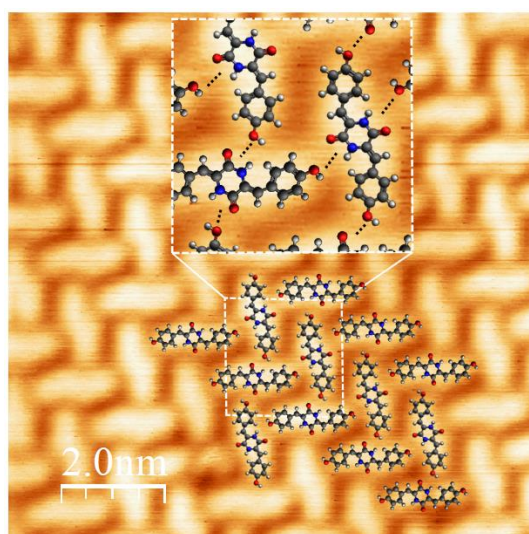


Figure 6.2.26. A modified model of the assembly of ddcYY on Au(111), using molecular conformations arising from the computational data. The potential for hydrogen bonding between phenol groups and proximal amide groups is indicated with black dashed lines. Inset image is approximately 2.2 nm x 2.2 nm.

6.2.8 Effect of annealing on the self-assembly of Cyclo-(L-Tyr-L-Tyr) on Gold (111): X-Ray Photoelectron Spectroscopy

In order to obtain further supporting evidence for the dehydrogenation, the previously described deposition of cYY on a Au(111) crystal was annealed to 475K, and XPS data gathered for the C 1s, O 1s and N 1s spectra (Figure 6.2.27). All data was again calibrated to the Au 4f_{7/2} peak at 84.0eV. The differences to the spectra gathered pre-anneal are subtle, but consist of small changes to the C 1s and O 1s and an overall decrease in intensity of all peaks. To address the intensity first, it is believed that a high coverage of molecules was initially present on the surface, and annealing has caused some to desorb, thereby weakening the C 1s, O 1s and N 1s XPS signals (which has the secondary effect of decreasing the signal-to-noise ratio).

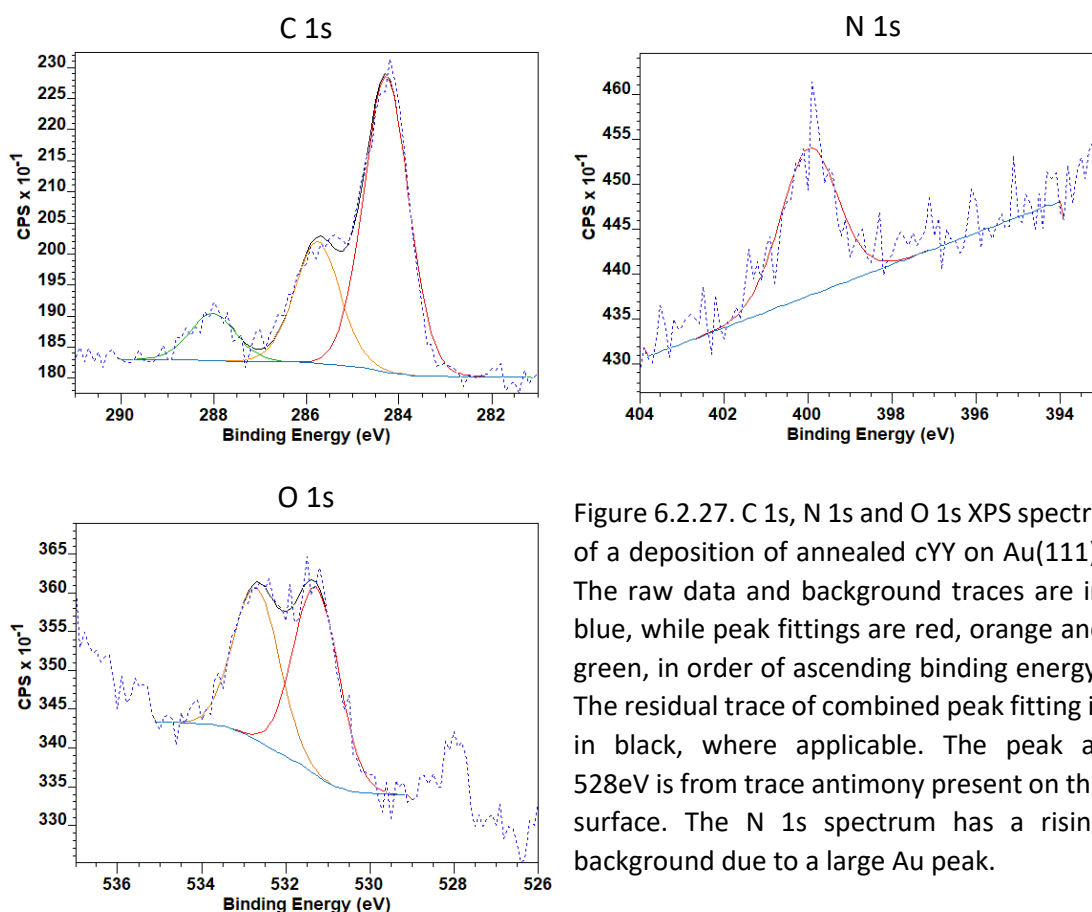


Figure 6.2.27. C 1s, N 1s and O 1s XPS spectra of a deposition of annealed cYY on Au(111). The raw data and background traces are in blue, while peak fittings are red, orange and green, in order of ascending binding energy. The residual trace of combined peak fitting is in black, where applicable. The peak at 528eV is from trace antimony present on the surface. The N 1s spectrum has a rising background due to a large Au peak.

In the C 1s spectrum three peaks are observed, at 284.3eV, 286.0eV and 288.0eV. The largest peak at 284.3eV is only shifted by 0.1eV from the cYY spectrum, aside from the aforementioned reduced intensity, and represents the twelve aromatic carbons.^{40,41,45}

Similarly, the smallest peak at 288.0eV is virtually unchanged from the cYY spectrum, and corresponds to the same two carbon atoms double bonded to oxygen in the carbonyl groups of the DKP ring.^{40,45} The middle peak at 285.7eV is more noticeably different from the original cYY experiment, being shifted downwards in binding energy by 0.3eV such that it appears less distinct from the larger peak. This peak arises from the four carbon atoms bonded to heteroatoms (but not via a double bond).^{40,46} Of these four atoms, two in the dehydrogenated molecule are now part of alkene double bonds, which will tend to shift their binding energies slightly towards those of the similar but more extensively conjugated aromatic ring. This would explain the change in the peak position compared to cYY and the appearance of becoming more of a shoulder of the major peak. The stoichiometry of the dehydrogenated molecule, calculated from the areas under the carbon peaks, is well preserved from the cYY, though with an increased error on the area of the middle peak – perhaps due to its shifted position that overlaps with the large aromatic carbon peak, and the overall weaker signal. The final ratio comes out at 12 : 4.7 : 1.9, compared to 12: 4.4 : 1.9 in the cYY experiment and the real 12 : 4 : 2.

The N 1s spectrum for ddcYY remains as a single peak, centred at 399.9eV. This is unshifted from the cYY peak, which is to be expected as the dehydrogenation process has no effect on the chemistry of the nitrogen atoms in the central ring. Although the oxygen atoms should by the same logic be unperturbed, there is a small difference in the O 1s spectrum after annealing. The two major peaks appear to be somewhat better resolved from one another, and there is less suggestion of a possible third peak in between them. Nevertheless, the peaks are found to be at the same binding energies as before annealing, at 532.7eV for the C-OH oxygens^{41,44} and 531.3eV for the C=O oxygens,⁴¹⁻⁴³ therefore the same functional groups are indeed present and are unaffected by the dehydrogenation.

In summary, there are few changes in the XPS spectra of ddcYY compared to cYY, in contrast to a similar comparison of ddcFF and cFF (see chapter 5). This is largely due to the absence of secondary N 1s peaks from alternative N-metal bonding, which aided the identification of ddcFF and cFF. However, there is evidence of dehydrogenation contained in a small shift in the C 1s spectrum, and no evidence of any other chemical change to the molecules to explain the change in the STM data. Additionally, as for the cYY, there continues to be no evidence of deprotonation of the alcohol groups in ddcYY.

6.2.9 Partial annealing of Cyclo-(L-Tyr-L-Tyr) on Gold (111)

An interesting additional phase of the cYY/ddcYY self-assembly was obtained on a single occasion, following a shorter anneal cycle of the cYY on Au(111). An archetypal image for this phase is shown in Figure 6.2.28. It should be noted that further annealing resulted in the previously described criss-cross assembly of ddcYY (as in Figure 6.2.17).

In this 'partially annealed' condition, the molecules are imaged as one of two appearances, either a relatively flat feature reminiscent of the post-anneal data, or a twin-lobed species with a node in the centre. The molecular arrangement is also different to both the pre- and post-anneal assemblies, with pairwise rows formed in the lengthways direction of the molecules. The types of molecular pairs are highlighted in Figure 6.2.28a. There appears to be no preference for pairs to contain the same type of molecule, with mixed pairs also appearing to be common. However, this could be driven by the overall excess of twin-lobe type molecules present (approximately 60:40 ratio). As with the pre-anneal data, there is a threefold symmetry of the possible island orientations, approximately overlapping with the primary surface directions of the Au(111).

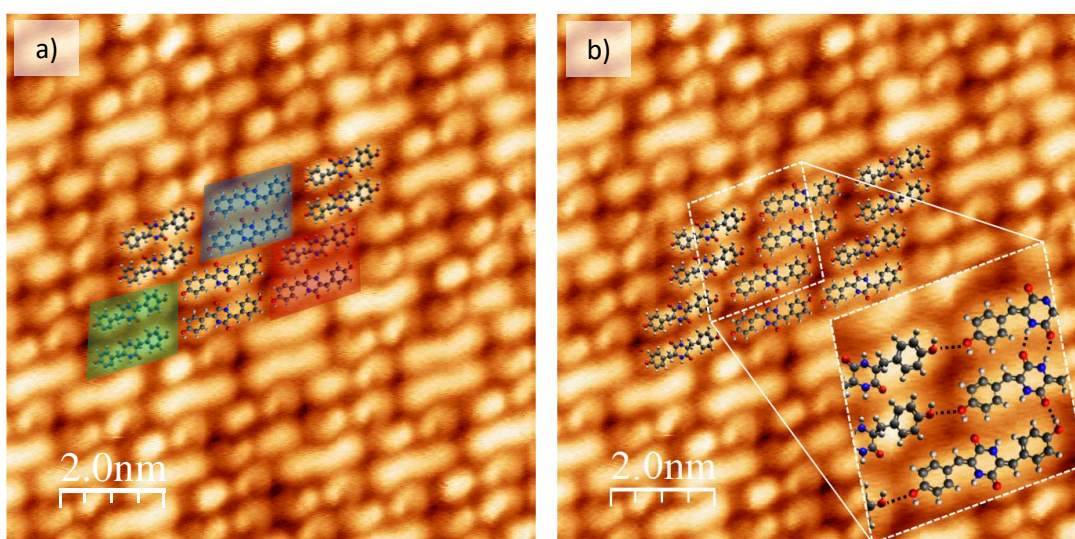


Figure 6.2.28. STM data from the partial annealing of cYY on Au(111), displaying an island of mixed molecular features. a) Examples of how cYY and ddcYY could fit the assembly: a cYY pair highlighted green, a ddcYY pair highlighted blue, and a mixed pair in red. b) An illustration of hydrogen bonding possibilities, with a particular focus on the end-to-end phenolic bonding. Inset image is approximately 2.2 nm x 2.2 nm.

A simple explanation for this unusual phase is that after only a short annealing, only a fraction of the cYY molecules have dehydrogenated, and a longer heating cycle is required to complete the process for all molecules. The lobed molecules would thus correspond to cYY,

in a similar contoured conformation as before annealing, but with visible differences likely due to an adsorption geometry change enforced by the new assembly. The dimensions of these twin-lobed features were comparable to those observed in the initial cYY experiments. The flatter features would correspond to dehydrogenated molecules, much like those after annealing. The mix of cYY and ddcYY does not phase separate into two islands of the previously observed assembly patterns however, and it seems to be instead beneficial to pack together in a mixed island. When creating a model for the assembly, it is apparent that a number of favourable hydrogen bonding interactions can be formed between molecules, but these are inconsistent in number and direction due to the random nature of which molecule is seen in which position. In the lengthways direction, though, it is possible that a hydrogen bond can be formed between neighbouring hydroxyl groups regardless of the species present (Figure 6.2.28b).

MD simulations of unordered cYY or ddcYY could not reproduce the pattern seen here, indicating it is unique to a mixed group of molecules. A mixed phase remains to be investigated computationally. Despite the uncertainty surrounding this intermediate phase, it is largely deemed to be a curiosity, as it was not reproduced, and with further annealing it is transformed into the better understood final phase of the dehydrogenated molecule.

6.2.10 Self-assembly of Cyclo-(L-Tyr-L-Tyr) on Cu (110)

To further investigate the behaviour of Cyclo-(L-Tyr-L-Tyr) and determine if its on-surface transformation might be more general, it was also studied on a Cu(110) single crystal. Cu(110) is more reactive than Au(111) and thus has a tendency for stronger interactions with adsorbed molecules,⁴⁸ and also has a surface structure with a characteristic two-fold symmetry. These factors are expected to affect the self-assembly of cYY substantially, and could also play a role in the dehydrogenation process. Moreover, this experiment serves as a more direct comparison of cYY to cFF, which was originally studied on Cu(110)^{6,49-51} (see also chapter 5). Experiments on Cu(110) can therefore help deepen the understanding of the on-surface reactions of cYY, and begin to build a broader picture of the potential of this molecule, as well as short peptides as a whole. STM data and supporting DFT calculations for cYY on Cu(110) are presented below.

6.2.11 Self-assembly of Cyclo-(L-Tyr-L-Tyr) on Cu (110): Scanning Tunnelling Microscopy

A submonolayer coverage of cYY was deposited on room temperature Cu(110) in an analogous fashion to the Au(111) experiment. The results of the STM imaging are summarised in Figure 6.2.29. The molecules assemble into short chains of typically three to eight 'units', all aligned in the same direction. The chains are oriented at $41^\circ (\pm 2^\circ)$ anticlockwise to the [001] axis of the surface, and the molecular features within are rotated approximately 100° from this, at 60° clockwise from the [001] axis. Broken or disjointed chains are relatively common, as well as other defects, due to the high mobility of molecules on the surface. Across subsequent images (time separations as low as 16s), molecules could frequently be observed adding to and removing from the end of chains, as well as laterally shifting to form defects. Additionally, entire chains were occasionally seen

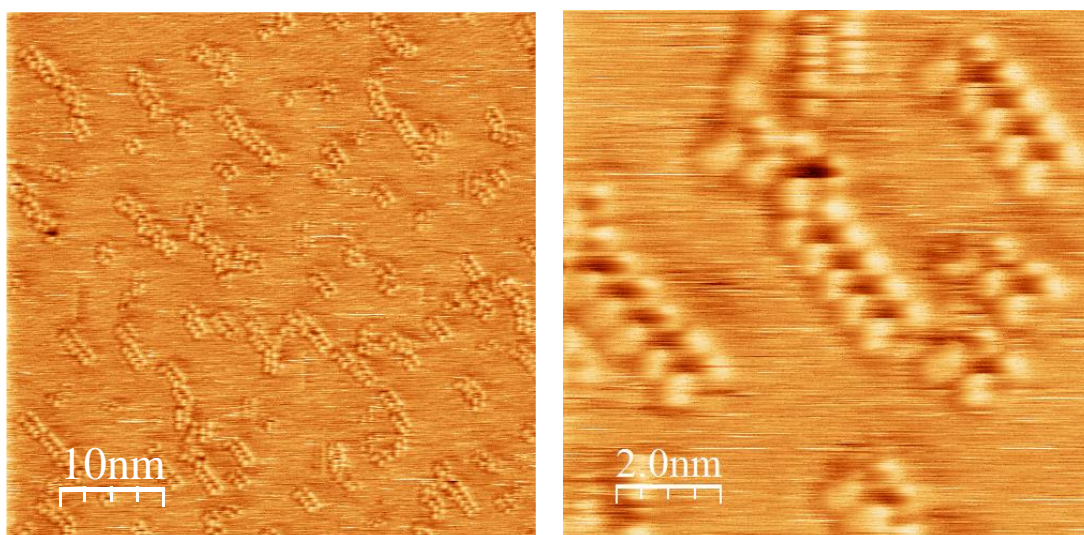


Figure 6.2.29. Typical STM data from a deposition of cYY on Cu(110). Though the molecules are highly mobile, the vast majority of stable images display chains of molecules in the same orientation, as demonstrated here.

to shift position between scans. Though chain formation was consistently observed, it is clear that the barrier to translation across the surface is relatively low outside of a chain, and at room temperature the molecules are in a considerable state of flux. Low temperature experiments at 115K did enable these thermal motions to be frozen, but most of the data analysis presented here is performed using room temperature data.

Despite the described mobility of the molecules, on numerous occasions a straight chain without defects could be stably imaged. The resolution within the chains is consistent, and shows that molecules lie alongside one another breadthways within the chains. Each molecule is composed of two bright lobes with a node in the middle, which is not dissimilar from their appearance on Au(111), and suggests comparable optimal geometry for landing on the surface (see section 6.2.3). By extension, both an up and down geometry might be expected to occur for Cu(110). A simple model for how a single cYY conformer can assemble into the observed chains is presented in Figure 6.2.30a.

Based on the experimental observations, we constructed a theory for how each molecule binds to specific surface sites (Figure 6.2.30b). In the model shown, molecules interact with the surface principally through the central DKP ring, with the nitrogen atoms in particular preferring to coordinate close to the top sites of the $[1\bar{1}0]$ channels. The side groups are thus elevated and are imaged as bright protrusions in the STM images. Chains appear to be held together by a relatively weak interaction between C=O of one molecule and C-H of its neighbour, much weaker than a full hydrogen bond.⁵²

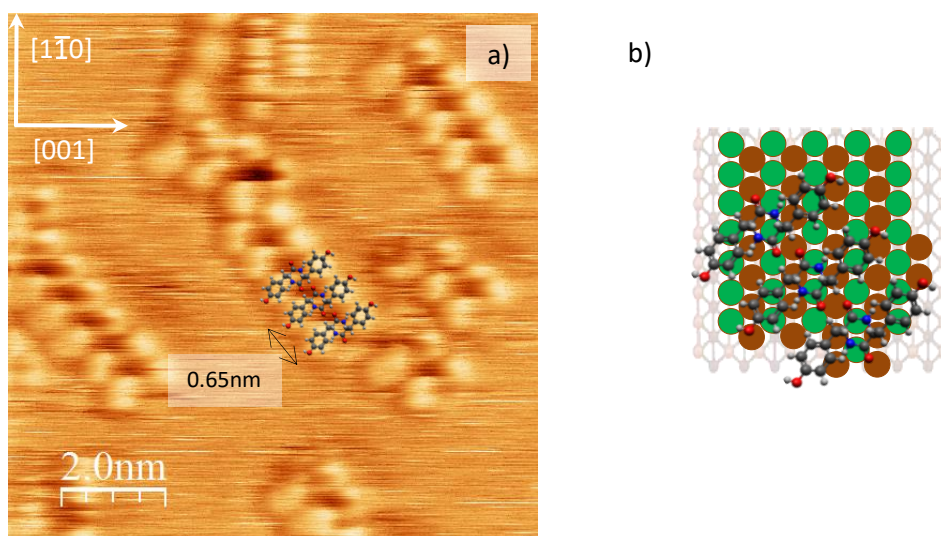


Figure 6.2.30. a) Overlay of a single cYY conformer to illustrate how the chains might be assembled on Cu(110). Periodicity standard deviation: 0.19\AA b) Suggested surface-mapped overlay of cYY molecules based on established surface orientations for the Cu(110) crystal in use. The rows of atoms presenting “top” sites are coloured green, with alternate rows coloured brown.

In contrast to what was observed on Au(111), it is expected that on Cu(110), the molecule-substrate interaction is the dominant factor over the intermolecular interactions. Indeed, only a single chain orientation on the anisotropic Cu(110) surface is indicative of a strongly

preferential molecule-surface binding mode. As the chain length increases, the molecules appear to be too densely packed to continue to adsorb to the surface in the same way. This is an indication that the molecular self-assembly is not completely commensurate with the surface, and may be the reason behind the limited length of the chains observed. If the assembly is indeed primarily dependent on the molecule-surface interaction, then chains will cease to grow if the addition of a further molecule would give an unfavourable surface registry. Attempts at finding alternative molecular conformations that could satisfy a sensible surface registry while ‘improving’ the level of intermolecular bonding were unsuccessful, as other conformations did not fit well with the resolved shape of an individual molecule in the STM. Additionally, only one landing of the molecule has been considered in creating the self-assembly model, due to the unidirectional nature of the chains – which is strongly indicative of conformational purity within these chains. Furthermore, replacing the molecules in the model with the ‘flipped’ analogue resulted in the same issue as discussed when trialling different conformers. Therefore, it is suggested the copper surface exerts a selective influence on the adsorption process, so that a single landing configuration is preferred, though as with Au(111) there may be a small quantity of other species on the surface that are not imaged due to their mobility.

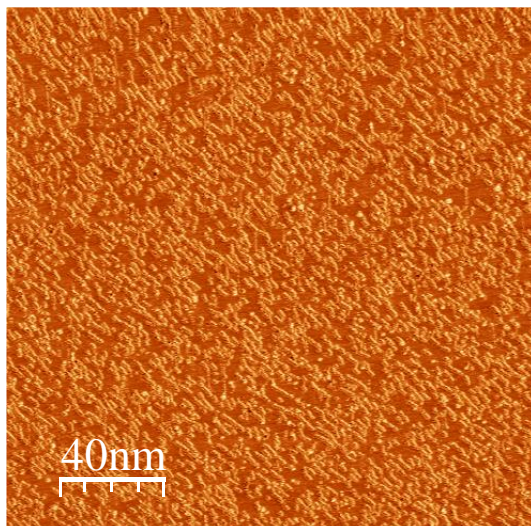


Figure 6.2.31. Typical STM image of cYY on Cu(110) at high coverage (approximately 0.85 monolayers). Large numbers of small and moderately sized chains can be seen, while no condensation into large islands is observed.

Experiments were also conducted at high coverage (~ 0.85 monolayers), to minimise the impact of molecular mobility and to determine if the chains would coalesce into islands. Large scale scans in Figure 6.2.31 illustrate that islands still did not form, and that the chains still suffer from similar defects and translational movement. Even at this elevated surface coverage, however, a different molecular or chain appearance is not seen, which adds weight to the landing selectivity argument. It is possible that in the Cu(110) case, electron transfer

and charging effects are more likely, adding a repulsive term to the intermolecular forces and thus favouring chains over islands.^{24,25}

A comparison can also be drawn with previous experiments on the cYY analogue cFF, studied on Cu(110) at low temperature and room temperature^{6,49} (see also chapter 5). Unidirectional chains of cFF were found to be the dominant mode of self-assembly, a behaviour which greatly resembles that of cYY. The orientation of the molecules and hence the chains differs slightly from those of cYY, undoubtedly driven by the small chemical differences between the two molecules, but other features such as average chain length and the internal resolution of each molecule are again comparable to images of cYY. Figure 6.2.32 illustrates some of these similarities. With the behaviour of both molecules being so alike, it might be expected that annealing experiments would also yield a similar result; that is, a dehydrogenation and a resultant flip of the orientation of the chains. This idea is explored further in the annealing section for cYY (6.2.13).

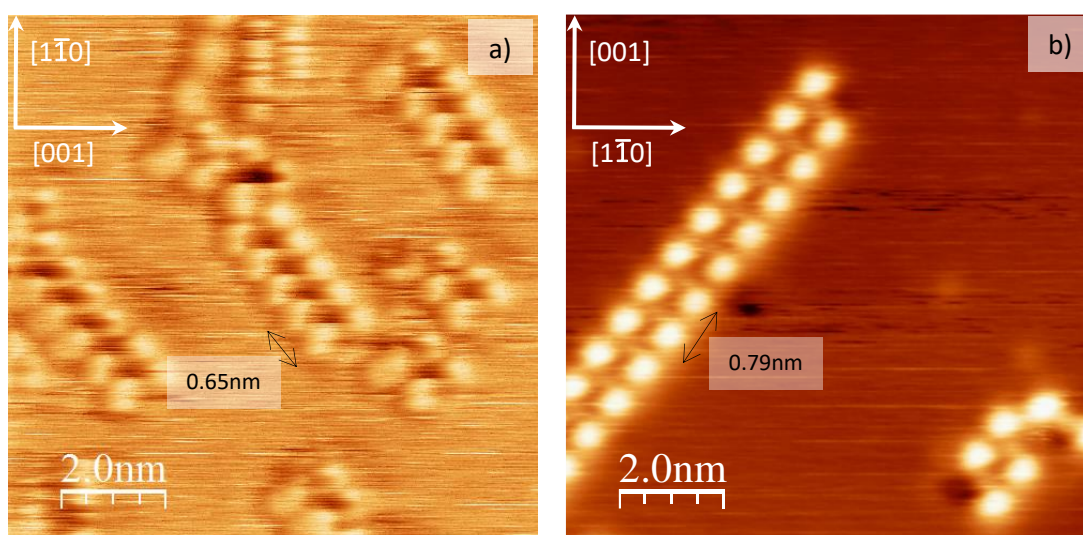


Figure 6.2.32. A side-by-side comparison of STM images of a) cYY on Cu(110), and b) cFF on Cu(110). While cFF forms longer chains on average, both molecules' assemblies resist island formation and display a range of chain lengths. The density of packing of the chains is also similar, suggesting this is largely governed by the molecule's core, not the side groups.

The theory proposed to explain the self-assembly of cYY on Cu(110), while supported by aspects of the STM data, cannot be sufficiently substantiated without further evidence. In order to attempt to address this issue, complementary DFT simulations are presented below.

6.2.12 Self-assembly of Cyclo-(L-Tyr-L-Tyr) on Cu (110): Density Functional Theory

DFT calculations were performed for isolated molecules of cYY on a Cu(110) surface, using the same methods and parameters as described for cYY on Au(111). A number of possible conformers for the deposited molecule were tested, based on the up and down models of the Au(111) simulations and different possible surface adsorption sites. Of these conformers, the two that are lowest in energy are separated only by a 0.03eV gap, and as such both are presented in Figure 6.2.33, referred to as conformation cYY-X and cYY-Y for reference. These conformers can be considered analogous to cYY-A and cYY-B on Au(111) respectively. The small energy difference between these species would typically indicate that both of these conformations should be seen experimentally, the DFT data showing that there is not a thermodynamic driving force for either to dominate. The lowest energy of these species, conformer Y, has a considerable resemblance for the model proposed from the STM data in Figure 6.2.30, in terms of molecule orientation and surface registry.

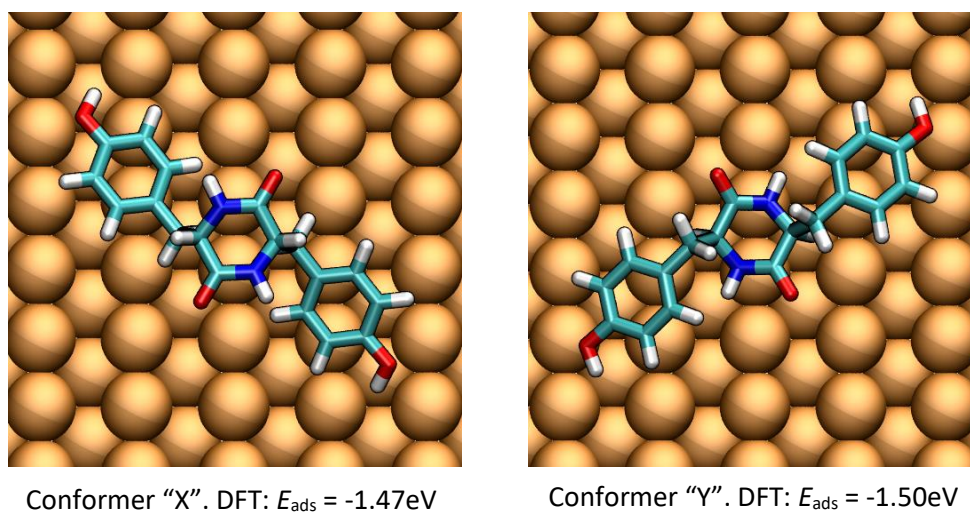


Figure 6.2.33. DFT models of cYY on Cu(110), using "up" and "down" landing conformers as starting points. A small energy difference of 0.03eV separates the two, suggesting both might occur on the surface, in contrast to the behaviour observed on Au(111).

Conformer X also offers similar surface registry but a different, almost mirrored, orientation. It is currently unclear why DFT should point to two species of similar energy on the surface, while only one is observed in the STM data. It is possible that an additional factor that dictates a preferential landing conformer is not represented in the DFT calculations, such as charge transfer or deprotonation, resulting in electrostatic effects even when compensated

for by the surface states. Such reactions may be conformation-gated, as a result of the distance between relevant parts of the molecule and the copper atoms of the surface. MD simulations and XPS data could shed further light on the conclusions here and, as such, will be explored in the future. The results of the annealing experiments below are also helpful in providing insight into the state of the surface pre-anneal.

6.2.13 Effect of annealing on the self-assembly of Cyclo-(L-Tyr-L-Tyr) on Cu(110): Scanning Tunnelling Microscopy

Annealing a deposition of cYY on Cu(110) to 425K gave rise to a complete change in the appearance of the molecules and their assembly across the entire surface. The molecules still appear to assemble into chains, but these are oriented differently and with a new internal structure (Figure 6.2.34). The dominant orientation for the molecules is now at 26° ($\pm 1^\circ$) clockwise from the [001] axis, arranged into lengthways chains, with 'horizontal' or 'diagonal' packing to form islands possible but irregular and small in scale. The molecules also seem flatter, similar to their appearance on annealed Au(111), indicative that dehydrogenation has most probably occurred. This transformation is also analogous to the behaviour of cFF on Cu(110) (chapter 5), though with the caveat that chains of ddcFF still assembled breadthways after re-orienting due to dehydrogenation.

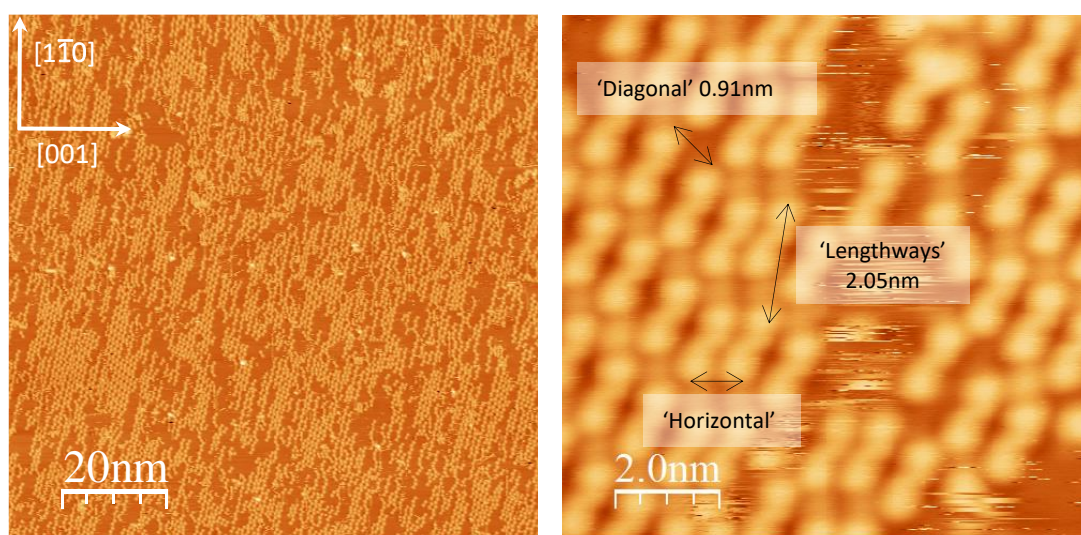


Figure 6.2.34. Typical STM images post-annealing a deposition of cYY on Cu(110) to 425K. Standard deviation for: lengthways periodicity 0.58\AA , 'diagonal' periodicity 0.72\AA .

The chains of ddcYY have a large internal spacing, with an average of 0.51 nm separation between molecules (measured from molecular edges defined as being at the FWHM of the height of each molecule). As with the assembly on Au(111) pre-annealing, such a gap is too large to be attributed to the usual intermolecular forces such as hydrogen bonds. The spacing is also quite regular, and always contains a distinct feature that is brighter than the bare surface (though dimmer than the molecules themselves). It is proposed that these features correspond to adatoms, or rather pairs of adatoms, bonded to the hydroxyl groups of the ddcYY molecules. Unlike Au(111), substrate adatom-bonded assemblies on Cu(110) are relatively common.⁵³⁻⁵⁶ Additionally, there is a considerable possibility that the hydroxyl groups deprotonate on Cu(110) at room temperature,⁵⁷⁻⁵⁸ which only serves to enhance the capability for adatom bonding. Since the molecule is much flatter after dehydrogenation (see Figure 6.2.22 earlier), the hydroxyl groups can come into much closer proximity with the surface, permitting a copper-catalysed deprotonation unavailable to the cYY species. A model for the assembly, using the same flattened dehydrogenated species as on Au(111), is presented in Figure 6.2.35 (DFT specific to Cu(110) was presented in section 6.2.12). This model uses a single conformer of ddcYY, though several conformers are possible as discussed for the Au(111) data. Pre-anneal data suggested a single landing mode was dominant, and DFT calculations have already demonstrated that a single dehydrogenation product is likely. The shape of the molecular features and the need to create a sensible bonding model also meant that only the species indicated was suitable, after trial-and-error fitting.

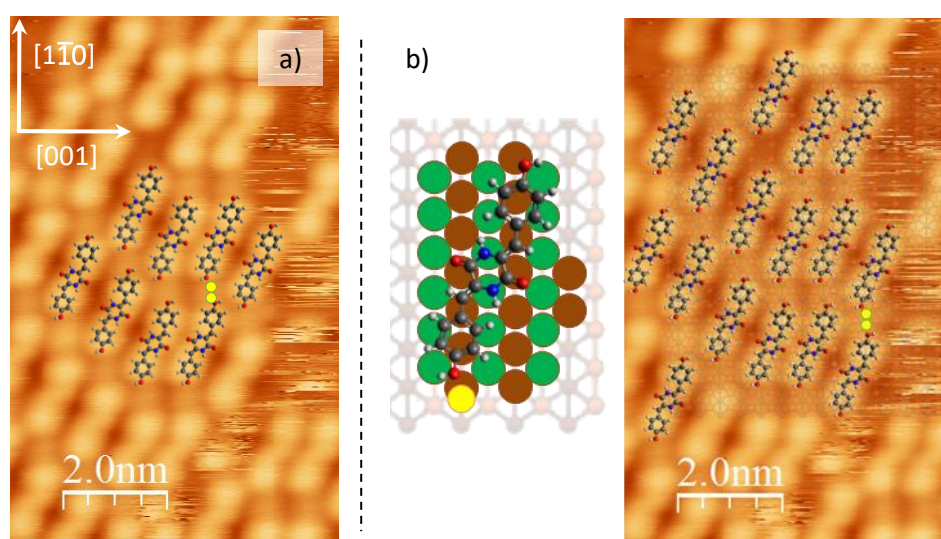


Figure 6.2.35. a) Models of ddcYY overlaid on to the post-anneal data on Cu(110). Two adatoms of Cu, to scale, are illustrated in yellow to demonstrate the potential for adatom coordination to explain the lengthways molecular spacing. b) Suggested surface-mapped overlay of ddcYY molecules, with a simplified image also transposed over the data. The rows of atoms presenting “top” sites are coloured green, with alternate rows coloured brown.

Overlaying the molecules on to a 2D representation of the Cu(110) surface, one finds that the molecule-surface registry is highly regular (Figure 6.2.35b), and a preferred binding mode can be suggested. Heteroatoms such as nitrogen, with their available lone pairs, can form stronger bonds with the copper atoms of the surface, and so the nitrogen atoms of the DKP ring are given priority positions on top sites. The carbonyl oxygens also are proximal to the next top sites along. Crucially, this positioning places the hydroxyl groups in the $[1\bar{1}0]$ channels, where adatoms can be readily accommodated. It is known in the literature that adatoms have high mobility within $[1\bar{1}0]$ channels, and that lateral movement across ridges is more energetically demanding.⁵⁹⁻⁶⁰ The channels (i.e. hollow and long bridge sites) also provide a local minimum in comparison to top sites,⁵⁹⁻⁶⁰ and will be preferential locations for adatoms. Therefore, it is statistically logical to place adatoms in the channel sites, and the hydroxyl groups nearby to bond with them. The aforementioned regularity of the surface registry means that this mode of bonding to the surface allows a commensurate superstructure, as experimentally observed, irrespective of whether the chains pack diagonally (at an angle of 47° to the $[1\bar{1}0]$ axis) or in the $[001]$ direction. This demonstrates that the adatom-bonded chains are the primary driving force for the observed self-assembly pattern, and that the way these chains bond with each other is a weaker, secondary interaction. Furthermore, while molecules adjacent in the $[001]$ direction may form weak bonds with one another in a similar fashion to the pre-anneal chains, diagonal neighbours are too distant (for hydrogen bonds, for example) with a periodicity of 0.91 nm on average.

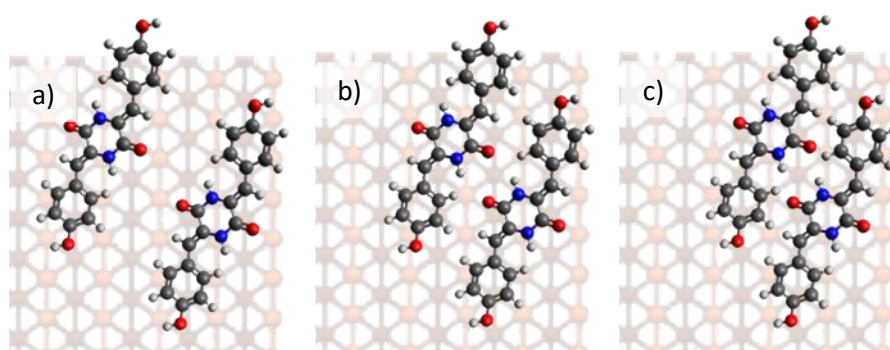


Figure 6.2.36. Illustration of the restrictions placed on the assembly of ddcYY by the registry with the Cu(110) surface. a) Models at a separation observed experimentally. b) Assembly close enough for hydrogen bonding, but causing nitrogen atoms to lose access to surface top sites. c) Maintaining nitrogen atoms on ridge sites causes steric clashes due to molecular proximity.

In Figure 6.2.36, alternative modes of diagonal packing are considered, to assist in understanding the packing observed experimentally. Figure 6.2.36b illustrates that diagonal neighbours could sit closer to one another in order to hydrogen bond, but this would disrupt the identified adatom bonding pattern. Alternatively, moving to the next $[1\bar{1}0]$ channel to maintain adatom bonding, as in Figure 6.2.36c, brings the molecules too close to one another, causing steric clashes. This further supports the idea that lateral packing of chains is a secondary factor, with the adatom-mediated chains being the primary driving force for the assembly.

Additional data was gathered at different levels of coverage, to record the differences in packing and gain further information about the primary assembly. At the lowest coverage used (Figure 6.2.37), the primary assembly is proven to be chains formed with adatoms, as none of the loosely packed islands are observed while the chains are frequently seen. Simple dimers with adatoms and completely isolated molecules are also common at this coverage. At the highest coverage used (Figure 6.2.38), the self-assembly is much the same as described for the original deposition. The coverage demands that more chains associate into the loosely packed islands than previously, but there is still a tendency to resist dense packing overall. It is clearer at this coverage that the diagonal secondary assembly is more common than the horizontal, even though this pattern has larger intermolecular distances and fewer potential intermolecular interactions. This suggests that there may be a degree of repulsion between molecules,²⁴ which can be viewed as possible evidence for the deprotonation of the hydroxyl groups⁵⁷⁻⁵⁸. The periodicity in the primary direction of a chain appears to be unaffected by coverage.

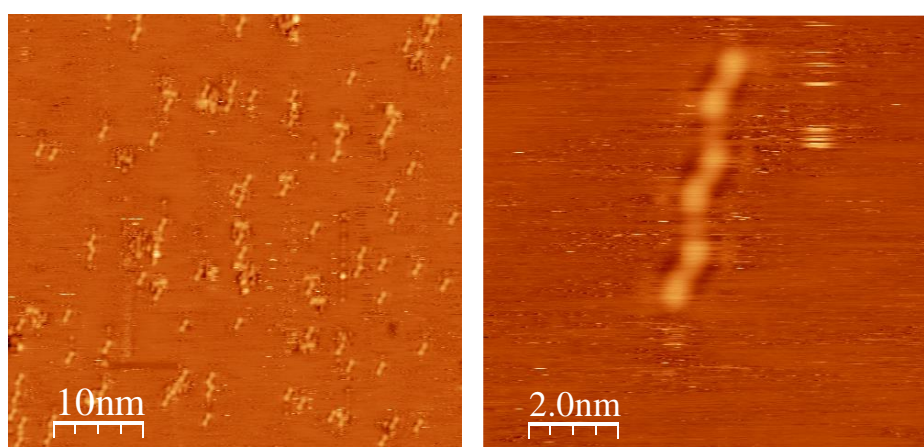


Figure 6.2.37. Very low coverage STM data of annealed cYY on Cu(110). Lateral packing is not observed, and only isolated molecules or short chains are recorded across the surface. The adatom-based assembly also appears to be prevalent at this coverage.

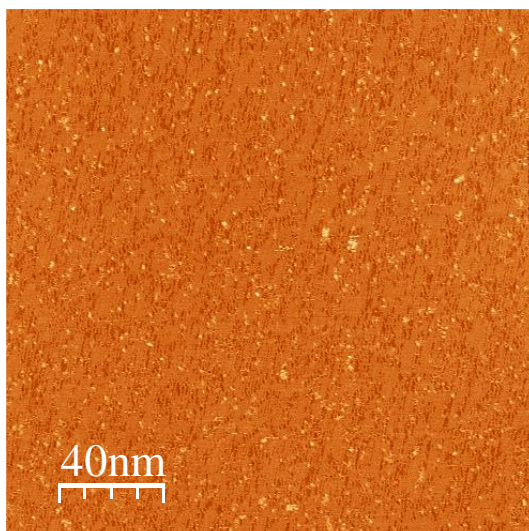


Figure 6.2.38. High coverage STM data of annealed cYY on Cu(110). A greater proportion of islands are observed at this coverage, but a general agglomeration still does not occur.

A comparison can again be made with the behaviour of ddcFF (chapter 5), which also preferred chain formation to islands (section 5.2.3). At very high coverages, it was possible to effect a change in the assembly of ddcFF, such that a new packing into dense islands was possible (see chapter 5, Figure 5.21). A phase of this type has however not been observed for ddcYY.

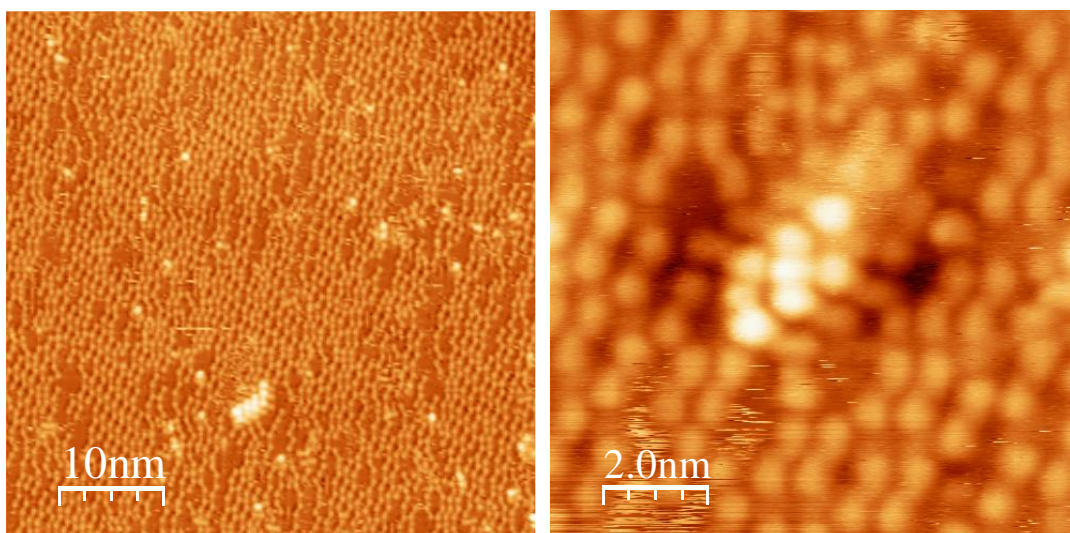


Figure 6.2.39. Evidence of the growth of a second layer of molecules of ddcYY on Cu(110). There are few occurrences of this phenomenon, but any ordered chains are in the same orientation, suggesting a favoured mode of bonding to the adlayer below.

At higher coverage, the beginnings of how a second layer might form can also be seen (Figure 6.2.39). Aside from some individual species scattered randomly on top of the first layer, most of the second layer molecules also arrange into chains that are aligned 59° clockwise from

the [001] direction, with the individual molecules oriented approximately along the [001] axis and lying breadthways alongside one another. One explanation for this behaviour would be that the molecules in the overlayer sit so that the DKP ring is atop the adatoms of the assembly below, enabling the nitrogen atoms in the ring to coordinate to the copper. This configuration also places the aromatic groups over those of the molecules underneath, thereby allowing π -stacking interactions.

The dominant conformation and assembly for ddcYY has been described, but there also a number of molecules that appear to be mirror images with respect to the [001] axis (Figure 6.2.40), oriented at $27^\circ (\pm 1^\circ)$ anticlockwise from the [001] axis. As with the gold data, the best fit for these images is a pair of molecules that arise from flipped over landing configurations. In contrast to the gold, however, the ratio of the two is approximately 90:10, whereas the gold was a perfect 50:50. One possible explanation is that the original molecular sample was not 100% enantiomerically pure, and has directly resulted in the final ratios on-surface. Alternatively, it may be the case that the original sample was pure but has partially racemised upon annealing. A further possibility is that the surface selects for a particular landing conformer, and subsequent dehydrogenation proceeds down a favoured path to leave the same ratio of products as reactants.

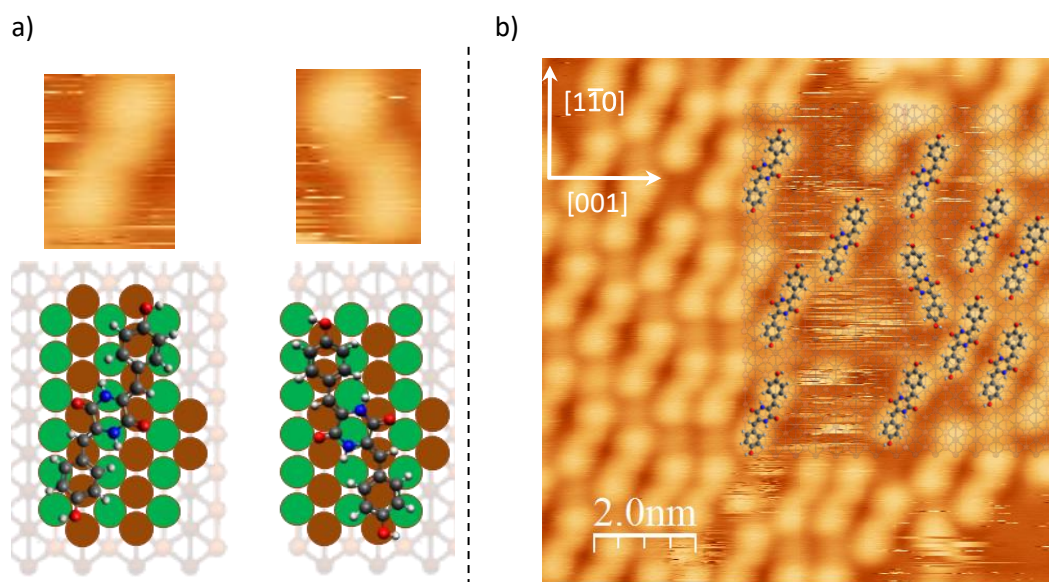


Figure 6.2.40. a) Surface-mapped overlay of ddcYY molecules arising from different landing conformers of cYY, and how they might relate to the molecular features from STM. The rows of atoms presenting “top” sites are coloured green, with alternate rows coloured brown. b) Overlay of the Cu(110) surface structure and both ddcYY surface conformers, demonstrating the fit to the experimental data.

The molecule-metal interactions are stronger on a Cu(110) surface compared to Au(111), and so the differences in energy of alternative landing conformations can become more pronounced. Moreover, stronger molecule-surface interactions decrease the chance of a molecule flipping over upon annealing, a process which was possible in MD simulations of cYY on Au(111) and may have enabled equilibration of stereoisomer ratios.

An exception to the two molecular orientations described can be found at certain steps in the copper surface. Some steps have chains of molecules that appear to straddle the step itself, and are aligned with the direction of the step as opposed to a particular primary axis of the surface (Figure 6.2.41). In regions of the surface where this occurs, the parts of the step with molecules bound are straight and stable, while other areas appear partially degraded and irregular. This phenomenon bears significant resemblance to reports of more extensive 'step faceting' on copper surfaces in the literature.⁶¹⁻⁶² It should be noted that as already discussed, there was not such an effect of the steps on the pre-anneal assembly of cYY. Using the structure of the dominant ddcYY species as a model (Figure 6.2.42), it is apparent that hydrogen bonding could occur between neighbouring molecules anchored to the step. In addition, it is possible that this mode of binding to the step enables nitrogen atoms to bind to top sites on the step, in a similar fashion to that described for the primary assembly. The driving force for this assembly seems to be great enough that steps can be restructured to make perfect straight edges on which a molecular chain can lie, potentially even through the degradation of nearby steps with no or fewer molecules bound. A final

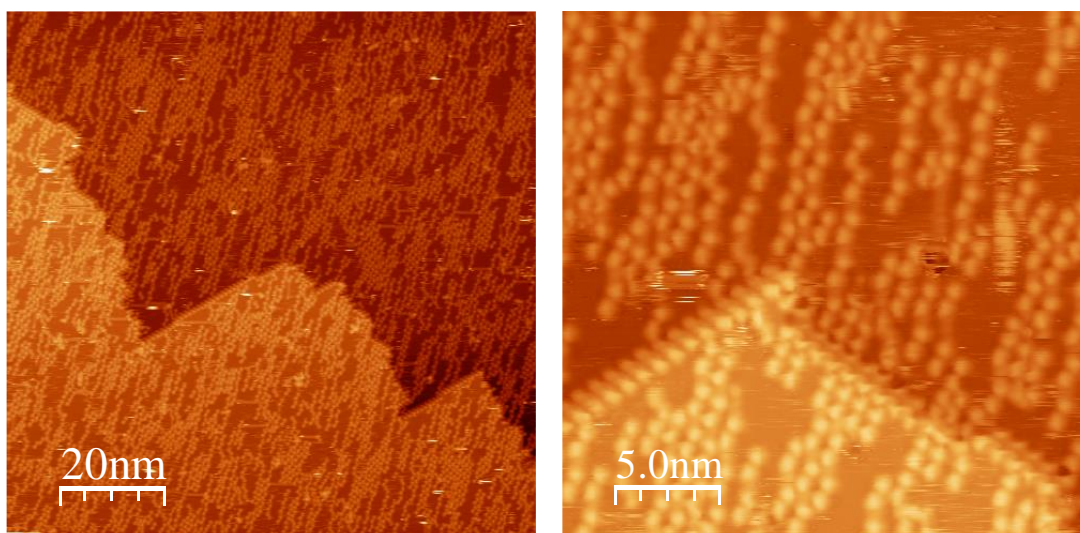


Figure 6.2.41. Step faceting of the Cu(110) surface where molecules of ddcYY appear to have adsorbed in rows. Such facets were relatively rare, but were stable across sequential scans.

note on this phenomenon is that it is only recorded as occurring at certain angles on the surface, the most prominent of which is $57^\circ (\pm 1^\circ)$ clockwise from the [001] plane (as in Figure 6.2.42). Of secondary importance are the chains at an angle of $56^\circ (\pm 1^\circ)$ anticlockwise from the [001] plane. The ratio between these two appeared to be similar to the 90:10 ratio discussed above, but the reason for specificity of the angles of the step-bound chains remains unclear.

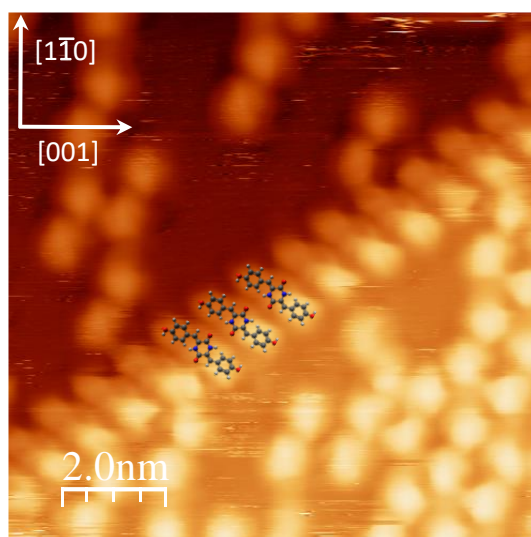


Figure 6.2.42. Overlaid ddcYY molecules to illustrate how a chain might form by the faceted Cu(110) step. Amide groups of adjacent molecules are theoretically close enough for hydrogen bonding.

6.2.14 Effect of annealing on the self-assembly of Cyclo-(L-Tyr-L-Tyr) on Cu(110): Density Functional Theory

DFT calculations were performed for isolated molecules of ddcYY on a Cu(110) surface, using the same methods and parameters as described for ddcYY on Au(111). For a given landing of the cYY molecule, a single dehydrogenation product is identified as the most stable on the Cu(110) surface, much like the outcome on Au(111). Figure 6.2.44 compares the computational model with that produced based on STM data. The similarities between the two are evident, with a preference for binding the nitrogen atoms in the central ring to ridge sites on the copper, and a comparable molecular angle with respect to the [001] axis. The angle is subtly different however, and the molecule's length overall spans more of the [001] channels. The computational model does not consider adatoms, nor deprotonation of the hydroxyl groups, and as such the oxygen atoms display a tendency to bond to Cu(110) ridge sites instead. It is anticipated that an adatom correction would create an even greater level of congruence between theory and experiment, by encouraging the molecule to re-align to

coordinate adatoms in the $[1\bar{1}0]$ channels. MD simulations of the assembly, factoring in adatoms, would be a useful next step for the simulations, and could be accompanied experimentally by XPS data to determine if deprotonation indeed occurs for ddcYY on Cu(110).

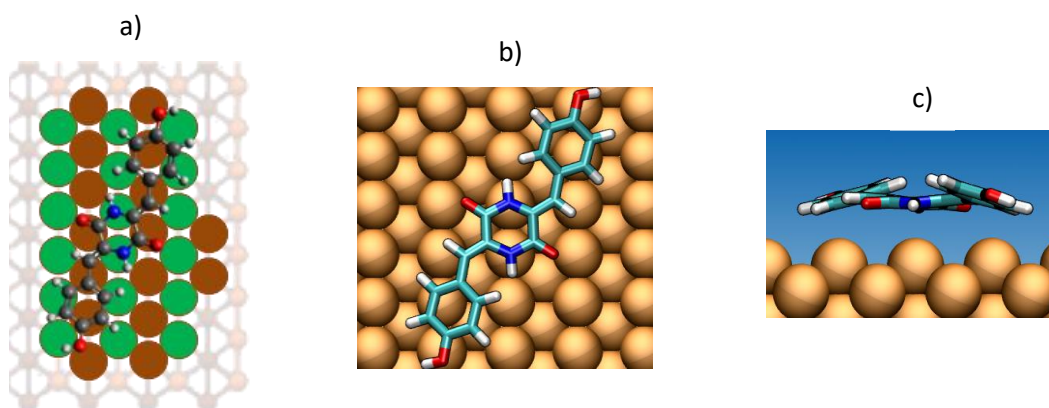


Figure 6.2.43. a) Model of the adsorption of ddcYY to Cu(110) as proposed from the STM data. b) Most-stable surface conformation of ddcYY on Cu(110), as determined by DFT. The similarity to the STM model is apparent. c) Side view of ddcYY adsorption on Cu(110) from DFT.

6.2.15 Concluding remarks

In conclusion, L-Tyr-L-Tyr has been proven to cyclise upon thermal sublimation in the same fashion as L-Phe-L-Phe, and therefore deposits on a metal surface in vacuum as the cyclised molecule, Cyclo-(L-Tyr-L-Tyr) (cYY). The self-assembly of this molecule on Au(111) and Cu(110) has been studied by STM, and the effects of annealing the surface recorded. Results are supported by DFT, MD and XPS data on Au(111), and by DFT on Cu(110). A significant body of evidence shows that in both cases, the assembly changes dramatically upon annealing due to a dehydrogenation of the cYY. This ddcYY product is a flatter molecule and has different molecule-surface and intermolecular interactions, resulting in the self-assembly transformation observed. This behaviour is also broadly analogous to that of Cyclo-(L-Phe-L-Phe). The mode of molecular adsorption on each surface is discussed in detail, as well as the effects this has on the dehydrogenated product. Au(111) does not appear to display a selectivity for the landing conformation of the cYY molecules, whereas on Cu(110), the annealed data revealed a 90:10 ratio, which may have originated from surface selectivity or from simpler issues of enantiomeric purity.

Of particular interest on Au(111) is evidence for adatom coordination by cYY, through an unusual spacing in the molecular islands imaged by STM. MD simulations do not recreate this spacing and suggest that the molecules alone should pack more densely. XPS, DFT and MD data show that these molecules do not deprotonate on the gold surface, and so the cYY molecule may be a rare case that can bond with adatoms on Au(111) without bearing a local charge, or possessing thiol functionality.

On Cu(110), the behaviour of cYY is comparable to cFF in terms of chain formation being the preferred assembly, and a complete shift in orientation of the molecules after annealing. In contrast to ddcFF, ddcYY incorporates adatoms into its chains, due to the hydroxyl groups present that are absent on ddcFF. These hydroxyl groups may deprotonate on the copper surface, enhancing the adatom bonding and causing a degree of intermolecular repulsion that may explain the resistance towards dense island formation.

The experiments on cFF and cYY together begin to suggest that there may be some degree of generality in the behaviour of these dipeptides and others of similar structure. It is known that some dipeptides, including Ala-Ala, Gly-Pro, Gly-Leu and Gly-Gly (see chapter 1.5 and chapter 4.5) do not cyclise upon sublimation, so it is tentatively proposed that the aromatic side chains of FF and YY are involved in the cyclisation process, and may even play a role in the on-surface dehydrogenation reaction. Such reactions being more general would open up a number of possibilities in terms of the chiral control of organic monolayers on metal surfaces, as well as having potential implications in enantioselective heterogeneous catalysis. There is considerable potential for expanding on this work, both in attempting to identify the precise reasons for this behaviour, and in exploring other related molecules that may display the same tendencies. These would naturally include other peptides with aromatic side chains, particularly dipeptides such as L-Trp-L-Trp and L-His-L-His. Beyond this, dipeptides of mixed monomers such as L-Phe-L-His could also be of interest, as well as those with only one aromatic side chain and one aliphatic, for example. Finally, a vast range of synthetic peptides are possible, into which a number of side groups with secondary functionality could be inserted.

6.2.16 References

1. I. Stensgaard, *Surf. Sci. Lett.*, 2003, **545**, L747-L752.
2. C. Méthivier, V. Lebec, J. Landoulsi and C. M. Pradier, *J. Phys. Chem. C*, 2011, **115**, 4041-4046.
3. V. Humblot, A. Tejada, J. Landoulsi, A. Vallée, A. Naitabdi, A. Taleb and C. M. Pradier, *Surf. Sci.*, 2014, **628**, 21-29.
4. V. Humblot, A. Vallée, A. Naitabdi, F. Tielens and C. M. Pradier, *J. Am. Chem. Soc.*, 2012, **134**, 6579-6583.
5. N. Kalashnyk, J. T. Nielsen, E. H. Nielsen, T. Skrydstrup, D. E. Otzen, E. Laegsgaard, C. Wang, F. Besenbacher, N. C. Nielsen and T. R. Linderroth, *ACS Nano*, 2012, **6**, 6882-6889.
6. M. Lingenfelder, PhD thesis, 2007, EPF Lausanne, Switzerland.
7. J. V. Barth, *Surf. Sci. Rep.*, 2000, **40**, 75-149.
8. C. F. Lin and L. E. Webb, *J. Am. Chem. Soc.*, 1973, **95**, 6803-6811.
9. E. Benedetti, R. E. Marsh and M. Goodman, *J. Am. Chem. Soc.*, 1976, **98**, 6676-6684.
10. M. Genest and M. Ptak, *Chem. Biol. Drug Des.*, 1978, **11** (3), 194-208.
11. M. Gdaniec and B. Liberek, *Acta Cryst.*, 1986, **42**, 1343-1345.
12. M. B. Avinash, D. Raut, M. K. Mishra, U. Ramamurty and T. Govindaraju, *Sci Rep.*, 2015, **5**, 16070.
13. A. Jeziorna, K. Stopczyk, E. Skorupska, K. Lubarda-Durnas, M. Oszajca, W. Lasocha, M. Górecki, J. Frelek and M. J. Potrzebowski, *Cryst. Growth. Des.*, 2015, **15**, 5138-5148.
14. K. D. Kopple and D. H. Marr, *J. Am. Chem. Soc.*, 1967, **89**, 6191-6193.
15. K. D. Kopple and M. Ohnishi, *J. Am. Chem. Soc.*, 1969, **91**, 962-970.
16. J. Fleischhauer, J. Grötzinger, B. Kramer, P. Krüger, A. Wollmer, R. W. Woody and E. Zobel, *Biophys. Chem.*, 1994, **49**, 141-152.
17. A. Lewandowska, I. Carmichael, G. Hörner, G. L. Hug and B. Marciniak, *Chem. Phys. Lett.*, 2011, **512**, 123-128.
18. F. L. Bettens, R. P. A. Bettens, R. D. Brown and P. D. Godfrey, *J. Am. Chem. Soc.*, 2000, **122** (24), 5856-5860.
19. A. G. Abo-Riziq, B. Crews, J. E. Bushnell, M. P. Callahan and M. S. De Vries, *Mol. Phys.*, 2005, **103**, 1491-1495.

20. A. P. W. Arachchilage, F. Wang, V. Feyer, O. Plekan and K. C. Prince, *J. Chem. Phys.*, 2012, **136**, 124301.
21. G.A. Jeffrey, *An introduction to hydrogen bonding*, Oxford University Press, Oxford, 1997.
22. E. N. Baker and R. E. Hubbard, *Prog. Biophys. Mol. Biol.*, 1984, **44**, 97-179.
23. W. Kabsch and C. Sander, *Biopolymers*, 1983, **22**, 2577-2637.
24. A. Della Pia, M. Riello, A. Floris, D. Stassen, T. S. Jones, D. Bonifazi, A. De Vita and G. Costantini, *ACS Nano*, 2014, **8**, 12356–12364.
25. M. Seul and D. Andelman, *Science*, 1995, **267**, 476.
26. M. N. Faraggi, N. Jiang, N. Gonzalez-Lakunza, A. Langner, S. Stepanow, K. Kern and A. Arnau, *J. Phys. Chem. C*, 2012, **116**, 46, 24558-24565.
27. A. Saywell, W. Greń, G. Franc, A. Gourdon, X. Bouju and L. Grill, *J. Phys. Chem. C*, 2014, **118**, 3, 1719-1728.
28. N. A. Kautz and S. A. Kandel, *J. Phys. Chem. C*, 2009, **113**, 19286–19291.
29. O. Voznyy, J. J. Dubowski, J. T. Yates and P. Maksymovych, *J. Am. Chem. Soc.*, 2009, **131**, 12989–12993.
30. P. Maksymovych, O. Voznyy, D. B. Dougherty, D. C. Sorescu and J. T. Yates, *Prog. Surf. Sci.*, 2010, **85**, 206–240.
31. Z. E. Hughes, L. B. Wright and T. R. Walsh, *Langmuir*, 2013, **29**, 13217-13229.
32. J. Björk and S. Stafström, *ChemPhysChem*, 2014, **15**, 2851-2858.
33. J. Carrasco, W. Liu, A. Michaelides and A. Tkatchenko, *J. Chem. Phys.*, 2014, **140**, 084704.
34. D. J. Carter and A. L. Rohl, *J. Comput. Chem.*, 2014, **35**, 2263-2271.
35. M. Rosa, S. Corni and R. Di Felice, *Phys. Rev. B*, 2014, **90**, 125448.
36. W. Liu, F. Maa, M. Willenbockel, C. Bronner, M. Schulze, S. Soubatch, F. S. Tautz, P. Tegeder and A. Tkatchenko, *Phys. Rev. Lett.*, 2015, **115**, 036104.
37. Z. E. Hughes and T. R. Walsh, *Phys. Chem. Chem. Phys.*, 2016, **18**, 17525-17533.
38. Z. E. Hughes, A. Baev, P. N. Prasad and T. R. Walsh, *Phys. Rev. B*, 2017, **95**, 205425.
39. L. B. Wright, M. P. Rodger, S. Corni and T. R. Walsh, *J. Chem. Theory Comput.*, 2013, **9**, 1616-1630.
40. A. V. Naumkin, A. Kraut-Vass, S. W. Gaarenstroom and C. J. Powell, NIST Standard Reference Database 20 (Version 4.1), <https://srdata.nist.gov/xps/>, 2012 (accessed 2018).

41. Y. Zubavichus, M. Zharnikov, A. Shaporenko, O. Fuchs, L. Weinhardt, C. Heske, E. Umbach, J. D. Denlinger and M. Grunze, *J. Phys. Chem. A*, 2004, **108** (20), 4557-4565.
42. O. Plekan, V. Feyer, S. Ptasíńska, N. Tsud and K. C. Prince, *Phys. Chem. Chem. Phys.*, 2014, **16**, 6657.
43. A. P. W. Arachchilage, F. Wang, V. Feyer, O. Plekan and K. C. Prince, *J. Chem. Phys.*, 2010, **133**, 174319.
44. N. Nelson, PhD thesis, 2016, Iowa State University, USA.
45. N. Graf, E. Yegen, T. Gross, A. Lippitz, W. Weigel, S. Krakert, A. Terfort and W. E. S. Unger, *Surf. Sci.*, 2009, **603**, 2849–2860.
46. G. Beamson and D. Briggs, *High Resolution XPS of Organic Polymers – The Scienta ESCA 300 Database*, John Wiley & Sons: Chichester, 1992.
47. C. Méthivier, V. Humblot and C.-M. Pradier, *J. Phys. Chem. C*, 2016, **120**, 27364–27368.
48. M. W. Roberts, “Surface reactivity of metal surfaces studied by scanning tunneling microscopy”, in *Encyclopedia of materials: science and technology*, ed. K. H. J. Buschow, R. W. Cahn, M. C. Flemings, B. Ilshner, E. J. Kramer, S. Mahajan and P. Veyssièrè, Elsevier, New York, 2001, p9050-9052.
49. G. Tomba, M. Lingenfelder, G. Costantini, K. Kern, F. Klappenberger, J. V. Barth, L. C. Ciacchi and A. De Vita, *J. Phys. Chem. A*, 2007, **111**, 12740-12748.
50. Y. Wang, M. Lingenfelder, T. Classen, G. Costantini and K. Kern, *J. Am. Chem. Soc.*, 2007, **129**, 15742-15743.
51. M. Lingenfelder, G. Tomba, G. Costantini, L. C. Ciacchi, A. De Vita and K. Kern, *Angew. Chem. Int. Ed.*, 2007, **46**, 4492-4495.
52. G. R. Desiraju, T. Steiner, *The Weak Hydrogen Bond in Structural Chemistry and Biology*, Oxford University Press, Oxford, 1999.
53. M. Kiskinova, *Chem. Rev.*, 1996, **96**, 4, 1431-1448.
54. M. C. Lennartz, N. Atodiresei, L. Müller-Meskamp, S. Karthäuser, R. Waser and S. Blügel, *Langmuir*, 2009, **25**, 2, 856-864.
55. L. Dong, Q. Sun, C. Zhang, Z. Li, K. Sheng, H. Kong, Q. Tan, Y. Pan, A. Hu and W. Xu, *Chem. Commun.*, 2013, **49**, 1735-1737.
56. B. Maughan, P. Zahl, P. Sutter and O. L. A. Monti, *J. Phys. Chem. C*, 2015, **119**, 49, 27416-27425.
57. M. Bowker and R. J. Madix, *Surf. Sci.*, 1982, **116**, 549–572.

58. S. Stepanow, T. Strunskus, M. Lingenfelder, A. Dmitriev, H. Spillmann, N. Lin, J.V. Barth, Ch. Wöll and K. Kern, *J. Phys. Chem. B*, 2004, **108**, 19392-19397.
59. M. Karimi, T. Tomkowski, G. Vidali and O. Biham, *Phys. Rev. B*, 1995, **52**, 5364.
60. H. Yildirim, A. Kara, S. Durukanoglu and T. S. Rahman, *Surf. Sci.*, 2006, **600**, 484–492.
61. F. M. Leibsle, S. Haq, B. G. Frederick, M. Bowker and N. V. Richardson, *Surf. Sci.*, 1995, **343**, L1175–L1181.
62. X. Zhao, Z. Gai, R. G. Zhao, W. S. Yang and T. Sakurai, *Surf. Sci.*, 1999, **424**, L347–L351.

6.3 Self-assembly of L-Trp-L-Trp on metal surfaces

6.3.1 Background

As discussed in chapter 1 (“Introduction”), L-Trp-L-Trp (WW) is an aromatic dipeptide, that together with FF and YY forms a set of naturally occurring, hydrophobic homodipeptides. By studying the thermal transformations and self-assembly of all 3 molecules, a trend in the behaviour of aromatic dipeptides can begin to be described. The data from chapter 5 (“Chemical transformations of the Phe-Phe dipeptide”) and chapter 6.2 (“Self-assembly of L-Tyr-L-Tyr on metal surfaces”) showed notable similarities in both the effects of thermal sublimation and the self-assembly arising from a deposited beam, and so WW was studied here to establish if the observed behaviours could be more general. WW was therefore sublimed and tested by mass spectrometry to test for thermal cyclisation, and deposited on Cu(110) and Au(111) surfaces for study by STM. In this chapter, the results of these experiments are presented. Sublimations tests prove that WW follows the trend of FF and YY by thermally cyclising, with no remaining trace of the linear starting material. STM data shows that the molecules have an appearance reminiscent of FF and YY, but perhaps more similar to dehydrogenated species than simply cyclised.

6.3.2 Sublimation of L-Trp-L-Trp

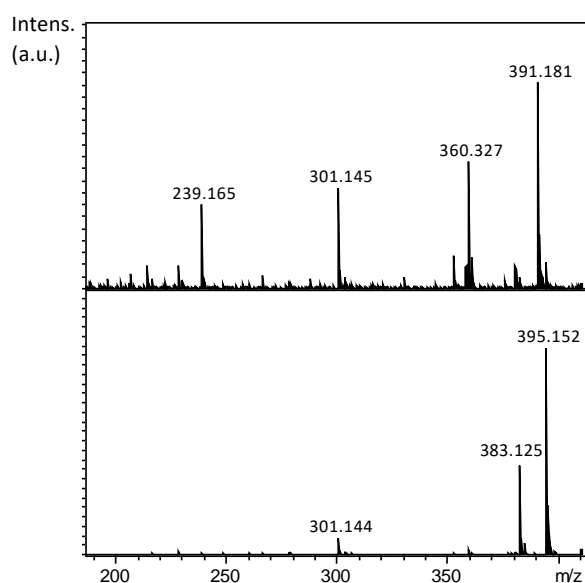


Figure 6.3.1. Mass spectra of [top] non-sublimed L-Trp-L-Trp and [bottom] L-Trp-L-Trp sublimed at 555K. Molecular ion occurs at $\sim m/z$ 391.

L-Trp-L-Trp was sublimed in HV conditions on to a glass substrate and the resulting film tested by ESI mass spectrometry in methanol, as described in chapter 2.2.2. The sublimation

temperature used was 555K. The resulting mass spectrum (Figure 6.3.1) contained several peaks, the largest of which at m/z 395.1 corresponds to the sodiated form of the cyclised molecule. The second largest peak is at m/z 767.2 (data not shown), which arises from a dimer of cyclised molecules with a single sodium adduct. A final major peak is found at m/z 383.1, corresponding to the protonated cyclised molecule. The molecular ion peak of WW, expected at 391.2, is absent from the sublimed sample, despite being dominant in the pristine, unsublimed material. From the data it is clear that the molecule has completely cyclised as a result of the thermal sublimation, and should be expected to deposit as such during sample preparation for STM experiments. However, other peaks of significant size are observed in the unsublimed spectrum, located at m/z 360.3, 301.1 and 239.2. The peak at 301.1 is reproduced in the sublimed spectrum and is typically caused by a common plasticiser. Even the use of higher resolution mass spectrometry, as described in chapter 2.2.1 and employed in chapter 4 (“The sublimation of short peptides”), did not enable the remaining peaks to be linked to either the linear or cyclic form of WW. It is apparent that the pristine sample of WW contains impurities and that while sublimation appears to improve the purity, the possibility of contamination must be taken into account when interpreting the STM data. The exact ratio of desired species to impurities is not possible to state without calibration, since mass spectrometry itself is not inherently quantitative (see chapter 4.2).

6.3.3 Self-assembly of Cyclo-(L-Trp-L-Trp) on Cu(110)

Depositing cWW (cyclised in the crucible as per the above) at submonolayer coverage on a Cu(110) surface gave rise to the assembly shown in Figure 6.3.2. The molecules were exclusively imaged in small islands elongated in the [001] direction, which frequently have a central striping around which the molecules are clustered. This striping is the product of oxygen contamination on the surface, and the characteristic (2x1) reconstruction¹⁻³ can be observed more clearly in Figure 6.3.3. The cWW molecules show a clear preference for assembling alongside the oxygen stripes, and were in fact not imaged without oxygen also being present on the surface. The islands formed around the oxygen are however ordered, with repeating patterns visible throughout. Individual molecules appear to resolve as two-lobed features, much like images of cYY and cFF, and these features are arranged in rows

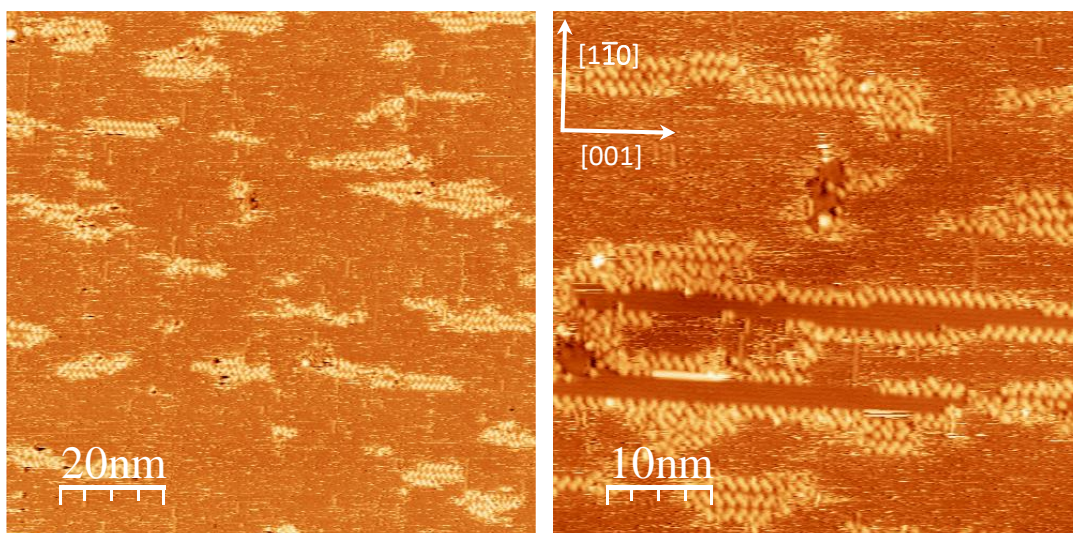


Figure 6.3.2. Typical STM images from a deposition of cWW on Cu(110). Only narrow, isolated islands are recorded, frequently with visible copper- oxygen (2x1) reconstruction stripes visible in the centre.

alongside each other (see Figure 6.3.3b). Subsequent rows are sometimes aligned in the same direction but they can also be mirrored, and a switch within a row as a result of a defect can also be seen. In all cases the molecular chain or island growth seems to have originated from the anchoring of a molecule via a single ‘lobe’ to the oxygen stripes. The island growth occurs predominantly in the form of the rows alongside the oxygen stripes, in the [001] direction of the surface. ‘Bare’ oxygen stripes were not observed, which suggests a strong

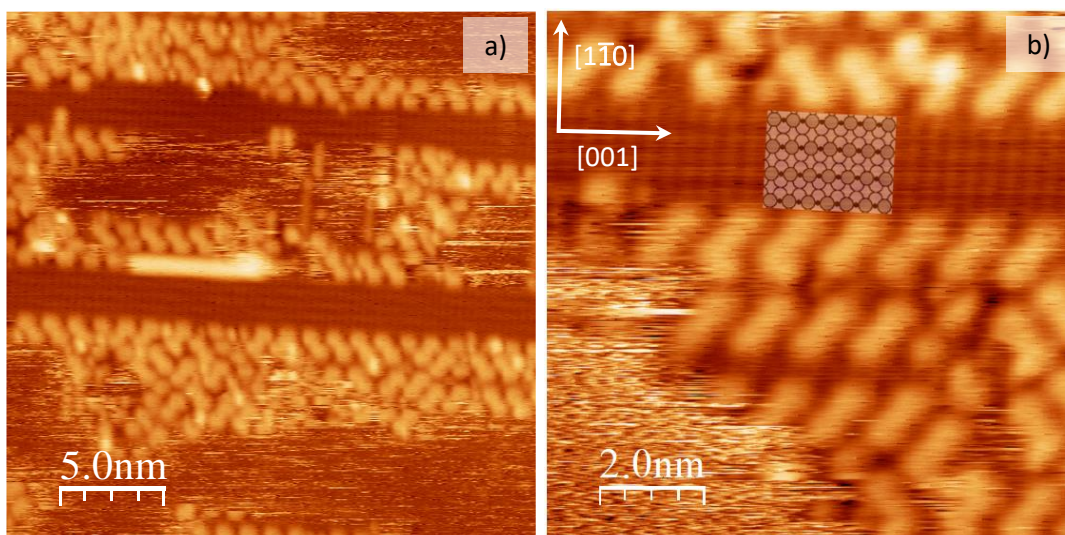


Figure 6.3.3. a) A closer view of Cu-O (2x1) striping on Cu(110) and the narrow molecular islands surrounding this phenomenon. b) An overlay of the (2x1) reconstruction on to the striping in the STM image. The dark circles between rows of reconstructed copper are the adsorbed oxygen atoms.

templating effect of the oxygen on the molecular assembly. The rows of molecules can contain ten to fifteen molecules in a continuous chain, or even as many as twenty to thirty across defects or changes in the oxygen pattern. The addition of further rows, extending the island in the $[1\bar{1}0]$ direction, appears to be more limited. Island thickness beyond three or four rows on a given side of the oxygen stripes is rare, with a number of smaller islands being favoured over fewer larger islands. This is evidence that the assembly with oxygen is the primary, dominant motif, while 2D molecular aggregation is a secondary factor.

Some of the islands imaged do not have such an obvious oxygen stripe in the centre, yet these islands appear to have grown in an identical fashion (Figure 6.3.4a). The same rows of molecules with the same orientations are observed within, and the average dimensions of an island are unchanged. It is therefore expected that the molecules are still clustering around the oxygen (2×1) reconstruction, albeit a smaller patch that is not well imaged or is simply overlain by molecules. Close inspection of these islands reveals that some of the features imaged are not the twin-lobed molecular species, but are apparently individual circular objects of similar dimensions to a single lobe of the molecules (see Figure 6.3.4b). These features are typically imaged in the central row of a cluster, but can also be seen at the edge. Height profiles indicate that the circular features are 10-15% lower in apparent

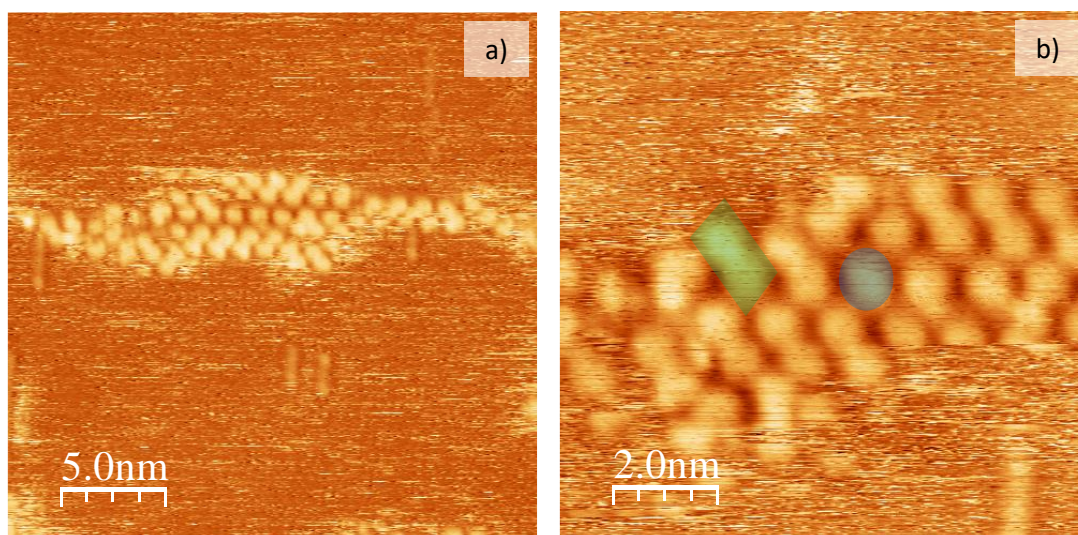


Figure 6.3.4. a) A complete molecular island without any visible Cu-O (2×1) reconstruction. b) Different features imaged within the island - a twin-lobed molecular feature in green and apparent single-lobed feature in blue.

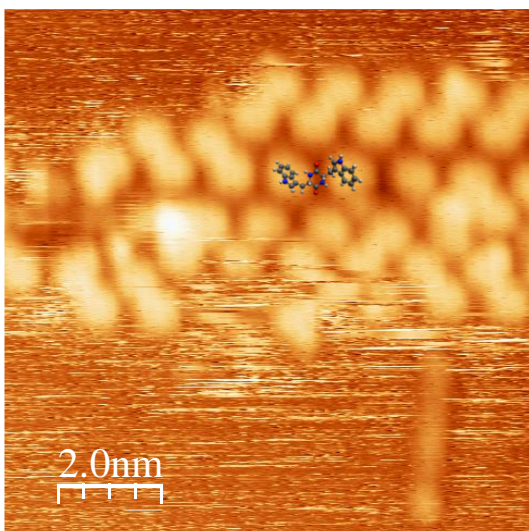


Figure 6.3.5. A scaled model of cWW overlain across two apparent single-lobed features, demonstrating the scale of the features with respect to an intact molecule. This Figure is hypothetical and does not represent a proposed conformation that could give rise to the observed data.

height than the nearby molecules, which suggests that they do not correspond to a 'standing up' molecule. The difference could instead be due to a conformational change of cWW, so that two apparently disparate lobes actually correspond to a single molecule, as proposed in Figure 6.3.5. It is proposed that these molecules are bound on top of oxygen stripes as discussed, which is evidenced by the reduced apparent height; as seen in Figure 6.3.3 and well-known in the literature, oxygen striping on Cu(110) often appears darker than the bare surface, which results in an artificially low height measurement.^{2,4,5} Such behaviour would explain the lack of directly visible oxygen stripes in this type of island. A final possibility is that molecular fragments are also deposited, and bind on top of oxygen stripes, hence the single lobe appearance. However, the mass spectrum of the sublimed material did not indicate any substantial fragments, and decomposition of the molecules upon landing is unlikely. Irrespective of the origin of this phenomenon, it only seems possible to occur in the smallest oxygen patches, however, as large bands do not display any such features at all. It may be the case that an alternative conformation of cWW, lying on top of the oxygen reconstruction, requires stabilisation by neighbouring rows of molecules in the original orientation described. In a wider band of oxygen (2x1), such an interaction would be weaker or even not possible.

Based on the mass spectrometry result for WW, and previous data on thermal dehydrogenation of cFF and cYY, it was assumed that all the intact molecules imaged in this deposition would be cWW. However, the molecular features in the images are quite uniform in height across their length, while the cWW molecules would be expected to give a more contoured appearance, in the same manner observed for STM data of cFF and cYY (see chapters 5 and 6.2). Flatter molecular profiles were only observed for ddcFF and ddcYY.

Additionally, minimising the energy of the cWW molecule in the Avogadro software results in conformers that do not fit well to the type of assembly imaged (though such models are only approximate). An alternative possibility is that the dehydrogenated molecule, ddcWW, is present on the surface, since the dehydrogenated species offers a considerably flatter molecular profile, one which could correlate with the flat features of the STM images. Overlaying the dehydrogenated molecule onto the STM images allows the construction of a feasible assembly model (Figure 6.3.6). Molecules in this arrangement have the potential for hydrogen bonding between rows, via the NH group in the side chains, and could potentially be anchored to the oxygen (2x1) reconstruction via the same NH functionality. Such interactions were not possible using the cyclised species, cYY. There remains however a significant gap breadthways between molecules along the rows, on the order of 0.40 nm, which is too large to allow intermolecular interactions such as hydrogen bonds and van der Waals forces. This might be because the anchoring of the molecules to the oxygen (2x1) reconstruction is significantly stronger than any intermolecular interactions, which fits with the above discussion of island dimensions. The positioning of molecules relative to one another is thus explained as a way of satisfying the need to bind to specific sites on the reconstruction, bringing molecules as close together as possible as a secondary concern, but not so close together as to clash with one another (Figure 6.3.7). It is important to note here that the molecular models used are for an isolated species in vacuum, so the conclusions drawn for the behaviour on a surface must be tempered somewhat. However, DFT and MD simulations for cYY and ddcYY did produce similar surface conformations to those in

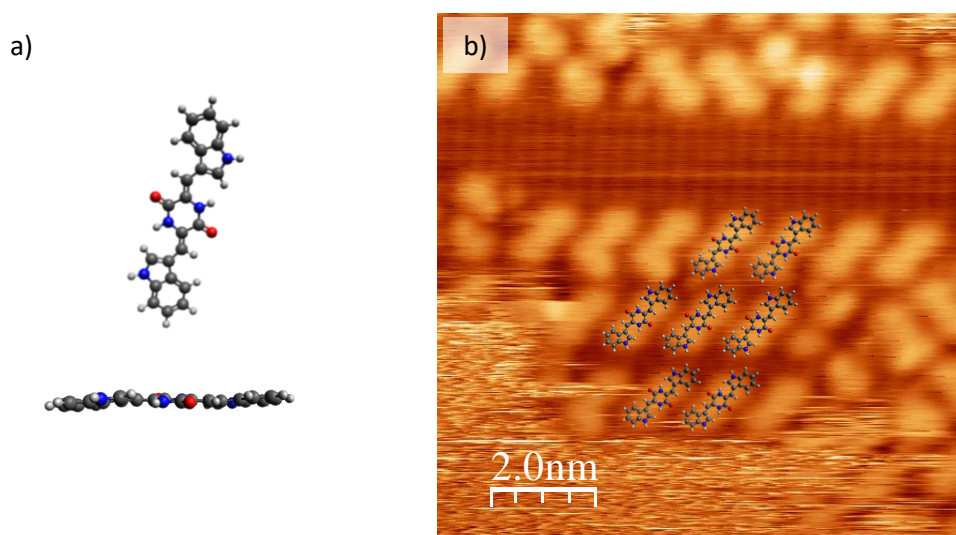


Figure 6.3.6. a) Top-down and side views of an energy-minimised ddcWW molecule (Avogadro). b) Overlay assembly of ddcWW on to rows of molecular features from STM. The shape and scale of these molecules is a good match for the data.

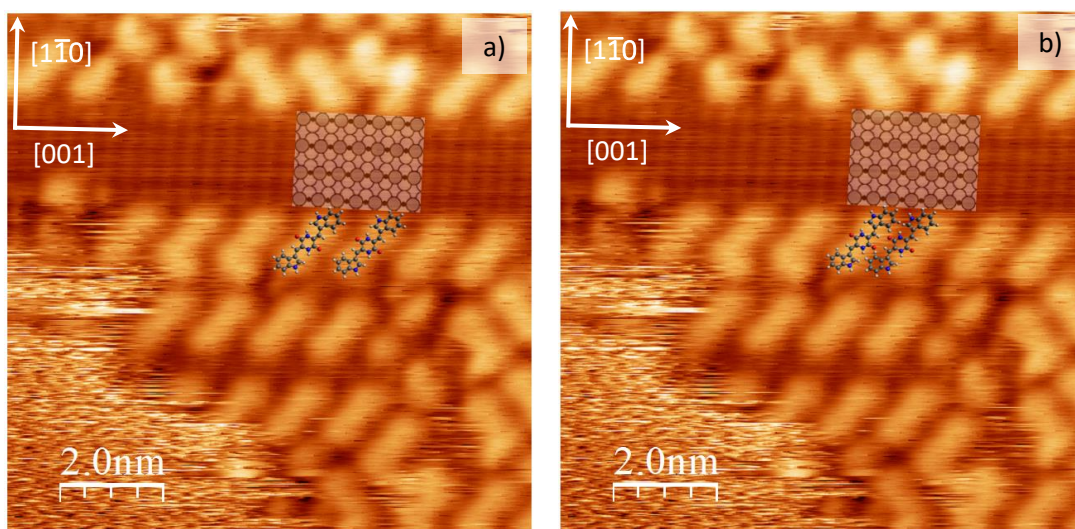


Figure 6.3.7. a) Overlain ddcWW molecules aligned with the Cu-O (2x1) reconstruction for a regular, repeating surface registry. This demonstrates how the observed features in the STM conform to this surface arrangement. b) A denser packing of ddcWW molecules that permits stronger intermolecular reactions, but disrupts the anchoring to the Cu-O (2x1) reconstruction.

vacuum, so it is reasonable to suggest that an analogous situation might be the case for cWW and ddcWW.

A question naturally arises from this description of the assembly, which is why the molecule should be dehydrogenated and not simply cyclised in this deposition. Mass spectrometry data indicated the cyclised species would be deposited, and previous experiments with cFF and cYY both required annealing of the surface to bring about a transition from cyclised to dehydrogenated species. Therefore, it is difficult to prove the presence of cWW without supporting evidence from spectroscopy or from simulations. However, analysis of the STM data is weighted considerably in favour of a dehydrogenated molecule, which better fits the images recorded, and a realistic reasoning for why the dehydrogenation occurs can be proposed here. The side chains of cWW consist of an indole group linked via a methylene bridge to the central ring, and this group crucially contains a secondary amine. In the previous work on cYY, nitrogen atoms were shown to play an important role in the anchoring of the molecule to the surface, and after dehydrogenation the heteroatom in the side chain (oxygen in that case) became heavily involved in the assembly via its bonding to adatoms. It is therefore likely that nitrogen in the side group of cWW also plays a significant role in its on-surface behaviour. When cWW lands on Cu(110) there is potential for the nitrogen to point downwards towards the surface without preventing the central ring also binding, and this would tend to agree with observations for lysine residues in the literature.⁶

A molecule-surface interaction that occurs through multiple bonding sites per molecule will be more stable and less prone to change or movement, much like the theory behind multidentate ligand stability in organometallic complexes. It is thus possible that this more stable bonding mode more easily facilitates the dehydrogenation process, by holding the relevant reactive groups in proximity with the surface for a greater period of time, whereas typically (e.g. with cFF or cYY) the side chains would be elevated from the surface. In addition, the surface is shown to be heavily contaminated with oxygen, and it may be the case that the presence of oxygen in some way accelerates the dehydrogenation process. It is certainly logical that the anchoring of the molecules near to the (2x1) reconstruction adds to the above stabilisation effect, even if the oxygen itself plays no additional role.

To establish whether an alternative molecular phase exists on the surface, unperturbed by oxygen but more mobile than the phase described above, the surface was cooled with liquid nitrogen to $\sim 115\text{K}$ to minimise thermal motion. However, scans of a cooled surface revealed no such assembly, as illustrated in Figure 6.3.8. Molecular bands around oxygen stripes are still prevalent, and smaller isolated clusters are rare and disordered. This adds weight to the argument that the bonding of the molecules to the (2x1) reconstruction is the primary driving force for the molecular aggregation observed, since the bonding between cWW and Cu-O band is stronger than that between cWW molecules. In some cases, islands were capable of growing larger than at room temperature (Figure 6.39). Images of these islands were not obtained in higher resolution due to tip instability, but from the scans gathered it appeared that a new type of ordering occurs in such an island. This illustrates that the previously discussed unusual spacing of the predominant molecular rows is indeed driven by the

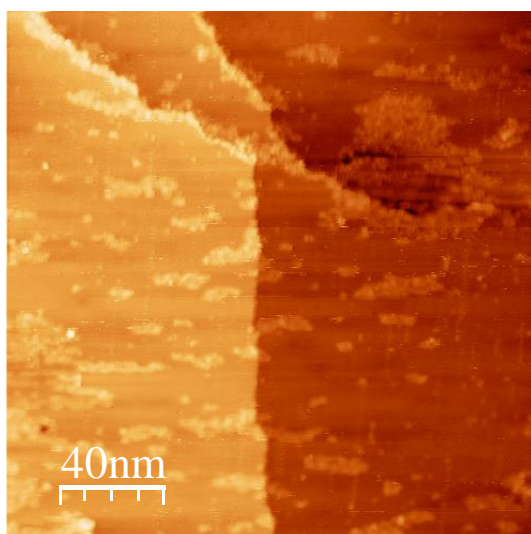


Figure 6.3.8. Typical STM image from a deposition of cWW on Cu(110), subsequently cooled to 115K. The assembly appears largely unchanged by the reduced thermal motion of molecules.

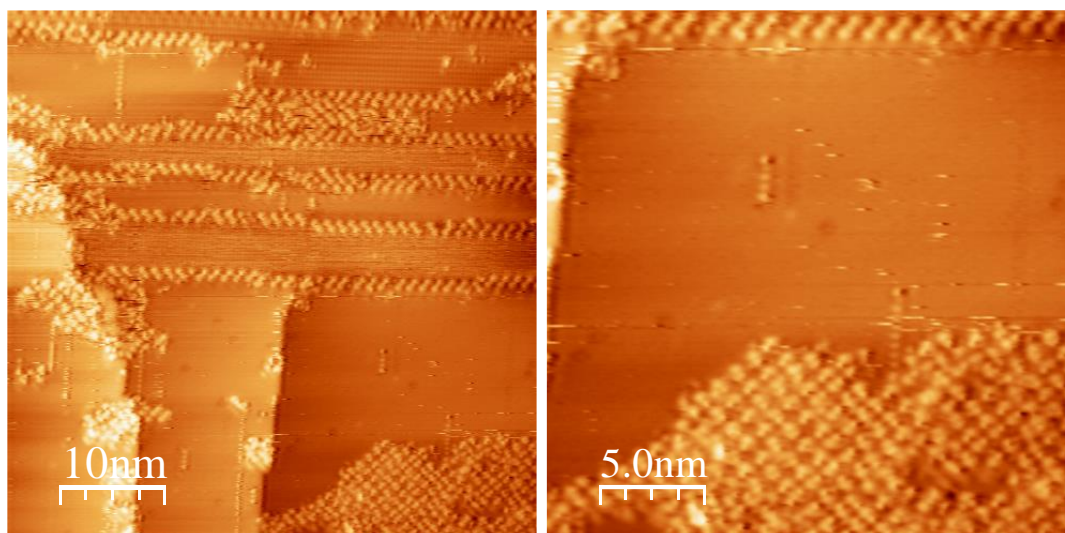


Figure 6.3.9. Low temperature (115K) STM images of the cWW deposition on Cu(110). a) Molecules demonstrated to still predominantly form rows around Cu-O (2x1) reconstruction patterns, though a larger island can be observed. b) Smaller scale scan of the larger island, illustrating the different type of molecular ordering within.

interaction with the (2x1) reconstruction. It is possible that aggregation into much larger islands would occur without the presence of oxygen breaking up the contiguous areas of flat surface, and these islands would then be more stable, but it is not possible to tell under the conditions of this experiment.

Attempts were made to reduce or eliminate the oxygen contamination of the Cu(110) surface by performing extensive sputtering and annealing cycles that were sufficient to clean the surface of visible oxygen. However, repeating the deposition resulted in a re-occurrence of the oxygen, along with the molecules again assembling adjacent to the (2x1) stripes. An overnight degassing of the WW/cWW crucible was carried out at the sublimation temperature to reduce the presence of water and impurities, in an effort to minimise the oxygen that could reach the surface. Unfortunately, many of the molecules also sublimed during this process, and subsequent deposition attempts on a newly cleaned surface yielded few molecules. Furthermore, oxygen levels on the surface still increased after a deposition. The oxygen was therefore unavoidable in the present experiment and is thought to be generated either as a product of the impurities in the sample, or as a by-product of the cyclisation process. Though the latter is known to produce water, the same reaction for YY and FF did not result in the presence of oxygen on Cu(110), and so it seems unlikely that the explanation lies here. A future experiment on WW/cWW would require thorough purification of the starting material to rule out any problems the contaminants cause.

6.3.4 Self-assembly of Cyclo-(L-Trp-L-Trp) on Au(111)

A submonolayer deposition of cWW, thermally cyclised in a crucible of WW, was carried out on a Au(111) surface using the same conditions as for Cu(110). At this level of molecular coverage, no stable images could be obtained of cWW on Au(111), and only after increasing the coverage could molecules occasionally be imaged along steps as in Figure 6.3.10. It was particularly likely to find molecules in regions of the surface where a number of steps were very close together.

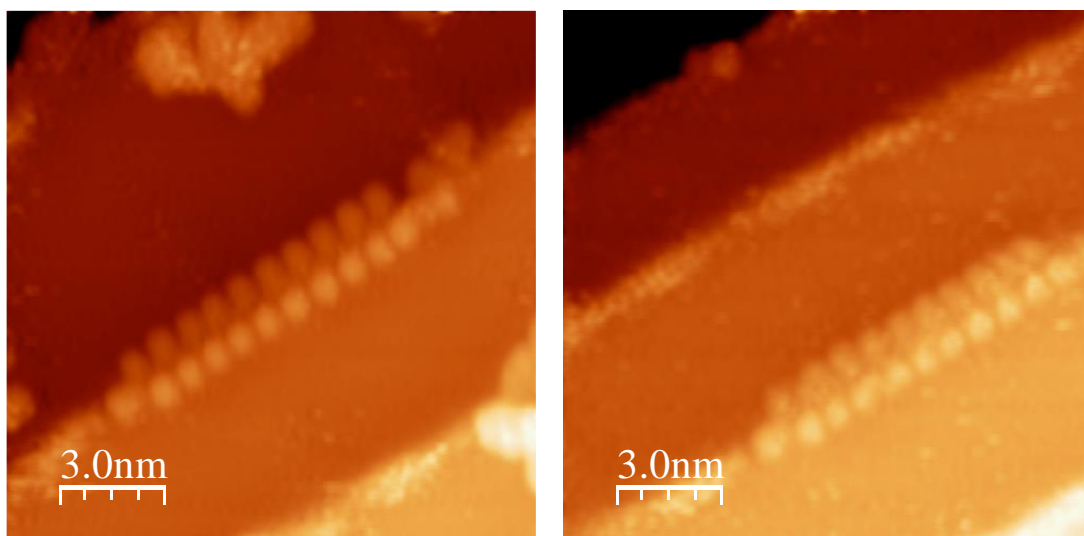


Figure 6.3.10. STM images from a deposition of cWW on Au(111). Such chains were the largest form of assembly observed across the surface, and exclusively found at steps.

The images obtained are of relatively low resolution, but it was possible to assess that molecules appear as twin-lobed species similar to those on Cu(110), anchored to the step via one lobe. Molecules lie adjacent to one another breadthways to form a short regular chain up to ten units long, with the potential for hydrogen bonding between DKP rings

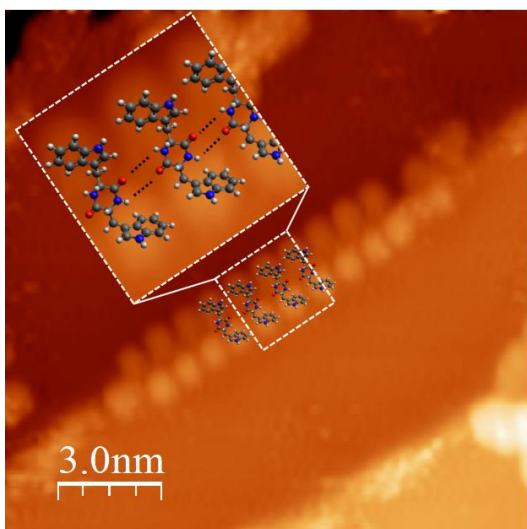


Figure 6.3.11. Overlain assembly of cWW molecular models on Au(111). The potential for hydrogen bonding between adjacent molecules is indicated in black. The conformation of the molecular models is illustrative and does not propose a firm theory for the adsorption. Inset image approximately 2.6 nm x 2.6 nm.

(see Figure 6.3.11). The ends of the chains notably appear distorted or irregular compared to the central repeat units. This anomalous appearance may be the product of molecular mobility at the chain ends. Continuous scans of the same area revealed that even these rare assemblies were unstable at room temperature, as illustrated in Figure 6.3.12, which shows three consecutive images where the chain visibly shrinks as molecules leave, until it disappears altogether. Overall the molecules are evidently highly mobile on the Au(111) surface. There is insufficient data to state whether the molecules are in the cyclised or dehydrogenated form on this surface, though it is anticipated that the cyclised form is more likely. This is based on the lower reactivity of the Au(111) surface compared to Cu(110), and the recorded higher activation temperature for dehydrogenation of cYY on Au(111) over Cu(110).

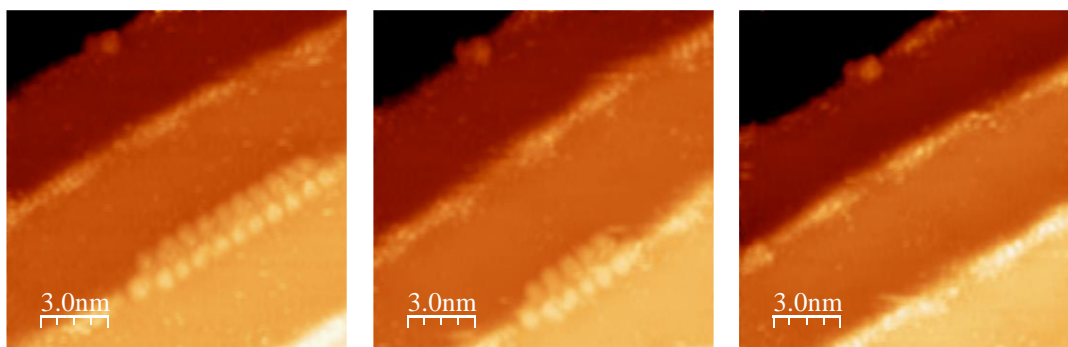


Figure 6.3.12. Sequential STM images of a deposition of cWW on Au(111), with approximately 90s passing between each image. The chain of molecules can be observed to shrink before completely disbanding, leaving the step free of adsorbed molecules.

6.3.5 Conclusion

In conclusion, L-Trp-L-Trp has been shown to cyclise upon thermal sublimation, in keeping with the behaviour of both L-Tyr-L-Tyr and L-Phe-L-Phe, and depositions of Cyclo-(L-Trp-L-Trp) were studied on Cu(110) and Au(111) on mica. STM data gathered on Au(111) was limited, but illustrated that the deposited molecules were highly mobile on the surface and only able to form assemblies stable enough to image at steps at room temperature. Scans of the adlayer on Cu(110) reveal that the molecules assemble exclusively around oxygen (2x1) stripes, which themselves are generated as a result of the deposition – either due to the presence of impurities in the crucible or water emission from the cyclisation process. The observed assembly is regular but of limited dimensions, and is primarily driven by the anchoring of the molecule to the (2x1) reconstruction. There is indication that the cWW

molecules might dehydrogenate on the Cu(110) surface at room temperature, though supporting data including XPS measurements and computational simulations would be required to confirm this hypothesis. Such an outcome would create an interesting contrast to cFF and cYY, both of which required surface annealing to bring about dehydrogenation, and thus could shed light on the dehydrogenation process itself and how to control it. The similarities in behaviour of the three molecules are however clear, and a degree of generality does begin to appear in this class of dipeptides with aromatic side chains. Further investigation into similar peptides is an essential next step in this study, followed by branching out into more diverse dipeptides, as already discussed in chapter 6.2 (“6.2 Self-assembly of L-Tyr-L-Tyr on metal surfaces”).

6.3.6 References

1. D. J. Coulman, J. Wintterlin, R. J. Behm and G. Ertl, *Phys. Rev. Lett.*, 1990, **64**, 1761.
2. F. Jensen, F. Besenbacher, E. Lægsgaard and I. Stensgaard, *Phys. Rev. B*, 1990, **41**, 10233.
3. S. Y. Liem, G. Kresse and J. H. R. Clarke, *Surf. Sci.*, 1998, **415**, 194–211.
4. L. D. Sun, M. Hohage, R. Denk and P. Zeppenfeld, *Phys. Rev. B*, 2007, **76**, 245412.
5. Q. Liu, L. Li, N. Cai, W. A. Saidi, and G. Zhou, *Surf. Sci.*, 2014, **627**, 75-84.
6. N. Kalashnyk, J.T. Nielsen, E.H. Nielsen, T. Skrydstrup, D. E. Otzen, E. Laegsgaard, C. Wang, F. Besenbacher, N. C. Nielsen and T. R. Linderoth, *ACS Nano*, 2012, **6**, 6882-6889.

Chapter 7: Conclusions

7.1 Conclusion and outlook

In recent years, short peptides have become increasingly common as candidates for the fabrication of functional nanostructured assemblies, with practical applications in multiple fields of research, including hydrogel formation, nanotube creation, drug discovery, and surface functionalisation. The ability of peptides to serve in such diverse applications is underpinned by the same core molecular features: biological relevance and biocompatibility, simple synthesis and ready availability, inherent chirality, functional group variation around a common backbone, and an intrinsic capability for self-assembly. The last of these properties is of particular interest in surface science, where building a surface molecular network with long-range order from small building blocks is a major research goal. The many beneficial qualities of short peptides make them molecules of great interest towards achieving this goal and, as such, their self-assembly behaviour on surfaces has been the focus of this thesis. The Cu(110) and Au(111) metal surfaces were used as prototypical substrates for these studies. Cu(110) serves as a highly chemically interacting substrate, with an anisotropic surface and therefore varying adsorption potential, while Au(111) represents more chemically inert surfaces, interacting less with adsorbed molecules and with a flatter adsorption potential. In addition, the thermally-induced chemical transformations of short peptides were explored, both as part of their sublimation behaviour and in terms of their on-surface reactions. In this way, a broad assessment of the potential of peptides for creating 2D self-assembled networks was carried out, an essential but still missing step in current research into this class of molecules.

In chapter 4, the sublimation of short peptides was studied in detail, using mass spectrometry to analyse the composition of peptide films deposited in high vacuum. Two peptide sequences were investigated as a function of chain length, those of alanine – the simplest chiral amino acid – and phenylalanine – a larger side chain that still does not form strong intermolecular bonds that might complicate the interpretation of the results. In both cases, the temperatures involved in the sublimation process resulted in fragmentation at a relatively short chain length; a pentapeptide of alanine displayed significant degradation post-sublimation, while the same was already true for a tetrapeptide of phenylalanine. Even amongst the shorter peptides some thermal transformations occurred, particularly with the dipeptide L-Phe-L-Phe (FF) displaying a strong tendency to cyclise when heated, even if not

subliming. The identity of cyclisation and fragmentation products was confirmed through the use of additional analytical tools including high resolution mass spectrometry and NMR spectroscopy. The data obtained, though only strictly representative of these two simple peptide series, strongly suggests that sublimation as a technique for depositing peptides in vacuum is substantially limited. Some variation between different peptides chains is inevitable, but the overall sublimation behaviour is not expected to differ greatly from the data gathered here, with peptides longer than 5-10 residues expected to be very unlikely to sublime intact. This result goes some way to explaining why so few UHV surface science studies of peptides on surfaces can be found, and indicates that alternative deposition strategies are essential if peptides are to be used to their full potential. In addition, the cyclisation reaction observed for Phe-Phe is of significant consequence both for historical studies of this dipeptide¹⁻⁴ and for the future use of similar molecules, which may display a similar behaviour.

In chapter 5, the deposition and self-assembly of the FF dipeptide was studied on a Cu(110) surface. To explore the cyclisation and on-surface reactions of this molecule, depositions were made of FF, Cyclo-Phe-Phe (cFF), and of both singly and double dehydrogenated versions of the cyclic molecule. STM and XPS data were acquired for each deposition, before and after annealing, enabling the thermal transformations of Phe-Phe to be followed, and the self-assembly pattern on Cu(110) to be better understood. Through the essentially indistinguishable datasets obtained from FF and cFF, it was demonstrated that FF must be deposited entirely as the cyclised species. Additionally, annealing these depositions produced XPS data that were identical to that obtained from a deposition of the doubly dehydrogenated species. The STM data was also a very close match, but with a key difference in chirality due to the method of generating the dehydrogenated prochiral species. These experiments proved that cFF undergoes an on-surface dehydrogenation, and in a single step since the singly dehydrogenated species is never observed. In fact, even a direct deposition of the singly dehydrogenated molecule gave the same end result, unless the sample was held at low temperature, indicating the strong driving force towards further dehydrogenation. The outcome of this set of experiments raises interesting considerations for controlling the chirality of a self-assembled monolayer on a surface. The deposition of a prochiral molecule normally gives rise to a racemic surface, but by generating the molecule on-surface from a chiral species, the stereochemistry is trapped in a single configuration based on the original adsorption. This, in essence, is a form of heterogeneous catalysis, facilitating the dehydrogenation and selecting for a single surface product. Such reactions can occur

routinely in biological systems, with the high-level of specificity that enzymes provide, but mimicking the synthesis in the lab is a multi-step process with a substantially lower yield.^{5,6} Therefore, it became of great interest to establish how general this on-surface reaction was, by studying peptides with similar chemistry – namely aromatic dipeptides.

In chapter 6, the experiments on further aromatic dipeptides (other than FF) were described. The molecules selected for study were the diastereomers of FF – namely L-Phe-D-Phe (LFDF) and D-Phe-L-Phe (DFLF) – as well as Tyr-Tyr (YY) and Trp-Trp (WW), which also possess aromatic side chains. It was determined that the cyclisation observed for FF also occurs consistently when subliming each of these peptides. This suggests a link between side chain structure and cyclisation, as other dipeptides lacking an aromatic group were shown to not cyclise in chapter 4. It is possible that the aromatic groups stabilise the transition state of the cyclisation reaction, via a favourable pi-cation/pseudocation interaction of the type known to the literature⁷⁻¹⁰ but this remains a hypothesis at this stage. Besides being a result of fundamental general interest, this cyclisation is also of considerable consequence for the vacuum deposition of short peptides, as it may be the case that aromatic dipeptides in general cannot be sublimed without cyclising. After these initial fundamental studies, the focus of chapter 6 is on the subsequent self-assembly of these deposited species, on Cu(110) and/or Au(111) surfaces.

The cFF(L/D) molecule, derived from the cyclisation of both LFDF and DFLF, was studied first. Being distinct from cFF(LL), the deposition of cFF(L/D) on Cu(110) produces a different end result for the stereochemistry of the surface. While dehydrogenating cFF(LL) on Cu(110) generates a single surface chirality, the same process for cFF(L/D) gives a racemic surface, much like what would be expected for a simple deposition of the dehydrogenated product. Evidently the chiral control is lost at some stage of the process for cFF(L/D), either in terms of the initial adsorption to the surface, or the dehydrogenation reaction itself. This is likely due to a difference in the optimal conformation of each molecule, a direct result of the change in stereochemistry. On a Au(111) surface, cFF(L/D) assembles into large islands of various orientations, appearing to be non-commensurate with the surface, reflecting the reduced interaction strength of a gold surface with respect to copper. Furthermore, upon annealing such a deposition, the dehydrogenation process seen on Cu(110) either does not occur, or the molecular layer is simply destroyed or sublimed. Therefore, while the surface dehydrogenation reaction of cFF is possible for all stereoisomers, the selection of a viable surface for the catalysis is nonetheless essential.

Subsequent experiments on the deposition of cYY revealed similar on-surface behaviour to cFF, with dehydrogenation again proving possible, though with some key differences. On a Cu(110) surface, cYY forms into chains much like cFF, albeit with a different orientation with respect to the copper surface directions. A further difference with cFF is that these chains were still relatively mobile at room temperature. Upon annealing, the orientation of the chains completely changes in a qualitatively similar fashion to annealed cFF, and reflects the changed chemical state of the molecules due to dehydrogenation, resulting in ddcYY. At higher molecular coverages, chains begin to assemble into islands but with low density lateral packing, indicating that chain formation is still the primary self-assembly motif, in contrast to high coverage data for ddcFF. The difference in the self-assembly is due to the inclusion of adatoms post-annealing, driven by the hydroxyl group of the tyrosine residues. An additional difference is seen in the chirality of the final surface state, with ddcYY generated by annealing not resulting in an enantiopure surface. The control of both the adsorption and dehydrogenation processes can clearly vary between molecules with only small structural differences, an important consideration when expanding the experiments to other aromatic dipeptides. On Au(111), cYY assembles into large islands rather than chains, but the assembly again undergoes a major change upon annealing. The islands transform into a large criss-cross network, which appears to lose its surface registry in favour a single dominant orientation. This transformation is again due to the dehydrogenation of cYY into ddcYY, a conclusion supported by XPS data as well as DFT and MD simulations. Here a major difference is seen between the on-surface reactions of cFF and cYY, as the former did not seem capable of dehydrogenating on a Au(111) surface. The dehydrogenation on gold is not, however, a simple reproduction of the reaction on Cu(110), as there is a noticeable difference in the chirality of the gold surface post annealing compared to copper. This reinforces the conclusion from the cFF data that the surface selection is highly relevant to the control of the dehydrogenation product. Overall, the self-assembly and thermally-induced surface reactions of cFF and cYY are highly similar, but with a considerable degree of variation possible due to a small chemical difference in the side chain. This adds considerable weight to the notion that such behaviour might be quite general across aromatic dipeptides.

The studies of cWW provided a more limited but still valuable contribution to the aromatic dipeptide series. On a Au(111) surface, cWW proved highly mobile and difficult to image,

indicative of a weak molecule-surface interaction. Based on cFF data, it might be expected that dehydrogenation is therefore not possible on Au(111) for cWW. On Cu(110), however, there is some indication that a cWW deposition immediately dehydrogenates on the surface, as the features in the observed assembly are much better described by the shape and size of a dehydrogenated species, and a more logical set of intermolecular binding motifs can be proposed. Complementary data from XPS, for example, would be required to support this analysis. Should the room temperature dehydrogenation of cWW be proven, then this molecule not only joins the class of aromatic dipeptides with broadly similar surface reactions, but demonstrates that even within this set a range of possible reaction conditions and stereochemical outcomes exist.

In summary, the results presented here demonstrate that while it may indeed be possible to suggest that all aromatic dipeptides will thermally cyclise when sublimed, and dehydrogenate on certain metal surfaces, the dehydrogenation is a complex process that is highly dependent on small variations in molecular structure, and on the surface selected. This in fact widens the potential use for such reactions, as the conditions can theoretically be tailored to suit a desired surface chirality and operating temperature, for example, by rational dipeptide design. Already demonstrated is the potential to generate ddcFF by several different means, with different chiral outcomes. In order to expand on this work, significant further study into the precise mechanism of on-surface dehydrogenation of dipeptides, and how it is affected by side chain structure, would be required. This could be partially tackled by the study of a number of other aromatic dipeptides with the same methods, including His-His but also mixed dipeptides such as Tyr-Phe and Trp-His. Working with additional metal surfaces would also be required, to further explain the role of the surface itself. A combination of STM and XPS data, together with theoretical simulations, could then provide a comprehensive body of data to help understand the reactions occurring; a method that has been applied in this thesis, especially for the case of Tyr-Tyr and its derivatives. The scope of the work also overlaps with other areas of chemistry, including organic synthesis and heterogeneous catalysis, both of which have been shown to be relevant to the on-surface dehydrogenation reactions discussed here. Therefore, the potential impact of a simple and reliable thermally-induced reaction on a surface is actually quite broad, and warrants considerable further investigation.

Discussed separately from the data on peptides in this thesis is the design and build of a new UHV-STM, in chapter 3. The rationale behind the overall structure of the system, as well as

details of individual design choices, is described. Crucially, the system was left open to expansion for molecular deposition techniques other than OMBE, with a particular intention to add an ESI deposition source. ESI has considerable potential for the vacuum deposition of peptides and other large molecules, as the technique is inherently soft enough to bring such molecules into the gas phase without fragmentation. Large proteins and DNA are just some of the molecules already deposited using this technique.¹¹⁻¹⁴ The use of ESI would enable many more peptides to be studied with surface science techniques such as STM, expanding the scope well beyond the limited pool offered by sublimation – as detailed in chapter 4. Additionally, aromatic dipeptides that have thus far universally cyclised when sublimed could be deposited in their linear state, enabling their self-assembly to be studied, as well as allowing the cyclisation process itself to be examined on-surface. Working with both OMBE and ESI in tandem would therefore offer the best chance to further understand the thermally-induced chemical transformations of short peptides.

7.2 References

1. M. Lingenfelder, PhD thesis, 2007, EPF Lausanne, Switzerland.
2. G. Tomba, M. Lingenfelder, G. Costantini, K. Kern, F. Klappenberger, J. V. Barth, L. C. Ciacchi and A. De Vita, *J. Phys. Chem. A*, 2007, **111**, 12740-12748.
3. Y. Wang, M. Lingenfelder, T. Classen, G. Costantini and K. Kern, *J. Am. Chem. Soc.*, 2007, **129**, 15742-15743.
4. M. Lingenfelder, G. Tomba, G. Costantini, L. C. Ciacchi, A. De Vita and K. Kern, *Angew. Chem. Int. Ed.*, 2007, **46**, 4492-4495.
5. S. Ando, A. L. Grote and K. Koide, *J. Org. Chem.*, 2011, **76**, 1155–1158.
6. A. D. Borthwick, *Chem. Rev.*, 2012, **112** (7), 3641-3716.
7. A. McCurdy, L. Jimenez, D. A. Stauffer and D. A. Dougherty, *J. Am. Chem. Soc.*, 1992, **114**, 10314–10321.
8. D. A. Dougherty, *Science*, 1996, **271**, 5246, 163-168.
9. S. Mecozzi, A. P. West and D. A. Dougherty, *Proc. Natl. Acad. Sci. USA*, 1996, **93**, 10566-10571.
10. G. Cooke and V. M. Rotello, *Chem. Soc. Rev.*, 2002, **31**, 275–286.
11. V. N. Morozov and T. Y. Morozova, *Anal. Chem.*, 1999, **71** (7), 1415-1420.
12. S. Rauschenbach, F. L. Stadler, E. Lunedei, N. Malinowski, S. Koltsov, G. Costantini and K. Kern, *Small*, 2006, **2**, 540–547.
13. C. Hamann, R. Woltmann, I. P. Hong, N. Hauptmann, S. Karan and R. Berndt, *Rev. Sci. Instrum.*, 2011, **82**, 033903.
14. Z. Deng, N. Thontasen, N. Malinowski, G. Rinke, L. Harnau, S. Rauschenbach and K. Kern, *Nano Lett.*, 2012, **12**, 2452–2458.